

Copyright  
by  
Siddharth Sood  
2013

**The Thesis Committee for Siddharth Sood  
Certifies that this is the approved version of the following thesis:**

**Analysis of Single Axis Flexure Bearings Approaching  
Ideal Bearing Characteristics**

**APPROVED BY  
SUPERVISING COMMITTEE:**

**Supervisor:**

---

Shorya Awtar

**Analysis of Single Axis Flexure Mechanisms Approaching Ideal Bearing  
Characteristics**

**by**

**Siddharth Sood, B.Tech.**

**Thesis**

Presented to the Faculty of the Graduate School of  
The University of Michigan in Partial Fulfillment  
of the Requirements for the Degree of

**Master of Science in Mechanical Engineering**

**The University of Michigan**

**Aug, 2013**

## **Acknowledgements**

I am very grateful to my advisor for sparking my interest in flexure mechanisms and sustaining it with stimulating conversations, remarkable insights and unwavering support. Especially, his ability to pick out the questions which at first glance appear to have deceptively simple solutions but seldom do, is one which I revere and envy the most. I am also very thankful to him for giving priority to my intellectual development as a researcher with exposure to a broad mix of tasks ranging from purely theoretical analysis to experimental setup design and implementation. He also helped me develop some aspects of research that I didn't attach sufficient importance to – writing and presentation skills. It is because of his constant encouragement and patience with me that I have been able to complete this thesis.

I would also like to thank my colleague Mohammad Olfatnia for fabricating and testing the comb-drive actuators with the optimized flexure designs. With his expertise in MEMS, we were able to address some issues specific to the realm of micro-scale devices which had to be incorporated into the design process of the flexure bearings in order to prevent any loss of performance.

Finally, I would like to express my gratitude for my colleagues – Shiladitya Sen, Gaurav Parmar and Anadi Bhatia. Shiladitya provided vital assistance in helping me build a strong foundation for the analysis of flexure mechanisms. With his instrumentation experience, Gaurav was extremely helpful in providing valuable technical support for setting up and troubleshooting sensors and actuators that I used in my experiment. Anadi

helped jump-start the project on the macro-scale validation of the CDPDP mechanism by assisting me with the FEA validation using ANSYS and CAD design in Solidworks. Without them, completing this project would have proved to be a formidable task.

## **Abstract**

### **Analysis of Single Axis Flexure Mechanisms Approaching Ideal Bearing Characteristics**

Siddharth Sood, M.S.

The University of Michigan, 2013

Supervisor: Shorya Awtar

This thesis presents analysis and metrics for comparing the bearing performance of single axis (linear) planar flexure mechanisms. In particular, analysis of two previously reported flexure mechanisms – the clamped paired double parallelogram (CDPDP) and the double parallelogram-double tilted beam (DP-TDP) parallelogram is presented which offer superior bearing performance compared to some conventionally used designs in terms of the metrics – range of motion, parasitic/off-axis motions, motion direction and bearing direction stiffness. Design of a macro-scale experiment in order to validate the closed form results obtained for the CDPDP mechanism is discussed and some preliminary results have been reported. Finally, as a case study, a holistic design procedure for comb-drive actuators employing the CDPDP and DP-TDP mechanisms is introduced with the objectives of obtaining large stroke with minimum actuator effort. For the flexure mechanism used, these objectives roughly translate into the goal for approaching ideal bearing characteristics namely – large range, negligible error motions,

small motion direction stiffness and large bearing direction stiffness. The devices designed using this procedure were separately fabricated and were shown to achieve much larger strokes compared to commonly used comb drive actuator designs.

## Table of Contents

List of Tables .....	xii
List of Figures .....	xiii
Chapter 1: Introduction .....	19
Chapter 2: Background .....	31
Direct Approach: Beam Constraint Model .....	31
Strain Energy Approach.....	43
Chapter 3: Prior Art .....	45
Two-Beam Parallelogram .....	45
BCM Analysis.....	45
Strain Energy Analysis .....	46
Performance .....	52
Range of Motion .....	52
Error Motions.....	52
Motion Direction Stiffness.....	55
Bearing Direction Stiffness.....	55
Multi-Beam Parallelogram.....	57
BCM Analysis.....	58
Strain Energy Analysis .....	59
Performance .....	59
Range of Motion .....	59



Error Motions.....	60
Motion Direction Stiffness.....	60
Bearing Direction Stiffness.....	60
Double Parallelogram and Paired Double Parallelogram .....	63
BCM Analysis.....	63
Strain Energy Method.....	64
Performance .....	67
Range of Motion .....	67
Error Motions.....	67
Motion Direction Stiffness.....	68
Bearing Direction Stiffness/Compliance .....	68
Lever-Double Parallelogram and Lever-Paired Double Parallelogram.....	74
Chapter 4: Novel Mechanisms: Clamped Paired Double Parallelogram (CDPDP) and Double Parallelogram – Tilted-beam Double Parallelogram (DP-DTB) .....	78
The Clamped Paired Double Parallelogram .....	78
BCM Analysis.....	82
Performance .....	92
Range of motion.....	93
Error motions .....	93
Motion Direction Stiffness.....	94
Bearing Direction Stiffness.....	98
The Double Parallelogram – Tilted-beam Double Parallelogram (DP-DTB)	102

Performance .....	105
Error motions .....	105
Motion Direction Stiffness.....	106
Bearing Direction Stiffness.....	107
 Chapter 5: Experimental Validation of the Clamped Paired Double Parallelogram (CDPDP) mechanism.....	 110
Measurement Scheme .....	110
Design of the setup.....	115
Actuation.....	115
Sensing.....	118
Manufacturing process and material selection.....	119
Design of Auxiliary Components and Dimensions .....	121
Error Analysis .....	126
Errors in Motion direction stiffness .....	127
Errors in bearing direction stiffness ( $K_x$ and $K_\theta$ ).....	127
Uncertainty in parasitic motions ( $E_x$ and $E_\theta$ ).....	129
FEA Validation and predicted results .....	129
Preliminary Results.....	134
 Chapter 6: Case Study: Comb drive optimization .....	 135
CDPDP optimization .....	137
Stroke Comparison.....	149
DP-TDP Optimization .....	151

Chapter 7: Conclusions and Future Work.....	160
Contributions.....	160
Future Work.....	163
Appendix A.....	166
BCM coefficients as functions of beam reinforcement $a_0$ .....	166
Appendix B.....	169
Justification and guidelines for approximations used in the derivation of the stiffness expressions for the CDPDP mechanism.....	169
Rotational stiffness of the clamp parallelograms (Equation (4.5))....	169
Motion direction stiffness of the clamp parallelograms (equation (4.6))	169
Appendix C.....	171
Upper bound on the clamp effectiveness imposed by finite rotational stiffness of the DP units in the CDPDP mechanism.....	171
Appendix D.....	174
Notes on the Center of stiffness of the Clamped paired double parallelogram mechanism .....	174
Location of the COS .....	174
X-direction displacement at COS .....	177
Appendix E.....	180
Derivation of the limit on pre-bending for comb drive actuators .....	180
References.....	182

## List of Tables

Table 1: Order of Magnitude estimates for a parallelogram.....	47
Table 2: Order of Magnitude estimates for a double parallelogram.....	64
Table 3: Typical dimensions for the clamp.....	86
Table 4: Effect of $\eta$ on displacement variables.....	89
Table 5: Dimensions of the DP-TDP flexure used in the FEA analysis.....	104
Table 6: Dimensions of the CDPDP mechanism.....	120
Table 7: Parameters of the measurement scheme.....	123
Table 8: Comb-drive actuators that were designed, fabricated, and tested. All dimensions are in micrometers.....	149
Table 9: Comb-drive actuators that were micro-fabricated and tested. Comb-drive dimensions are same in all cases: $G = 5 \mu\text{m}$ , comb-finger length $L_f = 190 \mu\text{m}$ , in-plane thickness $T_f = 6 \mu\text{m}$ , out-of-plane thickness $H_f = 50 \mu\text{m}$ , and $N = 70$ . Flexure beam length $L = 1000 \mu\text{m}$ and in-plane thickness $T = 3 \mu\text{m}$ in all cases. All dimensions are in microns. .....	157

## List of Figures

Figure 1: A Single Axis Bearing.....	19
Figure 2: A comb drive actuator with a flexure bearing[35] .....	22
Figure 3: Comb drive Parameters. The displacements of the mover comb in the bearing directions can be split into error motions ( $E_x, E_\theta$ ) and spring deformations ( $U_x, \theta_z$ ) as shown.....	24
Figure 4: Generalized Snap-In.....	27
Figure 5: A simple beam with a uniform cross-section .....	31
Figure 6: The S-Shaped Beam .....	33
Figure 7: A lumped compliance beam. In all future instances we would dimension a lumped compliance beam as follows (length i.e. $l$ , degree of compliance i.e $a_0$ ) without explicitly showing the rigid section. ....	37
Figure 8: Symmetry argument for calculating the maximum moment.....	38
Figure 9: Pre-bent Beam configuration.....	41
Figure 10: The parallelogram mechanism .....	46
Figure 11: Non-dimensionalized performance metrics for a parallelogram mechanism. Parameters: $t=1/50$ , $w=0.3$ , $S_y=1\text{GPa}$ , $E=169\text{GPa}$ .....	56
Figure 12: The multi-beam parallelogram .....	57
Figure 13: Comparison between the multi-beam and the two beam parallelograms.....	61
Figure 14: Stiffness Ratios of the flexures A,B and C.....	62
Figure 15: The Double Parallelogram and Paired Double Parallelogram Mechanisms. The forces and displacements at the secondary stages are also indicated.....	63
Figure 16: Stiffness ratio comparison between the double parallelogram and the parallelogram mechanisms. $T=1/50L$ , $a_0=0.5$ .....	70
Figure 17: Non-dimensionalized performance metrics for a double parallelogram mechanism. Parameters: $t=2/(50*N)$ , $w_1=0.25$ , $w_2=0.4$ , $S_y=1\text{GPa}$ , $E=169\text{GPa}$ . ....	71
Figure 18: The Lever Double Parallelogram .....	74

Figure 19: Bearing Direction Stiffness $K_x$ of the Lever Double Parallelogram (LDP). Parameters: $T=0.0123L$ , $H=0.39L$ , $E=69e9$ .....	75
Figure 20: Motion Direction Stiffness $K_y$ of the Lever Double Parallelogram (LDP). Parameters: same as those in Figure 19 .....	76
Figure 21: Exponential Rise in the motion direction stiffness of the LDP mechanism. Parameters: $L_1=L_2=L_3=0.1L$ , rest same as before.....	77
Figure 22: Response of the DPDP mechanism to an axial force $F_x$ . The differential displacement $\Delta$ would depend on $U_y$ and $F_x$ .....	79
Figure 23: The Clamped paired double parallelogram mechanism. The dimensions of the base DPDP mechanism are the same as before. ....	79
Figure 24: The constraint behavior of the CDPDP mechanism.....	80
Figure 25: Free Body Diagram of the CDPDP mechanism showing internal forces and moments .....	83
Figure 26: Response of the CDPDP mechanism to an external moment .....	91
Figure 27: Rotational stiffness of the CDPDP mechanism for different clamp dimension, $K_{\theta}(u_y=0)=2.7e^4Nm$ . $a_0^c=0.5$ , $h=h_3$ , $t=t_3=1/50$ , $l_2=1.4$ . Dimensions of the DPDP same as before. ....	91
Figure 28: CDPDP Mechanism with multiple grouped reinforced beam flexures. Normalization would still be done w.r.t the original parameters ( $T$ and $T_3$ ).....	93
Figure 29: The motion direction stiffness of the CDPDP mechanism for different dimensions of the clamp. The solid lines represent the predicted values whereas the circles show the corresponding FEA results. $w_1=1.0$ , $w_2=0.8$ , $l_2=0.9$ , $t=t_3=1/50$ , $h=h_3$ ...	94
Figure 30: Softening due to bearing direction loads in the motion direction. At large values of effectiveness, there is a clear discrepancy between FEA and closed form results .....	96
Figure 31: Softening in the motion direction due to bearing direction loads. Comparison between closed form solution with second order correction and corresponding FEA results .....	97

Figure 32: The bearing stiffness of the CDPDP mechanism for different values of effectiveness. The solid lines represent the predicted values whereas the circles show the corresponding FEA results. $w_1=1.0, w_2=0.8, l_2=0.9, t=t_3=1/50, h=h_3$ .	99
Figure 33: Bearing stiffness for $w_1=0.3, w_2=0.2, l_2=0.9, t=t_3=1/50, h=h_3$ .	99
Figure 34: Reason for discrepancy between predicted and FEA results at large values of effectiveness.	100
Figure 35: $l_3 _{\min}$ and $w_3 _{\min}$ for different clamp variations	102
Figure 36: The Double Parallelogram- Tilted Beam Double Parallelogram (DP-TDP).	103
Figure 37: Constraint behavior of the TDP flexure	104
Figure 38: X error motions of the DP-TDP mechanism. $\alpha, \beta$ are in radians.	105
Figure 39: Theta error motions of the DP-TDP mechanism.	106
Figure 40: Motion direction stiffness of the DP-TDP flexure	107
Figure 41: X direction stiffness of the DP-TDP flexure	108
Figure 42: $\theta$ Direction Stiffness of the DP-TDP mechanism	108
Figure 43: Center of stiffness of the mechanism	110
Figure 44: The placement of the sensors for measuring x-direction displacements and rotations of the stage.	113
Figure 45: Force application on the primary stage. Also, $\Delta U_{s11} = U_{s11} _{\text{load}=F_x1} - U_{s11} _{\text{no-load}}$ .	114
Figure 46: The DC-mic assembly	115
Figure 47: Three-string junction for load transmission to the primary stage of the mechanism	117
Figure 48: Top view of the three string junction. The manual stage can be moved in the y direction to keep marginal contact with the alignment pin.	117
Figure 49: Integration of the load-cell in the DC-mic assembly	118
Figure 50: Cap-probe assembly	119
Figure 51: The CDPDP flexure plate	121
Figure 52: The actuator isolator with dimension labels.	122
Figure 53: Implementation of the measurement scheme shown in Figure 45. $D^*=D-R_2-S/2$	122

Figure 54: Fillets at flexure supports .....	124
Figure 55: Thickness of rigid sections and stages .....	125
Figure 56: Complete Experimental Setup - 1) Dc-Mic, 2) Flexure Clamp, 3) Load Cell, 4) Actuator Isolator, 5) Cap-probes, 6) CDPDP mechanism, 7) DC-Mic amplifier, 8) Cap-probe amplifier, 9) NI USB-DAQ, 10) Alignment plate, 11) String for applying load, 12) Alignment pins, 13) Suspended Weight, 14) Manual stage and post.....	126
Figure 57: Sign conventions used for the experiment .....	129
Figure 58: Motion direction stiffness for the CDPDP flexure plate .....	130
Figure 59: X direction stiffness for the CDPDP flexure plate .....	131
Figure 60: Rotational stiffness for the CDPDP flexure plate .....	131
Figure 61: Location of the COS for the CDPDP flexure plate. The closed form expressions are given by equation (D.10).....	132
Figure 62: The expected displacement at the first cap-probe (S1) for loading on pin 1 and pin 2. ....	133
Figure 63: The expected rotations of the stage for loading on pin 1 and pin 2. Rotations are in radians. ....	133
Figure 64: Experimentally measured motion direction force vs. displacement curve....	134
Figure 65: Pre-Bending in a DPDP flexure .....	135
Figure 66: Effect of pre-bending on the stroke of a comb drive actuator. At the critical pre-bend, the stiffness ratio curve intersects the required stiffness curve at exactly 3 points.....	135
Figure 67: Design and performance space for a C-DP-DP flexure based comb-drive actuators .....	141
Figure 68: Reduction in predicted actuation stroke in the presence of finite rotational stiffness .....	143
Figure 69: A CDPDP comb drive actuator layout. All rigid sections are assumed to be of the same thickness $R_t$ .....	145
Figure 70: SEM image of a micro-fabricated comb-drive actuator employing the C-DP-DP flexure[32]. ....	147



Figure 71: The DP-TDP comb drive actuator layout.....	152
Figure 72: Contour plot of $E_x(m)$ for the DP-TDP mechanism. The tilt angles are in radians. ....	153
Figure 73: Contour plot of $E_\theta$ (in radians) for the DP-TDP mechanism. ....	154
Figure 74: Contour plot of $K_y$ (in N/m) for the DP-TDP mechanism. ....	155
Figure 75: Contour plot of $K_x$ (in N/m) for the DP-TDP mechanism. ....	155
Figure 76: Contour plot of $K_\theta/(K_x L^2_{off})$ for the DP-TDP mechanism. ....	156
Figure 77: Plot of the objective function for $U_y=0.2L$ . The maximum occurs at $\alpha=0.14$ , $\beta=0.17$ . The $(1+S)$ used here is simply the theoretical factor due to axial error motion ( $E_x$ ) and does not include the effect of imperfections .....	156
Figure 78: SEM image of micro-fabricated comb-drive actuators based on the DP-DP and DP-TDP flexures.....	158
Figure 79: Performance comparison between different comb drive actuators. The references are as follows: Legtenberg, 1996 [33], Chen, 2003 [66], Grade, 2003 [34], Grade, 2004 [67], Zhou, 2004 [37], .....	158
Figure 84: Bearing stiffness of the CDPDP mechanism with a revised value of effectiveness. $w_1=0.3$ , $w_2=0.2$ , $l_2=0.9$ , $t=1/50$ , $h=h_3$ .....	173
Figure 85: The simplified model of a near-ideal CDPDP mechanism .....	174
Figure 86: Comparison between theoretical (linear model) and FEA COS for $w_1=1.0$ , $w_2=0.8$ , $t=0.0123$ , $w_{off}=0.1$ , $w_3=0.5$ , $l_3=0.3$ . Almost no sensitivity was observed w.r.t. $f_x$ . ....	176
Figure 87: Special case of the CDPDP design.....	177
Figure 88: Right half of the CDPDP mechanism when a force is applied exactly at the COS.....	178
Figure 89: Closed form and FEA x-direction stiffness for the CDPDP design used in the experiment (Figure 51 ) .....	179

*For my parents*

## Chapter 1: Introduction

Flexure mechanisms comprise of a set of bodies, both rigid and compliant and provide motion guidance through the elastic deformation of its flexible members [1, 2]. Given their lack of traditional joints, flexure mechanisms completely eliminate friction and backlash, leading to smooth, repeatable and maintenance-free operation [3-5]. These merits make flexure mechanisms suitable for many precision guidance applications [6-15]. Moreover, their monolithic construction makes them suitable for water-jet and wire-electric discharge machining at the macro-scale and photolithography based fabrication techniques at the micro-scale. Thus, compared to their rigid-link counterparts with movable joints (e.g. revolute and prismatic joints), flexure mechanisms are simpler to fabricate and assemble thereby reducing cost and maintenance requirements. Finally, flexure mechanisms can be made very compact and light which is desirable for many aerospace applications [16, 17] and essential for MEMS [7, 18-22].

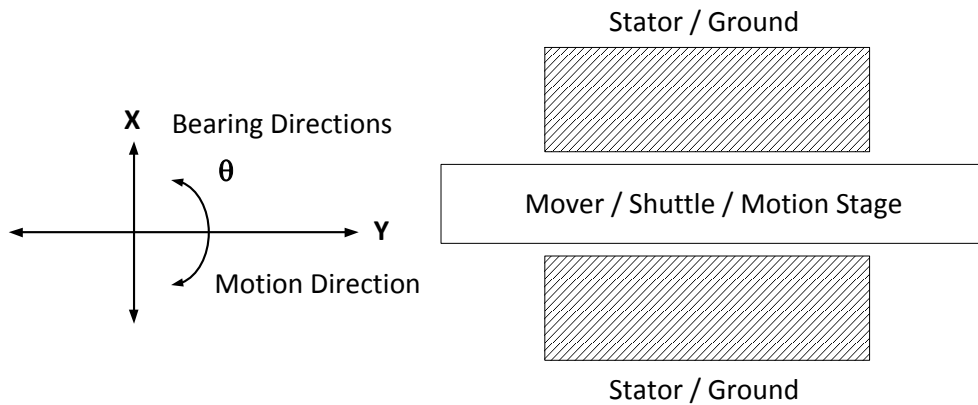


Figure 1: A Single Axis Bearing

From the perspective of precision machine design, flexures can be thought of as a means for providing constraints. Ideally, a constraining element or a *bearing* should provide infinite stiffness and zero displacements along certain directions, known as the *Degrees of Constraint* (DOC), and allow infinite motion and zero stiffness or resistance in all other directions, referred to as the *Degrees of Freedom* (DOF) [23, 24]. Moreover, these

attributes of the element remain unchanged over the whole range of motion. However, a flexure mechanism might fail to provide all of the above. Hence, in order to determine the quality or the *performance* of the flexure bearing, there is a need to formulate a set of metrics that can help compare it quantitatively with other bearing designs based on their deviation from ideal behavior. We are also interested in revealing and quantifying design tradeoffs between these metrics for a given flexure bearing. It should be noted that these would apply to any general non-ideal bearing and not just a flexure based one. All the analysis done in this thesis would be purely static and dynamic performance metrics like bandwidth would not be a discussed in great detail although some valuable insights about them can be obtained from the static analysis. In this thesis, we will focus specifically on planar single axis linear systems, which can be used as building blocks or modules for multi-axis systems [23, 25-30]. A single axis system with DOCs ( $x, \theta_z$ ) and DOF ( $y$ ) is shown in Figure 1. Displacements along the  $x, y$  and  $\theta$  directions are named  $U_x, U_y$  and  $\theta_z$  respectively. It is assumed that the out of plane directions ( $\theta_x, \theta_y, z$ ) would be adequately constrained and hence, wouldn't be dealt with specifically here. Thus, for single axis planar bearings, the metrics are listed below along with their corresponding design optimization goals that would enable these bearings to approach ideal behavior:

**1. Range of Motion ( $U_{y/max}$ )**

The range of motion along the degree of freedom ( $y$ ) of a single axis flexure bearing is limited by yielding or fracture of the constituent flexure beams and is thus finite. Thus, the first objective of the design optimization would be to:

$$\text{Maximize}(U_y |_{\text{yield/fracture}}) \quad (1.1)$$

**2. Error motions ( $E_x, E_\theta$ )**

Any deviations from ideal straight line motion along the degree of freedom in the absence of any external bearing direction loads are called *parasitic error* motions [23, 24]. The cause could be elastic deformation or kinematics of the mechanism and/or geometric

imperfections due to fabrications and are generally undesirable. Therefore, it is required to keep these as small as possible over the entire range of motion i.e.

$$\text{Minimize}(E_x(U_y)|_{\max}, E_\theta(U_y)|_{\max}) \quad (1.2)$$

### 3. Motion Direction Stiffness ( $K_y$ )

In a flexure bearing, the motion direction stiffness is usually small but finite. Apart from this, it may also vary with increasing displacement (Load-stiffening [31]) which leads to undesirable non-linearity. Stiffening also leads to an increased actuator effort. For example, in a comb drive actuator, the actuator displacement is calculated using the equilibrium relation between the spring and the electrostatic force. An increase in motion direction stiffness would lead to an increased spring force for the same motion direction displacement thereby requiring a greater electrostatic force and hence, a greater actuation voltage [32-34]. Thus, we need to impose the following restrictions on  $K_y$ :

$$\begin{aligned} &\text{Minimize}(K_y(U_y)|_{U_y=0}) \\ &\text{Minimize}\left(\left|\frac{\partial K_y(U_y)}{\partial U_y}\right|_{\max}\right) \end{aligned} \quad (1.3)$$

In a general bearing, we would aim to reduce the resistance to motion which could stem from a spring stiffness or friction. In applications that emphasize dynamic performance, this condition may have to be relaxed, or least bounded. This is because  $K_y$  dictates the resonant frequency of the motion systems.

### 4. Bearing Direction Stiffness ( $K_x$ )

The bearing direction stiffness of a flexure bearing is large but still finite. Also, it may vary, (in some cases, drop very sharply) with increasing  $y$  displacement. Thus, over the whole motion range, the following should be the objectives:

$$\begin{aligned}
& \text{Maximize}(K_x(U_y)|_{U_y=0}, K_\theta(U_y)|_{U_y=0}) \\
& \text{Minimize}\left(\left|\frac{\partial K_x(U_y)}{\partial U_y}\right|_{\max}, \left|\frac{\partial K_\theta(U_y)}{\partial U_y}\right|_{\max}\right)
\end{aligned} \tag{1.4}$$

The above conditions can also be formulated in terms of the compliance,  $C=1/K$ , and alternatively we can write:

$$\begin{aligned}
& \text{Minimize}(C_x(U_y)|_{y=0}, C_\theta(U_y)|_{y=0}) \\
& \text{Minimize}\left(\left|\frac{\partial C_x(U_y)}{\partial U_y}\right|_{\max}, \left|\frac{\partial C_\theta(U_y)}{\partial U_y}\right|_{\max}\right)
\end{aligned} \tag{1.5}$$

Depending on the application requirements, we can choose the weighing terms for each of these conditions in the design optimization of the mechanism.

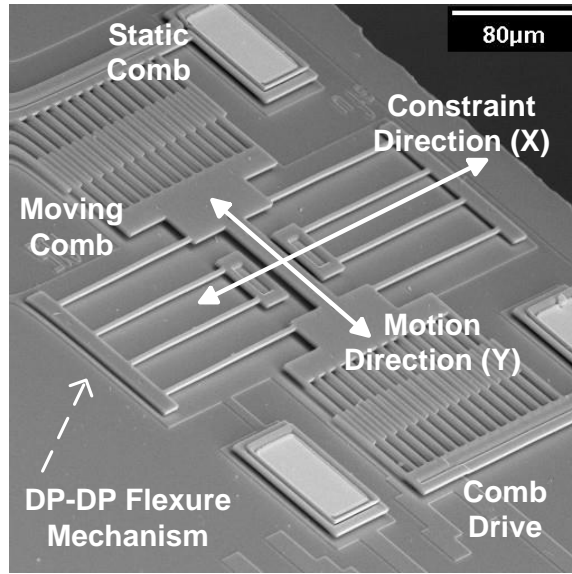


Figure 2: A comb drive actuator with a flexure bearing[35]

To illustrate the effect of non-ideal bearing behavior on the performance of a device and application specific design optimization of a flexure mechanism with the above-mentioned constraints, we can consider the use of flexure bearings in MEMS comb-drive actuators (Figure 2). Because of their numerous advantages highlighted previously, flexure mechanisms are often employed to provide motion guidance in these actuators

[32-34, 36, 37]. The strokes of these actuators get limited because of the phenomenon of *electrostatic snap-in*. This occurs when the bearing direction stiffness is inadequate to resist the electrostatic attraction forces along the same direction causing the moving comb to snap into the static comb. This limit is usually much lower than the yield/fracture limit of the flexure bearing and can get lowered further in the presence of error motions. *Snap-in* has been analyzed extensively in literature [34, 38, 39] and the maximum displacement before snap-in with zero error motions of the mechanism is given by the following equation:

$$\frac{U_y(U_y + U_{y0})}{G^2} = \frac{K_{xc}(U_y)}{K_y(U_y)} \leq \frac{K_x(U_y)}{K_y(U_y)} \quad (1.6)$$

Where,  $Y_0$  is the initial overlap between the comb fingers,  $Y$  is the displacement from the initial (rest position) of the bearing,  $G$  is the separation between the comb fingers in the absence of any error motions or offsets and  $K_x(U_y)$  and  $K_y(U_y)$  are stiffness of the flexure mechanism in the bearing and motion direction respectively (Figure 3). The implicit assumption here is that the rotational stiffness of the mechanism is large enough to be ignorable. However, if this assumption fails, equation (1.6) must be corrected to include the rotational stiffness [39]:

$$\frac{K_x(U_y)}{K_y(U_y)} \leq \frac{2U_y(U_y + U_{y0})}{G^2} \left( \frac{rL_{off}}{2L_{off} - 2(U_y + U_{y0}) + rL_{off}} \right) \quad (1.7)$$

Where  $L_{off}$  is the distance between the *center of stiffness*<sup>1</sup>(COS) [23, 24] of the flexure mechanism and the tip of the comb fingers (Figure 3) and  $r$  is given by:

---

<sup>1</sup> The center of stiffness of a mechanism is that at which if a force is applied, the resultant displacement has no rotational component

$$r = 2 \left( -\frac{3 - 3\left(\frac{U_y + U_{y0}}{L_{off}}\right) + \left(\frac{U_y + U_{y0}}{L_{off}}\right)^2 - 3\left(\frac{K_\theta}{K_x L_{off}^2}\right)}{3\left(2 - \left(\frac{U_y + U_{y0}}{L_{off}}\right)\right)} \right) + 2 \sqrt{\left( \frac{3 - 3\left(\frac{U_y + U_{y0}}{L_{off}}\right) + \left(\frac{U_y + U_{y0}}{L_{off}}\right)^2 - 3\left(\frac{K_\theta}{K_x L_{off}^2}\right)}{3\left(2 - \left(\frac{U_y + U_{y0}}{L_{off}}\right)\right)} \right)^2 + \frac{K_\theta}{K_x L_{off}^2}} \quad (1.8)$$

If the ratio  $K_\theta/(K_x(L_{off})^2)$  is greater than 5, the error in the stroke given by equation (1.6) would be less than 10%. Hence, by choosing dimensions such that the above condition is satisfied, provided that  $K_\theta$  can be varied independent of  $K_x$ , we can assume purely axial (along  $x$  direction) snap-in dictated by equation (1.6).

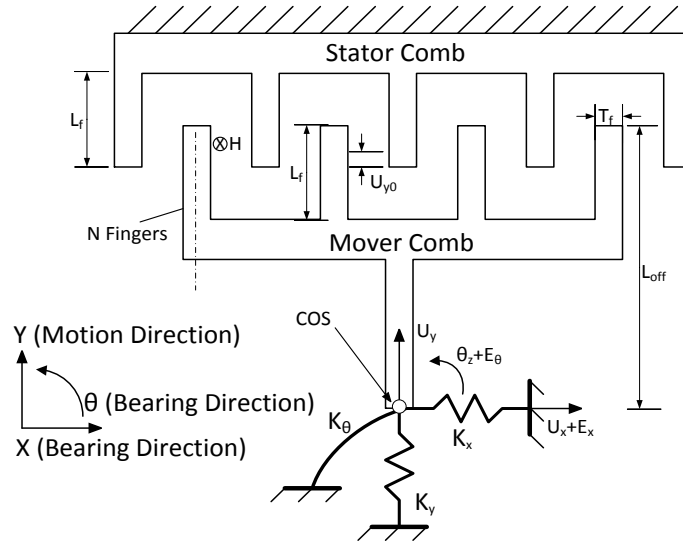


Figure 3: Comb drive Parameters. The displacements of the mover comb in the bearing directions can be split into error motions ( $E_x, E_\theta$ ) and spring deformations ( $U_x, \theta_z$ ) as shown.

In presence of error motions ( $E_x$  and  $E_\theta$ ), we can no longer obtain a simplified criterion for snap-in like that in equation (1.7). In this general case, the solution can be obtained numerically using the following steps:

1. At every  $x$  and  $y$  location, we simultaneously solve the  $x$  and  $\theta$  direction equilibrium equations to obtain the voltage required to maintain equilibrium



between the electrostatic and spring force. As  $U_x$  and  $\theta_z$  are dependent on each other, we assume  $U_x$  as the independent variable and solve for  $\theta_z$  as a function of  $U_x$ . Thus, the voltage obtained is a function of  $U_x$  and  $U_y$ . The equilibrium relations are given below:

$$\begin{aligned} & \frac{\varepsilon NHV^2}{2\theta_z} \left\{ \frac{1}{\left(G - (U_x + E_x) - L_{off}(\theta_z + E_\theta)\right)} - \frac{1}{\left(G - (U_x + E_x) - (L_{off} - (U_y + U_{y0}))(\theta_z + E_\theta)\right)} \right. \\ & \left. + \frac{1}{\left(G + (U_x + E_x) + L_{off}(\theta_z + E_\theta)\right)} - \frac{1}{\left(G + (U_x + E_x) + (L_{off} - (U_y + U_{y0}))(\theta_z + E_\theta)\right)} \right\} \\ & = (K_y(U_y))U_x \end{aligned} \quad (1.9)$$

$$\begin{aligned} & \frac{\varepsilon NHV^2}{2\theta_z} \left\{ (G - (U_x + E_x)) \left( \frac{1}{\left(G - (U_x + E_x) - L_{off}(\theta_z + E_\theta)\right)} - \frac{1}{\left(G - (U_x + E_x) - (L_{off} - (U_y + U_{y0}))(\theta_z + E_\theta)\right)} \right) \right. \\ & \left. \ln \left( \frac{G - (U_x + E_x) - L_{off}(\theta_z + E_\theta)}{G - (U_x + E_x) - (L_{off} - (U_y + U_{y0}))(\theta_z + E_\theta)} \right) - \ln \left( \frac{G + (U_x + E_x) + L_{off}(\theta_z + E_\theta)}{G + (U_x + E_x) + (L_{off} - (U_y + U_{y0}))(\theta_z + E_\theta)} \right) \right. \\ & \left. (G + (U_x + E_x)) \left( \frac{1}{\left(G + (U_x + E_x) + L_{off}(\theta_z + E_\theta)\right)} - \frac{1}{\left(G + (U_x + E_x) + (L_{off} - (U_y + U_{y0}))(\theta_z + E_\theta)\right)} \right) \right\} \\ & = (K_\theta(U_y))\theta_z \end{aligned} \quad (1.10)$$

2. The critical voltage at every  $y$  displacement is then given as:

$$\begin{aligned} V_{U_{x-crit}, U_y}^* &= \max_{U_x \in D} (V(U_x, U_y)) \\ D &: \{-G \leq U_x \leq G\} \end{aligned} \quad (1.11)$$

3. Finally, the equilibrium relation in the motion ( $Y$ ) direction gives the voltage corresponding to a certain  $Y$  displacement:

$$\frac{\varepsilon NHV_{eq}^2}{G} = (K_y(U_y))U_y \quad (1.12)$$

The stroke  $U_y|_{\max}$  is thus given by solution of the following equation:

$$U_y|_{\max} : V_{eq}(U_y) = V^*(U_{x-crit}, U_y) \quad (1.13)$$

If the rotational stiffness is large enough and the rotational error motions are zero i.e. if we can use a one dimensional model for snap-in, the above set of equations reduce to the following equation for a non-zero  $E_x$  [34, 38]:

$$\frac{K_x(U_y)}{K_y(U_y)} \geq \frac{K_{xc}(U_y)}{K_y(U_y)} = \frac{2U_y(U_y + U_{y0})}{G^2} \frac{1 + \frac{3X_c^2}{G^2}}{\left(1 - \frac{X_c^2}{G^2}\right)^2}; \quad E_x = \frac{4X_c^3}{G^2 + 3X_c^2} \quad (1.14)$$

Error motions can be classified into - theoretical arising from the geometry of the mechanism and those from fabrication imperfections. The former can be obtained using flexure analysis methods whereas the latter is usually indeterminate during the design stage. Thus, to include the effect of latter error motions, we include a stability factor  $S$ , analogous to a safety margin, in the above equation to obtain:

$$\frac{K_x(U_y)}{K_y(U_y)} \geq \frac{K_{xc}(U_y)}{K_y(U_y)} = (1+S) \frac{2U_y(U_y + U_{y0})}{G^2} \frac{1 + \frac{3X_c^2}{G^2}}{\left(1 - \frac{X_c^2}{G^2}\right)^2} \quad (1.15)$$

Moreover, we can combine the effect of both of these error motions to obtain a total stability factor ( $S_{tot}$ ):

$$\frac{K_x(U_y)}{K_y(U_y)} \geq (1+S) \frac{2U_y(U_y + U_{y0})}{G^2} \frac{1 + \frac{3X_c^2}{G^2}}{\left(1 - \frac{X_c^2}{G^2}\right)^2} = (1+S_{tot}) \frac{2U_y(U_y + U_{y0})}{G^2} \quad (1.16)$$

Moreover, the above equation can be graphically represented in Figure 4. The maximum stroke of the actuator would be given by the abscissa of the intersection point between *required stiffness ratio*  $K_{xc}(U_y)/K_y(U_y)$  and the *available stiffness ratio*  $K_x(U_y)/K_y(U_y)$ . This figure also shows the increasing required stiffness ratio due to increasing axial or x direction error motions (given by equation (1.14)) leading to pre-mature snap-in.

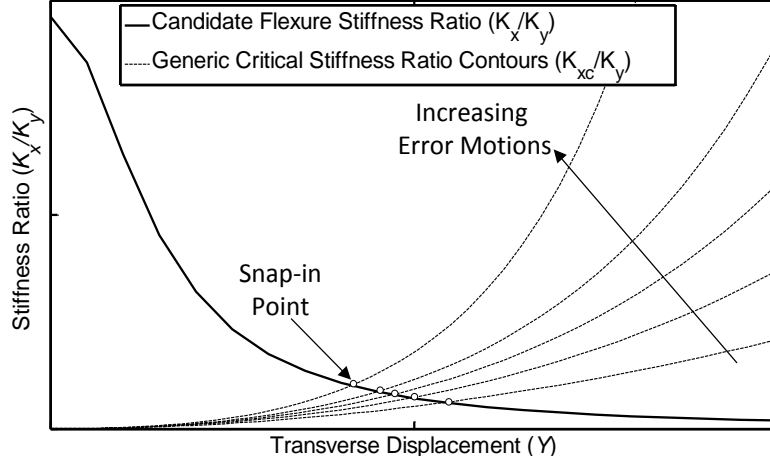


Figure 4: Generalized Snap-In

Thus, generally speaking, a bearing with a higher available stiffness ratio and small errors would give a larger stroke. In the design optimization of a comb drive actuator, our objective is not only increasing the stroke but also minimizing the effort i.e. the number of comb teeth ( $N$ ) and the actuation voltage ( $V$ ) required to achieve that stroke. The actuator effort can be easily determined using the equilibrium relation between the restoring spring force and the attractive electrostatic force in the motion direction:

$$K_y U_y |_{\max} = \frac{\varepsilon H}{G} N V^2 \quad (1.17)$$

Where  $\varepsilon$  is the permittivity of free space and  $H$  is the out-of-plane depth of the comb fingers. Eliminating  $G$  between equation (1.17) and a simplified version of equation (1.16) with zero initial overlap, we get:

$$\frac{(U_y |_{\max})^2}{N V^2} = \varepsilon_0 H \left[ \sqrt{\frac{K_x}{K_y^3 (1 + S_{tot})}} \right]_{@U_y=U_y |_{\max}} \quad (1.18)$$

Thus, to maximize the actuation stroke ( $U_y |_{\max}$ ) while minimizing the actuation voltage ( $V$ ) and device foot-print ( $N$ ), it is clear that that one has to maximize the right hand side of the above equation at the desired  $U_y |_{\max}$ . However, the above formulation assumes no constraint on the gap size  $G$  which is often limited by fabrication capabilities. Thus, a constraint equation has to be added to the above optimization problem to ensure that the

chosen flexure requires a gap size which is greater than the minimum feature size that can be fabricated using existing processes. The above metric combines the three objectives given by equations (1.2), (1.3) and (1.4). As mentioned before the yield or fracture limit of the mechanism is usually much larger than the stroke and hence, maximizing it is not a critical objective.

Similar constraints exist for electromagnetic actuators employing flexure mechanisms as linear guides. Off-axis electromagnetic forces can cause instability causing the mover to crash into the stator [40, 41] and therefore, one has to account for them while designing the flexure bearings. As before, error motions can further increase the stiffness requirements for maintaining stability. However, a simplified objective function like the one in equation (1.18) does not exist in previous literature for this class of actuators. In general, a flexure mechanism satisfying the objectives listed before would be desirable for any linear guidance application where significant side loading exists and there is little or no tolerance for any off-axis motions.

However, this is not easily achieved. Fundamental performance tradeoffs exist in flexure mechanisms. The parallelogram (P) (Figure 10) and double parallelogram (DP) (Figure 15) flexures are the most commonly used ones for linear guidance applications. In case of the P flexure, the error motion in the bearing direction is too high. In case of the DP flexure, the stiffness in the bearing direction drops precipitously with increasing motion direction stroke. In this thesis, the underlying reasons behind these tradeoffs have been identified and quantified. Several new flexure mechanisms will be presented which systematically deal with these tradeoffs using additional topological features and configurations to bridge the performance gap between a non-ideal flexure bearing and an ideal bearing. Moreover, wherever possible, closed-form expressions for the stiffness and error motions, validated experimentally or using finite element analysis, of these mechanisms will be provided.

The following list gives the organization of the rest of this thesis and highlights its specific contributions:

1. Chapter 2 presents the mathematical background, which can be found in previous literature [23, 24] for analysis in the subsequent sections. This will include the non-linear static force displacement relations for a lumped compliance beam obtained using both the Euler-Bernoulli stress-strain relations and strain energy methods. The yielding criterion for the same beam configuration has also been derived.
2. A review of some existing flexure mechanisms[1, 23, 24, 42] will be presented in Chapter 3 along with some closed-form or finite element results for the stiffness and error motions. The merits and demerits of each of these flexure mechanisms would be listed along with their causes. It will be shown that a mere shape optimization / careful dimension selection is not adequate to exceed a certain performance level. There are hard limits, which can be analytically quantified and physically explained.
3. Chapter 4 presents two novel flexure mechanisms recently invented by Shorya Awtar [43]- the Clamped Paired Double Parallelogram (C-DPDP) and the Double Parallelogram Tilted-Beam Double Parallelogram (DP-DTB), which provide a considerable improvement in performance compared to the existing mechanisms. This thesis presents a qualitative discussion on the working of the mechanisms followed by the derivation of the closed form expressions for the motion and the bearing direction stiffness of the C-DPDP mechanism. The chapter concludes with a discussion on possible variations to further boost the performance and optimization of the mechanisms in the context of comb drive actuators.
4. The setup for experimentally validating the stiffness expressions for the C-DPDP mechanism is described in Chapter 5. The experimental set-up was previously

designed by Shorya Awtar and Michael Wang to be modular, reconfigurable and low cost without compromising the precision and accuracy of the measurements. Specifically, this thesis presents a detailed discussion on the design and fabrication of the experimental setup. This is followed by a thorough error analysis, FEA validation and preliminary results.

5. Chapter 6 discusses the optimization of flexure designs – CDPDP and DP-TDP to obtain large stroke while keeping the footprint to a minimum in a comb drive actuator. The chapter also includes results from experimental fabrication and measurements performed by Dr. Mohammad Olfatnia separately, outside of this thesis, which validate the analytical predictions. Finally, a new metric is proposed for the comparison of performance of different comb drive actuator designs.

## Chapter 2: Background

A beam is one of the most common flexure elements and with the existing non-linear static beam bending analysis, we can analyze the performance metrics of several beam based flexure mechanisms presented in this thesis. While thermal effects can play an important role in the performance of flexures, we limit our present analysis to only the structural aspects. The beam flexure analyzed in this chapter has length  $L$  and a uniform rectangular cross-section with height  $T$  and width  $H$ , as shown in Figure 5. As in this thesis, we deal with only planar mechanisms, a state of plane strain is assumed for the beam implying that the dimension  $H \gg T$ . Moreover, the beam is sufficiently slender and long i.e.,  $L \gg T$  so that bending is the primary mode of deformation.

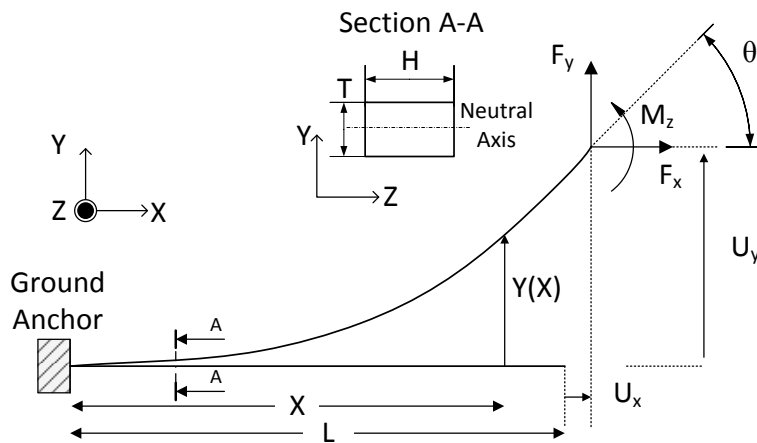


Figure 5: A simple beam with a uniform cross-section

### DIRECT APPROACH: BEAM CONSTRAINT MODEL

The mathematical background presented in this section is a summary of work published previously [23, 24]. All the desired characteristics of a beam can be obtained using the

principles of solid mechanics. In general, a formulation in mechanics comprises of the following three components:

1. Constitutive relationships
2. Force equilibrium relations or force compatibility relations
3. Geometric equilibrium or geometric compatibility relations

Each of these components might contribute some non-linearity to the overall force-displacement relations. As we step through the analysis, some of these would be retained while others neglected by conducting an order of magnitude analysis.

Constitutive relations relate loads to deformations and are dependent on the material properties and the geometry. In this case we can directly use *euler's* formula for pure bending given by:

$$\frac{E}{\rho} = \frac{M}{I} \quad (2.1)$$

Where  $M$  is the moment at a given cross-section in the beam,  $I$  is the second moment of area about the  $Z$  axis and for the cross-section shown in Figure 5, is equal to  $HT^3/12$ ,  $\rho$  is the radius of curvature and  $E = E^*/(1-\nu^2)$ , where  $E^*$  is the Young's modulus and  $\nu$  is the Poisson's ratio for the material. Unless otherwise mentioned, we would use this definition of  $E$  throughout this thesis.

The force equilibrium relations are applied in the deformed beam configuration to essentially capture the effect of an axial force  $F_x$  on the load-displacement relations. The moment at any location ( $x$ ) along the beam would be given by:

$$M(X) = M_z + F_y(L + U_x - X) - F_x(U_y - Y) \quad (2.2)$$

Where the forces  $F_x$ ,  $F_y$  and moment  $M_z$  applied at the beam end cause deflections  $U_x$ ,  $U_y$  and  $\theta_z$  respectively.



Finally, the geometric compatibility relation can be given as an expression for the beam curvature at any given  $X$  location along the beam length:

$$\frac{1}{\rho} = \frac{Y''}{(1+Y'^2)^{3/2}} \approx Y'' \text{ for small deformations} \quad (2.3)$$

When the curvature expressed in terms of the undeformed beam co-ordinates, the formula comes out to be slightly different [44]. Typically, the maximum displacement range is of the order of  $0.1L$ . Moreover, as most of the mechanisms analyzed in this thesis have a single linear DOF, the rotational direction  $\theta$  is a DOC. Therefore, the constituent beams deform in an approximately 'S' shape as shown in Figure 6. In this configuration, the maximum slope is achieved at  $x=L/2$  and for a maximum  $Y$  displacement of  $0.1L$ , is equal to about 0.15. For these values, the error in the approximation made in equation (2.3) is about 3.4% which is small enough to be neglected in order to obtain closed-form parametric results.

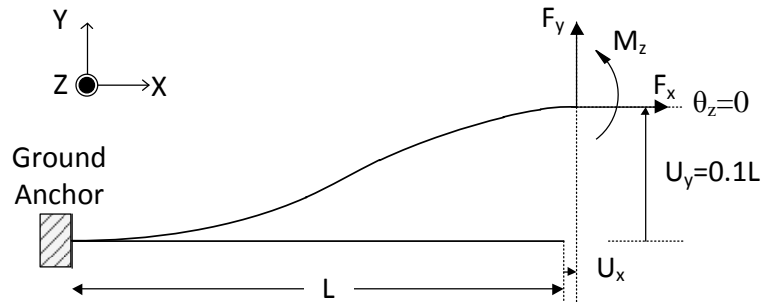


Figure 6: The S-Shaped Beam

Combining the above equations (2.1), (2.2) and (2.3), we obtain the following relation:

$$EIY'' = M_z + F_y(L + U_x - X) - F_x(U_y - Y) \quad (2.4)$$

At this point, we introduce a non-dimensionalizing scheme for the forces, displacements and the dimensions given as:

$$\begin{aligned}
y &= \frac{Y}{L} & x &= \frac{X}{L} & u_y &= \frac{U_y}{L} & u_x &= \frac{U_x}{L} & t &= \frac{T}{L} & h &= \frac{H}{L} \\
m_z &= \frac{M_z L}{EI} & f_y &= \frac{F_y L^2}{EI} & f_x &= \frac{F_x L^2}{EI}
\end{aligned} \tag{2.5}$$

Using this scheme, equation (2.4) can be rewritten as:

$$y'' = m_z + f_y(1 + u_x - x) - f_x(u_y - y) \tag{2.6}$$

Which can be double-differentiated to obtain:

$$y^{iv} = f_x y'' \Rightarrow y^{iv} = k^2 y'', f_x \triangleq k^2 \tag{2.7}$$

Finally, the above equation can be solved with appropriate boundary conditions to get the well-known [2] transverse direction load displacement relations:

$$\begin{aligned}
f_y &= \frac{k^3 \sinh k}{k \sinh k - 2 \cosh k + 2} u_y + \frac{k^2 (1 - \cosh k)}{k \sinh k - 2 \cosh k + 2} \theta \\
m_z &= \frac{k^2 (1 - \cosh k)}{k \sinh k - 2 \cosh k + 2} u_y + \frac{k^2 \cosh k - k \sinh k}{k \sinh k - 2 \cosh k + 2} \theta
\end{aligned} \tag{2.8}$$

The axial displacement comprises of an elastic component,  $u_x^e$  which is a result of pure axial stretching and a kinematic component,  $u_x^k$  which arises from the relation for beam arc-length conservation given as:

$$u_x^k = -0.5 \int_0^1 y'^2 dx \tag{2.9}$$

Where  $y'$  can be obtained from the solution of equation (2.7). Therefore, the net axial displacement is given by:

$$\begin{aligned}
u_x &= u_x^e + u_x^k \\
&= \frac{f_x}{k_{33}} - \begin{bmatrix} u_y & \theta_z \end{bmatrix} \begin{bmatrix} r_{11} & r_{12} \\ r_{21} & r_{22} \end{bmatrix} \begin{bmatrix} u_y \\ \theta_z \end{bmatrix}
\end{aligned} \tag{2.10}$$

Where  $k_{33} = 12/t^2$  for a beam with a uniform rectangular cross-section and:

$$r_{11} = \frac{k^2 (\cosh^2 k + \cosh k - 2) - 3 \sinh k (\cosh k - 1)}{2(k \sinh k - 2 \cosh k + 2)^2}$$

$$r_{12} = r_{21} = -\frac{k^2 (\cosh k - 1) + k \sinh k (\cosh k - 1) - 4(\cosh k - 1)^2}{4(k \sinh k - 2 \cosh k + 2)^2}$$

$$r_{22} = \frac{-k^3 + k^2 \sinh k (\cosh k + 2) - 2k(2 \cosh^2 k - \cosh k - 1) + 2 \sinh k (\cosh k - 1)}{4k(k \sinh k - 2 \cosh k + 2)^2}$$

Because of their transcendental nature, these equations give little engineering insight into the nature of the load-deformation characteristics. With a first order series approximation derived in [24], equations (2.8) and (2.10) can be rewritten as:

$$\begin{bmatrix} f_y \\ m_z \end{bmatrix} = \begin{bmatrix} k_{11}^{(0)} & k_{12}^{(0)} \\ k_{12}^{(0)} & k_{22}^{(0)} \end{bmatrix} \begin{bmatrix} u_y \\ \theta_z \end{bmatrix} + f_x \begin{bmatrix} k_{11}^{(1)} & k_{12}^{(1)} \\ k_{12}^{(1)} & k_{22}^{(1)} \end{bmatrix} \begin{bmatrix} u_y \\ \theta_z \end{bmatrix} \quad (2.11)$$

$$u_x = u_e + u_k + u_{ek}$$

$$= \frac{1}{k_{33}} f_x - \frac{1}{2} \begin{bmatrix} u_y & \theta_z \end{bmatrix} \begin{bmatrix} k_{11}^{(1)} & k_{12}^{(1)} \\ k_{12}^{(1)} & k_{22}^{(1)} \end{bmatrix} \begin{bmatrix} u_y \\ \theta_z \end{bmatrix} - f_x \begin{bmatrix} u_y & \theta_z \end{bmatrix} \begin{bmatrix} k_{11}^{(2)} & k_{12}^{(2)} \\ k_{12}^{(2)} & k_{22}^{(2)} \end{bmatrix} \begin{bmatrix} u_y \\ \theta_z \end{bmatrix} \quad (2.12)$$

Where constants  $k_{ij}^{(k)}$  depend only on the beam shape. These are three equations in six unknowns – three loads and three displacements and represent the beam constraint model or BCM for a beam flexure. Given any three, the remaining can now be easily solved for analytically in most cases. The maximum estimated error in the above expressions is less than 5% for normalized transverse displacements of  $\pm 0.1$  and axial forces and moments within  $\pm 10$ .

Using relations (2.11) and (2.12), we can make some important observations regarding the characteristics of a beam flexure:

1. Equation (2.11) shows the dependence of the transverse and rotational stiffness on the axial force,  $f_x$ . The expression clearly shows the two kinds of stiffness matrices- the *elastic* and *geometric*. It quantitatively captures how the transverse

stiffness increases in the presence of a tensile axial force and decreases with a compressive axial force. This effect is often called *load stiffening/softening* [23, 24] and can be attributed to the extra moment exerted by the axial force in the presence of a transverse displacement  $u_y$ .

2. The dependence of the axial stiffness on transverse and rotational displacements is captured by equation (2.12). The axial displacement has three components- the first one,  $u_e$  is a purely elastic component which results from the stretching of the beam, the second term,  $u_k$  is a purely kinematic component, and is a consequence of beam arc length conservation and the third term called the *elasto-kinematic* term,  $u_{ek}$  has both elastic and kinematic aspects and arises due to the contribution of the axial force to the bending moment in the deformed configuration. The purely kinematic term  $u_k$  which has no dependence on the axial loads, essentially quantifies the error motions defined in chapter 1 for a simple beam and thus, is a metric of the quality of the DOC. The elasto-kinematic term captures the degradation of the DOC stiffness with increasing DOF displacements.
  
3. Variations in the beam shape can be incorporated in the above equations without changing their general form. A basic shape variation shown in the Figure 7 given below where a rigid section with infinite stiffness is introduced in the center of the uniform beam. The end sections of the beam have the same cross-sectional dimensions as that of the uniform beam in Figure 5. The coefficients of the stiffness matrices in equations (2.11) and (2.12) can be expressed as functions of the degree of reinforcement or  $a_0$ . These have been tabulated in Appendix A. It can be seen that the transverse stiffness matrix becomes unbounded as  $a_0$  approaches 0<sup>2</sup>. However, the elastic axial displacement  $u_x^e$  also approaches 0

---

<sup>2</sup> The equations would not be valid in this region as Bernoulli's assumptions would start to fail. However, the trend would be; which is intuitively obvious.

which implies that the nominal axial stiffness would improve significantly. While considering future designs comprising of beam flexure elements, this can be used as a parameter for optimization without changing the overall formulation of the problem. It should be noted that this is just one of the several possible shape variations albeit an important one as it highlights the tradeoffs in simultaneously achieving all the objectives mentioned in chapter 1.

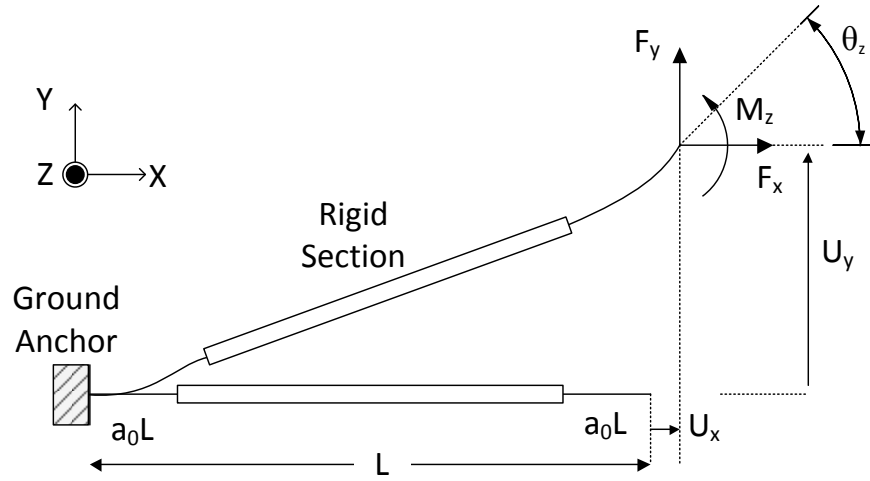


Figure 7: A lumped compliance beam. In all future instances we would dimension a lumped compliance beam as follows (length i.e.  $l$ , degree of compliance i.e.  $a_0$ ) without explicitly showing the rigid section.

4. For beams that deform in an approximate S shape, the yielding criterion and hence the maximum range can be obtained in terms of the material properties as well as the applied loads. At any location ( $x$ ) along the length of the beam, the strain  $\epsilon_{xx}$  caused due to bending at any  $y$ -location along the cross-section of the beam would be given by:

$$\epsilon_{xx} = -\frac{c}{\rho} \quad (2.13)$$

Where  $c$  is the  $y$ -distance from the neutral axis shown in Figure 5. For a rectangular cross-section, the maximum strain is achieved at a  $y$  distance of  $T/2$

from the neutral axis. As we are dealing primarily with linear elastic materials, the stress is directly proportional to the strain and thus, is also largest at the same locations. Using equation (2.1) for the curvature of the beam, the maximum stress can be written as:

$$\sigma_{xx}^{bending} \Big|_{\max} = E \varepsilon_{xx} \Big|_{\max} = \frac{M(x)}{I} \left( \frac{T}{2} \right) = 0.5 E m(x) t \quad (2.14)$$

Thus, along the length of the beam, the stress is maximum at the anchor or  $x=0$ . However, because of the symmetry of the  $S$  shaped beam, the magnitude of this moment is the same as that at  $x=L$  or:

$$m(x=0) = m_{z0} = f_y (1 - u_x) + m_z - f_x u_y = -m_z = -m(x=L) \quad (2.15)$$

This has been illustrated in Figure 8.

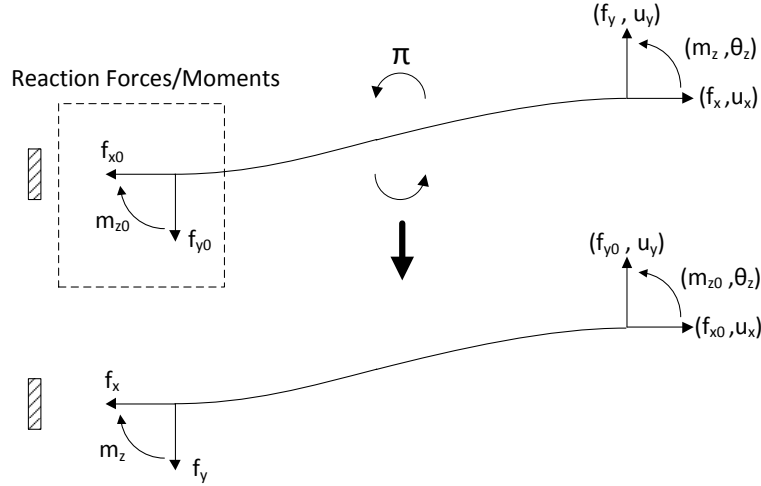


Figure 8: Symmetry argument for calculating the maximum moment.

Using equation (2.11) and  $\theta_z=0$  for an  $S$  shaped beam:

$$m_{z0} = (0.5k_{11}^{(0)} - f_x k_{12}^{(1)}) u_y \quad (2.16)$$

Moreover, the total normal stress at any location is given by the sum of the axial and the bending stresses where the axial stress is simply given as the axial force

divided by the cross-sectional area and is uniform over the entire cross-section. Using non-dimensional forces and dimensions, we obtain:

$$\sigma_{xx}^{axial} = \frac{Ef_x}{12} \left( \frac{T}{L} \right)^2 \quad (2.17)$$

Therefore, using equations (2.14) and (2.17), the total stress  $\sigma_{xx}$  is given as:

$$\begin{aligned} \sigma_{xx} &= \sigma_{xx}^{bending} + \sigma_{xx}^{axial} \\ &= 0.5Em_{z0}t + 0.083Ef_x t^2 \\ &= 0.5Et \left( 0.5k_{11}^{(0)}u_y + f_x \left( -k_{12}^{(1)}u_y + 0.167t \right) \right) \end{aligned} \quad (2.18)$$

Now using the *von-mises* stress criterion for yielding, we get:

$$\sqrt{\sigma_{xx}^2 + 3\tau_{xy}^2} \leq \frac{S_y}{\eta} \quad (2.19)$$

Where,  $S_y$  is the yield stress,  $\eta$  is the safety factor, and the stress  $\sigma_{xx}$  by equation (2.18) and  $\tau_{xy}$  is the shear stress on the cross-section and is given as the ratio between the transverse force  $f_y$  and the cross-sectional area:

$$\tau_{xy} = \frac{Ef_y}{12} t^2 \quad (2.20)$$

With sufficiently slender beams, the  $\tau_{xy} \ll \sigma_{xx}$  and can be ignored in the rest of the derivation. Combining equations (2.18) and (2.19), we get:

$$u_y \leq \left( \frac{1}{\eta} \right) \left( \frac{4}{k_{11}^{(0)} - 2f_x k_{12}^{(1)}} \right) \left( \frac{S_y}{E} - 0.08f_x t^2 \right) \frac{1}{t} \quad (2.21)$$

Generally, in comb drive applications, this force  $f_x$  is usually zero or small (in the presence of error motions) and hence, in that case, it can be excluded from our analysis in which case equation (2.21) reduces to:

$$u_y \leq \left( \frac{1}{\eta} \right) \left( \frac{4}{k_{11}^{(0)}} \right) \left( \frac{S_y}{E} \right) \left( \frac{1}{t} \right) \quad (2.22)$$

For  $a_0=0.5$ , the above relation further reduces to the familiar relation [23, 31]:

$$u_y \leq \left( \frac{1}{3\eta} \right) \left( \frac{S_y}{E} \right) \left( \frac{1}{t} \right) \quad (2.22)$$

The above derivation would remain the same for a generalized beam shown in Figure 7 and therefore,  $k_{II}^{(0)}$  can be a function of  $a_0$ . For flexures,  $l/t$  ratios of 50 are common, and  $S_y/E$  ratios range from  $4e-3$  for AL-6061 to  $1e-2$  for TI-13. The safety factor  $\eta$  may be chosen on the basis of stress concentration in the geometry. For typical values, the maximum deformation  $u_y|_{\max}$  ranges from  $0.05L$  to  $0.1L$ . We will aim to obtain results for deformations as large as  $0.1L$ , but in practice the deformations are kept well within this number, especially if fatigue loading is considered. At the micro-scale, this limit is usually much higher than this although it is not very well defined as the yield limit and the young's moduli of the materials are strongly related to the geometry and the fabrication process.

5. Arbitrary but constant initial orientations and curvatures of the beam can also be very easily incorporated in this model [45]. As a special case, the BCM relations for pre-bent beams are derived here. In a pre-bent configuration, the beam is initially given a shape such that it exactly mimics the profile of an *S*-shaped beam (a linearly varying curvature and zero end-slope) with a transverse end displacement of  $U_{ypre}$ . This is done so as to shift the  $x$ -direction stiffness profile of a mechanism comprised of these beams which can then be used to increase the stable working range of motion of comb-drive actuators.



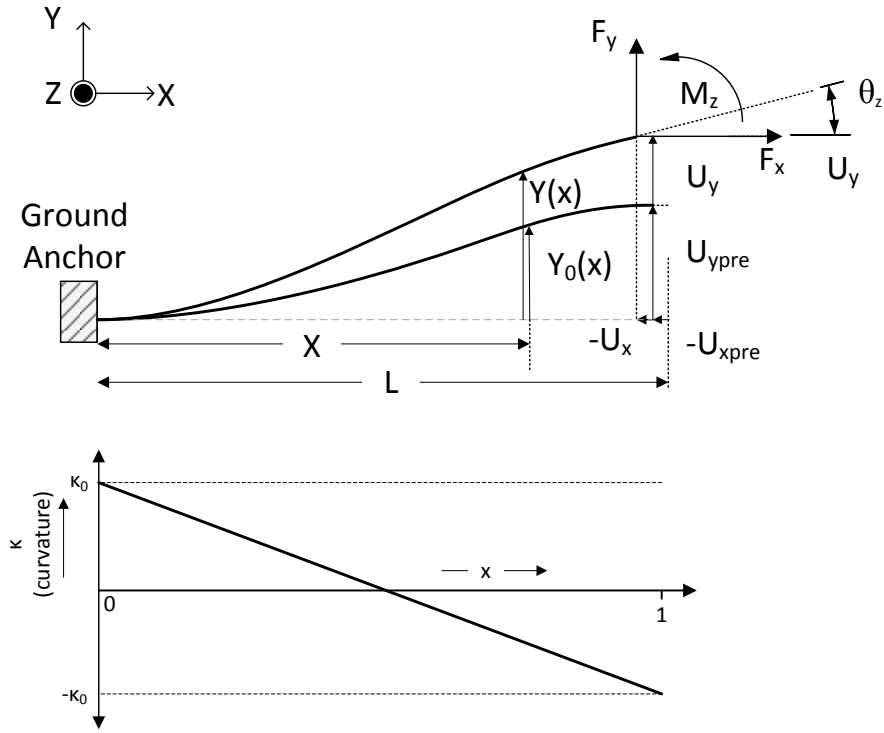


Figure 9: Pre-bent Beam configuration

The goal of this exercise is to obtain BCM relations for this configuration which validate the qualitative predictions about the shift in the stiffness profile. The pre-bent beam configuration is shown in Figure 9. For the linearly varying curvature also shown, we have:

$$\begin{aligned}
 y_0''(x) &= \kappa_0(1-2x) \\
 \Rightarrow y_0(x) &= \kappa_0 \left( \frac{x^2}{2} - \frac{x^3}{3} \right) + c_1x + c_2
 \end{aligned} \tag{2.23}$$

Applying end boundary conditions i.e.

$$y_0(0) = 0, y_0'(0) = y_0'(1) = 0 \tag{2.24}$$

Gives:

$$y_0(x) = \kappa_0 \left( \frac{x^2}{2} - \frac{x^3}{3} \right) \quad (2.25)$$

Expressing this in terms of the end displacement  $y_{pre}$ ,

$$y_0(x) = U_{ypre} (3x^2 - 2x^3) \quad (2.26)$$

Rewriting equation (2.6):

$$y''(x) - y_0''(x) = m_z + f_y(1 + u_x - x) - f_x(u_y + u_{ypre} - y(x)) \quad (2.27)$$

Upon double differentiating the above equation, we get the same result as that given in equation (2.7) as  $y_0^{iv}(x) = 0$ . However, the boundary conditions would now become:

$$y(0) = 0, y'(0) = 0, y(1) = u_y + u_{ypre}, y'(1) = \theta_z \quad (2.28)$$

Finally, the load boundary conditions at the beam end,  $x=l$  can be shown to be:

$$y'''(1) - y_0'''(1) = -f_y + f_x(y'(1)), y''(1) - y_0''(1) = m_z \quad (2.29)$$

Solving equation (2.7) with boundary conditions given by equations (2.28) and (2.29), we get:

$$\begin{bmatrix} f_y \\ m_z \end{bmatrix} = \begin{bmatrix} k_{11}^{(0)} & k_{12}^{(0)} \\ k_{21}^{(0)} & k_{22}^{(0)} \end{bmatrix} \begin{bmatrix} u_y \\ \theta_z \end{bmatrix} + f_x \begin{bmatrix} k_{11}^{(1)} & k_{12}^{(1)} \\ k_{21}^{(1)} & k_{22}^{(1)} \end{bmatrix} \begin{bmatrix} u_y + u_{ypre} \\ \theta_z \end{bmatrix} \quad (2.30)$$

Finally, applying beam arc-length conservation i.e.:

$$\int_0^{1+u_x^{(e)}} \left\{ 1 + \frac{1}{2} (y_0'(x))^2 \right\} dx = \int_0^{1+u_x+u_{ypre}} \left\{ 1 + \frac{1}{2} (y'(x))^2 \right\} dx \quad (2.31)$$

Where:

$$u_{ypre} = -\frac{1}{2} k_{11}^{(1)} u_{ypre}^2 \quad (2.32)$$

Is the initial kinematic axial displacement of the pre-bent beam. Solving equation (2.31):

$$u_x = \frac{1}{k_{33}} f_x - \frac{1}{2} [u_y + u_{ypre} \quad \theta_z] \begin{bmatrix} k_{11}^{(1)} & k_{12}^{(1)} \\ k_{12}^{(1)} & k_{22}^{(1)} \end{bmatrix} \begin{bmatrix} u_y + u_{ypre} \\ \theta_z \end{bmatrix} - f_x [u_y + u_{ypre} \quad \theta_z] \begin{bmatrix} k_{11}^{(2)} & k_{12}^{(2)} \\ k_{12}^{(2)} & k_{22}^{(2)} \end{bmatrix} \begin{bmatrix} u_y + u_{ypre} \\ \theta_z \end{bmatrix} - u_{ypre} \quad (2.33)$$

Expressions (2.30) and (2.33) are thus the required force-displacement relations. Except for the elastic terms in the equations, all other terms exhibit a coordinate shift along the  $y$  direction. This is understandable as firstly, the geometric transverse stiffness and elasto-kinematic axial displacement are caused by the extra moment applied by axial force  $f_x$  which is linearly related to the net transverse displacement  $u_y+u_{ypr}$ . Moreover, the net kinematic displacement is simply the difference between the displacement at the final position  $(u_y+u_{ypr}, \theta_z)$  and that at the initial position  $(u_{ypr}, 0)$  which can be clearly seen in equation (2.33). This equation also shows that the axial stiffness vs  $u_y$  curve would shift along the  $y$  direction by a displacement of  $u_{ypr}$  thereby confirming the qualitative predictions about the stiffness behavior of this beam.

### STRAIN ENERGY APPROACH

The above formulation is mathematically tedious as we have to account for all the internal forces and moments to arrive at the final force-displacement relations. This becomes especially cumbersome while solving for the characteristics of more complex mechanisms comprising of several beam elements in a serial or parallel arrangement or both. Strain energy methods [46] are mathematically more efficient and succinct. A non-linear strain energy formulation for the beam flexure should be consistent with the transverse-direction load-displacement and axial direction geometric constraint relations in the BCM. An explicit non-dimensionalized strain energy expression in terms of the beam end displacements that accommodates generalized loading conditions, boundary conditions, initial curvature, and beam shape has been derived in previous literature [47] and is presented below:

$$v = \frac{1}{2} k_{33} \frac{\left( u_x + \frac{1}{2} \{u_y \quad \theta_z\} \begin{bmatrix} k_{11}^{(1)} & k_{12}^{(1)} \\ k_{21}^{(1)} & k_{22}^{(1)} \end{bmatrix} \begin{Bmatrix} u_y \\ \theta_z \end{Bmatrix} \right)^2}{\left( 1 - k_{33} \{u_y \quad \theta_z\} \begin{bmatrix} k_{11}^{(2)} & k_{12}^{(2)} \\ k_{21}^{(2)} & k_{22}^{(2)} \end{bmatrix} \begin{Bmatrix} u_y \\ \theta_z \end{Bmatrix} \right)} + \frac{1}{2} \{u_y \quad \theta_z\} \begin{bmatrix} k_{11}^{(0)} & k_{12}^{(0)} \\ k_{21}^{(0)} & k_{22}^{(0)} \end{bmatrix} \begin{Bmatrix} u_y \\ \theta_z \end{Bmatrix} \quad (2.34)$$

The force displacement relations are obtained by equating the variation of the above strain energy expression in response to virtual displacements  $\delta u_x$ ,  $\delta u_y$  and  $\delta \theta_z$  to the virtual work done by the external forces, held constant over the entire displacement and applied at the beam tip i.e.

$$\delta v = f_x \delta u_x + f_y \delta u_y + m_z \delta \theta_z \text{ or,} \quad (2.35)$$

$$f_x = \frac{\partial v}{\partial u_x}, f_y = \frac{\partial v}{\partial u_y}, m_z = \frac{\partial v}{\partial \theta_z}$$

This approach is found to be very powerful for solving problems where simple geometric relationships exist between the end-displacements of the constituent beams e.g. in a parallelogram mechanism which would be discussed in greater detail in the next chapter. However, when this is not possible and end loads dictate these relationships as in a serial arrangement, equation (2.35) becomes a system of multivariate polynomial equations which might be almost impossible to solve analytically. In such cases, in order to reduce the complexity, it is helpful to make blocks comprising of two or more beams for which the net strain energy can be obtained in terms of the end displacements

Based on the results of this analysis, in chapter 2 we would analyze some existing flexure mechanisms in terms of the characteristics defined in chapter 1. Wherever possible, we would obtain the characteristics of these flexure based mechanisms using both the BCM and the strain energy method and highlight the relative merits of both these approaches.

## Chapter 3: Prior Art

In this chapter we would review the performance characteristics of some conventionally used flexure mechanisms. The non-linear force displacement relations have been obtained using the BCM analysis presented in the previous chapter for most of these mechanisms and with the strain energy method for some. We would do the complete derivation of the force displacement relations only in the cases where the analysis hasn't been done before. In all other cases, we would merely present the results and obtain the performance metrics ((1) to (4)) based on it.

### TWO-BEAM PARALLELOGRAM

A parallelogram [48], shown in Figure 10 provides a constraint arrangement that allows approximate straight-line motion. The  $y$  displacement represents a DOF, while  $x$  and  $\theta$  are DOC. These displacements are measured at the center of the stage where the forces and the moments are also applied. These displacements are composed of the differential displacements caused by the forces and the error motions of the mechanism. The two beams are treated as perfectly parallel and identical, at least initially, and the stage connecting these two is assumed rigid. Loads and displacements can be normalized with respect to the properties of either beam which are the same as those of the simple uniform beam discussed in the last chapter. In this case, the stage rotation  $\theta$  can be shown to be several orders of magnitude smaller than the  $y$  displacement. Therefore, higher order  $\theta$  terms are dropped wherever appropriate in the analysis.

### BCM Analysis

The derivation has been covered in [23, 24] and the normalized results are presented below for small  $\theta$ s:

$$u_y \approx \frac{f_y}{2k_{11}^{(0)} + f_x k_{11}^{(1)}} \quad (3.1)$$

$$u_x \approx \frac{f_x}{2k_{33}} - \frac{1}{2}u_y^2k_{11}^{(1)} - \frac{f_x}{2}u_y^2k_{11}^{(2)} \quad (3.2)$$

$$\theta_z = \frac{1}{2W^2} \left( \frac{1}{k_{33}} - u_y^2k_{11}^{(2)} \right) [m_z - u_y(2k_{12}^{(0)} + f_xk_{12}^{(1)})] \quad (3.3)$$

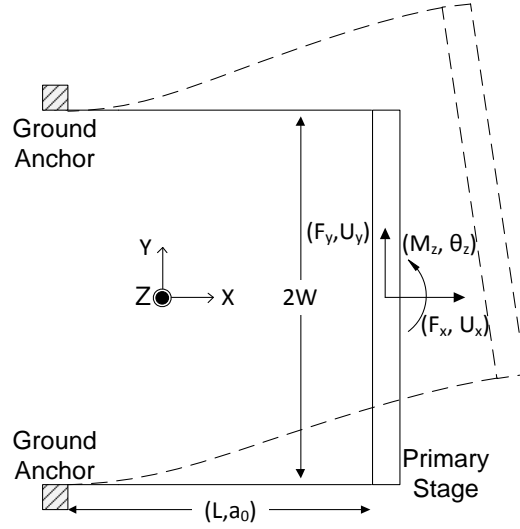


Figure 10: The parallelogram mechanism

Also, the above results are valid for a parallelogram mechanism with a reinforced beam flexure where the BCM coefficients would be functions of  $a_0$ .

### Strain Energy Analysis

For simplicity, we would only consider the uniform beam in this analysis. The strain energy function [47] of a beam  $i$  (where  $i=1,2$ ) in the parallelogram flexure as shown in figure is:

$$v(u_{xi}, u_{yi}, \theta_{zi}) = \frac{1}{2}k_{33} \frac{\left( u_{xi} + \frac{1}{2} \left( k_{11}^{(1)}u_{yi}^2 + 2k_{12}^{(1)}u_{yi}\theta_{zi} + k_{22}^{(1)}\theta_{zi}^2 \right) \right)^2}{\left( 1 - k_{33} \left( k_{11}^{(2)}u_{yi}^2 + 2k_{12}^{(2)}u_{yi}\theta_{zi} + k_{22}^{(2)}\theta_{zi}^2 \right) \right)} + \frac{1}{2} \left( k_{11}^{(0)}u_{yi}^2 + 2k_{12}^{(0)}u_{yi}\theta_{zi} + k_{22}^{(0)}\theta_{zi}^2 \right) \quad (3.4)$$

The net strain energy of the whole parallelogram will then be given as:

$$v_p(u_{x1}, u_{y1}, \theta_{z1}, u_{x2}, u_{y2}, \theta_{z2}) = v(u_{x1}, u_{y1}, \theta_{z1}) + v(u_{x2}, u_{y2}, \theta_{z2}) \quad (3.5)$$

However, in order to obtain the force displacement relations at the center of the stage, we would have to express the strain energy of the system entirely in terms of the displacements at the center i.e.  $u_x$ ,  $u_y$  and  $\theta_z$ . In this case, there exists a simple geometric relationship between the displacement variables  $u_{xi}$ ,  $u_{yi}$  and  $\theta_{zi}$  imposed by the rigid link connecting the two beams:

$$\begin{aligned} u_{xi} &\approx u_x - w_{(i)}\theta_z \\ u_{yi} &\approx u_y \\ \theta_{zi} &\approx \theta_z \end{aligned} \quad (3.6)$$

Substituting the above relations in equation (3.5):

$$v_p(u_x, u_y, \theta_z) = \frac{\left( k_{11}^{(0)}u_y^2 + 2k_{12}^{(0)}u_y\theta_z + k_{22}^{(0)}\theta_z^2 \right) + \left( u_x^2 + u_x \left( k_{11}^{(1)}u_y^2 + 2k_{12}^{(1)}u_y\theta_z + k_{22}^{(1)}\theta_z^2 \right) + \frac{1}{4} \left( k_{11}^{(1)}u_y^2 + 2k_{12}^{(1)}u_y\theta_z + k_{22}^{(1)}\theta_z^2 \right)^2 + w^2\theta_z^2 \right)}{k_{33} \left( 1 - k_{33} \left( k_{11}^{(2)}u_y^2 + 2k_{12}^{(2)}u_y\theta_z + k_{22}^{(2)}\theta_z^2 \right) \right)} \quad (3.7)$$

The above expression can be simplified to a great extent by making some order of magnitude estimates. However, this must be done carefully so as to obtain relations consistent with the BCM. In other words, a term can be dropped from the strain energy expression if the resultant force displacement relations obtained using equation (2.35) remain unchanged or approximately the same upon doing so.

Using relations (3.1), (3.2) and (3.3), we can set upper bounds on the displacement variables. These estimates can also be obtained using finite element analysis. These have been listed in the table below with their justifications:

*Table 1: Order of Magnitude estimates for a parallelogram*

<b><i>Variable</i></b>	<b><i>Order</i></b>	<b><i>Justification</i></b>
$f_x$	+/-10	Model limits

$m_z$	+/-10	Model limits
$t$	1/50	Typical Dimensions
$w$	0.3-1.0	Typical Dimensions
$u_y$	+/-0.1	Yield Limit
$u_x$	$O(10^{-2})$	Using relation (3.2)
$\theta_z$	$O(10^{-3})$	Using relation (3.3)

For complex systems the strain energy expression like that given in equation (3.7) may become long and unwieldy. Therefore, it is worthwhile to formulate an algorithm for this procedure which can be later implemented in code. The steps are outlined below:

1. As a first step, equation (3.7) can be rewritten as:

$$v_p(u_x, u_y, \theta_z) = \frac{N(u_x, u_y, \theta_z)}{D(u_x, u_y, \theta_z)} = \frac{\sum_{\kappa=1}^{Num(N)} N_{\kappa} u_x^{\alpha} u_y^{\beta} \theta_z^{\gamma}}{\sum_{\kappa'=1}^{Num(D)} D_{\kappa'} u_x^{\alpha'} u_y^{\beta'} \theta_z^{\gamma'}} \quad (3.8)$$

Where  $\alpha, \beta, \gamma, \alpha', \beta'$  and  $\gamma'$  can take non-negative integral values, the  $N_s$  and  $D_s$  are real coefficients associated with each of these terms.  $\kappa$  and  $\kappa'$  are non-repeating integers from 1 through  $Num(N \text{ or } D)$  where  $Num()$  gives the number of terms in an expression, associated with every unique tuple  $(\alpha, \beta, \gamma)$  and  $(\alpha', \beta', \gamma')$  respectively.

2. With each term in the numerator and denominator, we can associate a retention coefficient  $R_i$  ( $i=n/d$ ) which can be either 0 or 1. Therefore,

$$v_p(u_x, u_y, \theta_z) = \frac{N(u_x, u_y, \theta_z)}{D(u_x, u_y, \theta_z)} = \frac{\sum R n_{\kappa} N_{\kappa} u_x^{\alpha} u_y^{\beta} \theta_z^{\gamma}}{\sum R d_{\kappa'} D_{\kappa'} u_x^{\alpha'} u_y^{\beta'} \theta_z^{\gamma'}} \quad (3.9)$$

These coefficients determine whether a particular term in the strain energy expression must be retained or dropped. They would all be initialized to a value of 1.



3. We would now obtain the three force/moment displacement relations from the above expression using equation (2.35). Therefore, we can write:

$$\begin{aligned}
F_x &= \frac{\partial v_p}{\partial u_x} = \frac{\left( N \frac{\partial D}{\partial u_x} + \frac{\partial N}{\partial u_x} D \right)}{D^2} = \frac{\sum_{\kappa=1}^{Num(N)} \sum_{\kappa'=1}^{Num(D)} Rn_{\kappa} Rd_{\kappa'} \left( (N_{\kappa} D_{\kappa'}) (\alpha' + \alpha) u_x^{\alpha+\alpha'-1} u_y^{\beta+\beta'} \theta_z^{\gamma+\gamma'} \right)}{\sum_{\kappa=1}^{Num(D)} \sum_{\kappa'=1}^{Num(D)} Rd_{\kappa} Rd_{\kappa'} \left( (D_{\kappa} D_{\kappa'}) u_x^{\alpha+\alpha'} u_y^{\beta+\beta'} \theta_z^{\gamma+\gamma'} \right)} \\
F_y &= \frac{\partial v_p}{\partial u_y} = \frac{\left( N \frac{\partial D}{\partial u_y} + \frac{\partial N}{\partial u_y} D \right)}{D^2} = \frac{\sum_{\kappa=1}^{Num(N)} \sum_{\kappa'=1}^{Num(D)} Rn_{\kappa} Rd_{\kappa'} \left( (N_{\kappa} D_{\kappa'}) (\beta + \beta') u_x^{\alpha+\alpha'} u_y^{\beta+\beta'-1} \theta_z^{\gamma+\gamma'} \right)}{\sum_{\kappa=1}^{Num(D)} \sum_{\kappa'=1}^{Num(D)} Rd_{\kappa} Rd_{\kappa'} \left( (D_{\kappa} D_{\kappa'}) u_x^{\alpha+\alpha'} u_y^{\beta+\beta'} \theta_z^{\gamma+\gamma'} \right)} \\
M_z &= \frac{\partial v_p}{\partial \theta_z} = \frac{\left( N \frac{\partial D}{\partial \theta_z} + \frac{\partial N}{\partial \theta_z} D \right)}{D^2} = \frac{\sum_{\kappa=1}^{Num(N)} \sum_{\kappa'=1}^{Num(D)} Rn_{\kappa} Rd_{\kappa'} \left( (N_{\kappa} D_{\kappa'}) (\gamma + \gamma') u_x^{\alpha+\alpha'} u_y^{\beta+\beta'} \theta_z^{\gamma+\gamma'-1} \right)}{\sum_{\kappa=1}^{Num(D)} \sum_{\kappa'=1}^{Num(D)} Rd_{\kappa} Rd_{\kappa'} \left( (D_{\kappa} D_{\kappa'}) u_x^{\alpha+\alpha'} u_y^{\beta+\beta'} \theta_z^{\gamma+\gamma'} \right)}
\end{aligned} \tag{3.10}$$

These can be remapped to a new set of coefficients such that:

$$\begin{aligned}
F_x &= \frac{\sum_{\kappa=1}^{Num(N)} \sum_{\kappa'=1}^{Num(D)} Rn_{\kappa} Rd_{\kappa'} \left( (N_{\kappa} D_{\kappa'}) (\alpha' + \alpha) u_x^{\alpha+\alpha'-1} u_y^{\beta+\beta'} \theta_z^{\gamma+\gamma'} \right)}{\sum_{\kappa=1}^{Num(D)} \sum_{\kappa'=1}^{Num(D)} Rd_{\kappa} Rd_{\kappa'} \left( (D_{\kappa} D_{\kappa'}) u_x^{\alpha+\alpha'} u_y^{\beta+\beta'} \theta_z^{\gamma+\gamma'} \right)} \\
&= \frac{\sum_{\lambda=1}^{Num(N)^* Num(D)} Rnx_{\lambda} \left( Nx_{\lambda} u_x^{\alpha(\lambda)+\alpha(\lambda)-1} u_y^{\beta(\lambda)+\beta(\lambda)} \theta_z^{\gamma(\lambda)+\gamma(\lambda)} \right)}{\sum_{\lambda=1}^{Num(D)^* Num(D)} Rdx_{\lambda} \left( Dx_{\lambda} u_x^{\alpha(\lambda)+\alpha(\lambda)} u_y^{\beta(\lambda)+\beta(\lambda)} \theta_z^{\gamma(\lambda)+\gamma(\lambda)} \right)} \\
F_y &= \frac{\sum_{\kappa=1}^{Num(N)} \sum_{\kappa'=1}^{Num(D)} Rn_{\kappa} Rd_{\kappa'} \left( (N_{\kappa} D_{\kappa'}) (\beta + \beta') u_x^{\alpha+\alpha'} u_y^{\beta+\beta'-1} \theta_z^{\gamma+\gamma'} \right)}{\sum_{\kappa=1}^{Num(D)} \sum_{\kappa'=1}^{Num(D)} Rd_{\kappa} Rd_{\kappa'} \left( (D_{\kappa} D_{\kappa'}) u_x^{\alpha+\alpha'} u_y^{\beta+\beta'} \theta_z^{\gamma+\gamma'} \right)} \\
&= \frac{\sum_{\lambda=1}^{Num(N)^* Num(D)} Rny_{\lambda} \left( Ny_{\lambda} u_x^{\alpha(\lambda)+\alpha(\lambda)} u_y^{\beta(\lambda)+\beta(\lambda)-1} \theta_z^{\gamma(\lambda)+\gamma(\lambda)} \right)}{\sum_{\lambda=1}^{Num(D)^* Num(D)} Rdy_{\lambda} \left( Dy_{\lambda} u_x^{\alpha(\lambda)+\alpha(\lambda)} u_y^{\beta(\lambda)+\beta(\lambda)} \theta_z^{\gamma(\lambda)+\gamma(\lambda)} \right)} \\
M_z &= \frac{\sum_{\kappa=1}^{Num(N)} \sum_{\kappa'=1}^{Num(D)} Rn_{\kappa} Rd_{\kappa'} \left( (N_{\kappa} D_{\kappa'}) (\gamma + \gamma') u_x^{\alpha+\alpha'} u_y^{\beta+\beta'} \theta_z^{\gamma+\gamma'-1} \right)}{\sum_{\kappa=1}^{Num(D)} \sum_{\kappa'=1}^{Num(D)} Rd_{\kappa} Rd_{\kappa'} \left( (D_{\kappa} D_{\kappa'}) u_x^{\alpha+\alpha'} u_y^{\beta+\beta'} \theta_z^{\gamma+\gamma'} \right)} \\
&= \frac{\sum_{\lambda=1}^{Num(N)^* Num(D)} Rnz_{\lambda} \left( Nz_{\lambda} u_x^{\alpha(\lambda)+\alpha(\lambda)} u_y^{\beta(\lambda)+\beta(\lambda)} \theta_z^{\gamma(\lambda)+\gamma(\lambda)-1} \right)}{\sum_{\lambda=1}^{Num(D)^* Num(D)} Rdz_{\lambda} \left( Dz_{\lambda} u_x^{\alpha(\lambda)+\alpha(\lambda)} u_y^{\beta(\lambda)+\beta(\lambda)} \theta_z^{\gamma(\lambda)+\gamma(\lambda)} \right)}
\end{aligned} \tag{3.11}$$

6. At this point, we can use the order of magnitude estimates given in Table 1 to obtain retention coefficients for the numerator and the denominator for each of the relations given above. This can be obtained as follows:

$$Rki_{\lambda} = \begin{cases} 1 & \text{if } \left( Abs \left( \frac{Ki_{\lambda} u_x^{p(\lambda)} u_y^{q(\lambda)} \theta_z^{r(\lambda)}}{Max_{\gamma=1..Num(Ki)} \left( Ki_{\gamma} u_x^{l(\gamma)} u_y^{m(\gamma)} \theta_z^{n(\gamma)} \right)} \right) > Tol \right) \\ 0 & \text{otherwise} \end{cases} \quad (3.12)$$

Where  $i=x,y$  or  $z$ ,  $K=N$  or  $D$ ,  $k=n$  or  $d$  and  $Tol$  is used to eliminate the small quantities when compared to large ones in the expression. In other words, we would assign the numerical value of 1 to the retention coefficient if the ratio between the corresponding term and the maximum term in the sum is greater than the tolerance ( $Tol$ ) that we set. The numerical estimates for each of the displacement variables are used. However, neglecting terms in a sum can sometimes not be this straightforward. This is because a sum could be composed of several moderately sized terms which can add up to become comparable to large ones. As an illustration, consider the set:  $\langle 50, 1, 1, 1, 1, \dots, 1 \rangle$ . Using the above scheme, the retention vector would be  $\langle 1, 0, 0, \dots, 0 \rangle$ . This is obviously an incorrect approximation as the sum of a large number of small terms (1) can become comparable to the large one (50). However, there is a scope for making the algorithm more robust which can be taken up in future work.

7. Moreover, the retention coefficients obtained in equation (3.12) can be related to their parent coefficients given in equation (3.9). If  $Num(D)$  is the number of terms in the denominator and  $Num(N)$  is the number of terms in the numerator of the strain energy expression, for the  $x$  force displacement relation:

$$\begin{aligned} Rnx_{\kappa'+Num(D)*(\kappa-1)} &= Rn_{\kappa} Rd_{\kappa'} \\ Rdx_{\kappa'+Num(D)*(\kappa-1)} &= Rd_{\kappa} Rd_{\kappa'} \end{aligned} \quad (3.13)$$

$$\kappa' = 1, 2, \dots, Num(D), \kappa = 1, 2, \dots, Num(N)$$

Now, for the denominator, this relation can be expanded as follows:

$$\begin{aligned} & \left[ Rdx_1, Rdx_2, \dots, Rdx_{Num(D)}, Rdx_{Num(D)+1}, \dots, Rdx_{2num(D)}, \dots, Rdx_{Num(D)^2} \right] \\ & = [Rd_1 Rd_1, Rd_1 Rd_2, \dots, Rd_1 Rd_{Num(D)}, \dots, Rd_{Num(D)}^2] \end{aligned} \quad (3.14)$$

A simple way to link the parent terms ( $Rd$ ) to the reduced terms ( $Rdx$ ) would be to use the following scheme:

$$\begin{aligned} Rd_i = Rd_j = 1 \text{ if } Rdx_{num(D)*(i-1)+j} = 1 \\ i, j = 1, Num(D) \end{aligned} \quad (3.15)$$

Similarly, the numerator can be expanded as follows:

$$\begin{aligned} & \left[ Rnx_1, Rnx_2, \dots, Rnx_{Num(D)}, Rnx_{Num(D)+1}, \dots, Rnx_{2num(D)}, \dots, Rnx_{Num(D)Num(N)} \right] \\ & = [Rd_1 Rn_1, Rd_1 Rn_2, \dots, Rd_1 Rn_{Num(D)}, \dots, Rd_{Num(D)} Rn_{num(N)}] \end{aligned} \quad (3.16)$$

Finally, we can evaluate the retention vector for the numerator using a simple scheme shown below:

$$\begin{aligned} Rd_i = Rn_j = 1 \text{ if } Rnx_{Num(D)*(i-1)+j} = 1 \\ i = 1, Num(D); j = 1, Num(N) \end{aligned} \quad (3.17)$$

Thus, from equations (3.15) and (3.17), we get two different  $Rds$ , the union of which would give the retention vector for the denominator of the strain energy expression. At the end of this step we have two parent retention vectors associated with every force-displacement relation ( $(Rn(F_x), Rd(F_x)), (Rn(F_y), Rd(F_y)), (Rn(M_z), Rd(M_z))$ ). These retention vectors basically signify the terms that have to be retained in the original strain energy expression to arrive at the corresponding approximate force displacement relation.

8. Finally, the union of the three retention vectors for the numerator ( $Rn(F_x, F_y, M_z)$ ) and three vectors for the denominator ( $Rd(F_x, F_y, M_z)$ ) would give us the final retention vectors for the strain energy expression i.e.

$$\begin{aligned} Rn &= Rn(F_x) \cup Rn(F_y) \cup Rn(M_z) \\ Rd &= Rd(F_x) \cup Rd(F_y) \cup Rd(M_z) \end{aligned} \quad (3.18)$$

Using relation (3.9) and (3.18), we can now obtain the approximate expression for the strain energy.

Using the above algorithm for a parallelogram, the approximate strain energy expression can be given as:

$$v_p(u_x, u_y, \theta_z) = \frac{\left( k_{11}^{(0)}u_y^2 + k_{33}u_x^2 - k_{33} \left( k_{11}^{(0)}k_{11}^{(2)} - 0.25 \left( k_{11}^{(1)} \right)^2 \right) u_y^4 + k_{11}^{(1)}k_{33}u_xu_y^2 + 2k_{12}^{(0)}\theta_zu_y + 2k_{12}^{(1)}k_{33}\theta_zu_xu_y \right) + k_{33}k_{22}^{(1)}\theta_z^2u_xk_{11}^{(1)} + k_{33} \left( 2k_{11}^{(0)}k_{12}^{(2)} - k_{11}^{(1)}k_{12}^{(1)} + 2k_{11}^{(2)}k_{12}^{(0)} \right) \theta_zu_y^3 - k_{33}\theta_z^2w^2}{\left( 1 - k_{33} \left( k_{22}^{(2)}\theta_z^2 + 2k_{12}^{(2)}\theta_zu_y + k_{11}^{(2)}u_y^2 \right) \right)} \quad (3.19)$$

Moreover, we observe that for the force displacement relations for the  $x$  and  $y$  directions, all terms containing  $\theta_z$  can be dropped. Therefore, for that case, the strain energy would be:

$$v_p(u_x, u_y, \theta_z) = \frac{\left( k_{11}^{(0)}u_y^2 + k_{33}u_x^2 - k_{33} \left( k_{11}^{(0)}k_{11}^{(2)} - 0.25 \left( k_{11}^{(1)} \right)^2 \right) u_y^4 + k_{11}^{(1)}k_{33}u_xu_y^2 \right)}{\left( 1 - k_{33}k_{11}^{(2)}u_y^2 \right)} \quad (3.20)$$

Using these expressions we can recover the force displacement relations (3.1), (3.2) and (3.3) after applying the appropriate retention vectors obtained in step 5.

## Performance

The performance of this mechanism can now be quantified in the following manner:

### *Range of Motion*

The range of motion of a parallelogram mechanism is simply the maximum stroke of a single beam before yielding/fracture as both beams would get displaced by the same amount because of the geometric constraint imposed by the rigid link. Therefore, the range of motion would be given by equation (2.22)

### *Error Motions*

Using the definition of error motions,

$$e_x(u_y) = u_x(f_x = 0) = -\frac{1}{2}u_y^2 k_{11}^{(1)} \quad (3.21)$$

It is important to note here that the error in the  $x$  direction  $e_x$  only depends on one mechanism geometric parameter  $a_0$  and the lower bound of  $k_{11}^{(1)}(a_0)$  is 1.0, which occurs as  $a_0 \rightarrow 0$ , therefore, this error motion cannot be reduced beyond  $0.5u_y^2$ . This is a fundamental limit and is true for any arbitrary beam shape and not just the lumped compliance one. This result can be obtained using the calculus of variations as follows – The objective would be to minimize the kinematic  $x$  displacement given in equation (2.9) i.e.

$$\text{Min} \left( 0.5 \int_0^1 (y')^2 dx \right) \quad (3.22)$$

Moreover, it is also known that:

$$\int_0^1 y' dx = u_y \quad (3.23)$$

Finally, we have the boundary conditions given as:

$$\begin{aligned} y(0) &= 0, y'(0) = 0 \\ y(1) &= u_y, y'(1) = 0 \end{aligned} \quad (3.24)$$

Taking the variation of equation (3.22), at the minima, we obtain:

$$\begin{aligned} \delta \left( \int_0^1 (y')^2 dx \right) &= 0 \\ \Rightarrow \int_0^1 \delta (y')^2 dx &= 0 \\ \Rightarrow \int_0^1 y' \delta y' dx &= 0 \end{aligned} \quad (3.25)$$

Applying integration by parts on the above equation,

$$\begin{aligned} \int_0^1 y' \delta y' dx &= y' \int_0^1 \delta y' dx - \int_0^1 y'' \delta y dx = 0 \\ \Rightarrow y' \delta y \Big|_0^1 - \int_0^1 y'' \delta y dx &= 0 \end{aligned} \quad (3.26)$$

Now,  $y$  displacement is known at both ends of the beam implying that the variation is also zero at those points i.e.  $\delta y = 0$  @  $x = 0, L$ . Therefore, the first term in equation (3.26) is zero and we have:

$$\int_0^1 y'' \delta y dx = 0 \quad (3.27)$$

Finally, as the variation  $\delta y$  is arbitrary over the length of the beam except at the ends, we can write:

$$y'' = 0 \Rightarrow y' = c = \text{const.} \forall x \in (0,1) \quad (3.28)$$

Using equation (3.23), we get:

$$\int_0^1 y' dx = u_y \Rightarrow \int_{0^+}^{1^-} c dx = u_y \Rightarrow c = u_y \quad (3.29)$$

Thus, the minimum value of error motion will be:

$$\text{Min}(e_x(u_y)) = -0.5 \int_{0^+}^{1^-} u_y^2 dx = -0.5 u_y^2 \quad (3.30)$$

It should be noted that throughout the above derivation, no assumptions have been made regarding the beam shape or the forces applied. Moreover, if the beam is very stiff in the axial ( $x$ ) direction, this error motion would dominate the axial displacement  $u_x$  given by (3.2).

The theta error motions can be obtained by setting the bearing direction forces/moments ( $f_x$  and  $M_z$ ) to zero:

$$e_\theta(u_y) = \frac{1}{2w^2} \left( \frac{1}{k_{33}} - u_y^2 k_{11}^{(2)} \right) [-u_y (2k_{12}^{(0)})] \quad (3.31)$$

Because of the constraint arrangement, these error motions would be very small and can be reduced further by increasing the beam separation  $w$  or reducing the beam thickness  $t$ . These error motions occur because of the fact that the point of application of the load (center of the stage) does not coincide with that of the center of stiffness. The force  $f_y$  which brings about the  $y$  displacement applies a moment about this point causing a net rotation. However, as the  $y$  direction is a DoF, this force would be small. Moreover, the theta direction is a DoC (provided that  $w$  is large enough) implying that the rotational stiffness would be large. Thus, the overall effect would be a negligibly small rotational error motion. For some typical numbers –  $t=1/50, w=0.3, u_y=0.1$ , we get  $e_\theta=1.2e-4$  which

is several orders of magnitude smaller than the  $x$  error motion. With  $a_0$  approaching zero, this error motion also tends to zero as the mechanism approaches a four bar linkage.

### ***Motion Direction Stiffness***

The motion direction stiffness is given by:

$$k_y = \frac{\partial f_y}{\partial u_y} = (2k_{11}^{(0)} + f_x k_{11}^{(1)}) \quad (3.32)$$

Also,

$$\frac{\partial k_y}{\partial u_y} = 0 \quad (3.33)$$

Therefore, the parallelogram mechanism has negligible stiffening in  $y$  direction with increasing  $y$  displacement and  $k_y$  can be minimized by increasing  $a_0$ . As expected, axial load causes stiffening or softening depending on its action (tension or compression).

### ***Bearing Direction Stiffness***

The stiffness in the bearing directions are given by:

$$k_x = \frac{\partial f_x}{\partial u_x} = \frac{2}{\left( \frac{1}{k_{33}} - u_y^2 k_{11}^{(2)} \right)} \quad (3.34)$$

$$k_\theta = \frac{\partial m_z}{\partial \theta_z} = \frac{2w^2}{\left( \frac{1}{k_{33}} - u_y^2 k_{11}^{(2)} \right)} \quad (3.35)$$

Also, to maximize both these values over the whole motion range, we could minimize the compliances  $c_x = 1/k_x$ ,  $c_\theta = 1/k_\theta$  and  $\partial c_x / \partial u_y$ ,  $\partial c_\theta / \partial u_y$ .

$$c_x = \left( \frac{1}{2k_{33}} - \frac{u_y^2 k_{11}^{(2)}}{2} \right); \frac{\partial c_x}{\partial u_y} = -u_y k_{11}^{(2)} \quad (3.36)$$

$$c_\theta = \frac{1}{w^2} \left( \frac{1}{2k_{33}} - \frac{u_y^2 k_{11}^{(2)}}{2} \right); \frac{\partial c_\theta}{\partial u_y} = -\frac{u_y k_{11}^{(2)}}{w^2} \quad (3.37)$$

Thus, we need to minimize the elasto-kinematic term  $k_{11}^{(2)}$  to reduce the stiffness drop and maximize  $k_{33}$  to increase the nominal ( $u_y=0$ ) stiffness both of which imply reducing  $a_0$ .

When we consider objectives (1.1) to (1.4) in conjunction, there is a clear tradeoff in choosing the value of  $a_0$  (Figure 11). From Figure 11, we can see that with decreasing  $a_0$ , the bearing stiffness increases at a much higher rate than the motion direction stiffness implying that a low value of  $a_0$  is favorable for better stiffness performance. A very low value of  $a_0$  would also imply a smaller range of motion and motion direction stiffness approaching infinity. However, one of the major drawbacks of this mechanism is the fundamentally large axial error motion which cannot be reduced via any beam shape optimization.

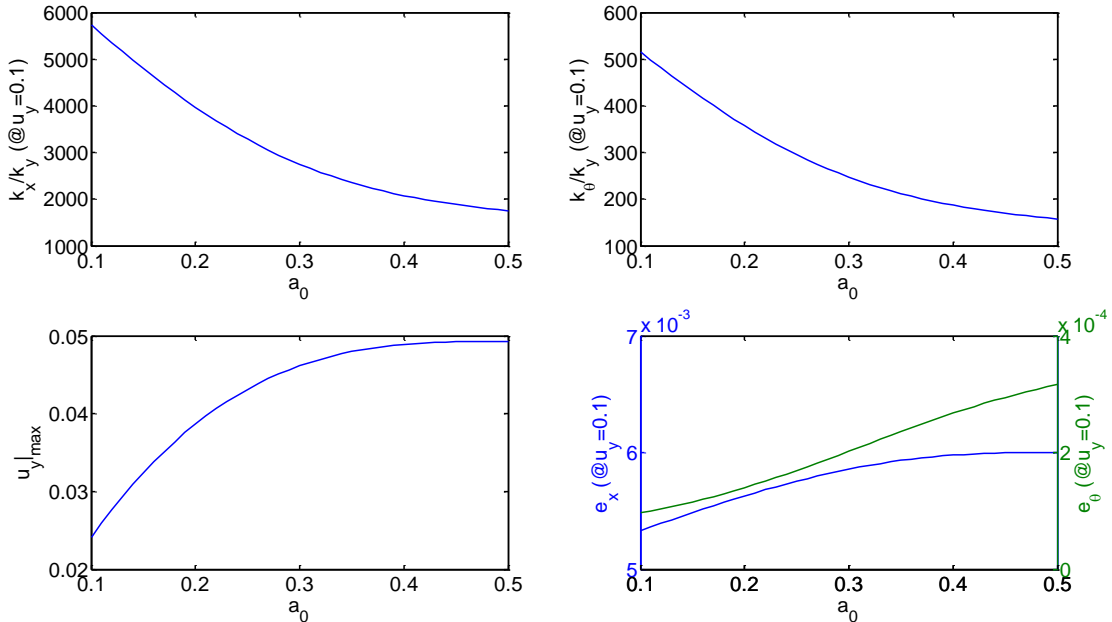


Figure 11: Non-dimensionalized performance metrics for a parallelogram mechanism. Parameters:  $t=1/50$ ,  $w=0.3$ ,  $S_y=1\text{GPa}$ ,  $E=169\text{GPa}$ .



## MULTI-BEAM PARALLELOGRAM

In a parallelogram, we can include more beams ( $n$ ) in the same configuration to obtain a *multi-beam parallelogram* (shown in Figure 12). This mechanism would be highly over constrained according to Grubler's criterion and for an equivalent rigid link mechanism with revolute joints, it would function only when the beams are exactly identical and parallel with little or no tolerance for manufacturing imperfections. However, because of elastic averaging, small geometric imperfections wouldn't cause significant over-constraint in a flexure based mechanism [49]. For this analysis, all the  $n$  beams are assumed to be identical with the same degree of reinforcement  $a_0$ . Normalization of the forces and displacement is done with respect to the properties of either beam. Finally, in order to simplify the final results, the mechanism is assumed to be symmetrical about the axis parallel to the  $x$  axis and passing through the center of the beam shown as a dotted line in Figure 12. The general case when this is not true can be analyzed without any added complexity.

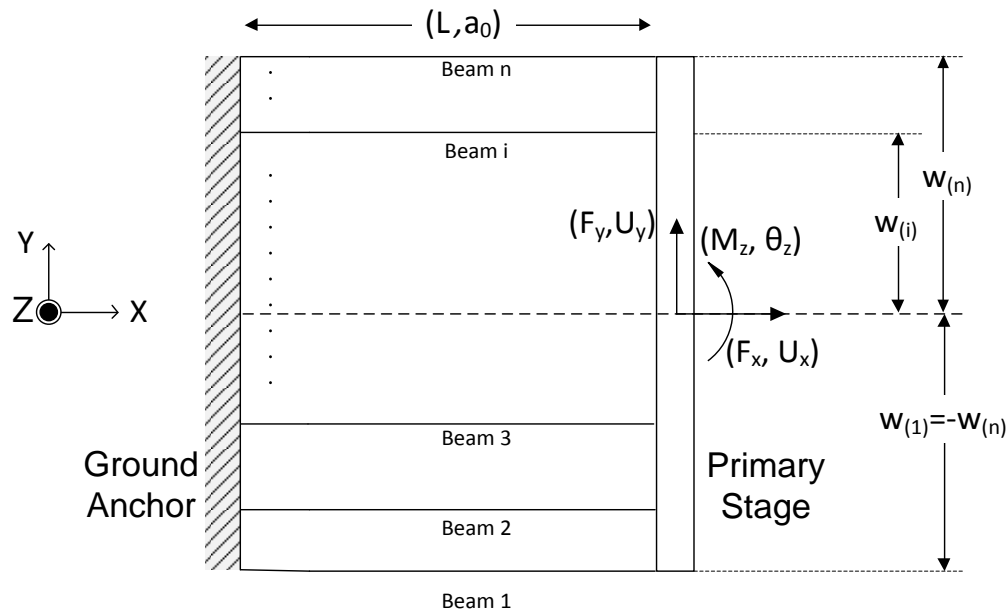


Figure 12: The multi-beam parallelogram

## BCM Analysis

This derivation for the force displacement relations for this mechanism is along similar lines to that for the two beam parallelogram. At tip of the  $i^{th}$  beam, we would have reaction forces/moments and displacement pairs  $(F_{yi}, U_{yi})$ ,  $(F_{xi}, U_{xi})$  and  $(M_{zi}, \theta_{zi})$ . As before the rigid stage imposes a geometric constraint on these displacements and we can write them in terms of the displacements at the center of the stage  $(U_y, U_x, \theta_z)$ :

$$\begin{aligned} U_{yi} &\approx U_y \\ U_{xi} &\approx U_x - w_i \theta_z \\ \theta_{zi} &\approx \theta_z \end{aligned} \quad (3.38)$$

Applying the force equilibrium conditions on the free body diagram of the mechanism, the reaction forces can be related to the forces at the center of the stage as follows:

$$\begin{aligned} F_x &= \sum_{i=1}^n F_{xi} \\ F_y &= \sum_{i=1}^n F_{yi} \\ M_z &= \sum_{i=1}^n (M_{zi} - F_{xi} w_i) \end{aligned} \quad (3.39)$$

Now, applying the normalized force displacement relations (2.11) and (2.12) for every  $i^{th}$  beam in the mechanism, we get:

$$\begin{aligned} \begin{bmatrix} f_{yi} \\ m_{zi} \end{bmatrix} &= \begin{bmatrix} k_{11}^{(0)} & k_{12}^{(0)} \\ k_{12}^{(0)} & k_{22}^{(0)} \end{bmatrix} \begin{bmatrix} u_{yi} \\ \theta_{zi} \end{bmatrix} + f_{xi} \begin{bmatrix} k_{11}^{(1)} & k_{12}^{(1)} \\ k_{12}^{(1)} & k_{22}^{(1)} \end{bmatrix} \begin{bmatrix} u_{yi} \\ \theta_{zi} \end{bmatrix} \\ u_{xi} &= \frac{1}{k_{33}} f_{xi} - \frac{1}{2} \begin{bmatrix} u_{yi} & \theta_{zi} \end{bmatrix} \begin{bmatrix} k_{11}^{(1)} & k_{12}^{(1)} \\ k_{12}^{(1)} & k_{22}^{(1)} \end{bmatrix} \begin{bmatrix} u_{yi} \\ \theta_{zi} \end{bmatrix} - f_{xi} \begin{bmatrix} u_{yi} & \theta_{zi} \end{bmatrix} \begin{bmatrix} k_{11}^{(2)} & k_{12}^{(2)} \\ k_{12}^{(2)} & k_{22}^{(2)} \end{bmatrix} \begin{bmatrix} u_{yi} \\ \theta_{zi} \end{bmatrix} \end{aligned} \quad (3.40)$$

Combining relations (3.38), (3.39) and (3.40) and using the small  $\theta$  approximation, the force displacement relations for the multi-beam parallelogram would be given by:

$$\begin{aligned} f_y &= nk_{11}^{(0)} + f_x k_{11}^{(1)} u_y \\ m_z &= n \left( k_{12}^{(0)} u_y + k_{22}^{(0)} \theta_z \right) + f_x \left( k_{12}^{(0)} u_y + k_{22}^{(0)} \theta_z \right) + \frac{k_{33} \theta_z}{(1 - k_{33} k_{11}^{(2)} u_y^2)} \sum w_i^2 \\ u_x &= \frac{f_x}{nk_{33}} - \frac{1}{2} k_{11}^{(1)} u_y^2 - \frac{f_x}{n} k_{11}^{(2)} u_y^2 \end{aligned} \quad (3.41)$$

## Strain Energy Analysis

The strain energy method for this case [47] is simpler to apply compared to the direct BCM because of the existence of purely geometric relationships between the displacement variables at every beam tip given by equation (3.38). Equation (3.7) can be modified for the multi-beam case:

$$v_{mp}(u_x, u_y, \theta_z) = \frac{1}{2}n(k_{11}^{(0)}u_y^2 + 2k_{12}^{(0)}u_y\theta_z + k_{22}^{(0)}\theta_z^2) + \frac{1}{2}k_{33} \sum_{i=1}^n \left( u_x - w_i\theta_z + \frac{1}{2}(k_{11}^{(1)}u_y^2 + 2k_{12}^{(1)}u_y\theta_z + k_{22}^{(1)}\theta_z^2) \right)^2 \left( 1 - k_{33}(k_{11}^{(2)}u_y^2 + 2k_{12}^{(2)}u_y\theta_z + k_{22}^{(2)}\theta_z^2) \right) \quad (3.42)$$

The above equation can now be used to obtain the force displacement relations, an analysis that has been carried out previously[47]. With appropriate approximations, the results agree with those obtained using the direct BCM method (equation (3.41)).

## Performance

Using equation (3.41), the performance metrics can be calculated:

### *Range of Motion*

The range of motion is the same as that of a parallelogram in the absence of bearing loads. However, with a bearing direction load  $f_x$ , the range of motion can be calculated using equation (2.21):

$$u_y \leq \left( \frac{1}{\eta} \right) \left( \frac{4}{k_{11}^{(0)} - 2 \frac{f_x}{n} (k_{12}^{(1)})} \right) \left( \frac{S_y}{E} - 0.08 \frac{f_x}{n} \left( \frac{T}{L} \right)^2 \right) \left( \frac{L}{T} \right) \quad (3.43)$$

This shows that the reduction in the maximum range in the presence of a tensile bearing load can be decreased by adding multiple beams.

### ***Error Motions***

The error motion  $e_x$  would be the same as that of a two-beam parallelogram. The theta error motions on the other hand would have a dependence on the rotational stiffness and would be given by:

$$e_{\theta}(u_y) = \frac{1}{\sum_{i=1}^n w_i^2} \left( \frac{1}{k_{33}} - u_y^2 k_{11}^{(2)} \right) [-u_y (2k_{12}^{(0)})] \quad (3.44)$$

### ***Motion Direction Stiffness***

From equation (3.41), the motion direction stiffness is given by:

$$k_y = (nk_{11}^{(0)} + f_x k_{11}^{(1)}) \quad (3.45)$$

This shows that the new stiffness is simply the sum of y direction stiffness expressions of individual beams (with an axial bearing load of  $f_x/n$ ) in the *multi-beam* parallelogram. An important observation that we can make from the above expression is that the sensitivity of the motion direction stiffness to the axial load  $f_x$  also reduces by a factor of  $n$ .

### ***Bearing Direction Stiffness***

The bearing direction stiffness expressions are given by:

$$k_x = \frac{n}{\left( \frac{1}{k_{33}} - k_{11}^{(2)} u_y^2 \right)} \quad (3.46)$$

$$k_{\theta} = \frac{\sum_{i=1}^n w_i^2}{\left( \frac{1}{k_{33}} - k_{11}^{(2)} u_y^2 \right)} \quad (3.47)$$

The expression for the x-direction stiffness is simply  $n/2$  times that of a parallelogram.

The advantage of using this mechanism over the two beam parallelogram is not immediately obvious. This mechanism offers a better way of improving the stiffness

properties of the two beam parallelogram over merely thickening the constituent beams. A comparison between a two beam parallelogram mechanism with thickened beams and a multi-beam one is presented below.

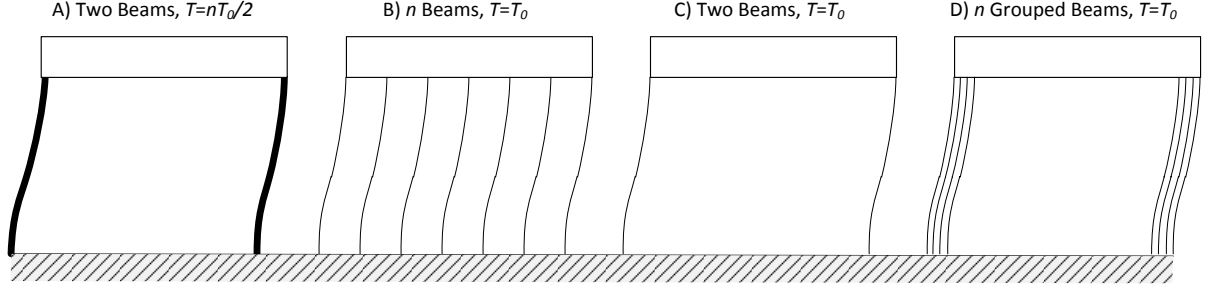


Figure 13: Comparison between the multi-beam and the two beam parallelograms

Consider the three mechanisms shown in the Figure 13. If the forces and moments are normalized with respect to the properties of the third parallelogram (C), the motion and bearing stiffness of each of these flexures would be given by:

$$\begin{aligned}
 k_y^A &= \frac{n^3}{8} (2k_{11}^{(0)}) & k_x^A &= \frac{n^3}{8} \left( \frac{2}{\left(\frac{n^2}{4}\right) \frac{1}{k_{33}} - k_{11}^{(2)} u_y^2} \right) \\
 k_y^B &= \frac{n}{2} (2k_{11}^{(0)}) & k_x^B &= \frac{n}{2} \left( \frac{2}{\frac{1}{k_{33}} - k_{11}^{(2)} u_y^2} \right) \\
 k_y^C &= (2k_{11}^{(0)}) & k_x^C &= \left( \frac{2}{\frac{1}{k_{33}} - k_{11}^{(2)} u_y^2} \right)
 \end{aligned} \tag{3.48}$$

We find that by merely increasing the thickness of the beams, we obtain an  $n^3/8$  increase in the motion direction stiffness but only a nominal stiffness increase of  $n/2$  in the bearing stiffness. On the other hand, for the multi-beam parallelogram, we obtain a proportional

increase of  $n/2$  in both the motion and the bearing direction stiffness. This is graphically illustrated in Figure 14 by comparing the stiffness ratios  $k_x/k_y$ .

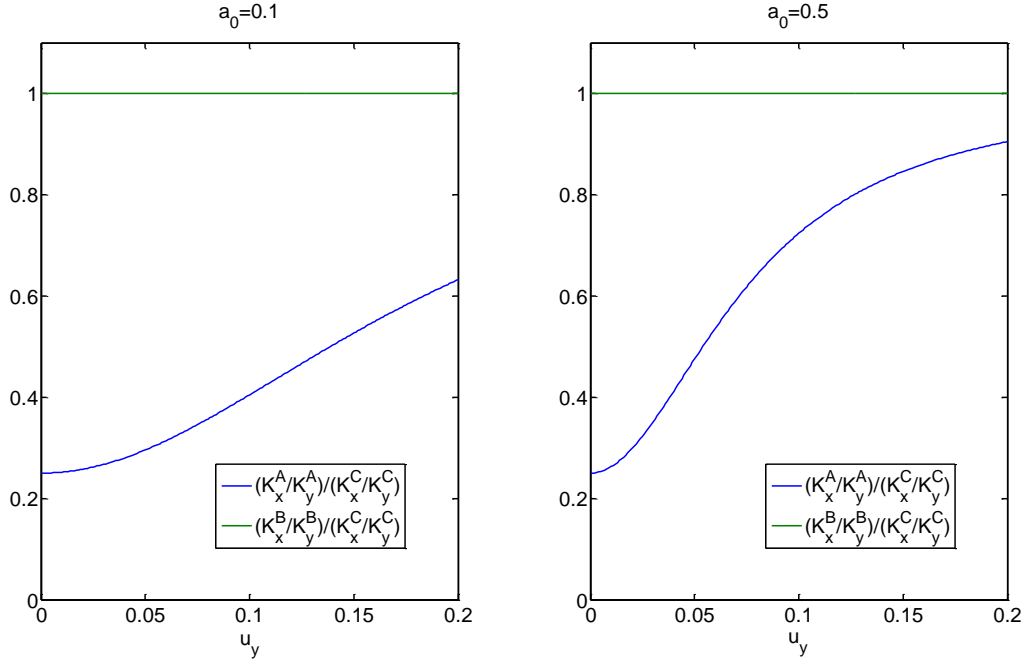


Figure 14: Stiffness Ratios of the flexures A,B and C

For lower values of  $a_0$  the effect of elastic stiffness term  $1/k_{33}$  starts dominating the elasto-kinematic term  $k_{11}^{(2)}u_y^2$  and therefore, the advantage of using a multi-beam parallelogram over the two-beam one would become more prominent as can be seen in Figure 14. The gain in the rotational stiffness would also be similar as long as the beams are grouped together at the ends (mechanism D in Figure 13). In that case, the rotational stiffness would be given as:

$$k_\theta^D = \frac{\sum_{i=1}^n w_i^2}{\left(\frac{1}{k_{33}} - k_{11}^{(2)}u_y^2\right)} \approx \frac{n}{2} \left( \frac{2w^2}{\left(\frac{1}{k_{33}} - k_{11}^{(2)}u_y^2\right)} \right) \quad (3.49)$$

## DOUBLE PARALLELOGRAM AND PAIRED DOUBLE PARALLELOGRAM

A double parallelogram (DP) [48] flexure with two parallelogram units connected in series, and paired double parallelogram (DP-DP) flexure, with two DP units connected in parallel, are shown in Figure 15. The two rigid stages are referred to as the primary and secondary stages, as indicated. Loads  $f_y$ ,  $m_z$ , and  $f_x$  are applied at the center of the primary stage. The two parallelograms are identical, except for their beam spacing –  $w_1$  and  $w_2$ . Both parallelograms would have the same magnitude of axial error motions given by equation (3.21) but in the opposite directions. Thus, these error motions get absorbed in the secondary stage leading to a theoretically zero net error motion at the primary stage. As before, the forces and displacements are normalized against the properties of any of the constituent beams.

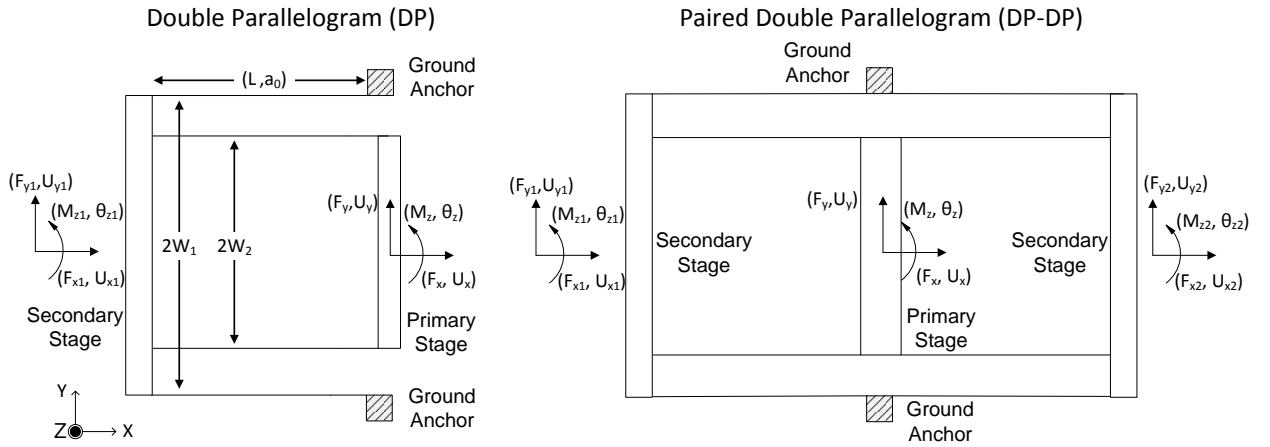


Figure 15: The Double Parallelogram and Paired Double Parallelogram Mechanisms. The forces and displacements at the secondary stages are also indicated.

## BCM Analysis

Applying the results derived for a single parallelogram in the last section sequentially on the outer and the inner parallelograms, the force displacement relations for a double parallelogram with no loads ( $f_{x1}=f_{y1}=m_{z1}=0$ ) on the secondary stage can easily be derived. The results were derived previously [24] and are presented below for a DP mechanism:

$$u_{y1} = \frac{f_y}{(2k_{11}^{(0)} - f_x k_{11}^{(1)})}; u_y - u_{y1} = \frac{f_y}{(2k_{11}^{(0)} + f_x k_{11}^{(1)})} \quad (3.50)$$

$$\Rightarrow u_y = \frac{4k_{11}^{(0)} f_y}{(2k_{11}^{(0)})^2 - (f_x k_{11}^{(1)})^2}$$

$$u_{x1} = -\frac{f_x}{2k_{33}} - \frac{u_{y1}^2}{2} (k_{11}^{(1)} - f_x k_{11}^{(2)}); u_x - u_{x1} = \frac{f_x}{2k_{33}} - \frac{(u_y - u_{y1})^2}{2} (k_{11}^{(1)} + f_x k_{11}^{(2)}) \quad (3.51)$$

$$\Rightarrow u_x = \frac{f_x}{k_{33}} + f_x u_y^2 \frac{k_{11}^{(2)} \left( (2k_{11}^{(0)})^2 + (f_x k_{11}^{(1)})^2 \right) + 4k_{11}^{(0)} (k_{11}^{(1)})^2}{(4k_{11}^{(0)})^2}$$

$$\theta_z = \frac{1}{2w_1^2} \left( \frac{1}{k_{33}} - \frac{f_y^2}{(2k_{11}^{(0)} - f_x k_{11}^{(1)})^2} k_{11}^{(2)} \right) \left( m_z - f_y \left( 1 - \frac{f_x}{(2k_{11}^{(0)} + f_x k_{11}^{(1)})} + \frac{(2k_{12}^{(0)} - f_x k_{12}^{(1)})}{(2k_{11}^{(0)} - f_x k_{12}^{(1)})} \right) \right) \quad (3.52)$$

$$+ \frac{1}{2w_2^2} \left( \frac{1}{k_{33}} - \frac{f_y^2}{(2k_{11}^{(0)} + f_x k_{11}^{(1)})^2} k_{11}^{(2)} \right) \left( m_z - \frac{f_y}{(2k_{11}^{(0)} + f_x k_{11}^{(1)})} (2k_{12}^{(0)} + f_x k_{12}^{(1)}) \right)$$

Force displacement relations in the presence of non-zero loading on the secondary stages can also be derived using a similar process without any added complexity.

### Strain Energy Method

The strain energy for a double parallelogram is simply the sum of the non-dimensional strain energies (as both parallelograms are identical) of its two constituent parallelograms given by equation (3.19). This resultant strain energy depends on the displacements of both the primary and the secondary stages:

$$v_{dp}(u_x, u_y, \theta_z) = v_p(-u_{x1}, u_{y1}, -\theta_{z1}) + v_p(u_x - u_{x1}, u_y - u_{y1}, \theta_z - \theta_{z1}) \quad (3.53)$$

As in the case of a parallelogram, we can obtain order of magnitude estimates for the displacement of a double parallelogram using equations (3.50) to (3.52).

Table 2: Order of Magnitude estimates for a double parallelogram

<i>Variable</i>	<i>Order</i>	<i>Justification</i>
-----------------	--------------	----------------------



$f_x$	+/-10	Model limits
$m_z$	+/-10	Model limits
$t$	1/50	Typical Dimensions
$w_1, w_2$	0.3-1.0	Typical Dimensions
$u_{y1}$	+/-0.1	Yield Limit
$u_y$	+/-0.2	Yield Limit
$u_x, u_{x1}$	$O(10^{-2})$	Using relation (3.51)
$\theta_z, \theta_{z1}$	$O(10^{-3})$	Using relation (3.52)

Using these estimates, we can now formulate an approximate expression for the strain energy of a double parallelogram. Equating the variation of the strain energy to the sum of the virtual work done by the forces and moments on the mechanism, we obtain six force displacement relations – three each at the primary and the secondary stage. Thus, have:

$$\delta v = f_x \delta u_x + f_y \delta u_y + m_z \delta \theta_z + f_{x1} \delta u_{x1} + f_{y1} \delta u_{y1} + m_{z1} \delta \theta_{z1} \text{ or,}$$

$$f_x = \frac{\partial v}{\partial u_x}, f_y = \frac{\partial v}{\partial u_y}, m_z = \frac{\partial v}{\partial \theta_z} \quad (3.54)$$

$$f_{x1} = \frac{\partial v}{\partial u_{x1}}, f_{y1} = \frac{\partial v}{\partial u_{y1}}, m_{z1} = \frac{\partial v}{\partial \theta_{z1}}$$

The retention vectors for the numerator and the denominator of the strain energy expression (3.53), can be written as:

$$\begin{aligned} Rn &= Rn(F_x) \cup Rn(F_y) \cup Rn(M_z) \cup Rn(F_{x1}) \cup Rn(F_{y1}) \cup Rn(M_{z1}) \\ Rd &= Rd(F_x) \cup Rd(F_y) \cup Rd(M_z) \cup Rd(F_{x1}) \cup Rd(F_{y1}) \cup Rd(M_{z1}) \end{aligned} \quad (3.55)$$

Now, in relation (3.54), we have six equations in six (known) forces and six (unknown) displacements. As the primary stage is the output stage, these equations have to be reduced to a set of three equations between the forces and displacements at the primary stage only; implying that the displacements at the secondary stage ( $u_{x1}, u_{y1}, \theta_{z1}$ ) have to be solved for in terms of those at the primary stage ( $u_x, u_y, \theta_z$ ). For each of the force

displacement relations, we can individually apply their retention vectors (Using equation (3.12)) to further simplify the problem. We observe that the dependence of the  $x$  and  $y$  direction forces on the rotational displacements is weak. Hence, we can decouple these force-displacement relations from the moment ones:

$$f_x = H(Rnx, Rdx) \frac{\partial v}{\partial u_x} (u_x, u_{x1}, u_y, u_{y1}), f_y = H(Rny, Rdy) \frac{\partial v}{\partial u_y} (u_x, u_{x1}, u_y, u_{y1}) \quad (3.56)$$

$$f_{x1} = H(Rnx1, Rdx1) \frac{\partial v}{\partial u_{x1}} (u_x, u_{x1}, u_y, u_{y1}), f_{y1} = H(Rny1, Rdy1) \frac{\partial v}{\partial u_{y1}} (u_x, u_{x1}, u_y, u_{y1})$$

And,

$$M_z = H(Rnz, Rdz) \frac{\partial v}{\partial \theta_z} (u_x, u_{x1}, u_y, u_{y1}, \theta_z, \theta_{z1}), \quad (3.57)$$

$$M_{z1} = H(Rnz1, Rdz1) \frac{\partial v}{\partial \theta_{z1}} (u_x, u_{x1}, u_y, u_{y1}, \theta_z, \theta_{z1})$$

Where  $H(Rni, Rdi)$  is the retention operator:

$$H(Rni, Rdi) = \frac{\sum_{\lambda=1}^{Num(N)*Num(D)} (Ni_{\lambda} u_x^{p(\lambda)} u_y^{q(\lambda)} u_{x1}^{p1(\lambda)} u_{y1}^{q1(\lambda)} \dots)}{\sum_{\lambda=1}^{Num(N)*Num(D)} (Di_{\lambda} u_x^{p(\lambda)} u_y^{q(\lambda)} u_{x1}^{p1(\lambda)} u_{y1}^{q1(\lambda)} \dots)} = \frac{\sum_{\lambda=1}^{Num(N)*Num(D)} Rni_{\lambda} (Ni_{\lambda} u_x^{p(\lambda)} u_y^{q(\lambda)} u_{x1}^{p1(\lambda)} u_{y1}^{q1(\lambda)} \dots)}{\sum_{\lambda=1}^{Num(N)*Num(D)} Rdi_{\lambda} (Di_{\lambda} u_x^{p(\lambda)} u_y^{q(\lambda)} u_{x1}^{p1(\lambda)} u_{y1}^{q1(\lambda)} \dots)} \quad (3.58)$$

$i = x, x1, y, y1, z, z1$

Using equation (3.56), we can solve for the four displacements in terms of the forces applied at the primary and the secondary stages. Finally, we can substitute these four displacements in equation (3.57) to solve for the rotations  $\theta_z$  and  $\theta_{z1}$ .

Unfortunately, the scheme for approximating ratios of polynomials fails in this case. This is because dropping terms based on magnitude neglects the possibility of sums of small or large terms becoming large or small respectively. Particularly, in the expression for  $f_{y1}$  given in equation (3.56), it was observed that the sum of the large terms which were retained after the approximation procedure was applied, reduced to a small number when typical magnitudes of the displacement variables were used thereby becoming comparable to the ‘small’ terms which were dropped previously. Therefore, there was a huge discrepancy between the approximate and the actual expressions.

Moreover, without the use of this algorithm the resulting multivariate polynomial equations turn out to be too complex to be solved even numerically, let alone analytically. Unless, a better, more robust way is formulated to simplify the force displacement equations, it is unlikely that this algorithm would yield good results for more complex mechanisms. In this thesis, this method would not be used for any of the mechanisms discussed subsequently as there is little merit in doing so.

## Performance

### *Range of Motion*

The yield limit of the DP would be the sum of the yield limits of its constituent parallelograms as they are connected in a serial configuration. As they are identical, it would just be twice that of a single parallelogram. For the DP-DP mechanism, the yield limit would be the same as both the DP units are connected in parallel and thus, have the same deflections. Thus, the maximum displacement of a DP (and DPDP) flexure is:

$$u_y \leq \left(\frac{2}{\eta}\right) \left(\frac{4}{k_{11}^{(0)}}\right) \left(\frac{S_y}{E}\right) \left(\frac{1}{t}\right) \quad (3.59)$$

### *Error Motions*

In the absence of any geometric imperfections, the  $x$  error motions for a DP mechanism would be zero. However, the theta error motions would be small but finite arising due to the same reasons as those in the case of a parallelogram:

$$\begin{aligned} e_x(u_y) &= 0 \\ e_\theta(u_y) &= \frac{1}{2w_1^2} \left( \frac{1}{k_{33}} - \frac{u_y^2}{4} k_{11}^{(2)} \right) \left( -k_{11}^{(0)} u_y \left( 1 + \frac{k_{12}^{(0)}}{k_{11}^{(0)}} \right) \right) \\ &+ \frac{1}{2w_2^2} \left( \frac{1}{k_{33}} - \frac{u_y^2}{4} k_{11}^{(2)} \right) (-u_y k_{12}^{(0)}) \end{aligned} \quad (3.60)$$

The DPDP mechanism would on the other hand, have zero error motions but because of symmetry and would have more robustness towards imperfections. It would however, have a slight stiffening in the motion direction due to conflicting  $\theta$  error motions.

### ***Motion Direction Stiffness***

The motion direction stiffness of the DP mechanism is given by:

$$k_y = k_{11}^{(0)} - \frac{(k_{11}^{(1)} f_x)^2}{4k_{11}^{(0)}} \quad (3.61)$$

Also,

$$\frac{\partial k_y}{\partial u_y} = 0 \quad (3.62)$$

An axial load  $f_x$  causes a net softening irrespective of the direction but the effect is much smaller than that seen in a parallelogram. This can be explained as follows - when a load is applied on the primary stage in the positive direction, the inner parallelogram would be in compression, causing it to soften whereas the outer one would be in tension, thereby leading to stiffening. The parallelograms would simply reverse roles when the loading is applied in the opposite direction. As both these parallelograms are in series, these two effects would oppose each other thereby reducing the sensitivity of the motion direction stiffness to the axial loading.

### ***Bearing Direction Stiffness/Compliance***

The bearing direction compliances of the DP mechanism (For the DPDP mechanism, the compliances are half those of the DP) are given by:

$$c_x = \left( \frac{1}{k_{33}} + \frac{u_y^2}{4} \left( -k_{11}^{(2)} + \frac{(k_{11}^{(1)})^2}{k_{11}^{(0)}} \right) \right) \quad (3.63)$$

$$c_\theta = \left( \frac{w_1^2 + w_2^2}{2w_1^2 w_2^2} \right) \left( \frac{1}{k_{33}} - \frac{u_y^2}{4} (k_{11}^{(2)}) \right) \quad (3.64)$$

Also, the stiffness drops are given by:

$$\begin{aligned} \frac{\partial C_x}{\partial u_y} &= \frac{u_y}{2} \left( -k_{11}^{(2)} + \frac{(k_{11}^{(1)})^2}{k_{11}^{(0)}} \right) \\ \frac{\partial C_\theta}{\partial u_y} &= - \left( \frac{w_1^2 + w_2^2}{2w_1^2 w_2^2} \right) \frac{u_y k_{11}^{(2)}}{2} \end{aligned} \quad (3.65)$$

The purely elastic term in  $x$ -stiffness expression is expected and is similar to the one in equation (3.36). However, the elasto-kinematic term is significantly different and consists of the terms  $k_{11}^{(2)}$  and  $(k_{11}^{(1)})^2/k_{11}^{(0)}$ , the latter, being two orders larger than the former thus dictating the axial compliance. When a  $y$  displacement is imposed on the primary stage, the transverse stiffness values of the two parallelograms would be the same if no axial loading is applied on the primary or the secondary stage. Thus, this  $y$  displacement gets distributed equally across the two parallelograms leading to half the  $y$  displacement of the primary stage at the secondary stage. When an axial load  $F_x$  is applied on the primary stage in the positive direction, the transverse stiffness of the inner parallelogram increases while that of the outer one decreases (using equation (3.32)). This results in a proportional redistribution of the  $y$  displacement between the two as given by equation (3.50). In this case, the outer parallelogram would deflect more than that in the unloaded case ( $u_y/2$ ) whereas the inner one would deflect less. Since the kinematic axial displacement ( $u_k$ ) of each parallelogram has a quadratic dependence on its corresponding transverse displacement, and considering the fact that for a parallelogram, the kinematic component dominates the axial displacement, the net axial displacement of the outer parallelogram exceeds that of the inner one. This difference results in the unexpectedly large elasto-kinematic component -  $(k_{11}^{(1)})^2/k_{11}^{(0)}$  mentioned before causing a precipitous stiffness drop [23, 24]. The scenario remains the same when the  $F_x$  is negative, except the two parallelograms switch roles. The axial stiffness of DP and DPDP mechanisms are plotted against the transverse displacement ( $u_y$ ) in Figure 16, which shows that the

bearing stiffness drops by 90% for a  $u_y$  of 0.1. This is significantly larger than that of the parallelogram mechanism for the same dimensions and is a serious limitation in the constraint characteristics of the DP flexure module.

As the motion direction stiffness of the parallelograms have a very weak dependence on the applied moment, an application of a moment doesn't cause any significant redistribution of  $y$  displacements. This effect is further attenuated as the parallelogram mechanism doesn't have any significantly large kinematic theta error motions which are strongly dependent on the  $y$  displacement. Thus, both the parallelograms have approximately the same rotational stiffness over the whole range of  $y$  displacements and applied loads. Consequently, the net rotational stiffness of the double parallelogram is simply the serial sum<sup>3</sup> of the stiffness of the constituent parallelograms.

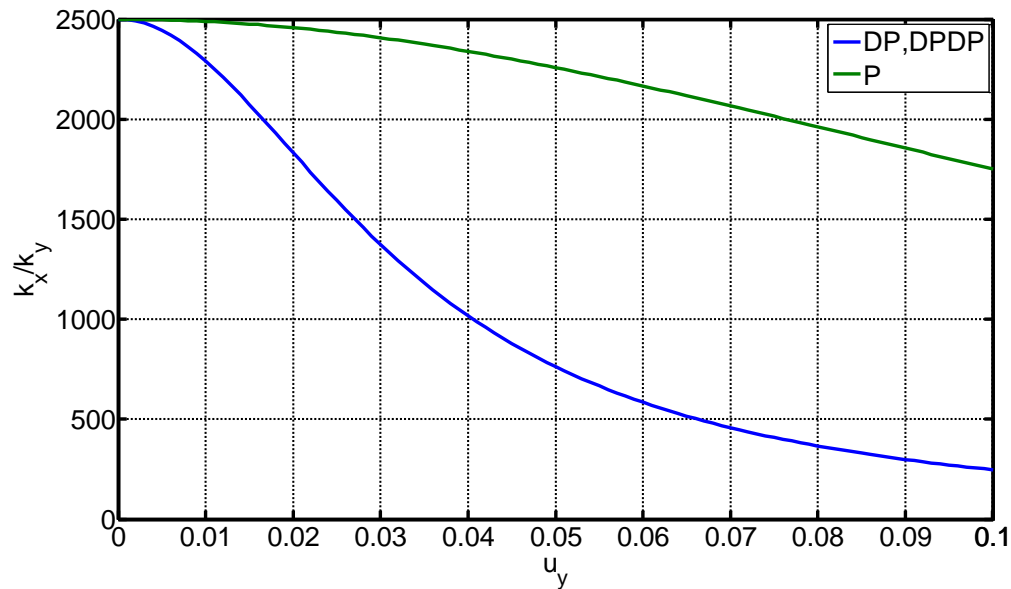


Figure 16: Stiffness ratio comparison between the double parallelogram and the parallelogram mechanisms.  $T=1/50L$ ,  $a_0=0.5$

<sup>3</sup> The serial sum is defined as the equivalent spring stiffness of two springs (with stiffness  $k_1$  and  $k_2$ ) in a series connection i.e.  $k_{eq}=(k_1k_2)/(k_1+k_2)$

For the double parallelogram we can implement all the basic variations that were discussed previously – reinforced beam flexures and the use of multiple beams in every parallelogram. The performance metrics 1 through 4 have been plotted in figure.  $N$  represents the number of beams in every parallelogram and  $a_0$  represents the degree of reinforcement. Also, the beams in the parallelograms are grouped at the ends like in Figure 13 (D). The trends seen in the rotational stiffness and the maximum range are expected and similar to those seen in the case of a parallelogram. The theta error motions drop with decreasing  $a_0$  and increasing  $N$  due to the increasing rotational stiffness of the mechanism and resistance to the moment applied by the motion direction force  $f_y$  about the center of stiffness of the mechanism. It is interesting to see that the axial stiffness ratio remains relatively unaffected with changes in the  $N$  and  $a_0$ . This shows that this phenomenon is fundamental to the mechanism like the arcuate motion of a parallelogram and cannot be eliminated without making appropriate topological alterations.

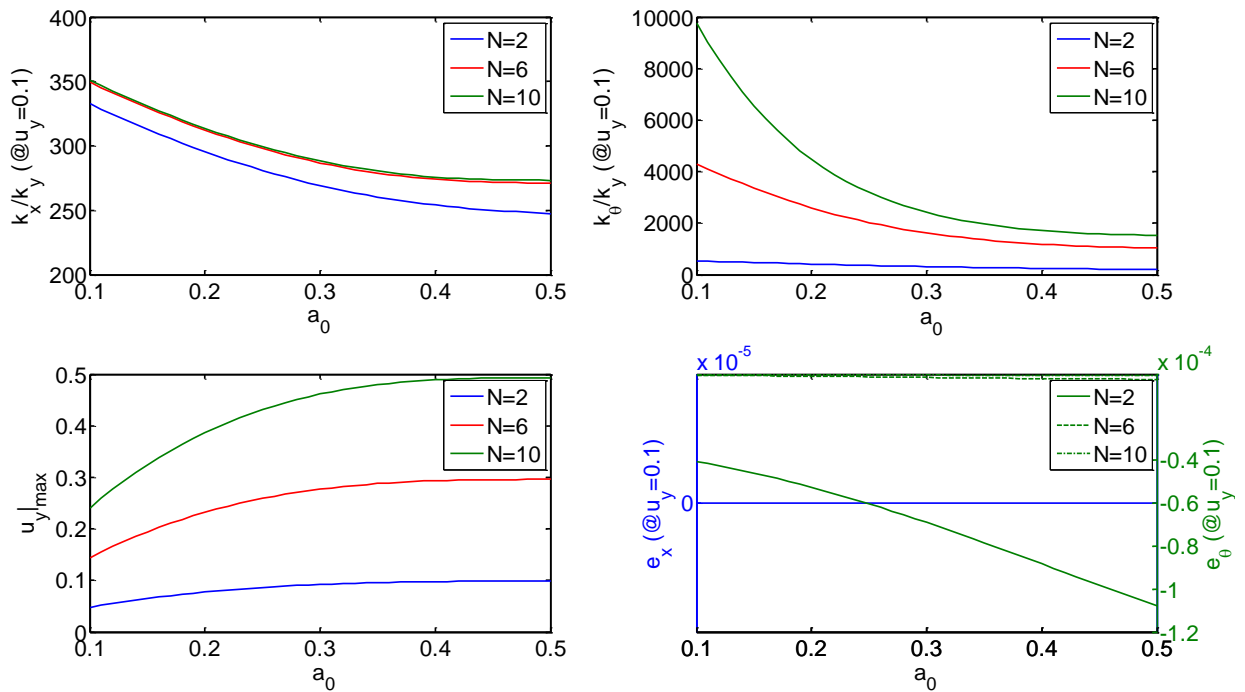


Figure 17: Non-dimensionalized performance metrics for a double parallelogram mechanism. Parameters:

$$t=2/(50*N), w_1=0.25, w_2=0.4, S_y=1GPa, E=169GPa.$$

Thus, in the transition from a parallelogram to a double parallelogram flexure, while geometric reversal improves the range of motion of the DOF and eliminates the purely kinematic component of the bearing displacement, it proves to be detrimental to stiffness along the  $X$  direction DOC.

The axial stiffness drop in the DP mechanism occurs due to the unconstrained motion of the secondary stages[23, 24]. In other words, the secondary stage *accommodates* the axial force  $f_x$  by displacing in the motion direction. This can be prevented if the stage is adequately constrained i.e. held at its equilibrium displacement of  $u_y/2$  even in the presence of an axial load [50-53]. Rewriting equation (3.50) and (3.51) for non-zero forces ( $f_{xl}, f_{yl}$ ) on the secondary stage (Figure 15), we get:

$$u_{y1} \approx \frac{u_y}{2} = \frac{f_y + f_{y1}}{(2k_{11}^{(0)} - (f_x + f_{x1})k_{11}^{(1)})} \quad (3.66)$$

$$u_y - u_{y1} \approx \frac{u_y}{2} = \frac{f_y}{(2k_{11}^{(0)} + f_x k_{11}^{(1)})}$$

$$u_{x1} = \frac{(f_x + f_{x1})}{2k_{33}} + \frac{u_y^2}{8} (k_{11}^{(1)} - (f_x + f_{x1})k_{11}^{(2)}) \quad (3.67)$$

$$u_x - u_{x1} = \frac{f_x}{2k_{33}} - \frac{u_y^2}{8} (k_{11}^{(1)} + f_x k_{11}^{(2)})$$

We now have 5 unknowns namely  $u_x, u_y, u_{x1}, f_{x1}$  and  $f_{y1}$  and four equations. Choosing  $f_{x1}$  as an input parameter and solving for the remaining variables, we get:

$$u_y = \frac{2f_y}{(2k_{11}^{(0)} + f_x k_{11}^{(1)})}$$

$$u_x = \frac{(2f_x + f_{x1}) \left( 4(k_{11}^{(0)})^2 + 4f_x k_{11}^{(0)} k_{11}^{(1)} + f_x^2 (k_{11}^{(1)})^2 - f_y^2 k_{11}^{(2)} k_{33} \right)}{4(2k_{11}^{(0)} + f_x k_{11}^{(1)})^2 k_{33}} \quad (3.68)$$

And,

$$f_{y1} = \frac{-f_y k_{11}^{(1)} (2f_x + f_{x1})}{(2k_{11}^{(0)} + f_x k_{11}^{(1)})} = -u_y k_{11}^{(1)} \left( f_x + \frac{f_{x1}}{2} \right) \quad (3.69)$$



Assuming that  $f_{x1}=0$ , we notice that the large elasto-kinematic term  $(k_{11}^{(1)})^2/k_{11}^{(0)}$  is no longer present in the expression for  $u_x$  and hence, the stiffness properties of this configuration are very similar to those of a parallelogram. The required constraint force  $f_{y1}$  for the secondary stage can also be calculated (equation (3.69)) and as is perhaps intuitively obvious, is directly proportional to the axial force  $f_x$  and the motion direction displacement  $u_y$ . Upon investigating further into the effect of  $f_{x1}$ , we find that it introduces an error motion term in  $u_x$  ( $u_x@f_x=0$ ) which might be undesirable. Moreover, if we try to counter this effect by introducing symmetry in the mechanism like in the DPDP mechanism, it leads to load stiffening/softening in the motion direction. Setting  $u_x=0$  with no external axial forces applied in equation (3.68), we get:

$$f_x|_{\text{internal}} = -0.5f_{x1} = 0.5f_{x2} \quad (3.70)$$

Where  $f_x|_{\text{internal}}$  is the force experienced by the left half of the DPDP mechanism shown in Figure 15. Substituting this in equation (3.68) for  $u_y$ :

$$u_y = \frac{2f_y}{\left(2k_{11}^{(0)} - 0.5f_{x1}k_{11}^{(1)}\right)} \quad (3.71)$$

An outward (negative) force  $f_{x1}$  would cause load stiffening in the mechanism which would be undesirable. On the other hand, reversing the direction will cause softening which would reduce the actuator effort.

Based on the above analysis, in order to rectify the shortcomings of the DP (DPDP) mechanism we need to impose a constraint which has the following properties:

1. A motion direction constraint force  $f_{y1}$  given by equation (3.69) that would restrain the secondary stages at a displacement of  $0.5u_y$
2. A non-negative bearing direction force  $f_{x1}$ . In other words, all  $x$ -direction forces (if any) on the secondary stages must be acting inwards.

## LEVER-DOUBLE PARALLELOGRAM AND LEVER-PAIRED DOUBLE PARALLELOGRAM

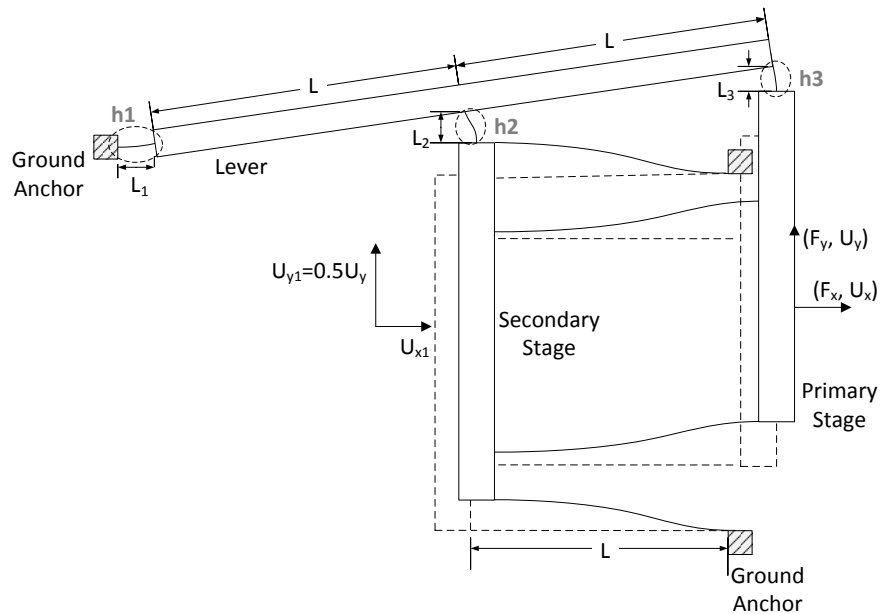


Figure 18: The Lever Double Parallelogram

A method for constraining the motion of the secondary stages using a lever arm like the one shown in Figure 18 was first proposed by Jones et.al. [48]. The same design was employed in comb drive actuators by Brouwer et.al [54] and Jerman et. al [53] and was found to produce a significantly improved range of motion. The lever *exactly* constrains the secondary stages to half the displacement of the primary using short flexural hinges ( $h1$ ,  $h2$ ,  $h3$  in Figure 18). A thorough design study of this mechanism does not exist in previous literature and a very rigorous mathematical analysis wouldn't be pursued here. Instead, a few qualitative observations regarding the performance of this mechanism will be presented which would be supplemented with results from non-linear finite element analysis.

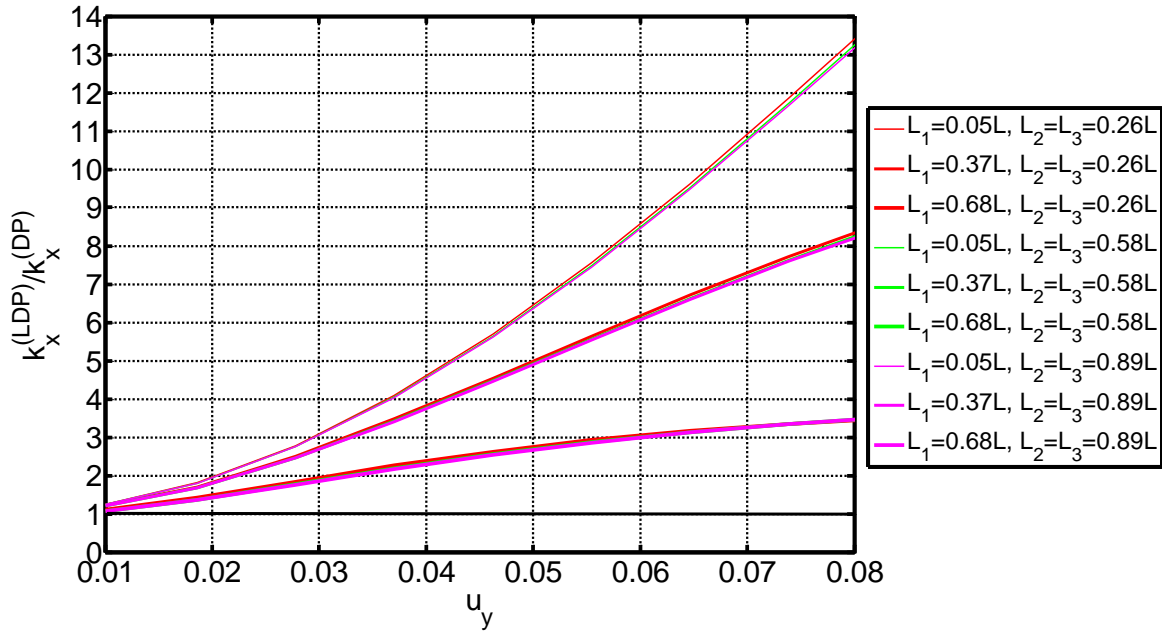


Figure 19: Bearing Direction Stiffness  $K_x$  of the Lever Double Parallelogram (LDP). Parameters:  
 $T=0.0123L$ ,  $H=0.39L$ ,  $E=69e9$

It can be seen that for the lever to be effective in providing the motion direction constraint on the secondary stage, the hinge  $h1$  should have a high rotational ( $\theta$ ) compliance but small transverse ( $y$ ) direction compliance. We know that the rotational compliance is proportional to the length of the flexure whereas the  $y$  direction compliance is proportional to the cube of the length. Therefore, reducing the length of the beam would make it stiffer in the  $y$  direction compared to the  $\theta$  direction. Consequently, shorter the length  $L_i$ , the greater would be the improvement in the bearing stiffness of the mechanism. As long as hinges  $h2$  and  $h3$  have adequate axial stiffness, their dimensions wouldn't significantly affect the bearing stiffness. Non-linear finite element analysis (using ANSYS<sup>4</sup>) validates the above claims as shown in Figure 19.

---

<sup>4</sup> With BEAM 4 Elements for the beams, MPC184 elements for the rigid section, NLGEOM (large deflection static analysis) turned on and shear coefficients set to zero. These settings were used for all FEA results shown in this thesis.

The motion direction stiffness of the LDP mechanism is higher than that of the DP mechanism because of the rotational stiffness of the hinge  $hl$  adding to the motion direction stiffness of the DP mechanism. Moreover, this stiffness is inversely proportional to length of the hinge  $L_1$  and hence, shortening it would significantly increase the motion direction stiffness. From Figure 20, we can see that the lever can cause up-to 95% increase in the base stiffness of the DP mechanism for the required bearing stiffness.

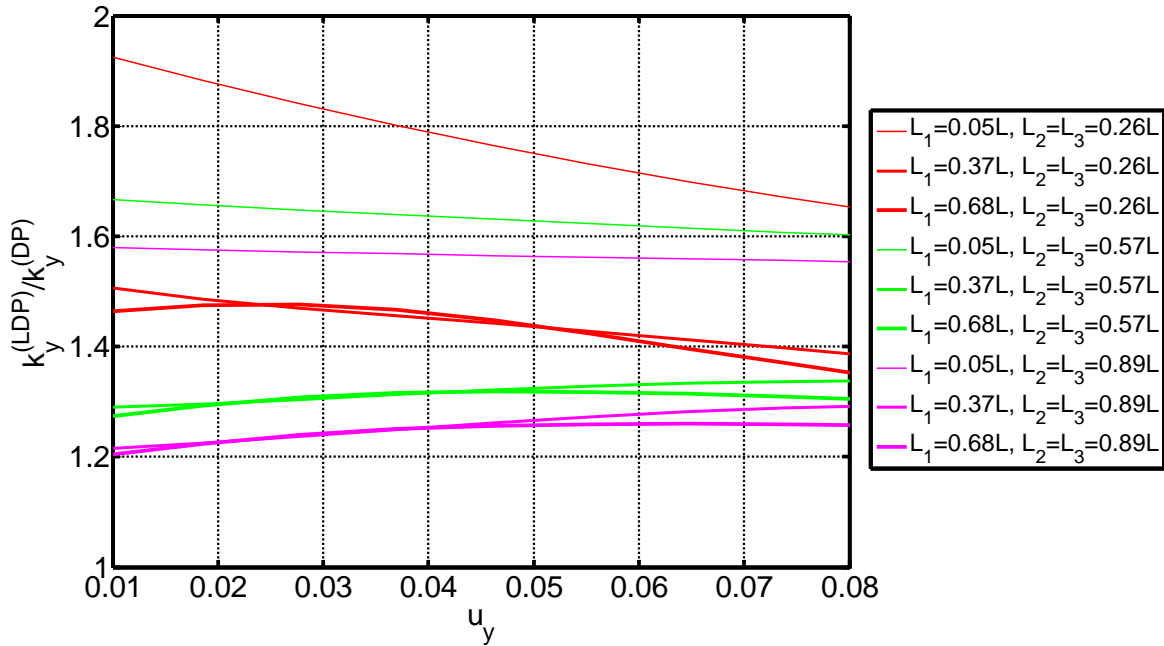


Figure 20: Motion Direction Stiffness  $K_y$  of the Lever Double Parallelogram (LDP). Parameters: same as those in Figure 19

Thus, shortening  $L_1$  improves the bearing stiffness but significantly increases the motion direction stiffness as well. This tradeoff cannot be overcome with any of the beam shape or multiple beam modifications suggested before and is inherent to the geometry of the mechanism. Apart from this, another minor drawback is the limited range of motion as the motion of the lever and the secondary and primary stages in the  $x$  direction would oppose each other causing the motion direction stiffness to increase exponentially beyond

a certain displacement (Figure 21). However, this effect can be avoided by making  $L_2$  and  $L_3$  large enough while maintaining the bearing direction stiffness.

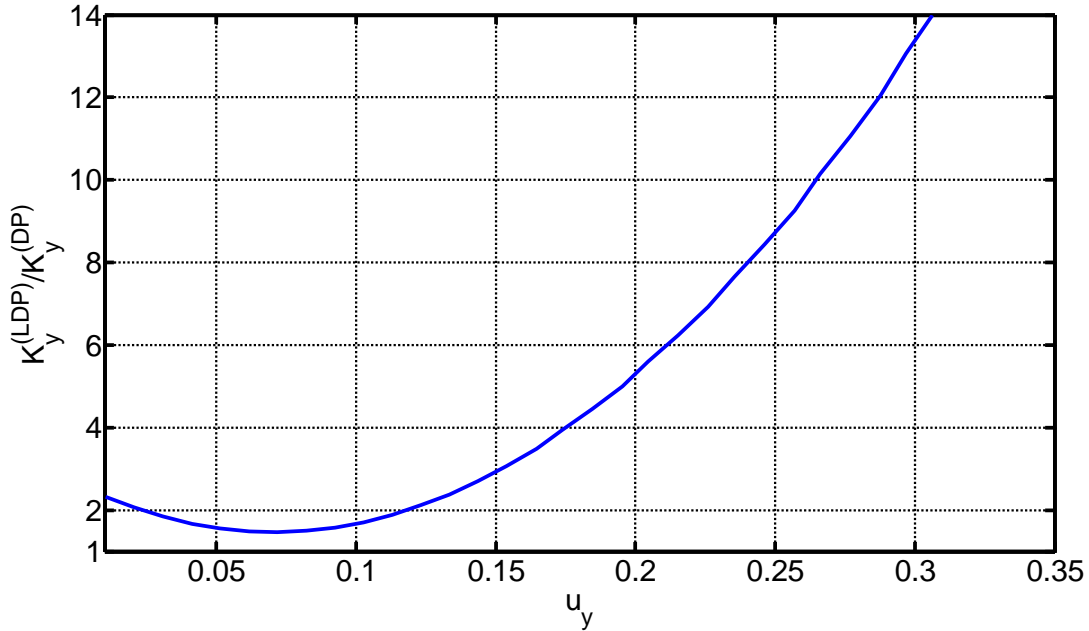


Figure 21: Exponential Rise in the motion direction stiffness of the LDP mechanism. Parameters:  $L_1=L_2=L_3=0.1L$ , rest same as before.

In the next chapter two alternative mechanism designs would be analyzed which can be optimized to satisfy both the requirements listed in the previous section to obtain improved bearing stiffness without causing any significant stiffening in the motion direction.

## **Chapter 4: Analysis of the Clamped Paired Double Parallelogram (CDPDP) and Double Parallelogram – Tilted-beam Double Parallelogram (DP-DTB)**

In the last chapter, we analyzed the reasons behind the precipitous bearing stiffness drop in the Double Parallelogram Mechanism i.e. the unconstrained motion of the secondary stages. We also discussed a method, invented previously, of constraining these secondary stages by using a lever. However, this mechanism has some drawbacks like increased motion direction stiffness and larger footprint and therefore, there is a scope for further improvement. In this chapter, the analysis of two flexure mechanisms [43] which perform better in terms of the metrics defined in chapter 1 is presented. Wherever feasible, we will provide the complete derivation of the force displacement relations using BCM and strain energy approaches and a validation of the results using non-linear finite element analysis.

### **THE CLAMPED PAIRED DOUBLE PARALLELOGRAM**

When we apply an axial force on the primary stage of a DPDP mechanism, the secondary stages respond by moving in opposite directions from their equilibrium positions at half the primary stage  $y$  displacement. Because of symmetry, these differential displacements would be equal and opposite as shown in Figure 22.

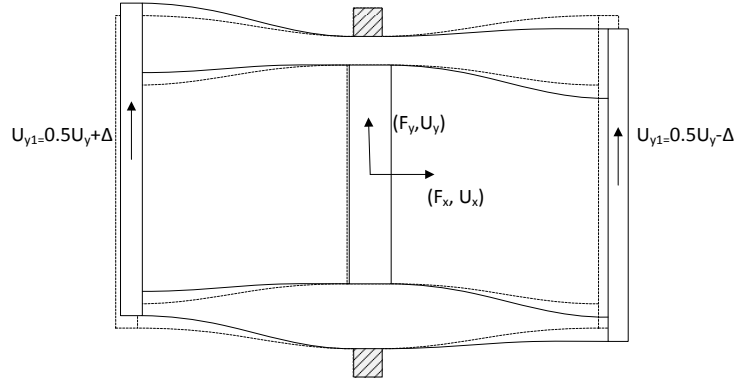


Figure 22: Response of the DPDP mechanism to an axial force  $F_x$ . The differential displacement  $\Delta$  would depend on  $U_y$  and  $F_x$

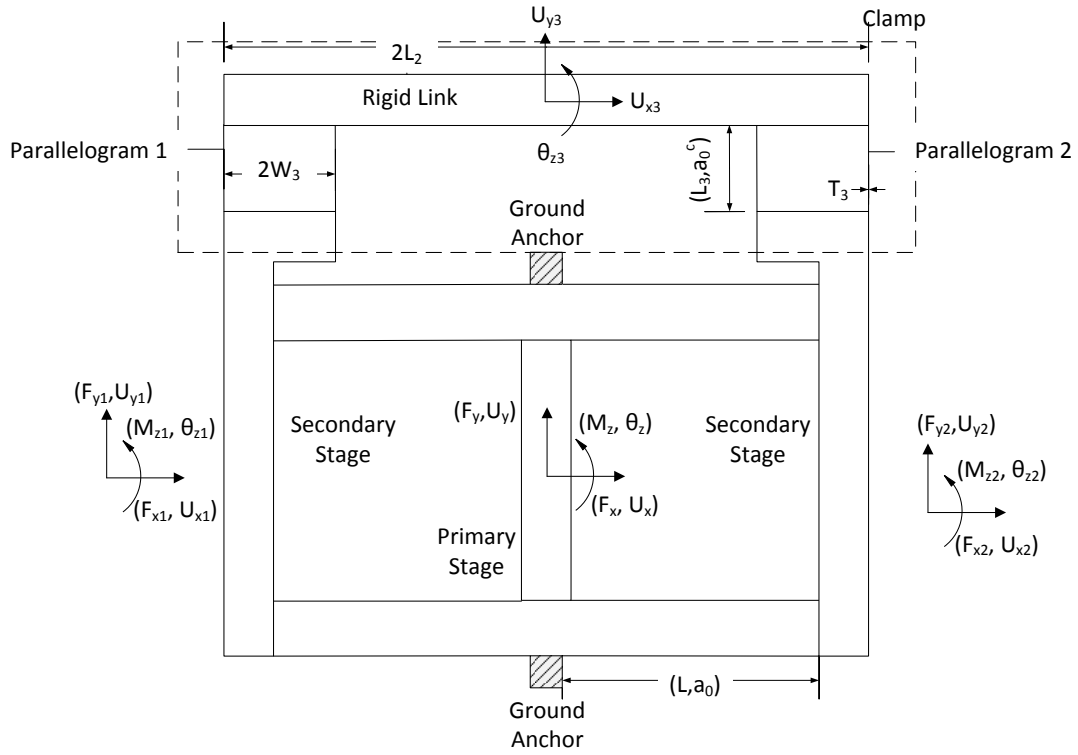


Figure 23: The Clamped paired double parallelogram mechanism. The dimensions of the base DPDP mechanism are the same as before.

In the CDPDP mechanism, the two secondary stages are connected to each other in such a manner that any relative displacement between the two is prevented. Consequently, the stages naturally get restrained to a mean position of  $0.5U_y$ . This connector, also called a *clamp*, comprises a rigid link and two pairs of flexure beams which connect the link to the secondary stages as shown in Figure 24. Any relative displacement between the two stages directly translates into the rotation of the link. As the rotational stiffness of the parallelograms formed by flexure pairs is very large (as it is a constraint direction), the clamp rotates by a very small amount and hence, the secondary stages have almost equal motion direction displacements. This satisfies the first requirement for the constraint force as mentioned in the previous chapter.

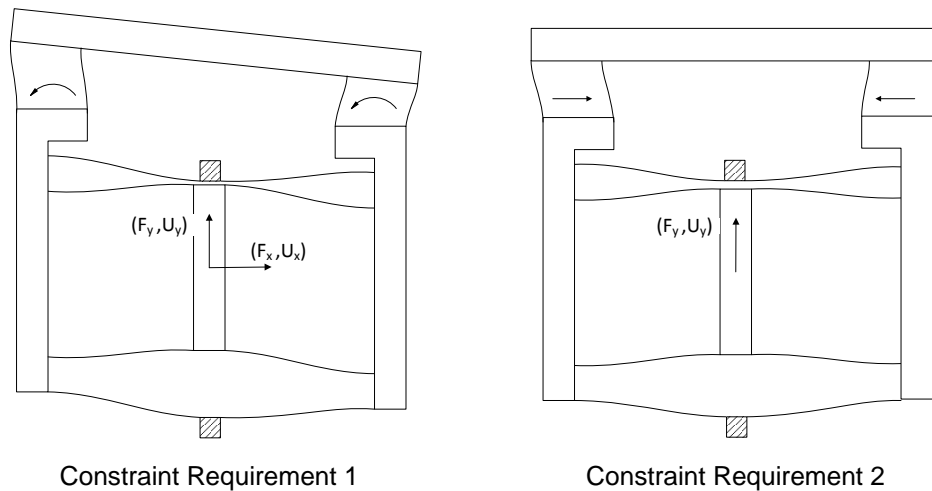


Figure 24: The constraint behavior of the CDPDP mechanism

Moreover, the clamp provides very small impedance to any motions of the secondary stages in the  $x$  direction as its parallelogram connectors are fairly compliant in this direction. Even though it doesn't exactly satisfy the second requirement as the force  $f_{x1}$  and  $f_{x2}$  would be acting outwards on the secondary stages, using some basic dimensional optimization, these forces can be made negligibly small without affecting the bearing direction stiffness.



Before we discuss the closed form analysis of this mechanism, we can make a few qualitative observations regarding the effect of the dimensions of the clamp. Such an approach can give valuable insights into the working of a mechanism and would be useful in cases where closed form results can't be obtained very easily. Broadly speaking, the two constraint requirements translate into the following:

1. *Maximize the rotational stiffness of the parallelograms*

Re-dimensionalizing equation (3.35) for the two parallelograms shown in figure, we get:

$$K_{\theta_i} = \frac{EH_3T_3^3}{12L_3} \frac{2W_3^2}{\left(\frac{T_3^2}{12} - U_{xi}^2k_{11}^{(2)}\right)}, i = 1, 2 \quad (4.1)$$

Thus, we can improve the rotational stiffness by increasing  $W_3$ ,  $H_3$ ,  $T_3$  or by decreasing  $L_3$

2. *Minimize the motion direction stiffness of the parallelograms*

Rewriting equation (3.32) in its dimensionalized form with no axial loads ( $f_x=0$ ):

$$K_y = \frac{EH_3T_3^3}{12L_3^3} (2k_{11}^{(0)}) \quad (4.2)$$

Therefore, we can reduce the motion direction stiffness by increasing  $L_3$  or reducing  $H_3$  and  $T_3$ .

Considering these two objectives in conjunction, we observe that tradeoffs exist in choosing the dimensions  $L_3$ ,  $H_3$  and  $T_3$ . However, we also notice that we can increase the rotational stiffness independently by increasing the beam separation  $2W_3$  as long as the footprint is not significantly affected. Thus, there is a scope for making the clamp very *effective* i.e. achieve the desired bearing direction stiffness without stiffening the motion direction. In the next few sections, we would analytically derive the bearing direction and

motion direction stiffness of the CDPDP mechanism. In chapter 6, these results would be used to optimize the mechanism for maximizing the stroke of a comb-drive actuator with given footprint and voltage specifications.

### BCM Analysis

All forces and displacements are normalized with respect to the beam parameters of the original paired double parallelogram unit. The mechanism comprises of 6 parallelograms with 3 force/moment relations each, 3 known forces (at the primary stage), 12 unknown displacements (3 at the primary stage, 6 at the secondary stages, 3 at the center of the rigid link) and 6 unknown forces (3 at each secondary stage). Thus, using the direct approach, we would have a total of 18 equations which in their original form might be almost impossible to solve analytically. We would therefore, employ a different approach by making many simplifying assumptions and approximations and eventually arrive at approximate stiffness expressions which are very close (to within 5% for  $u_y \leq 0.2$ ) to those predicted by FEA. We would list these assumptions with their justifications as we step through the derivation. Such an approach can be used for many other complex mechanisms where a very high accuracy of the results is not required.

Figure 25 shows the free body diagram of a CDPDP mechanism when acted upon by forces at its primary stage. Writing the force and moment equilibrium relations for just the clamp, we find that:

$$\begin{aligned} F_{x1} &= -F_{x2} \\ F_{y1} &= -F_{y2} \\ M_{z1} + M_{z2} &= 2F_{y1}L_2 + F_{x1}(U_{y2} - U_{y1}) \end{aligned} \quad (4.3)$$

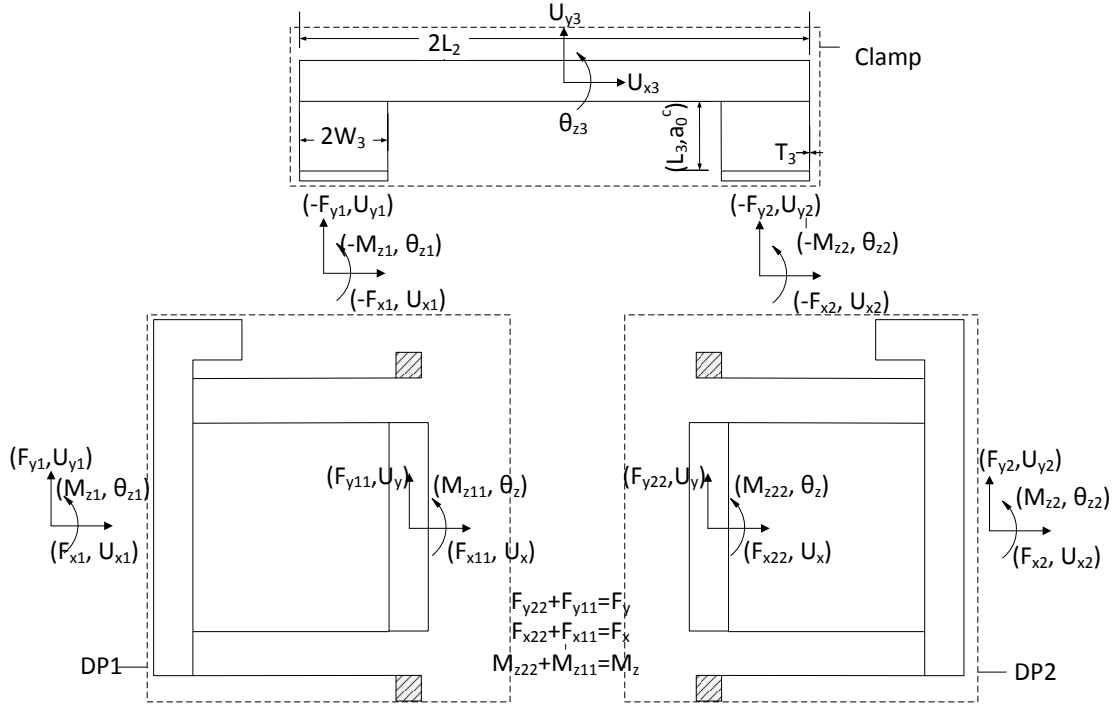


Figure 25: Free Body Diagram of the CDPDP mechanism showing internal forces and moments

Assuming that the beam separation in the base DPDP mechanism is large enough, the rotations  $\theta_{z1}$  and  $\theta_{z2}$  would be much smaller than the rotation of the clamp  $\theta_{z3}$ . Therefore, the parallelograms in the clamp would rotate by the same amount:  $\theta_{z3}$ . Moreover, we can relate this rotation to the relative motion direction displacement between the two secondary stages:

$$\theta_{z3} = \frac{(U_{y2} - U_{y1})}{2L_2} \quad (4.4)$$

Using relation (3.3) for a parallelogram and using the fact that the displacements  $U_{x1}$  and  $U_{x2}$  would be small, we can neglect the contribution of the elasto-kinematic term and approximately write (For a more detailed justification, the reader is referred to Appendix B):

$$\theta_{z3} = \frac{L_3^2}{2W_3^2} \left( \frac{a_0^c T_3^2}{6L_3^2} \right) \left( \frac{12M_{z2}L_3}{EH_3 T_3^3} \right) = \frac{L_3^2}{2W_3^2} \left( \frac{a_0^c T_3^2}{6L_3^2} \right) \left( \frac{12M_{z1}L_3}{EH_3 T_3^3} \right) \quad (4.5)$$

$$\Rightarrow M_{z1} = M_{z2} = \frac{EH_3 T_3 W_3^2}{a_0^c L_3} \theta_{z3}$$

It should be noted that when re-dimensionalizing the equation, the dimensions of the clamp parallelograms are used. Moreover, the forces  $F_{x1}$  and  $F_{x2}$  can be obtained by using the motion direction stiffness equation for a parallelogram:

$$F_{x1} \approx -2k_{11}^{(0)}(a_0^c) \left( \frac{EH_3 T_3^3}{12L_3^3} \right) (U_{x1} - U_{x3}), F_{x2} \approx -2k_{11}^{(0)}(a_0^c) \left( \frac{EH_3 T_3^3}{12L_3^3} \right) (U_{x2} - U_{x3}) \quad (4.6)$$

Here, we have assumed that the forces  $F_{y1}$  and  $F_{y2}$  do not cause any significant stiffening/softening in the motion direction (Appendix B). Another point to note here is that the BCM coefficients  $k_{11}^{(0)}$  are functions<sup>5</sup> of the degree of reinforcement of the beams in the clamp parallelograms  $a_0^c$  as shown in Figure 23. Using equation (4.3), we can obtain a relation between  $U_{x1}$ ,  $U_{x2}$  and  $U_{x3}$ :

$$U_{x3} = \frac{(U_{x1} + U_{x2})}{2} \quad (4.7)$$

Combining relations (4.3), (4.4) and (4.5), we get:

$$M_{z1} + M_{z2} = -\frac{2EH_3 T_3 W_3^2}{a_0^c L_3} \frac{(U_{y2} - U_{y1})}{2L_2} = 2F_{y1}L_2 + F_{x1}(U_{y2} - U_{y1}) \quad (4.8)$$

$$\Rightarrow F_{y1} = \left( \frac{EH_3 T_3 W_3^2}{2a_0^c L_2 L_3} - \frac{F_{x1}}{2L_2} \right) (U_{y2} - U_{y1})$$

At this point, it would be useful to obtain an order of magnitude estimate of the force  $F_{x1}$ . In the absence of any bearing load ( $F_x=0$ ), the secondary stages would displace in the y direction by equal amounts i.e.  $U_y/2$ . Using equation (3.2) for the outer parallelograms in DP1 and DP2, we can write:

---

<sup>5</sup> Unless explicitly mentioned, these BCM coefficients are functions of  $a_0$ , the degree of reinforcement of the beams in the base DPDP.

$$\begin{aligned}
U_{x1} = -U_{x2} &= \frac{1}{2}k_{11}^{(1)}(a_0) \left( \frac{U_y^2}{4L} \right) \\
\Rightarrow U_{x3} &= 0
\end{aligned} \tag{4.9}$$

To obtain an order of magnitude estimate, we can assume that the  $F_{x1}$  obtained from equation (4.6) using the above displacement would remain fairly unchanged when a bearing direction force is applied. This is valid as in case of a parallelogram, the kinematic displacement (equation (4.9)) would dominate the elastic and elasto-kinematic displacements for magnitudes of axial force  $f_x$  up-to 10. Substituting the expression for  $F_{x1}$  using relations (4.6) and (4.9) in equation (4.8):

$$F_{y1} \approx \frac{EH_3T_3}{L_3L_2} \left( \frac{W_3^2}{2a_0^cL_2} + k_{11}^{(0)}(a_0^c)k_{11}^{(1)}(a_0) \left( \frac{T_3^2U_y^2}{96L_3^2L} \right) \right) (U_{y2} - U_{y1}) \tag{4.10}$$

Using some typical estimates for the variables involved (Table 2 and Table 3) the latter term is found to be about four orders of magnitudes smaller than the former. Hence, we can rewrite the above equation as:

$$\begin{aligned}
F_{y1} &\approx \frac{EH_3T_3W_3^2}{2a_0^cL_3L_2^2} (U_{y2} - U_{y1}) \\
\Rightarrow f_{y1} = -f_{y2} &\approx \eta (u_{y2} - u_{y1}), \eta = 6 \frac{h_3t_3w_3^2}{a_0^cL_3L_2^2ht^3}
\end{aligned} \tag{4.11}$$

The above force displacement relation has been non-dimensionalized using (2.5) w.r.t the dimensions of the base DPDP mechanism. Similarly, the axial forces  $F_{x1}$  and  $F_{x2}$  can also be non-dimensionalized:

$$f_{x1(@f_x=0)} = -f_{x2(@f_x=0)} \approx -\gamma u_y^2, \gamma = k_{11}^{(0)}(a_0^c)k_{11}^{(1)}(a_0) \left( \frac{h_3t_3^3}{4ht^3l_3^3} \right) \tag{4.12}$$

With the above two sets of forces, we can now isolate the clamp from the rest of the mechanism and analyze the DPDP mechanism with external forces acting on its secondary stages, similar to the analysis done in the previous chapter. The parameters  $\gamma$  and  $\eta$  essentially capture the effect of the dimensions of the clamp in its entirety.

Table 3: Typical dimensions for the clamp

<i>Variable</i>	<i>Order</i>
$l_3$	0.1-1.0
$t_3$	1/50
$w_3$	0.3-1.0
$l_2$	1-2

The rest of the analysis is divided into two parts – In the first one, we would obtain the motion direction stiffness of the mechanism in the absence of bearing direction force. This case can be handled very easily using symmetry arguments and the analysis done in the last chapter. We would conduct a very rudimentary optimization beyond this step to eliminate some more variables for the subsequent analysis. The second part deals with obtaining the bearing direction stiffness for a wide range of clamp effectiveness and the motion direction stiffness in the presence of bearing loads.

When there is no bearing force acting on the primary stage, the mechanism is symmetrical about the y axis passing through the primary stage. Thus, the force  $f_y$  would get split equally between DP1 and DP2 i.e.  $f_{y11}=f_{y22}=0.5f_y$  (Figure 25). The effect of  $f_{x1}$  on the motion direction stiffness has been captured in equation (3.71) and can be directly used in this case for DP1 (or DP2):

$$\begin{aligned}
 u_y &= \frac{2f_{y11}}{\left(2k_{11}^{(0)} - 0.5f_{x1}k_{11}^{(1)}\right)} = \frac{f_y}{\left(2k_{11}^{(0)} - 0.5f_{x1}k_{11}^{(1)}\right)} \\
 \Rightarrow f_y &= \left(2k_{11}^{(0)} + 0.5\gamma k_{11}^{(1)}u_y^2\right)u_y
 \end{aligned}
 \tag{4.13}$$

The above equation represents the motion direction force displacement relation for the CDPDP mechanism with  $f_x=0$ . The clamp introduces a non-linear stiffening term which is very similar to that seen in a clamped-clamped beam.

The expression for  $f_{xI}$  given by equation (4.12) is an approximate one. In reality, the displacement  $U_{xI}$  would be affected by this force and hence would be smaller than the purely kinematic component given by equation (4.9). However, if each of the parallelograms is adequately stiff in the bearing direction, we can ignore this contribution whereby the approximation becomes a good one for this analysis.

The stiffness can be calculated as follows:

$$k_y = \frac{\partial f_y}{\partial u_y} = \left( 2k_{11}^{(0)}(a_0) + 1.5\gamma k_{11}^{(1)}(a_0)u_y^2 \right) \quad (4.14)$$

If we wish to limit this stiffening to less than say 5%, we can easily calculate the dimensions of the clamp required to achieve this. Using equation (4.14), we can write:

$$\begin{aligned} \frac{1.5\gamma k_{11}^{(1)}(a_0)u_y^2}{2k_{11}^{(0)}(a_0)} &< \frac{1.5\gamma k_{11}^{(1)}(a_0)(u_y)_{\max}^2}{2k_{11}^{(0)}(a_0)} < 0.05 \\ \Rightarrow l_3 &> \left( 3.75 \left( \frac{h_3 t_3^3}{h t^3} \right) \left( \frac{k_{11}^{(0)}(a_0^c) (k_{11}^{(1)}(a_0))^2}{k_{11}^{(0)}(a_0)} \right) (u_y)_{\max}^2 \right)^{1/3} \end{aligned} \quad (4.15)$$

Assuming  $h_3=h$  and  $t_3=t$  and distributed compliance beams, ( $a_0=a_0^c=0.5$ ) this limit comes out to be around 0.5. For optimizing the bearing direction stiffness, we can now use this lower limit and determine the values of the other independent variables ( $W_3$  and  $L_2$ ) to obtain the required stiffness. For the next part, we would assume that the stiffening force  $f_{xI}$  is much smaller than the bearing force  $f_x$  and hence, we would exclude it from the analysis. Doing this might lead to some loss of accuracy for larger  $y$  displacements and small bearing forces but would make the equations easier to solve which in turn would enable us to obtain closed form parametric results for the stiffness.

Rewriting equations (3.66) and (3.67) for each of the double parallelograms DP1 and DP2 shown in Figure 25 while neglecting the contribution of  $f_{xI}$  and assuming that the clamp is not perfect i.e.  $u_{y1}, u_{y2} \neq 0.5u_y$ :

$$\begin{aligned}
\text{DP1} \quad u_{y1} &= \frac{f_{y11} + f_{y1}}{(2k_{11}^{(0)} - f_{x11}k_{11}^{(1)})} \\
u_y - u_{y1} &= \frac{f_{y11}}{(2k_{11}^{(0)} + f_{x11}k_{11}^{(1)})} \\
u_{x1} &= \frac{f_{x11}}{2k_{33}} + \frac{u_{y1}^2}{2} (k_{11}^{(1)} - f_{x11}k_{11}^{(2)}) \\
u_x - u_{x1} &= \frac{f_{x11}}{2k_{33}} - \frac{(u_y - u_{y1})^2}{2} (k_{11}^{(1)} + f_{x11}k_{11}^{(2)}) \\
\text{DP2} \quad u_{y2} &= \frac{f_{y22} - f_{y1}}{(2k_{11}^{(0)} + f_{x22}k_{11}^{(1)})} \\
u_y - u_{y2} &= \frac{f_{y22}}{(2k_{11}^{(0)} - f_{x22}k_{11}^{(1)})} \\
u_{x2} &= \frac{f_{x22}}{2k_{33}} - \frac{u_{y2}^2}{2} (k_{11}^{(1)} + f_{x22}k_{11}^{(2)}) \\
u_x - u_{x2} &= \frac{f_{x22}}{2k_{33}} + \frac{(u_y - u_{y2})^2}{2} (k_{11}^{(1)} - f_{x22}k_{11}^{(2)})
\end{aligned} \tag{4.16}$$

Also,

$$\begin{aligned}
f_{x11} + f_{x22} &= f_x \\
f_{y11} + f_{y22} &= f_y
\end{aligned} \tag{4.17}$$

Therefore, we have 10 equations in 10 variables ( $u_x, u_{x1}, u_{x2}, u_y, u_{y1}, u_{y2}, f_{x11}, f_{x22}, f_{y11}, f_{y22}$ ). Solving the above equations along with equation (4.11) for the constraint force  $f_{y1}$ , we obtain the following results<sup>6</sup>:

$$f_{x11} \approx f_{x22} = 0.5f_x \tag{4.18}$$

$$\begin{aligned}
f_{y11} &= k_{11}^{(0)} \left( 1 + \frac{f_x k_{11}^{(1)}}{4k_{11}^{(0)}} \right) \left( 1 - \frac{f_x k_{11}^{(1)}}{2(\eta + 2k_{11}^{(0)})} \right) u_y \\
f_{y22} &= k_{11}^{(0)} \left( 1 - \frac{f_x k_{11}^{(1)}}{4k_{11}^{(0)}} \right) \left( 1 + \frac{f_x k_{11}^{(1)}}{2(\eta + 2k_{11}^{(0)})} \right) u_y
\end{aligned} \tag{4.19}$$

$$\begin{aligned}
u_{y1} &= \frac{u_y}{2} + \frac{f_x k_{11}^{(1)} u_y}{4(\eta + 2k_{11}^{(0)})} \\
u_{y2} &= \frac{u_y}{2} - \frac{f_x k_{11}^{(1)} u_y}{4(\eta + 2k_{11}^{(0)})}
\end{aligned} \tag{4.20}$$

And the primary stage force-displacement relations:

---

<sup>6</sup> These expressions are approximate because of series truncation.



$$u_y = \frac{f_y}{2k_{11}^{(0)} \left( 1 - \frac{(f_x k_{11}^{(1)})^2}{8k_{11}^{(0)} (\eta + 2k_{11}^{(0)})} \right)} \quad (4.21)$$

$$u_x = f_x \left( \frac{1}{2k_{33}} + \frac{u_y^2}{8} \left( -k_{11}^{(2)} + \frac{2(k_{11}^{(1)})^2}{(\eta + 2k_{11}^{(0)})} \right) \right) + O(f_x^2) \quad (4.22)$$

The above results very compactly capture the effect of the clamp on the performance of the mechanism. They show that parameter  $\eta$  is directly correlated (positively) with the strength or *effectiveness* of the clamp. Table 4 lists the values of some variables of interest for the extrema of effectiveness ( $\eta=0, \infty$ ). The second column ( $\eta=0$ ) lists the exact same results that were obtained for the DPDP mechanism in the previous chapter. This is equivalent to the clamp being completely ineffective i.e. applying no constraint forces on the secondary stages ( $f_{y1}=0$  from equation (4.11)). On the other hand, the column under ( $\eta=\infty$ ) shows results for the case when the clamp behaves as an ideal constraint i.e. restricts the secondary stages to exactly  $0.5u_y$ . As expected the expression for the bearing direction force displacement relation is devoid of the large kinematic term  $(k_{11}^{(1)})^2/k_{11}^{(0)}$  and hence, there is a significant improvement in the bearing direction stiffness. The y direction force displacement relation is completely independent of the bearing direction loading  $f_x$  which implies that as long as the requirement (4.15) is met, the motion direction stiffness would be almost constant over the whole range of displacements and loads.

Table 4: Effect of  $\eta$  on displacement variables

<b>Parameter</b>	$\eta=0$	$\eta=\infty$
$u_{y1}, u_{y2}$	$\frac{u_y}{2} \pm \frac{f_x k_{11}^{(1)} u_y}{8k_{11}^{(0)}}$	$\frac{u_y}{2}$

$u_y$	$\frac{2k_{11}^{(0)} f_y}{\left( (2k_{11}^{(0)})^2 - (0.5 f_x k_{11}^{(1)})^2 \right)}$	$\frac{f_y}{2k_{11}^{(0)}}$
$u_x$	$f_x \left( \frac{1}{2k_{33}} + \frac{u_y^2}{8} \left( -k_{11}^{(2)} + \frac{k_{11}^{(1)}}{k_{11}^{(0)}} \right) \right)$	$f_x \left( \frac{1}{2k_{33}} - \frac{u_y^2}{8} k_{11}^{(2)} \right)$

The rotational stiffness of the DPDP mechanism wouldn't be significantly affected by the clamp. Due to the weak dependence of the  $y$  force displacement relations on the applied moment, there isn't a significant redistribution of  $y$  displacements when a moment is applied implying that  $u_{y1} \approx u_{y2} \approx 0.5u_y$ . This in turn implies that the clamp rotation, moments  $M_{z1,2}$  and forces  $F_{y1,2}$  would be small. Moreover, as both the secondary stages would rotate in the same direction when a moment is applied as shown in Figure 26, the clamp would also rotate along with the secondary stage by almost the same amount thereby failing to provide any constraint forces ( $f_{y1}$ ) or moments ( $M_{z1,2}$ ) on the secondary stages. The stiffening forces would still continue to act but they can also be minimized by increasing  $l_3$  (equation (4.15)). Thus, the clamp would barely influence the rotational stiffness and we can expect it to be the same as that for a DPDP mechanism i.e. twice the stiffness given by equation (3.64). This has been validated using non-linear FEA<sup>7</sup> for a wide range of clamp dimensions (Figure 27).

---

<sup>7</sup> With BEAM 4 elements and 20 elements per beam

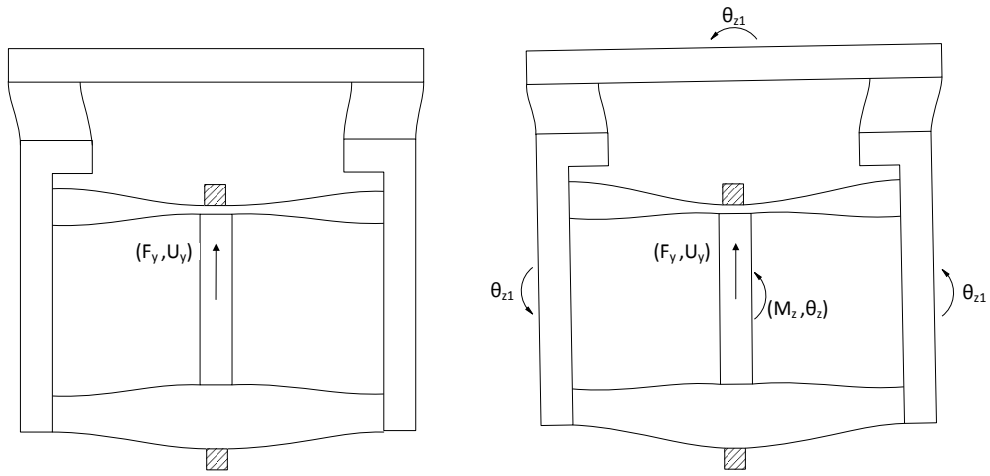


Figure 26: Response of the CDPDP mechanism to an external moment

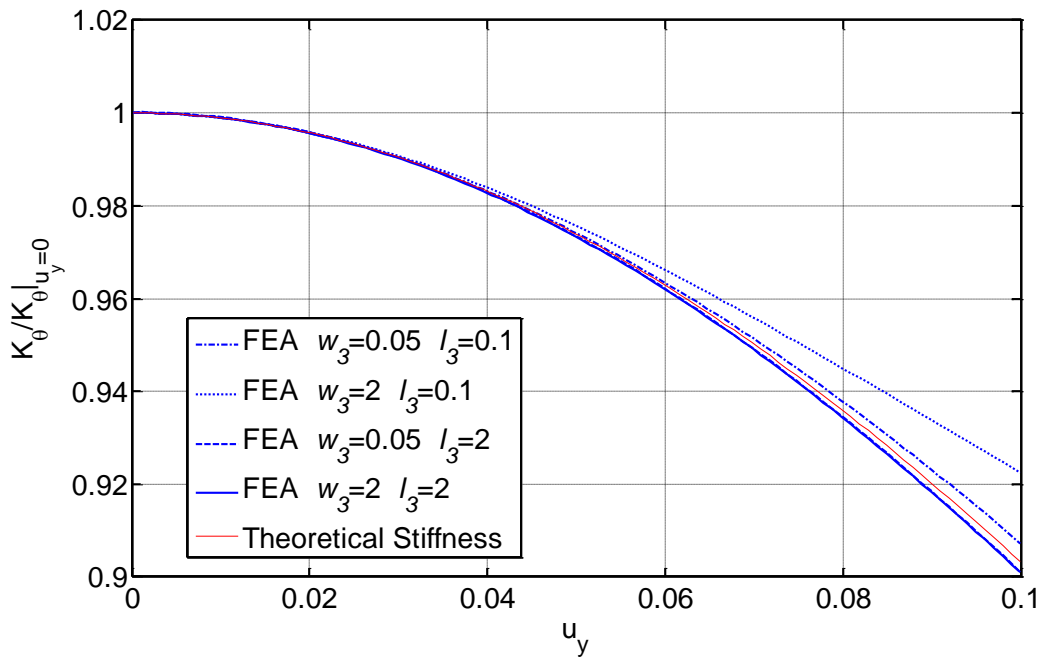


Figure 27: Rotational stiffness of the CDPDP mechanism for different clamp dimension,  $K_{\theta}(u_y=0)=2.7e^4 Nm$ .  $a_0^c=0.5$ ,  $h=h_3$ ,  $t=t_3=1/50$ ,  $l_2=1.4$ . Dimensions of the DPDP same as before.

Some of the salient features of the above analysis are listed below:

1. Using reasonable approximations, we can significantly reduce the complexity of the solution procedure. This in turn, enables us to obtain closed form parametric

results quantifying the qualitative estimates that we made in the beginning of this chapter.

2. With some insight into the working of the mechanism, we can decide whether there is a merit in carrying out a rigorous mathematical derivation to obtain its properties. For example, for the rotational stiffness of the mechanism, we chose not to pursue a complete derivation as with some intuitive arguments, we could conclude that doing so would not yield any significant gains; a claim that was later validated by FEA.
3. The expressions obtained cover the entire gamut of clamp dimensions in a compact parametric manner making subsequent optimization much simpler.

### **Performance**

Based on the results obtained from the previous analysis, we can now summarize the performance metrics for the CDPDP mechanism. We would also examine the effect of introducing beam shape variations (changing  $a_0$  and  $a_0^c$ ) and adding multiple beams in the parallelograms that the mechanism comprises of (Figure 28).

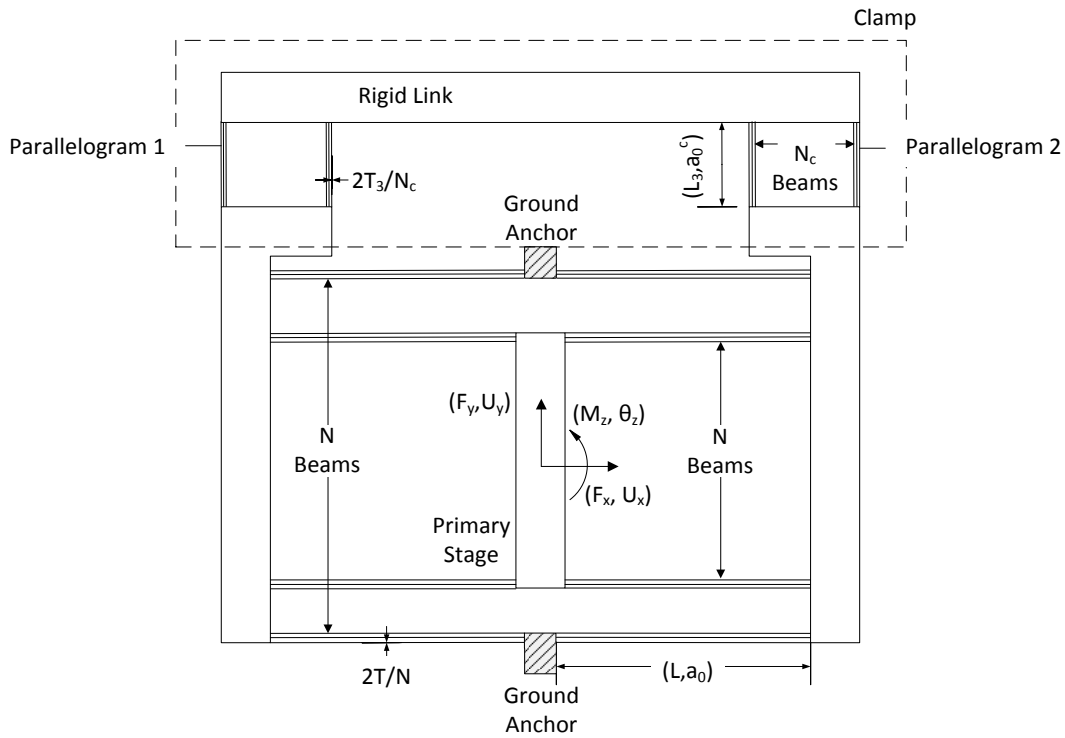


Figure 28: CDPDP Mechanism with multiple grouped reinforced beam flexures. Normalization would still be done w.r.t the original parameters ( $T$  and  $T_3$ )

### ***Range of motion***

The range of motion of the mechanism would be the same as that of the DP and the DPDP mechanisms given by equation (3.59). Moreover, the effect of adding multiple beams or varying the degree of reinforcement  $a_0$  would also be the same as that shown in Figure 17.

### ***Error motions***

Like in the case of the DPDP mechanism, due to symmetry, both the axial and rotational error motions would be theoretically zero.

### Motion Direction Stiffness

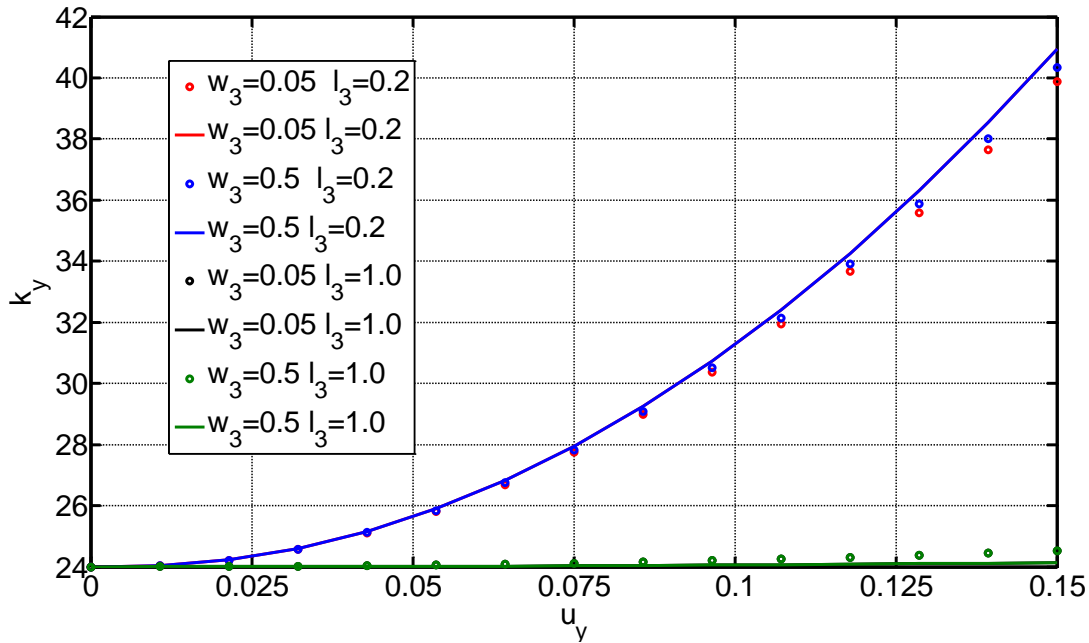


Figure 29: The motion direction stiffness of the CDPDP mechanism for different dimensions of the clamp.

The solid lines represent the predicted values whereas the circles show the corresponding FEA results.

$$w_1=1.0, w_2=0.8, l_2=0.9, t=t_3=1/50, h=h_3$$

The motion direction stiffness in the absence of a bearing direction load is given by equation (4.14). The predicted (equation (4.14)) and the FEA results<sup>8</sup> for different clamp dimensions have been found to be in good agreement (<5% error) as can be seen from Figure 29. As expected, there is virtually no dependence on the dimensions  $W_3$  and  $L_2$ . For cases where stiffening is small, there is some discrepancy between the plots. This can be attributed to motion direction stiffening in the DPDP mechanism which was not captured in the BCM model. Because of the non-zero opposing theta error motions (3.60) of each of the double parallelograms, internal moments get generated. Furthermore, due to the weak dependence of the y direction force displacement relations of the double parallelogram on the applied moment, these moments, in turn, cause stiffening.

<sup>8</sup> The stiffness was calculated using the forward difference method i.e.  $K_y(i)=(F_y(i)-F_y(i-1))/(U_y(i)-U_y(i-1))$

For the multiple-beam configuration, equation (4.14) can be rewritten as:

$$\begin{aligned} k_y &= \frac{4}{N^2} \left( 2k_{11}^{(0)}(a_0) + \frac{3}{2} \gamma k_{11}^{(1)}(a_0) u_y^2 \right) \\ \gamma &= \left( \frac{N^2}{N_c^2} \right) k_{11}^{(0)}(a_0^c) k_{11}^{(1)}(a_0) \left( \frac{h_3 t_3^3}{4 h t^3 l_3^3} \right) \end{aligned} \quad (4.23)$$

The above equation shows that we can decrease the nominal stiffness of the mechanism by increasing the number of beams (while simultaneously thinning them) in the parallelograms of the base DPDP mechanism. However, if we wish to decrease the relative amount of stiffening, we should increase the number of beams in the clamp parallelograms in a manner such that  $N_c > N$ . Doing this would also reduce the lower bound on the  $l_3$  which is evident from the updated version of equation (4.15):

$$l_3 > \left( 3.75 \left( \frac{N}{N_c} \right)^2 \left( \frac{h_3 t_3^3}{h t^3} \right) \left( \frac{k_{11}^{(0)}(a_0^c) (k_{11}^{(1)}(a_0))^2}{k_{11}^{(0)}(a_0)} \right) (u_y)_{\max}^2 \right)^{1/3} \quad (4.24)$$

In a later section, we would see how this would increase the scope for making the clamp more compact.

In the presence of a bearing load, which is much larger than the stiffening force  $f_x l$ , this stiffness is given as:

$$k_y = 2k_{11}^{(0)} \left( 1 - \frac{(f_x k_{11}^{(1)})^2}{8k_{11}^{(0)} (\eta + 2k_{11}^{(0)})} \right) \quad (4.25)$$

As discussed before, the clamp reduces the softening effect of the bearing force and in the limiting case it is completely eliminated. In Figure 30, we plot this stiffness for different values of  $\eta$  (and  $\gamma$ ) and compare it with FEA results. The Figure 30 shows that for small to moderate values of  $\eta$ , the values match closely. However, for larger values where the softening term is expected to decrease continuously with increasing  $\eta$ , the FEA results show that this term saturates to a constant value.

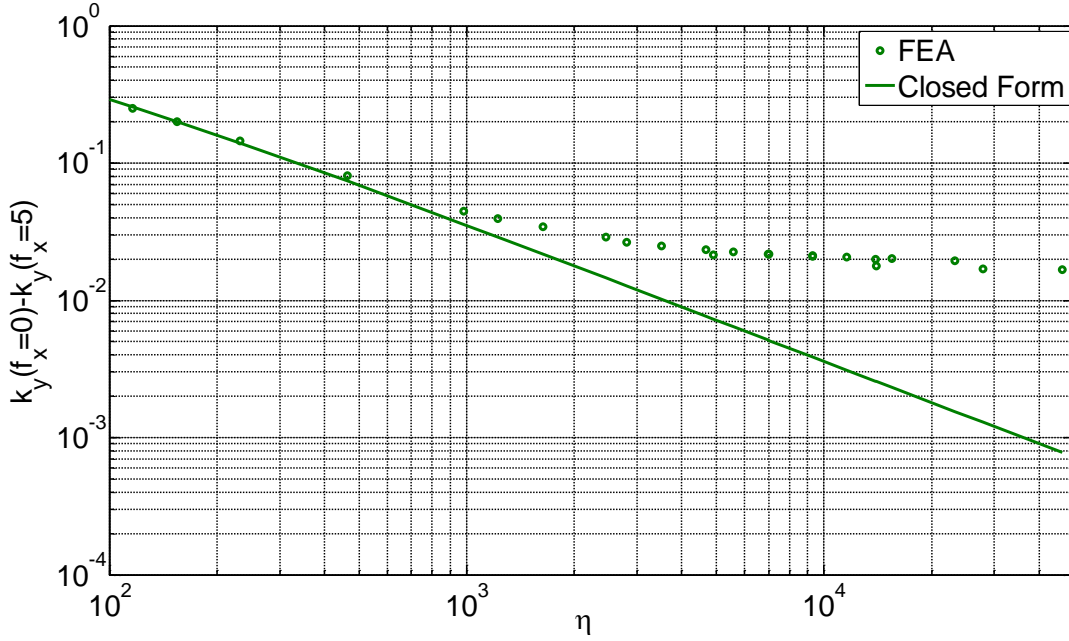


Figure 30: Softening due to bearing direction loads in the motion direction. At large values of effectiveness, there is a clear discrepancy between FEA and closed form results

This discrepancy can be eliminated if we include the second order terms in the expression for the motion direction stiffness of a parallelogram i.e.:

$$f_y = \left( 2k_{11}^{(0)} + f_x k_{11}^{(1)} + \frac{f_x^2}{2} k_{11}^{(2)} \right) u_y \quad (4.26)$$

Substituting this expression in the transverse direction relations in equation (4.16), and thereafter rewriting equations (4.19):

$$\begin{aligned} f_{y11} &= k_{11}^{(0)} \left( 1 + \frac{f_x k_{11}^{(1)}}{4k_{11}^{(0)}} + \frac{f_x^2 k_{11}^{(2)}}{16k_{11}^{(0)}} \right) \left( 1 - \frac{f_x k_{11}^{(1)}}{2(\eta + 2k_{11}^{(0)})} \right) u_y \\ f_{y22} &= k_{11}^{(0)} \left( 1 - \frac{f_x k_{11}^{(1)}}{4k_{11}^{(0)}} + \frac{f_x^2 k_{11}^{(2)}}{16k_{11}^{(0)}} \right) \left( 1 + \frac{f_x k_{11}^{(1)}}{2(\eta + 2k_{11}^{(0)})} \right) u_y \end{aligned} \quad (4.27)$$

Finally, using equations (4.17) and (4.27) we get:

$$f_y = 2k_{11}^{(0)} \left( 1 - \left( \frac{(k_{11}^{(1)})^2}{8k_{11}^{(0)}(\eta + 2k_{11}^{(0)})} - \frac{k_{11}^{(2)}}{8} \right) f_x^2 \right) u_y \quad (4.28)$$



Figure 31 shows the comparison between the stiffness given by the above equation and the corresponding FEA results and shows good agreement between the two. Thus, for large effectiveness, we still have a small softening term left over. Nevertheless, we can still say that an effective clamp makes the motion direction stiffness fairly insensitive to non-linearity arising due side loading which can simplify the design of controllers in the case of comb drive actuators where errors in fabrication can lead to an offset between the comb banks causing an unpredictable bearing force.

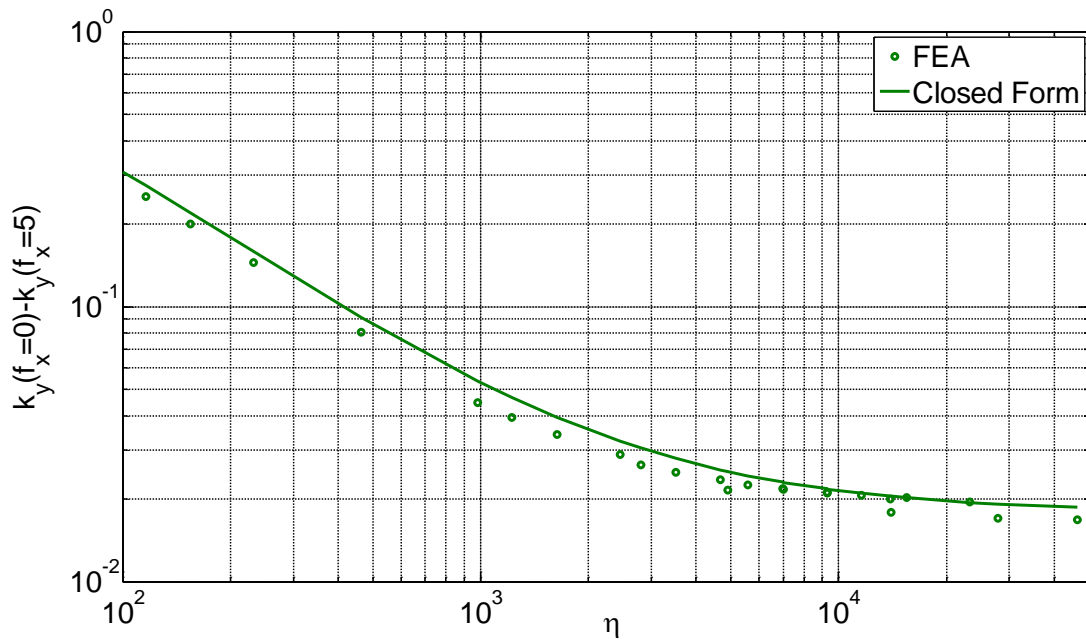


Figure 31: Softening in the motion direction due to bearing direction loads. Comparison between closed form solution with second order correction and corresponding FEA results

With multiple beams, equation (4.25) becomes:

$$k_y = 2k_{11}^{(0)} \left( \frac{2}{N} \right)^2 \left( 1 - \left( \frac{N}{2} \right)^4 \frac{(f_x k_{11}^{(1)})^2}{2k_{11}^{(0)} \left( \left( \frac{N}{2} \right)^2 \eta + 2k_{11}^{(0)} \right)} \right) \quad (4.29)$$

The above expression is completely independent of  $N_c$ . Moreover, increasing  $N$  causes a reduction in the nominal stiffness but increases the softening due to the applied force significantly (proportional to  $N^4$  when the  $\eta=0$  and  $N^2$  as  $\eta$  becomes large).

### ***Bearing Direction Stiffness***

The bearing direction ( $x$ ) stiffness can be obtained using equation (4.22):

$$k_x = \frac{1}{\left( \frac{1}{2k_{33}} + \frac{u_y^2}{8} \left( -k_{11}^{(2)} + \frac{2(k_{11}^{(1)})^2}{(\eta + 2k_{11}^{(0)})} \right) \right)} \quad (4.30)$$

The bearing stiffness is plotted against FEA data for different values of the effectiveness  $\eta$  in Figure 32. The plot shows that there is less than a 5% discrepancy between the predicted and the FEA results which is acceptable for most applications. In our analysis, we have not imposed any bounds on the effectiveness assuming that we can make it as large as possible by just changing the dimensions of the clamp. However, this is not true and the effectiveness is directly limited by the rotational stiffness of the double parallelogram. Figure 33 shows the bearing stiffness for different values of effectiveness for a smaller rotational stiffness of the double parallelogram (small  $w_1$  and  $w_2$ ). The error increases at larger values of effectiveness which is probably because for these dimensions, the rotational stiffness of the clamp becomes comparable to that of the DPDP. This in turn causes the secondary stages to rotate with the clamp reducing the net deflection of the clamp parallelograms which leads to lower moments  $M_{z1,2}$ , a lower constraint force  $F_{y1}$  and consequently lowers the effectiveness of the clamp. This effect has been illustrated in Figure 34. This case has been dealt with in some detail in Appendix C.

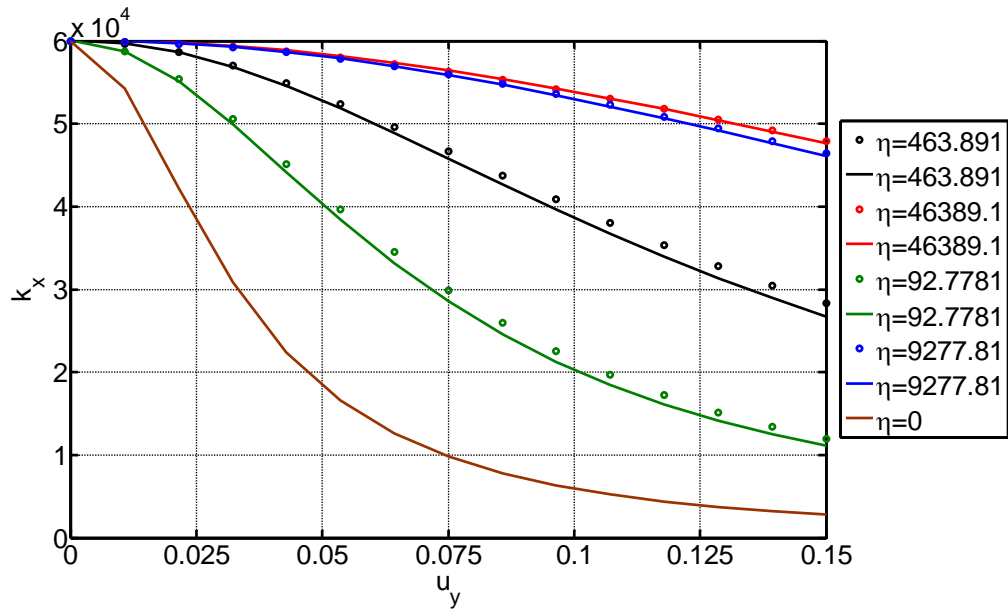


Figure 32: The bearing stiffness of the CDPDP mechanism for different values of effectiveness. The solid lines represent the predicted values whereas the circles show the corresponding FEA results.  $w_1=1.0$ ,  $w_2=0.8$ ,  $l_2=0.9$ ,  $t=t_3=1/50$ ,  $h=h_3$ .

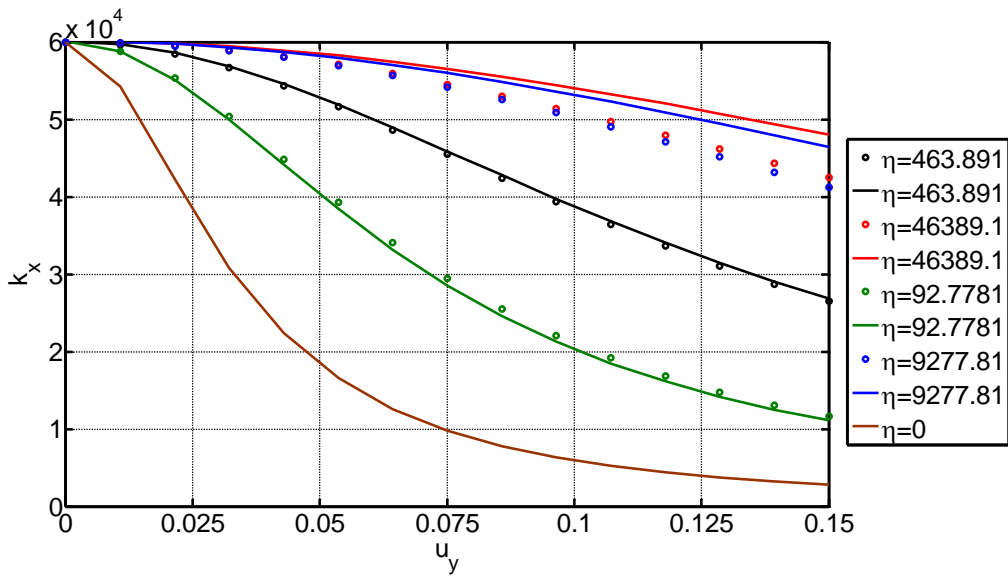


Figure 33: Bearing stiffness for  $w_1=0.3$ ,  $w_2=0.2$ ,  $l_2=0.9$ ,  $t=t_3=1/50$ ,  $h=h_3$ .

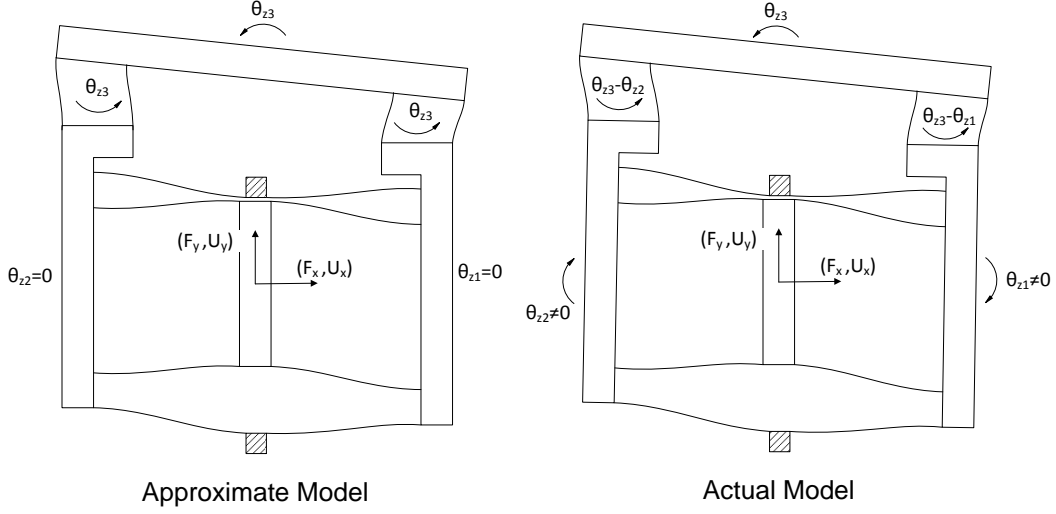


Figure 34: Reason for discrepancy between predicted and FEA results at large values of effectiveness

Rewriting the above equation for the multi-beam case,

$$k_x = \left(\frac{2}{N}\right)^2 \frac{1}{\left( \left(\frac{2}{N}\right)^2 \frac{1}{2k_{33}} + \frac{u_y^2}{8} \left[ -k_{11}^{(2)} + \frac{2(k_{11}^{(1)})^2}{\left(\left(\frac{N}{2}\right)^2 \eta + 2k_{11}^{(0)}\right)} \right] \right)} \quad (4.31)$$

Based on the constraints imposed on the bearing stiffness we can determine the other dimensions of the clamp. As we have more variables than constraints, we choose  $l_2$ ,  $h_3$  and  $t_3$  to be fixed user-specified values leaving  $l_3$  and  $w_3$  as variables to be solved for. We can set the lower bound on  $l_3$  (say  $l_3|_{\min}$ ) using the constraint equation for the motion directions stiffness given by (4.24) in this step. As an example, let us set the kinematic term in the above equation which is a function of the effectiveness  $\eta$ , to be less than 5% of the elasto-kinematic term  $k_{11}^{(2)}$  i.e.

$$\frac{2(k_{11}^{(1)})^2}{\left(\left(\frac{N}{2}\right)^2 \eta + 2k_{11}^{(0)}\right)} < 0.05k_{11}^{(2)} \quad (4.32)$$

$$\Rightarrow \eta > \left(\frac{2}{N}\right)^2 \left(\frac{40(k_{11}^{(1)})^2}{k_{11}^{(2)}} - 2k_{11}^{(0)}\right)$$

Substituting the value of  $\eta$  from equation (4.11)

$$w_3 > \sqrt{\left(\frac{2}{N}\right)^2 \left(\frac{a_0^c}{6}\right) \left(\frac{ht^3 l_2^2}{h_3 t_3}\right) \left(\frac{40(k_{11}^{(1)}(a_0))^2}{k_{11}^{(2)}(a_0)} - 2k_{11}^{(0)}(a_0)\right) (l_3|_{\min})} \quad (4.33)$$

Using a value of  $l_3=0.57$  (for a motion direction stiffening of 5%) and assuming  $h=h_3$ ,  $t=t_3$ ,  $l_2=2$ ,  $a_0=a_0^c=0.5$ ,  $N=2$ ,  $T=1/200$ ,  $l_2=2$ , the required  $w_3$  comes out to be 0.44. As we would see later, there is seldom a need for such conservative bounds on the bearing and motion direction stiffness in which case, the overall clamp dimensions can be made smaller. Moreover, by using multiple beams such that  $N_c > N$ ,  $l_3|_{\min}$  can be reduced (equation (4.24)) and consequently the lower bound on  $w_3$  would decrease according to equation (4.33). Finally, the degrees of reinforcement  $a_0$  and  $a_0^c$  can be changed to further alter the bounds on  $l_3$  and  $w_3$ . The choice of  $a_0$  and  $N$  would be made based on the application requirements as they primarily dictate the motion and the bearing direction stiffness of the mechanism (assuming that the clamp is effective). Beyond this point, using equations (4.24) and (4.33), we can choose  $a_0^c$  and  $N_c$  to obtain the smallest possible size of the clamp.

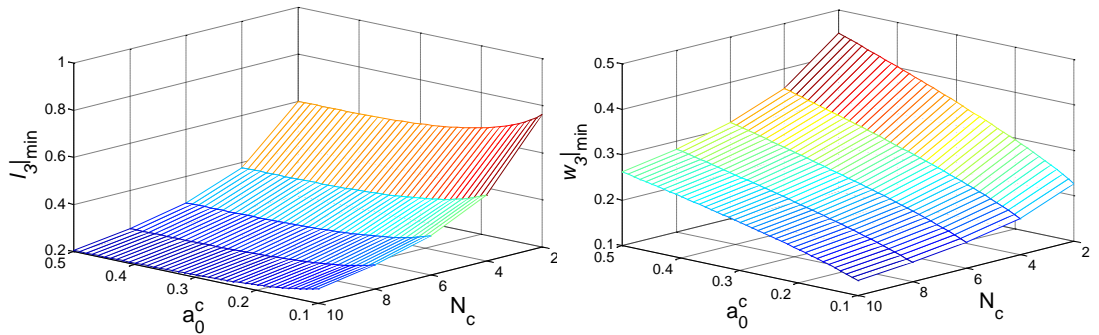


Figure 35:  $l_3|_{\min}$  and  $w_3|_{\min}$  for different clamp variations

As an example, let us assume  $a_0=0.5$  and  $N=2$ . Figure 35 shows  $l_3|_{\min}$  and  $w_3|_{\min}$  for different values of  $N_c$  and  $a_0^c$ . From the plots, we can infer that a large value of  $N_c$  would be preferred. However, this is not always possible as the minimum thickness and hence the largest possible  $N_c$  is often limited by manufacturing capabilities. Increasing  $a_0^c$  decreases  $l_3|_{\min}$  but increases  $w_3|_{\min}$ . However, we notice that:

$$\left( \frac{\partial w_3|_{\min}}{\partial a_0^c} \right)_{N_c=N_{c0}} > - \left( \frac{\partial l_3|_{\min}}{\partial a_0^c} \right)_{N_c=N_{c0}} \quad (4.34)$$

i.e. the rate of increase of  $w_3|_{\min}$  with increasing  $a_0^c$  is larger compared to the rate of increase in  $l_3|_{\min}$  with decreasing  $a_0^c$  which implies that the optimum point would be close to  $a_0^c=0.1$ . The exact optimization would depend on the relative weights assigned to the two dimensions. For example, if the footprint is not sensitive to small variations in  $w_3|_{\min}$ , the optimization can be solely done to minimize  $l_3$  (i.e.  $a_0^c \rightarrow 0.5$  and large  $N_c$ ).

The rotational stiffness, as we discussed before, would remain relatively unchanged and hence, would exhibit the same trends as those seen in Figure 17.

### **THE DOUBLE PARALLELOGRAM – TILTED-BEAM DOUBLE PARALLELOGRAM (DP-DTB)**

The DP-DTB mechanism shown in Figure 36 offers an improved bearing stiffness compared to the DPDP mechanism without using any additional topological features like in the Lever-DPDP and Clamped-DPDP mechanisms. This mechanism has been presented and discussed previously [24, 36, 43] and a summary is presented here. The improved bearing stiffness of this mechanism is due to the complementary behavior of the DP and the TDP flexures. Referring to Figure 37, if the primary stage of a TDP mechanism is not rotationally constrained, the secondary stage is free to move in the  $y$  direction when a  $y$  displacement is applied at the primary stage. This unconstrained

motion of the secondary stage, in a manner similar to that in the DP-DP mechanism, causes a bearing stiffness drop in the TDP mechanism as well. However, when a  $\theta$  constraint is applied at the primary stage along with a specified  $y$  location, two conflicting instantaneous centers of rotation C1 and C2 are created for the secondary stage locking its motion. (This affect does not occur in a DP flexure as in that case C1 and C2 are at infinity). The DP flexure with its superior rotational stiffness, provides this constraint and hence stiffens the TDP flexure in the bearing direction subsequently improving the bearing stiffness of the entire mechanism. Furthermore, unlike the DP-DP flexure, the decline in the stiffness ratio in this case is dictated by the weak elastokinematic effect, which can be further reduced via beam shape optimization (degree of reinforcement  $a_0$ ).

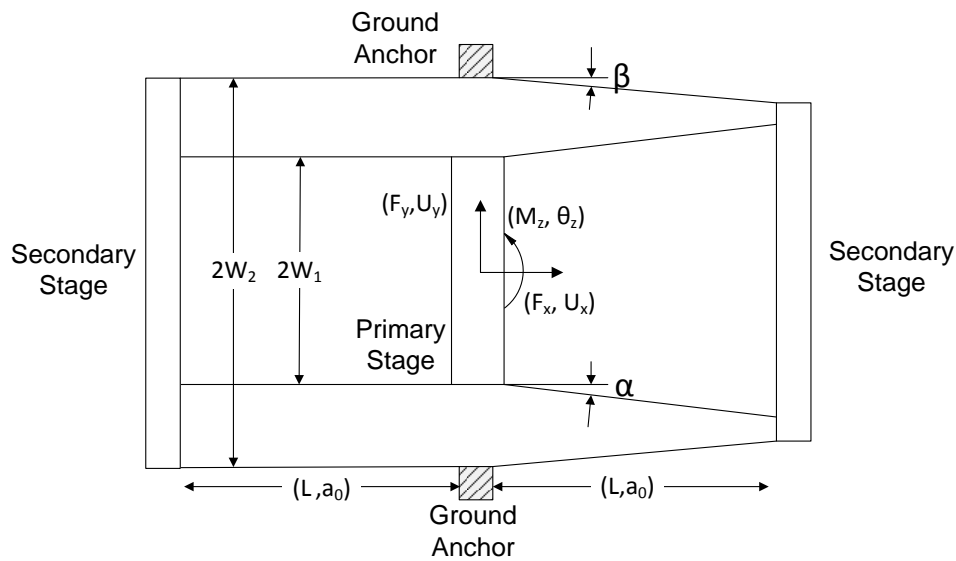


Figure 36: The Double Parallelogram- Tilted Beam Double Parallelogram (DP-TDP)

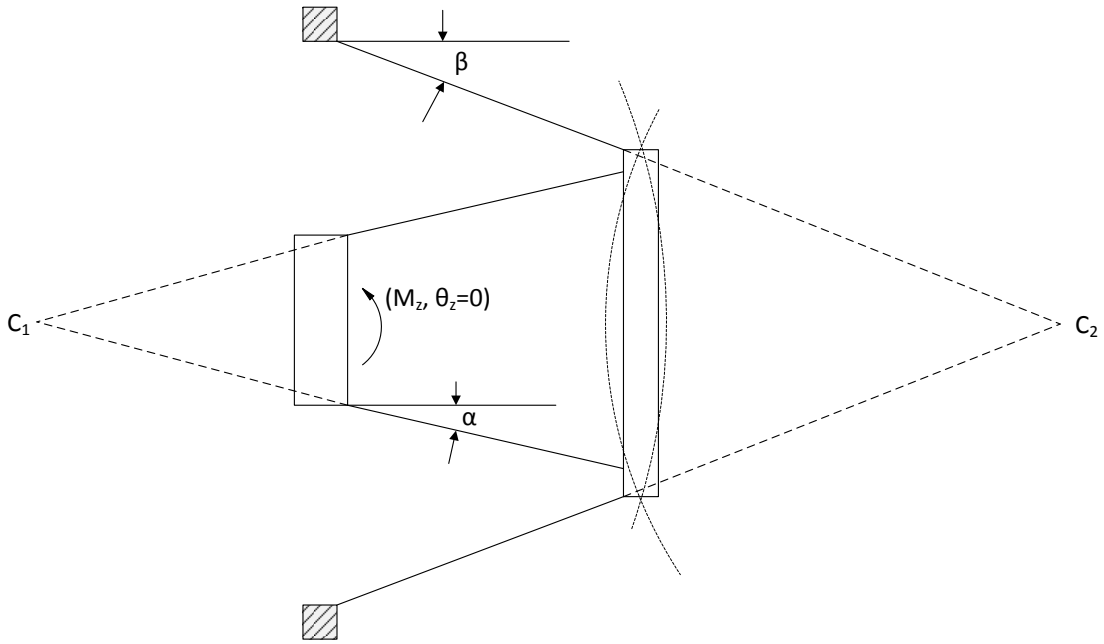


Figure 37: Constraint behavior of the TDP flexure

The analysis for the TDP flexure has been done by awtar et.al. [24]. However, due to the asymmetric nature of the overall DP-TDP mechanism, obtaining a closed form analytical solution is difficult, if not impossible. Another problem is the large internal forces and moments that get generated between the two halves of the mechanism. For such large forces, the approximate BCM model might no longer be valid and hence, the solution that we obtain using the model could be fairly inaccurate. Hence, we resort to using extensive FEA analysis to qualitatively discuss some characteristics of this mechanism. Table 5 shows the parameters used for the non-linear FEA. The tilt angles  $\alpha$  and  $\beta$  were chosen as the variables for this analysis as they have the strongest influence on the characteristics of the mechanism.

Table 5: Dimensions of the DP-TDP flexure used in the FEA analysis.

<i>Dimension</i>	<i>Value (microns)</i>
<i>L</i>	1000



$T$	3
$H$	50
$W_1$	325
$W_2$	525

## Performance

### *Error motions*

As we saw in chapter 3, the DP mechanism has theoretically zero  $x$  error motions and very small  $\theta$  error motions. Thus, any error motions of the DP-TDP mechanism would be caused by the TDP mechanism. As the  $x$  and  $\theta$  directions are DoCs of the DP mechanism, the overall error motion would be smaller than that of just the TDP at the expense of generating internal forces and moments between the two halves of the mechanism. These internal forces might introduce undesirable stresses in the beams causing premature failure and therefore reduced range of motion. From the figures, we can see that the error motions are very small close to the  $\alpha=\beta$  line, which is understandable as due to symmetry the error motions of the individual tilted beam parallelograms nullify (almost) each other.

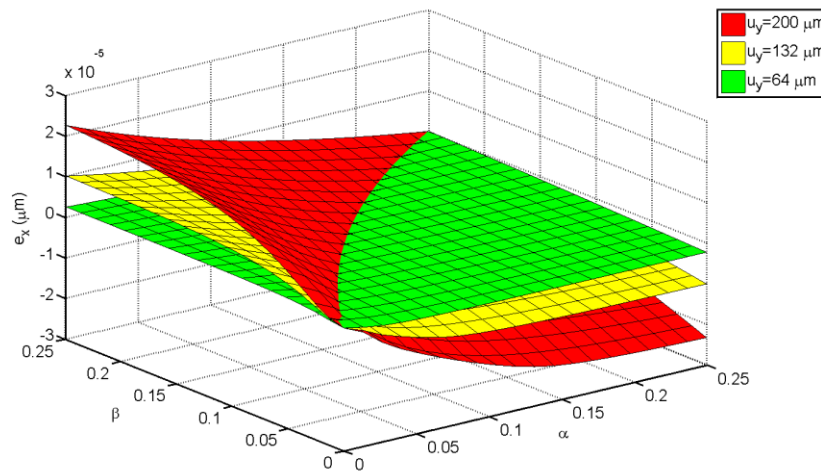


Figure 38: X error motions of the DP-TDP mechanism.  $\alpha, \beta$  are in radians.

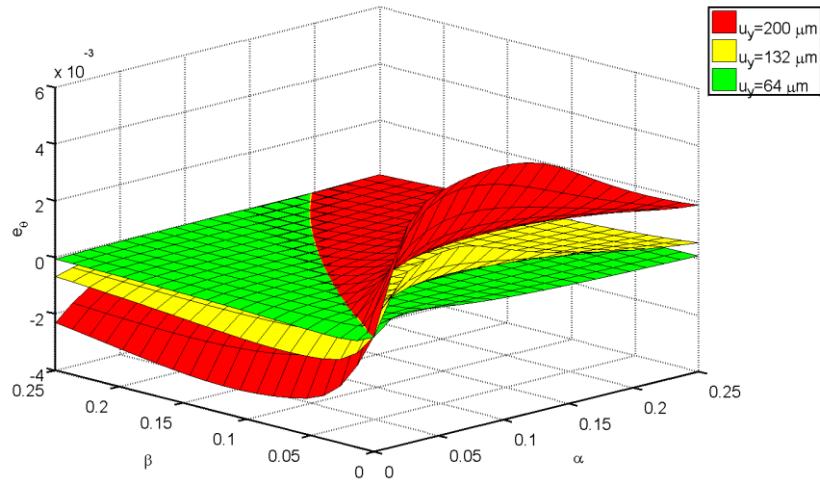


Figure 39: Theta error motions of the DP-TDP mechanism

### ***Motion Direction Stiffness***

The tilted configuration of the beams in the TDP flexure causes an increase in the nominal motion direction stiffness of the mechanism. For every tilted beam parallelogram in the TDP flexure, the  $y$  direction stiffness is directly proportional to the secant of the tilt in the beams. But as the tilt angles are small, the increase in stiffness is not significant. In the DP-TDP flexure, the primary cause for motion direction stiffening is the internal bearing direction forces and moments brought about by the kinematic conflict between the error motions of the DP (theoretically zero) and the TDP flexure. It is because of similar reasons that the P-P flexure has a  $K_y$  which increases exponentially with  $y$  displacements which makes it a poor single axis bearing even though it has a satisfactory bearing stiffness  $K_x$ . Therefore, the trends seen in  $K_y$  of the mechanism is similar to those seen in the error motions and as before, the tilt angles close to the  $\alpha=\beta$  line would be optimal.

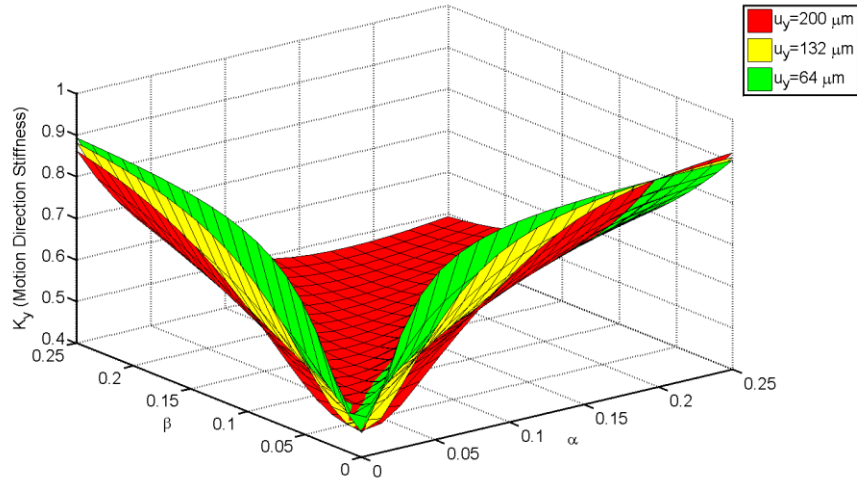


Figure 40: Motion direction stiffness of the DP-TDP flexure

### ***Bearing Direction Stiffness***

For the TDP flexure, in the limiting case as  $\alpha, \beta \rightarrow 0$  i.e. as it approaches the DP flexure, the instantaneous centers of rotation tend to infinity and hence, no longer oppose each other allowing unconstrained  $y$  motion of the secondary stage. As these angles increase in magnitude, the kinematic constraint on the secondary stage also increases. Figure 41 shows that for tilt angles greater than 0, we see an improvement in the  $x$  direction stiffness which gradually increases as either or both of them increase and saturates at a certain angle (where the elasto-kinematic effect starts dominating the stiffness drop). Beyond this point, the trend reverses and we see a small decline in the stiffness because of the effect of the reduced nominal stiffness due to the tilt of the beams. The analysis also shows that the bearing stiffness depends on the magnitude and direction of the axial force and moment. However, they don't change the trends seen in the plots and therefore, for the purpose of this qualitative discussion, we would ignore this dependence.

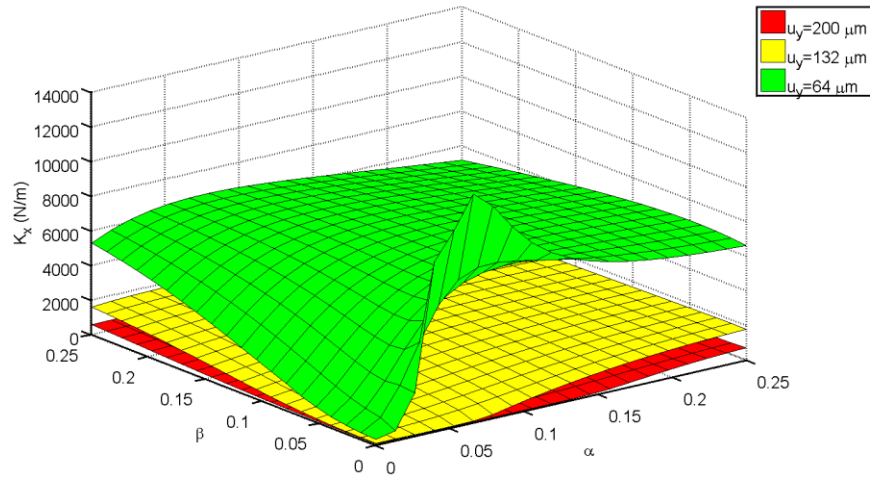


Figure 41: X direction stiffness of the DP-TDP flexure

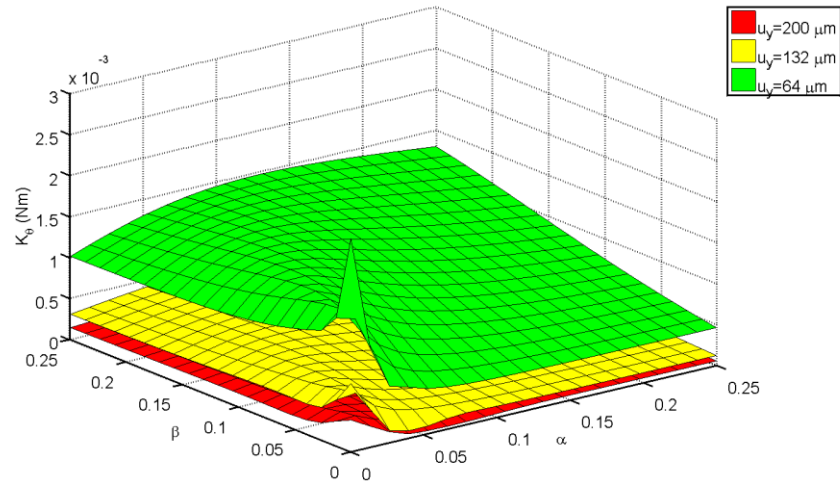


Figure 42:  $\theta$  Direction Stiffness of the DP-TDP mechanism

The rotational stiffness falls significantly for  $\alpha, \beta > 0$ . In fact  $K_\theta$  for the DP-TDP mechanism is almost half that of the DP-DP mechanism. This is understandable as the rotational stiffness of the TDP flexure is much smaller than that of the DP flexure due to the presence of instantaneous centers of rotation  $C_1$  and  $C_2$ . Figure 42 shows that tilt angles such that  $\alpha \leq \beta$  would be preferred.

Considering all the characteristics discussed so far in conjunction, almost equal tilt angles  $\alpha, \beta$  less than 0.15 radians would yield the most desirable properties of the DP-TDP

flexure. In chapter 6, we would use these results to conduct a case specific optimization using the objective function given by equation (1.18).

In the next chapter, we would discuss the direct experimental validation for the results obtained for the CDPDP mechanism using a macro-scale modular, low cost and high precision setup. In a subsequent chapter, we would also briefly touch upon the indirect measurement of these attributes using micro-scale comb drive actuators.

## Chapter 5: Experimental Validation of the Clamped Paired Double Parallelogram (CDPDP) mechanism

Closed form parametric results for the stiffness and error motions were obtained in the last chapter for the CDPDP mechanism which were validated using FEA analysis. In this chapter, we would further validate these results by directly measuring forces and displacements at the primary stage in a macro-scale experimental setup. The experiment was designed to be reconfigurable so as to accommodate some variations of the mechanism without redesigning the entire setup. Moreover, as cost was a constraint, some novel low-cost methods were used for load application and measurement without compromising the precision of the results.

### Measurement Scheme

An obvious question is where should we apply the loads and measure the resultant displacements? In all our previous analysis, the point of application of the loads was arbitrarily chosen to be at the center of the primary stage. However, if this location does not exactly coincide with the location of the center of stiffness of the mechanism, there would be a moment that would be generated in addition to the force causing a small rotation. This moment doesn't affect the bearing or motion direction stiffness of the mechanism because of the decoupling between the  $x$ ,  $y$  and the  $\theta$  direction force displacement relations.

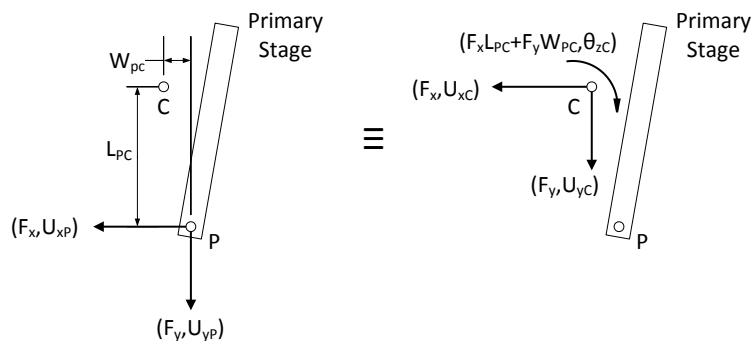


Figure 43: Center of stiffness of the mechanism

In the experimental setup, however, the  $x$  (or  $y$ ) displacement measured at any point would comprise of the pure  $x$  (or  $y$ ) displacement brought about by the application of the load  $f_x$  (or  $f_y$ ) and the rotation due to the moment applied about the COS (Figure 43) i.e.:

$$U_{xP} = U_{xC} + L_{PC}\theta_C \quad (5.1)$$

As the stiffness is defined w.r.t. displacement and forces at the COS of the mechanism, we need to decouple the two components of the  $x$  displacement. For doing this, we need to know the location of the COS. Although the location of the COS, which is a function of the  $y$  displacement in most cases, can be determined using the BCM model and finite element analysis, its exact location in the actual setup might differ significantly due to manufacturing imperfections. It is because of the same reasons that we cannot apply loads and measure displacements at the COS directly. Thus, we would need a method to determine the COS experimentally as well. The derivation of the COS for the CDPDP mechanism has been done in the Appendix D. It was observed that the COS has a very weak dependence on the magnitude of the force  $f_x$  but depends on the displacement  $u_y$ . Hence, for the experimental validation, we can assume the COS to be a function of  $u_y$  only.

The objective of the experiment would be to obtain the following characteristics of the mechanism:

1. Location of the center of stiffness at every  $y$  displacement (C)
2. Error motions ( $e_x(u_y)$ ,  $e_\theta(u_y)$ )
3. Motion direction stiffness ( $k_y$ )
4. Bearing direction stiffness ( $k_x$ ,  $k_\theta$ )

The last three properties have to be found w.r.t. the COS of the mechanism. The above objectives translate to the following:

*Apply*

1. A motion direction displacement  $U_y$
2. An  $x$ -direction force which maintains perpendicularity with the motion direction at all displacements
3. A moment on the primary stage

*Measure*

1. Motion direction load  $F_y$  at every  $U_y$
2.  $X$ -displacement of the primary stage
3. Rotation of the primary stage

Due to symmetry of the mechanism about the axis parallel to the  $y$ -axis and passing through the center of the primary stage, we can assume that the  $x$ -location of the COS is close to this axis. Hence, we can decouple the measurement of the  $Y$ -direction stiffness from  $x$  and  $\theta$  direction measurements. Thus, using a force sensor to measure  $F_y$  and a displacement sensor to measure  $U_y$ , we can find the motion direction stiffness of the mechanism. For this, we could use the forward difference approach:

$$K_y(U_{yi}) = \frac{(F_y(U_{yf}) - F_y(U_{yi}))}{(U_{yf} - U_{yi})} \quad (5.2)$$

Where  $(U_{yf} - U_{yi})$  is small. Or instead, we could obtain a polynomial curve-fit for the data points  $-(F_y, U_y)$  and use the slope of the curve to obtain the motion direction stiffness.



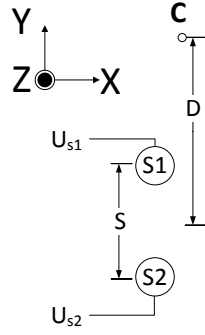


Figure 44: The placement of the sensors for measuring  $x$ -direction displacements and rotations of the stage.

For obtaining the rest of the properties, we use two displacement sensors for the primary stage which would measure rotation as well as the  $x$  direction displacement of the stage. For now, let us assume that these sensors labeled  $S1$  and  $S2$  are placed a distance  $D$  (unknown) from the  $C$  with a separation of  $S$  (known) between each other as shown in the Figure 44. The sensors measure displacements  $U_{s1}$  and  $U_{s2}$  in the  $x$ -direction. From these two readings, we can obtain the rotation and the  $x$  displacement at the COS:

$$\begin{aligned} \theta_{zC} &= \frac{(U_{s2} - U_{s1})}{S} \\ U_{xC} &= U_{s1} - \left( D - \frac{S}{2} \right) \theta \end{aligned} \quad (5.3)$$

The error motions can be obtained in terms of  $D$  by actuating the motion stage in the  $Y$  direction with no bearing loads acting on it i.e.:

$$\begin{aligned} E_{\theta}(U_y) &= \frac{(U_{s2}|_{No-Load} - U_{s1}|_{No-Load})}{S} \\ E_x(U_y) &= U_{s1}|_{No-Load} - \left( D - \frac{S}{2} \right) E_{\theta}(U_y) \end{aligned} \quad (5.4)$$

We now have three unknowns  $D(U_y)$ ,  $K_x(U_y)$  and  $K_{\theta}(U_y)$  left to determine. For this we use a scheme where we apply two forces at different  $y$  locations of the primary stage individually at every  $y$  displacement as shown in Figure 45.

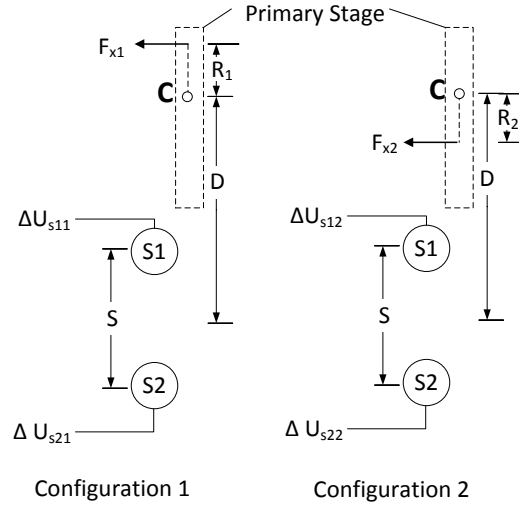


Figure 45: Force application on the primary stage. Also,  $\Delta U_{s11} = U_{s1}|_{load=F_{x1}} - U_{s1}|_{no-load}$ .

Using this we get two separate sets of sensor displacements for every force applied. For every force we can write out four equations as follows:

$$\begin{aligned}
 \theta_{z1}(U_y) &= \frac{(\Delta U_{s21} - \Delta U_{s11})}{S} & \theta_{z2}(U_y) &= \frac{(\Delta U_{s22} - \Delta U_{s12})}{S} \\
 K_\theta(U_y, F_{x1}, F_{x1}R_1) &\approx K_\theta(U_y) = \frac{F_{x1}R_1}{\theta_{z1}(U_y)} & K_\theta(U_y, F_{x2}, -F_{x2}R_2) &\approx K_\theta(U_y) = -\frac{F_{x2}R_2}{\theta_{z2}(U_y)} \quad (5.5) \\
 U_{x1}(U_y) &= \Delta U_{s11} - \left(D - \frac{S}{2}\right)\theta_{z1}(U_y) & U_{x2}(U_y) &= \Delta U_{s12} - \left(D - \frac{S}{2}\right)\theta_{z2}(U_y) \\
 K_x(U_y, F_{x1}, F_{x1}R_1) &\approx K_x(U_y) = \frac{F_{x1}}{U_{x1}(U_y)} & K_x(U_y, F_{x2}, -F_{x2}R_2) &\approx K_x(U_y) = \frac{F_{x2}}{U_{x2}(U_y)}
 \end{aligned}$$

Moreover, the  $y$  separation between the two forces can be known beforehand giving:

$$R_{sep} = R_1 + R_2 \quad (5.6)$$

If we take into account all the dependencies of the  $x$  and  $\theta$  stiffness expressions on the magnitude of the forces and moments applied, we have an under-determined system with 10 unknowns and 9 equations implying that we need to know the exact location of the COS to begin with in order to calculate the  $x$  and  $\theta$  stiffness. However, if we ignore these dependencies in the rotational stiffness, we can determine all the unknowns in the equations at every  $y$  displacement  $u_y$ .

## Design of the setup

The first task was to choose the dimensions of the mechanism. As there wasn't a particular application that had to be designed for, the mechanism was designed around the available sensors, actuators and manufacturing capabilities. These are listed below:

### Actuation

#### Motion (Y) Direction

The motion direction has to be actuated using a position actuator. For this purpose, a PI actuator M-227.25 [55] with a lead-screw driven by a closed loop DC motor (Figure 46) was used. It has a stroke of 25 mm, can provide a maximum push/pull force of 40N and can withstand a maximum lateral force of 0.1N. Moreover, it also houses the rotary encoder with a minimum incremental motion of 0.05  $\mu\text{m}$ . Finally, the actuator has a backlash of 2  $\mu\text{m}$ . The actuator thus imposes the following constraints on the mechanism:

$$\begin{aligned} F_y |_{\max} &\leq 40N \\ F_{x-actuator} |_{\max} &\leq 0.1N \\ -12.5\text{mm} &\leq U_y |_{\max} \leq 12.5\text{mm} \\ \Delta U_y &\geq 2\mu\text{m} \end{aligned} \tag{5.7}$$

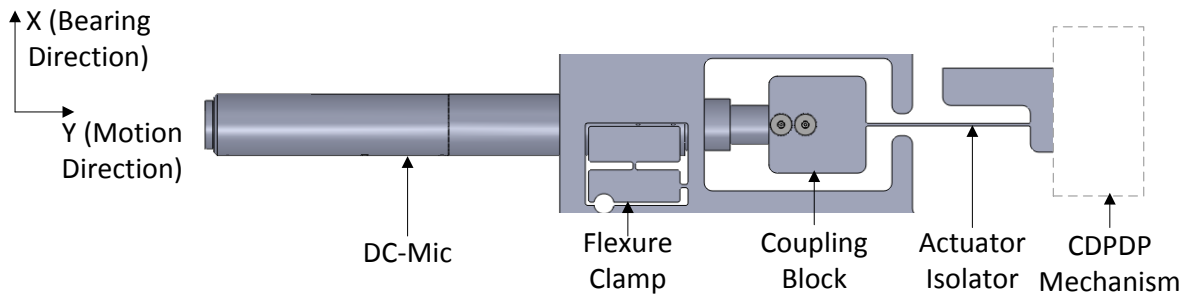


Figure 46: The DC-mic assembly

The DC-mic is held in place by a flexure clamp as shown in Figure 46 to apply an even distributed clamping force on the body of the actuator. To prevent damage on the DC-mic due to lateral forces, an actuator isolator between the mechanism and the actuator is necessary. In this case it is simply a beam with high stiffness in the  $y$  direction but large compliance in the  $x$  direction which helps absorb parasitic displacements in that direction.

### Bearing (X) direction

A side load has to be applied on the motion stage at two different locations for different  $u_y$ . This loading has to maintain perpendicularity with the motion direction at all  $y$  displacements. For this purpose a novel scheme was utilized.

Firstly, instead of using a pulley and weights suspension to apply the side load where because of friction, total load transmission might not occur, a virtual pulley in the form of a three string junction was used for load transmission as shown in Figure 47. By choosing the angle between the strings, we can control the amount of load applied on the stage:

$$F_x = F_L \cot \phi = W \cot \phi \quad (5.8)$$

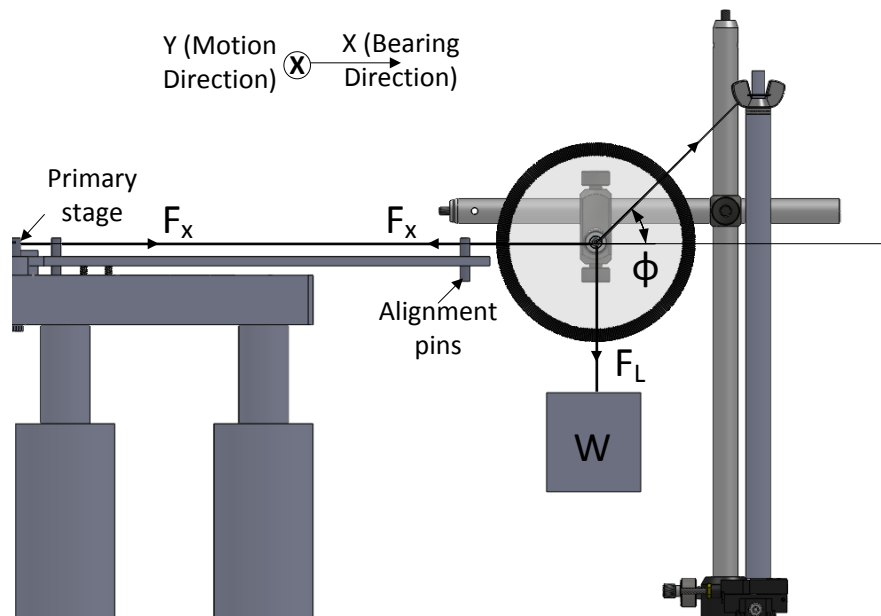


Figure 47: Three-string junction for load transmission to the primary stage of the mechanism

Moreover, as we know that for typical millimeter-scale dimensions, the  $x$ -direction motion would be of the order of a few microns<sup>9</sup>, we can assume that the angle between the strings wouldn't change significantly when the weights are suspended thereby avoiding the need for readjusting the angle every time after applying the load or displacing the stage in the  $y$  direction. A protractor can be used to measure the angles to within a degree. We would later see that this uncertainty wouldn't significantly affect the accuracy of the measurements.

In order to maintain perpendicularity, an alignment plate was used with embedded dowel pins. The pivot of the string setup is on a stand resting on a manual  $xy$  stage (Thor Labs MT1) which has a range of 0.5" in each direction. Thus, whenever the primary stage is displaced, the manual stage can also be displaced along with the suspended weight to ensure marginal contact with the outer dowel. This scheme imposes the following restriction on the mechanism:

$$-6.35\text{mm} \leq U_y |_{\max} \leq 6.35\text{mm} \quad (5.9)$$

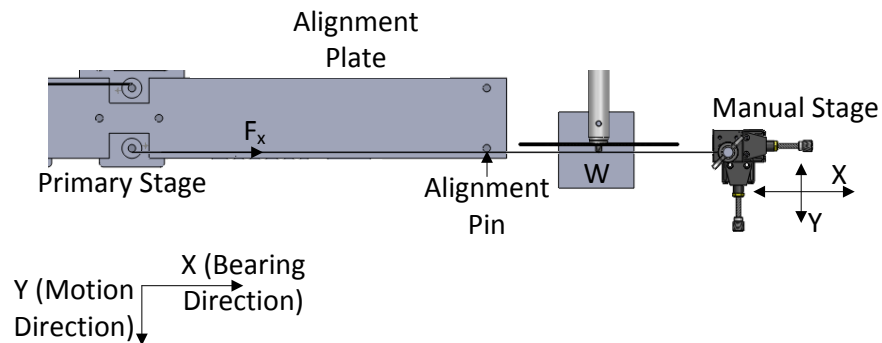


Figure 48: Top view of the three string junction. The manual stage can be moved in the  $y$  direction to keep marginal contact with the alignment pin.

<sup>9</sup> Later, after all the dimensions are selected, this condition would be checked again to ensure that it is still satisfied.

## *Sensing*

Motion (Y) direction force  $F_y$

A load cell (ELFS- T3E-20L) [56] was sandwiched between the DC-mic and the mechanism to measure the force  $F_y$  as shown in Figure 49. The range of the load cell was 20 Lb, much higher than the maximum load that the DC-mic can withstand. As the experiment was essentially a quasi-static one, the noise in the measurement could be minimized significantly by using strong low-pass filters and/or long sampling windows.

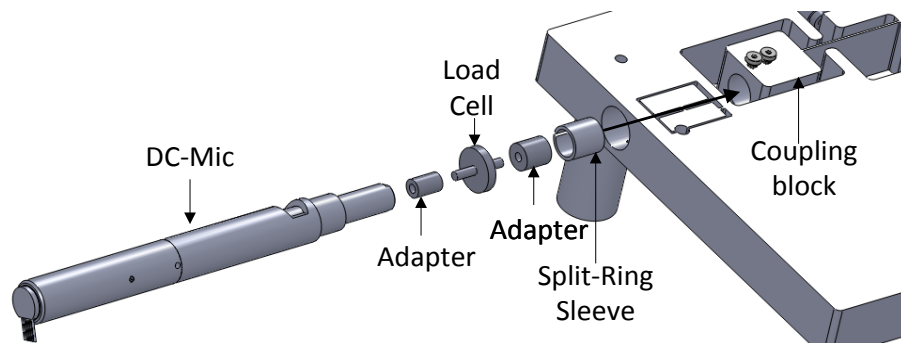


*Figure 49: Integration of the load-cell in the DC-mic assembly*

Bearing direction displacements ( $U_x$  and  $\theta_z$ )

Two capacitive probes (C23-C Low Resolution [57]) in a configuration shown in Figure 44 are used for measuring these displacements. These are implemented in the setup as shown in Figure 50. These are ideally suited for this application as they are tolerant to relatively large  $Y$  displacements perpendicular to their measurement axis and have a small range (50 microns) with a high achievable resolution ( $\sim 10\text{nm}$ ).

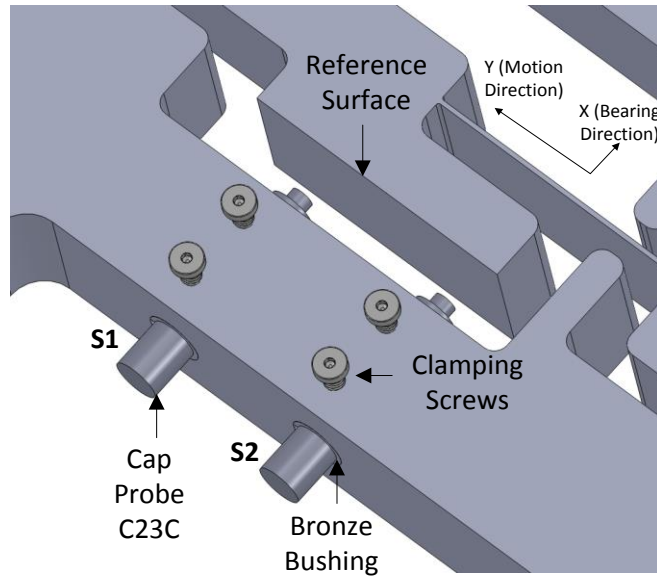


Figure 50: Cap-probe assembly

Each probe was mounted via a bronze bushing that is split along its length and is held in place via a radial set-screw as shown in Figure 50. The bushing helps distribute the force from the set-screw uniformly over the probe length, thus preventing any damage to the probe surface and associated loss of calibration.

### ***Manufacturing process and material selection***

As the mechanism is planar, it was made from a precision ground Al6061-T651 plate using wire electric discharge machining (wire-EDM) which provides very tight dimensional, flatness and angular tolerances for the flexure components while keeping the residual stresses low. Al6061 was chosen due to its good strength, corrosion resistance, machinability and electrical conductivity. The thickness of the plate was chosen to be 1" due to availability and to ensure sufficient out-of-plane stiffness. All other features and components were machined on a conventional CNC milling machine.

The dimensions of the CDPDP flexure were chosen by imposing the above constraints, choosing a large enough effectiveness, keeping the stiffening in the motion direction to

be less than 5% and maintaining an adequate safety margin against yielding, and have been tabulated in Table 6 along with their justifications. The CDPDP flexure plate is also shown in Figure 51. The clamp has been moved inside the outer parallelogram to make the mechanism more compact.

Table 6: Dimensions of the CDPDP mechanism

<i>Dimension</i>	<i>Value</i>	<i>Justification</i>
$L$	65mm	Keeping the maximum displacement around 0.1L to maintain adequate safety margin against yielding of the beams.
$T$	0.8mm	To ensure that the maximum motion direction force is less than 40N
$a_0$	0.3	Optimum value: Improves bearing stiffness considerably while not significantly increasing the y-direction stiffness
$H$	25.4 mm	Standard thickness of the plate
$W_1$	70.52mm	Rotational stiffness of the DPDP unit >> rotational stiffness of the clamp
$W_2$	24.14mm	
$W_3$	32.5mm	Large clamp effectiveness
$L_2$	90.5mm	
$L_3$	32.5mm	Low stiffening in motion direction and large



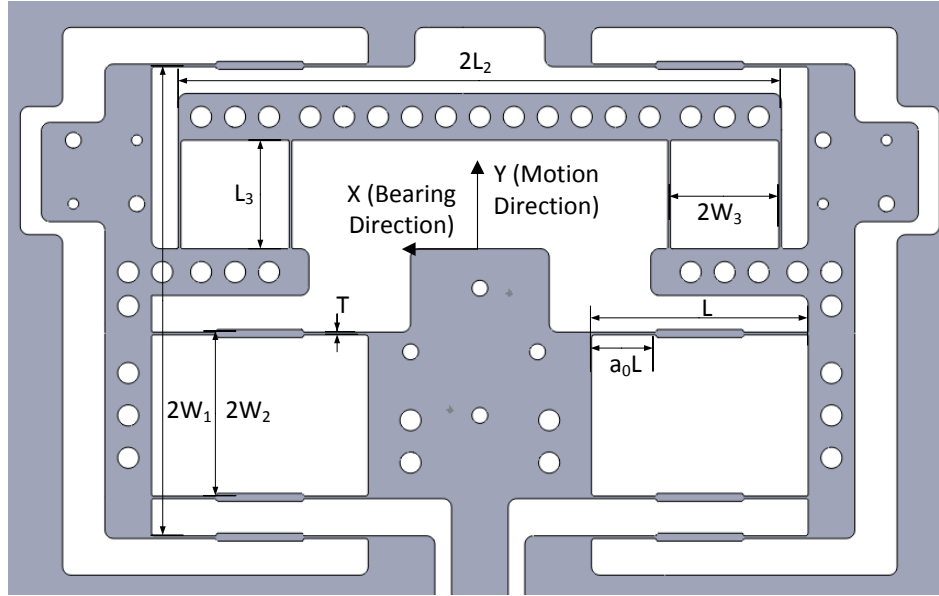


Figure 51: The CDPDP flexure plate

### ***Design of Auxiliary Components and Dimensions***

#### **Actuator Isolator**

The actuator isolator shown in Figure 52, i.e. a single beam positioned along the motion direction  $y$ , must be significantly more compliant in the  $x$  direction compared to the CDPDP mechanism. Therefore, its dimensions were chosen such that the stiffness of the isolator is almost four orders of magnitude smaller than the lowest  $x$ -direction stiffness of CDPDP mechanism i.e.

$$\frac{k_{x-Isolator}}{k_{x-CDPDP}(U_y = 6mm)} < 10^{-4} \quad (5.10)$$

Using equation (4.30) for the bearing stiffness of the CDPDP mechanism with the dimensions given in Table 6 and the motion direction stiffness of a single beam given by equation (2.11), the length  $L_i$  of the actuator isolator was chosen to be 50mm (the beam cross-section was chosen to be the same as that in the CDPDP mechanism).

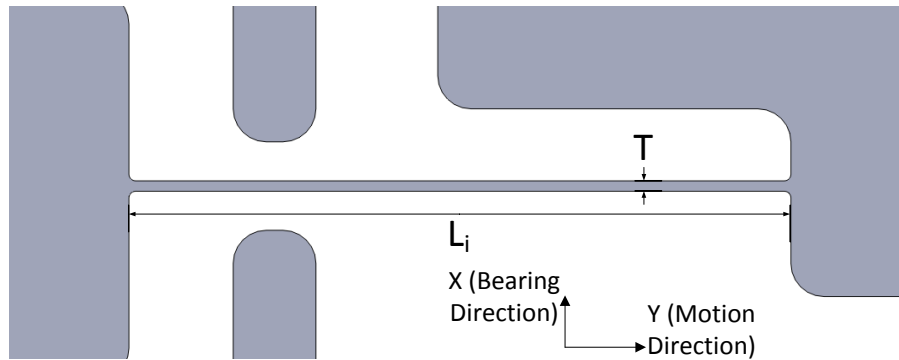


Figure 52: The actuator isolator with dimension labels

Separation between cap-probes (D) and points of load application ( $R_{sep}$ )

The sensor and actuation arrangement for the bearing stiffness measurement shown in Figure 45 is implemented on the flexure plate as shown in Figure 53. Table 7 shows the values of the dimensions involved.

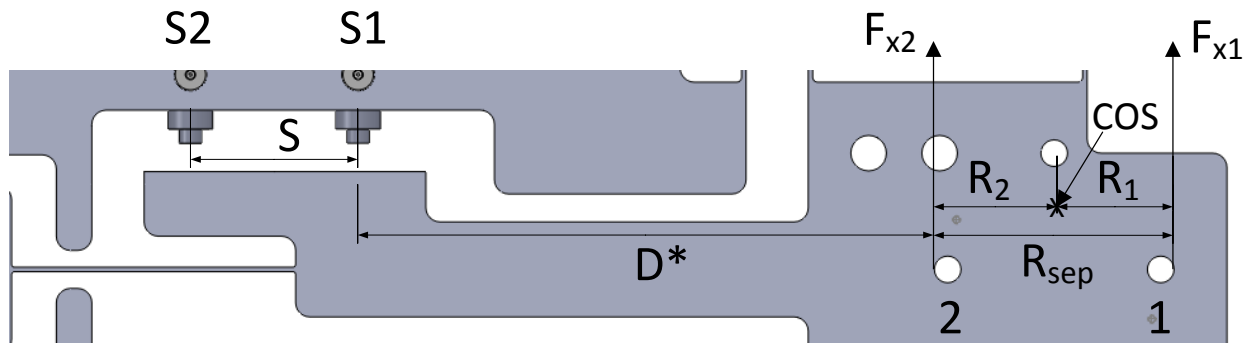


Figure 53: Implementation of the measurement scheme shown in Figure 45.  $D^*=D-R_2-S/2$

Table 7: Parameters of the measurement scheme

<i>Dimension</i>	<i>Value</i>
$S$	30mm
$R_{sep}$	43mm
$D^*$	103mm

#### Fillets at flexure ends

In the absence of fillets at the ends, the stiffness of the flexure beams can be significantly smaller than that predicted by closed form and FEA analysis which assume the support to be perfectly rigid. This is due to additional local flexibility at the juncture of a support and a flexure beam. Moreover, sharp corners can lead to large stress concentrations thereby causing premature static or fatigue failure of the mechanism. Howell et.al. [58] have analyzed this configuration and have obtained optimal fillet radii to mitigate these effects given below:

$$\begin{aligned} R_{fillet} &= 0.64T \quad \text{For half-plane junctures} \\ R_{fillet} &= 1.1T \quad \text{For quarter-plane junctures} \end{aligned} \tag{5.11}$$

These fillet radii have been used in all flexure-support junctions (Figure 54) in the mechanism.

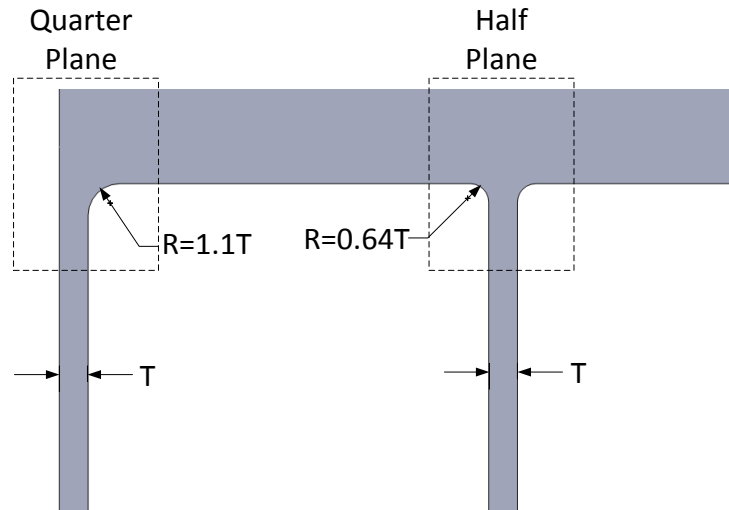
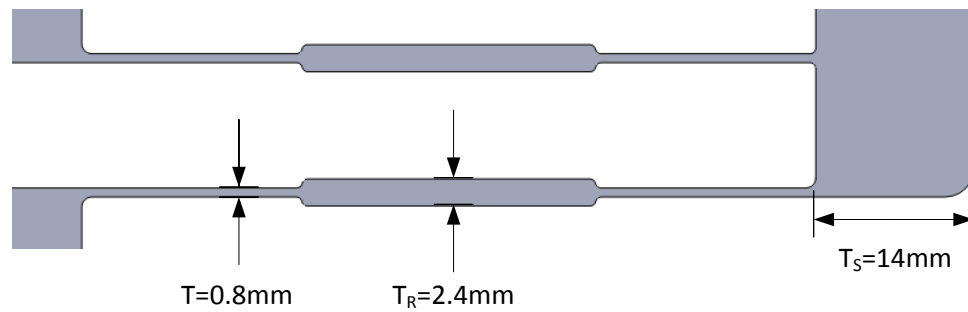


Figure 54: Fillets at flexure supports

#### Thickness of 'rigid' sections and stages

In all the previous analysis, all the stages were assumed to be perfectly rigid. In order to ensure this, the thickness of the stages was chosen to be such that the bending stiffness is almost three orders of magnitude larger than the flexure bending stiffness. As exact expressions are cumbersome to derive and an overkill for this purpose, we simply use the fact that the bending stiffness is proportional to  $(T/L)^3$ . Comparing the bending stiffness between the stages and flexure strips and setting the ratio between them at  $O(10^3)$ , a minimum stage thickness of 14mm was obtained (Figure 55).

For the sections between flexure strips, an order of magnitude difference was set between bending stiffness ratio for the compliant and rigid sections leading to a thickness value of  $3T$  for the rigid sections.



*Figure 55: Thickness of rigid sections and stages*

Finally, Figure 56 shows the entire setup with all the components labeled including the load-cell and cap-probe amplifiers and the DC-mic driver along with the USB data-acquisition board connected to a host computer (not shown). The entire setup rests on a vibration isolation table to minimize effects of floor vibration (moreover, as mentioned before, long sampling windows are also used to further minimize the effects of extraneous noise and vibrations).

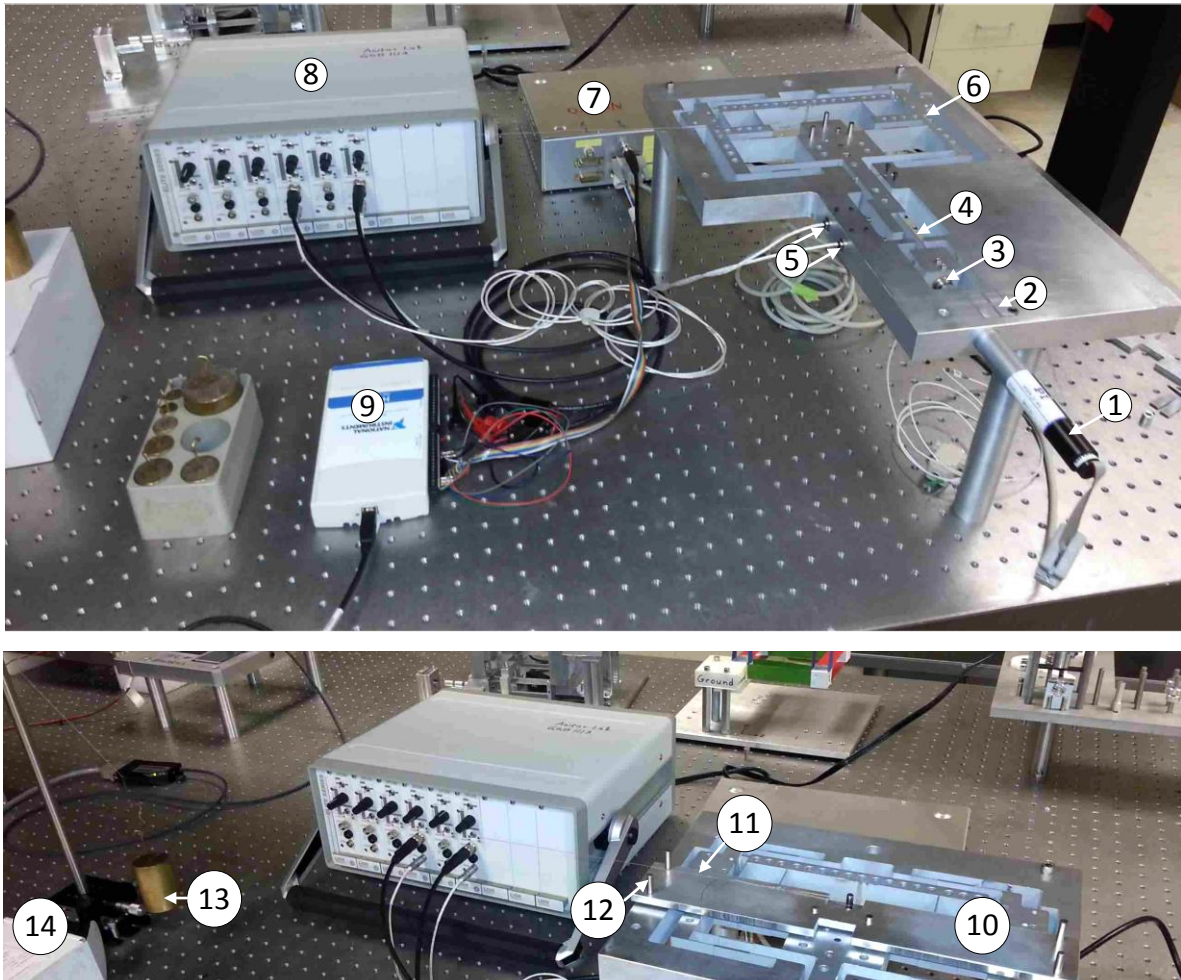


Figure 56: Complete Experimental Setup - 1)Dc-Mic, 2) Flexure Clamp, 3)Load Cell, 4)Actuator Isolator, 5)Cap-probes, 6)CDPDP mechanism, 7) DC-Mic amplifier, 8)Cap-probe amplifier, 9)NI USB-DAQ, 10)Alignment plate, 11)String for applying load, 12)Alignment pins, 13)Suspended Weight, 14) Manual stage and post

## Error Analysis

The primary sources of measurement error/uncertainty in this experiment are the following:

1. Cap-Probe Resolution –  $\delta U_s$  (m)

2. Load-cell Resolution –  $\delta F_y$  (N)
3. DC-Mic Encoder Resolution –  $\delta U_y$  (m)
4. String Angle Resolution –  $\delta\varphi$  (rad)

All other angle misalignment errors – between the cap-probes and the reference surface Figure 50 and between the bearing load ( $F_x$ ) transmitting string and the horizontal/ground Figure 47 or motion direction  $y$  Figure 48 can be ignored as they would vary as cosines of the error and hence, would be small. Errors in the elastic modulus of the material can be assumed to be less than 5% [59].

#### ***Errors in Motion direction stiffness***

The motion direction stiffness is given by equation (5.2). Taking the variation on both sides:

$$\begin{aligned} \delta K_y &= \frac{\delta(U_{yf} - U_{yi})(F_y(U_{yf}) - F_y(U_{yi})) - (U_{yf} - U_{yi})\delta(F_y(U_{yf}) - F_y(U_{yi}))}{(U_{yf} - U_{yi})^2} \\ \Rightarrow \frac{\delta K_y}{K_y} &= \frac{2\delta U_y}{(U_{yf} - U_{yi})} + \frac{2\delta F_y}{(F_y(U_{yf}) - F_y(U_{yi}))} \end{aligned} \quad (5.12)$$

#### ***Errors in bearing direction stiffness ( $K_x$ and $K_\theta$ )***

Referring to Figure 45, the displacement measured by any particular cap-probe  $\Delta U_{ij}$  where  $i$  indicates the probe number and  $j$  corresponds to the pin on which the load  $f_x$  is applied is given by:

$$\Delta U_{ij} = U_{ij} |_{load=f_x} - U_{ij} |_{load=0} \quad (5.13)$$

The error can be obtained by taking variation on both sides:

$$\begin{aligned}\delta(\Delta U_{ij}) &= \delta U_{ij} |_{load=f_{xj}} - \delta U_{ij} |_{load=0} \\ \Rightarrow \delta(\Delta U_{ij}) &= \delta U_s + \delta U_s = 2\delta U_s\end{aligned}\quad (5.14)$$

Using equation (5.5), the error in the measurement of the rotation  $\theta_{zj}$  can be obtained:

$$\delta\theta_{zj} = \delta\left(\frac{(\Delta U_{s2j} - \Delta U_{s1j})}{S}\right) = 4\frac{\delta U_s}{S}\quad (5.15)$$

Similarly, the uncertainty in the applied loads  $F_{xj}$  due to errors in measurement of the angle  $\phi$  can also be calculated using equation (5.8):

$$\begin{aligned}\delta F_{xj} &= \delta(W_j \cot \phi_j) = W_j \frac{\delta\phi}{\sin^2 \phi_j} \\ \Rightarrow \frac{\delta F_{xj}}{F_{xj}} &= \frac{2\delta\phi}{\sin(2\phi_j)}\end{aligned}\quad (5.16)$$

Using equations (5.5) and (5.6), the rotational stiffness can be solved for:

$$K_\theta(U_y) = \frac{R_{sep} F_{x1} F_{x2}}{(F_{x2} \theta_{z1} - F_{x1} \theta_{z2})}\quad (5.17)$$

Taking the variation of the above on both sides:

$$\frac{\delta K_\theta}{K_\theta} = \frac{\delta F_{x1}}{F_{x1}} + \frac{\delta F_{x2}}{F_{x2}} + \left| \frac{(F_{x1} + F_{x2}) \delta\theta_{z1} + |\theta_{z2}| \delta F_{x1} + |\theta_{z1}| \delta F_{x2}}{(F_{x2} \theta_{z1} - F_{x1} \theta_{z2})} \right|\quad (5.18)$$

Where errors in  $F_x$  and  $\theta_z$  are given by equations (5.16) and (5.15) respectively. The location of the center of stiffness is given by:

$$R_2 = -\frac{K_\theta \theta_{z2}}{F_{x2}}\quad (5.19)$$

Again, taking the variation of the above equation:

$$\frac{\delta R_2}{R_2} = \frac{\delta K_\theta}{K_\theta} + \frac{\delta\theta_{z2}}{|\theta_{z2}|} + \frac{\delta F_{x2}}{F_{x2}}\quad (5.20)$$

Next, the error in the axial displacement can be calculated using equation (5.5):

$$\begin{aligned}\delta U_{x1}(U_y) &= \delta U_{s11} + \delta(D^* + R_2) |\theta_{z1}| + \delta\theta_{z1} (D^* + R_2) \\ &= 2\delta U_s + \delta R_2 |\theta_{z1}| + \delta\theta_{z1} (D^* + R_2)\end{aligned}\quad (5.21)$$



Finally, the uncertainty in the  $x$ -direction stiffness can be given by:

$$\frac{\delta K_x}{K_x} = \frac{\delta F_{x1}}{F_{x1}} + \frac{\delta U_{x1}}{|U_{x1}|} \quad (5.22)$$

### ***Uncertainty in parasitic motions ( $E_x$ and $E_\theta$ )***

The parasitic motions are given by equation (5.4). Following a procedure similar to one shown above, the estimates of uncertainty in these measurements are given below:

$$\begin{aligned} \delta E_\theta(U_y) &= \frac{2\delta U_s}{S} \\ \delta E_x(U_y) &= \delta U_s + (D^* + R_2)\delta E_\theta(U_y) + E_\theta(U_y)\delta R_2 \end{aligned} \quad (5.23)$$

### **FEA Validation and predicted results**

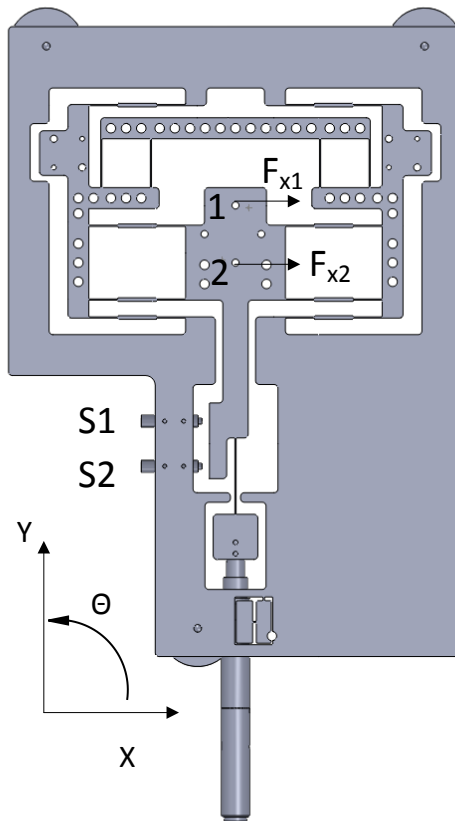


Figure 57: Sign conventions used for the experiment

The experimental setup and procedure was simulated using FEA and the predicted stiffness and displacement estimates were obtained. Figure shows the sign conventions adopted for this experiment. As before, BEAM 4 elements were used to model the compliant flexures and a force convergence tolerance of  $10^{-3}$  was used. Figures Figure 58 to Figure 61 show the motion, rotational, axial stiffness and the distance  $R_2$  of the COS from Pin 2 (Figure 53) calculated using FEA (solid lines) and closed-form results (circles) for the mechanism with dimensions tabulated in Table 6. Error bars have also been added using expressions derived in the last section. The values for measurement uncertainties:  $\delta U_s$ ,  $\delta F_y$ ,  $\delta U_y$  and  $\delta \varphi$  were chosen to be 5nm, 0.01N, 5  $\mu\text{m}$  and 1 deg respectively. Moreover,  $F_{x1}=F_{x2}=40\text{N}$  and  $\varphi_1 = \varphi_2=0.25\pi$  Rad.

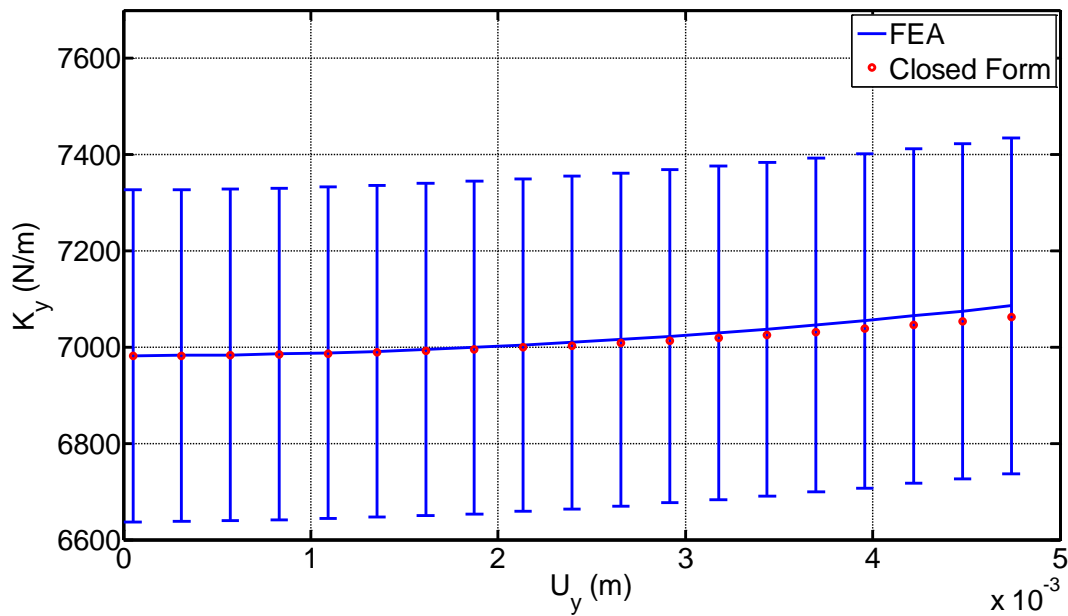


Figure 58: Motion direction stiffness for the CDPDP flexure plate

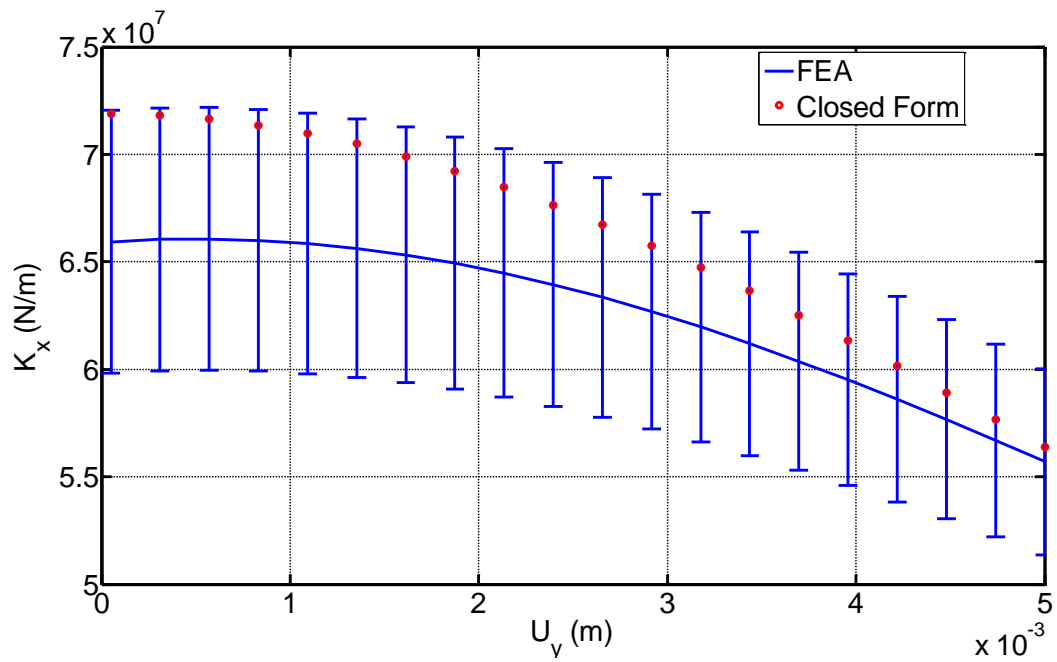


Figure 59: X direction stiffness for the CDPDP flexure plate

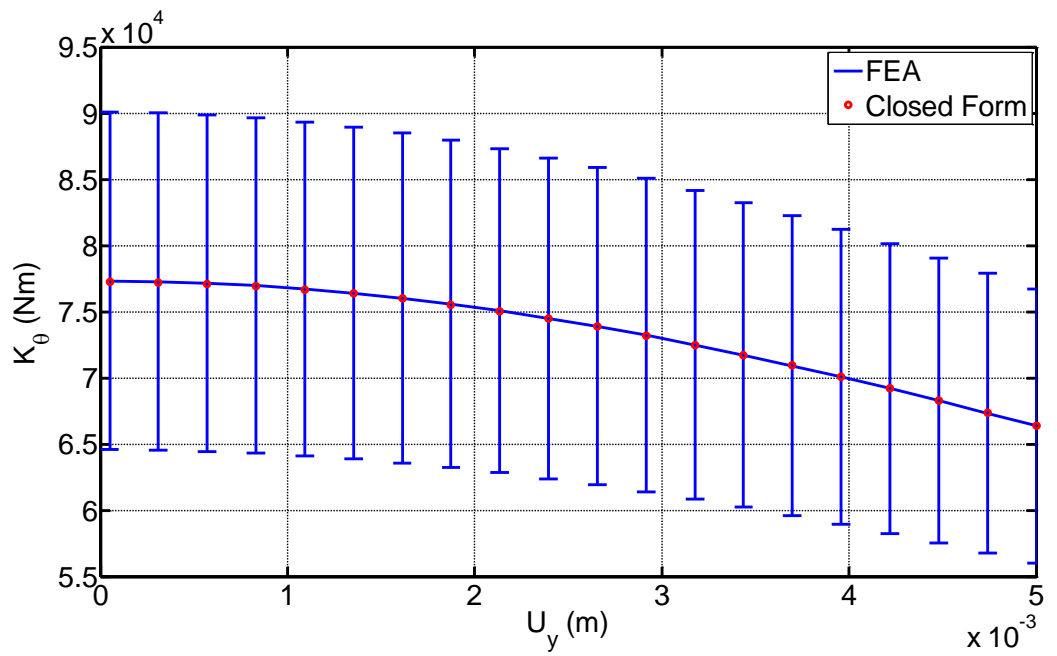


Figure 60: Rotational stiffness for the CDPDP flexure plate

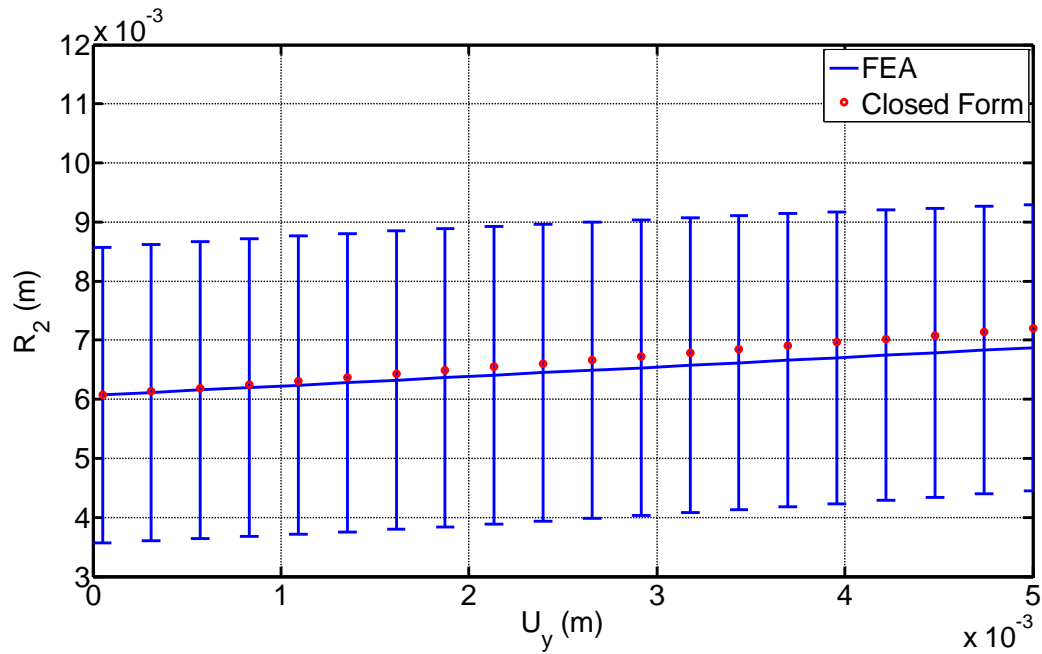


Figure 61: Location of the COS for the CDPDP flexure plate. The closed form expressions are given by equation (D.10)

Significant discrepancy can be seen between the FEA results and closed form results for the  $X$ -direction stiffness shown in Figure 59. This can be explained by taking into account the coupling between the  $x$  and  $\theta$  direction relations. This case has been dealt with in Appendix D and this error has been eliminated to some degree. Finally, the expected displacements at the cap-probes and the rotations  $\theta_{z1}$  and  $\theta_{z2}$  have also been plotted in Figure 62 and Figure 63.

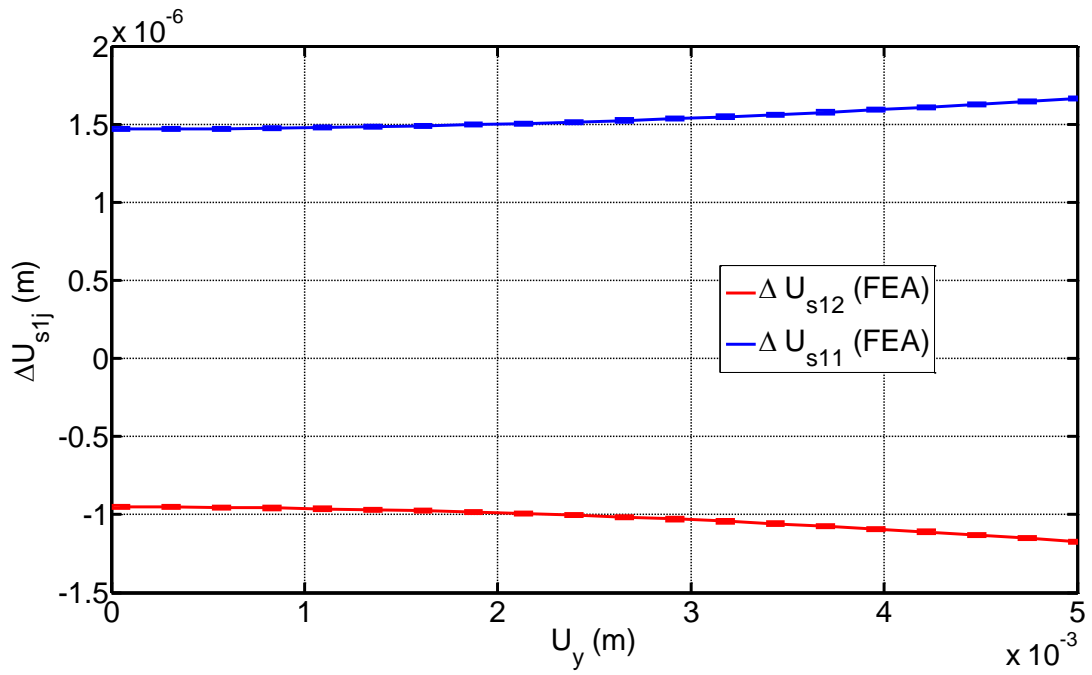


Figure 62: The expected displacement at the first cap-probe (S1) for loading on pin 1 and pin 2.

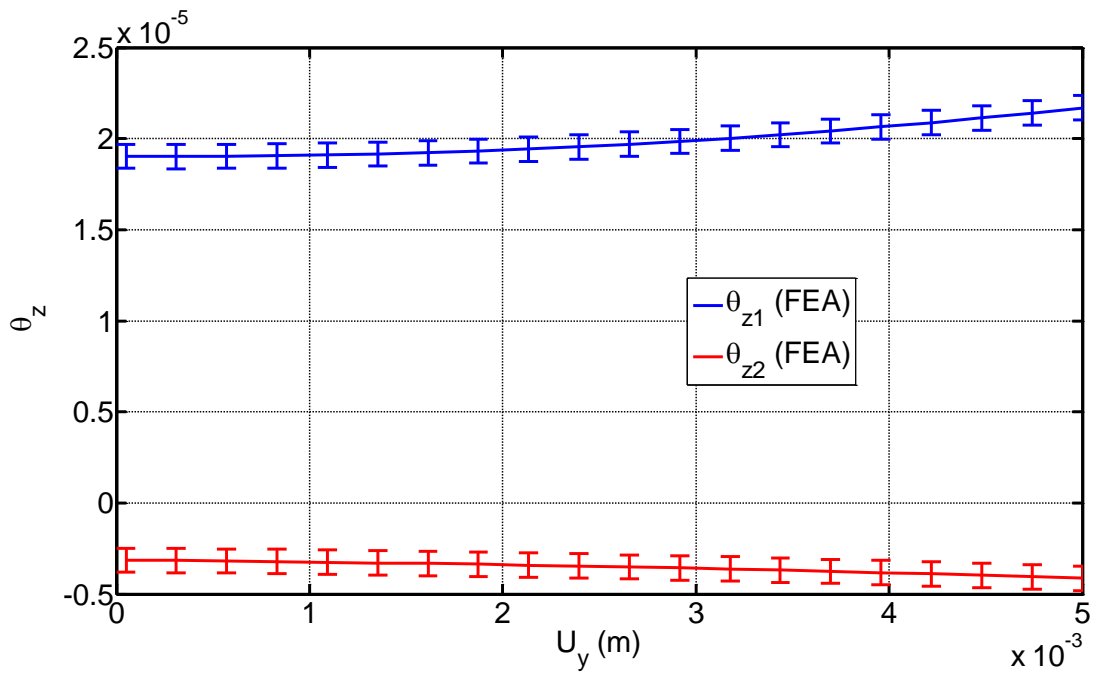


Figure 63: The expected rotations of the stage for loading on pin 1 and pin 2. Rotations are in radians.

## Preliminary Results

### *Motion Direction Stiffness*

The motion direction force vs. displacement curve is shown in Figure 64. The force was observed to be predominantly linear with non-linearity of less than 3% over the range of 5mm. Thus, the clamp has negligible influence on the motion direction stiffness which is desirable.

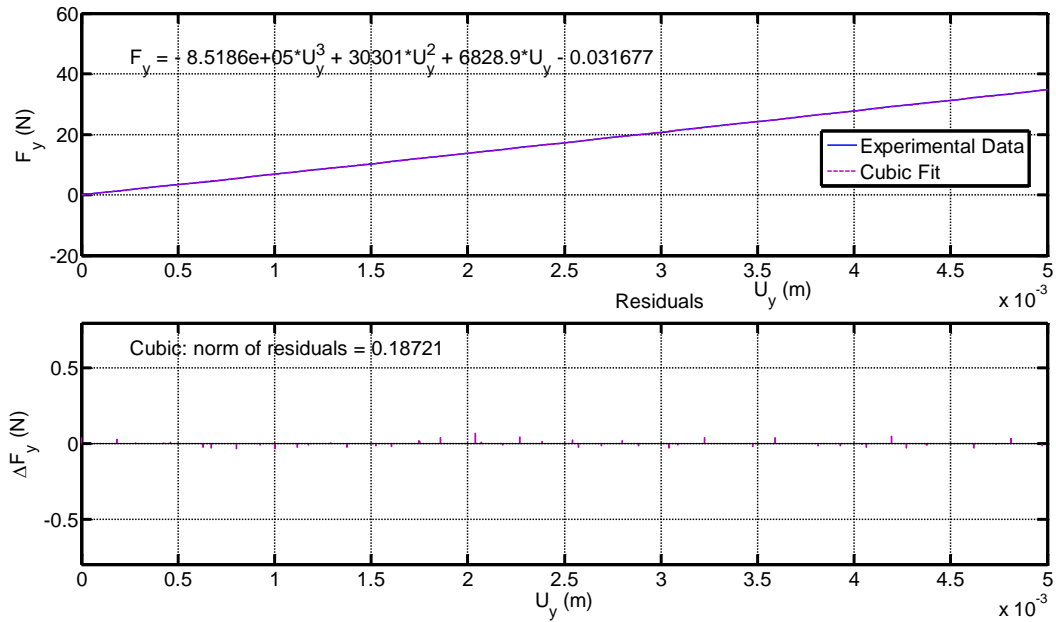


Figure 64: Experimentally measured motion direction force vs. displacement curve

## Chapter 6: Case Study: Comb drive optimization

The comb drive actuator is an example of a single axis system whose performance is directly affected by the quality of the flexure bearing. In this chapter, we use the results obtained in chapter 4 to design comb drive actuators employing the CDPDP and DP-TDP flexures as motion guides with the objectives of achieving the largest possible stroke with minimum possible actuator effort and footprint. A systematic procedure to design comb drive actuators with these attributes which are desirable in micro and nano-positioners [60, 61] and micro-grippers [62, 63], would also be developed which can be used for other flexure guides as well. This procedure also encompasses restrictions imposed by fabrication capabilities and system requirements.

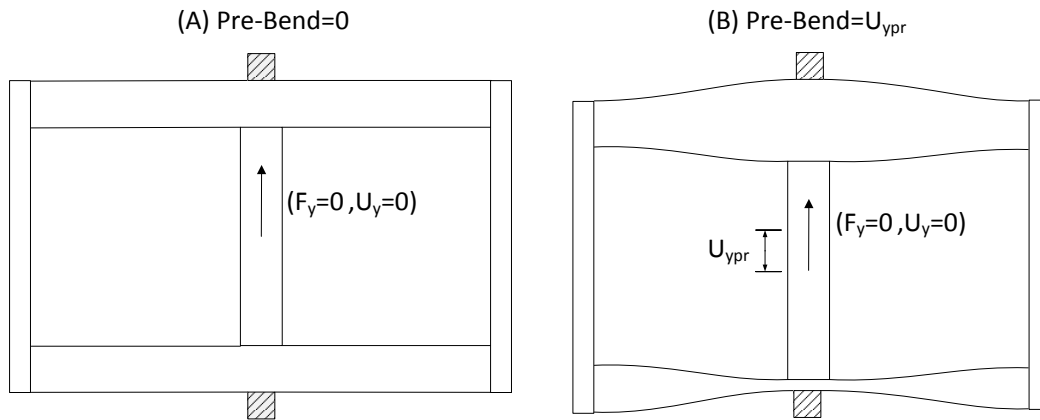


Figure 65: Pre-Bending in a DPDP flexure

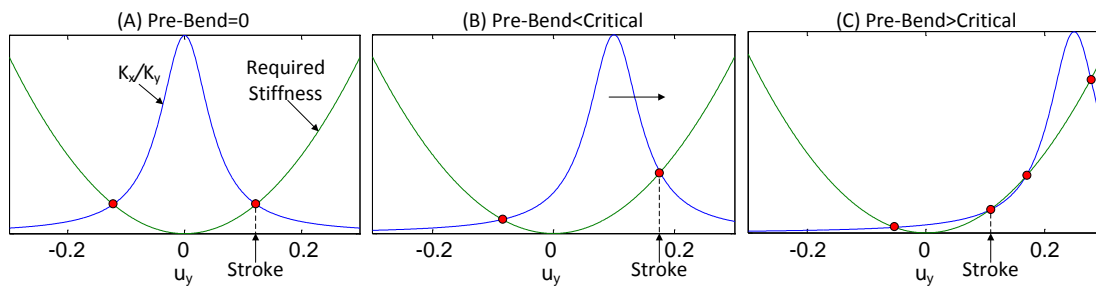


Figure 66: Effect of pre-bending on the stroke of a comb drive actuator. At the critical pre-bend, the stiffness ratio curve intersects the required stiffness curve at exactly 3 points.

We would include certain design variations of the flexures – reinforced beams (Figure 7) and pre-bending or pre-tilting [37, 64] (Figure 65) to further boost the performance of the devices. Although the multi-beam parallelogram (Figure 12) can easily be incorporated in the design process, it has been excluded from this analysis as it offers no obvious advantage for this particular application. By pre-bending beams in a particular direction, one can shift the stiffness profile of the flexure thereby delaying the onset of snap-in and consequently increasing the stroke. This is illustrated in Figure 66 (B). However, there exists a limit beyond which additional pre-bending can cause a pre-mature intersection with the required stiffness curve (Figure 66 (C)). Thus, in order to maintain an adequate safety margin to disturbances and manufacturing imperfections, the actual pre-bend is kept sufficiently below this limit which can be easily determined for a flexure mechanism based on its stiffness properties.

There are some fundamental differences between the optimization procedures for the CDPDP and DP-TDP cases. The CDPDP mechanism has theoretically zero error motions whereas the DP-TDP could have non-zero error motions (depending on the tilt angles). Moreover, because of asymmetry, the sensitivity to fabrication imperfections would be larger in the case of the DP-TDP mechanism which in turn would imply that the safety margin given by equation (1.15) must be larger for this flexure. For the CDPDP mechanism, we can simply use the snap-in condition given by equation (1.7) along with the closed form stiffness expressions derived in chapter 4. Moreover, as its rotational stiffness can be increased independent of the axial stiffness by increasing the beam separations  $w_1$  and  $w_2$ , we can further assume a purely one dimensional snap-in model given by equation (1.6) instead of the two dimensional one (equation (1.7)) and choose the separations to ensure that the difference in strokes predicted by (1.7) and (1.6) is negligible. Consequently, for the optimization of the CDPDP mechanism for a comb drive actuator, we can directly use the objective function given in equation (1.18). Such a simplified governing equation for snap-in and hence a closed form objective function for optimization does not exist for the DP-TDP case. Moreover, we do not have complete



parametric results for the stiffness and error motions of this mechanism yet. Therefore, we would merely do a first-pass qualitative optimization for the DP-TDP mechanism here and lay out some guidelines for future work.

### CDPDP optimization

In this section, we present a systematic procedure for holistically designing a CDPDP flexure based comb-drive actuator to maximize its actuation stroke while minimizing device foot-print and actuation voltage. Given the several constraints and tradeoffs involved, the goal here is to obtain a good starting point for the flexure and comb-drive dimensions shown in Figure 23 and Figure 3 respectively ( $L$ ,  $T$ ,  $a_0$ ,  $W_1$ ,  $W_2$ ,  $L_2$ ,  $L_3$ ,  $W_3$ ,  $G$ ,  $L_f$ , and  $T_f$ ) based on some simplifying assumptions, and subsequently iterate to further refine the overall design.

The following assumptions are made initially and are revisited during later design steps:

1. Analytical results in the chapter 4 show that the optimization of the external clamp is decoupled from the final stiffness of the C-DP-DP flexure, as long as the clamp is effective. Since a clamp can be designed to provide near-optimal performance i.e. a high  $\eta$  ( $\rightarrow \infty$ ) and low  $\gamma$  ( $\rightarrow 0$ ), corresponding motion and bearing stiffness values are assumed at the on-set of this design procedure.

$$K_y \approx 2 \frac{EI_{zz}}{L^3} k_{11}^{(0)}(a_0) \quad (5.23)$$

$$K_x \approx 2 \frac{EI_{zz}}{L^3} \frac{1}{\left( \frac{1}{k_{33}(a_0)} - \frac{u_y^2}{4} k_{11}^{(2)}(a_0) \right)} \quad (5.23)$$

$$K_\theta = \frac{EI_{zz}}{L^3} \left( \frac{4W_1^2W_2^2}{W_1^2 + W_2^2} \right) \frac{1}{\left( \frac{1}{k_{33}(a_0)} - \frac{u_y^2}{4} k_{11}^{(2)}(a_0) \right)} \quad (5.23)$$

Where  $I_{zz} = HT^3/12$  is the area moment of inertia of the beams in the base DPDP.

2. The motion stage, secondary stage, external clamp, ground anchors, and beam reinforcements are all assumed to be perfectly rigid.
3. Since the in-plane rotational stiffness ( $K_\theta$ ) of the C-DP-DP flexure can be made independently high, it is assumed large enough to be ignored in the first iteration.
4. A Stability Margin of  $S = 1$  is assumed to provide robustness against non-deterministic factors arising due to fabrication imperfections.
5. Silicon is chosen as the flexure and comb-drive material, which sets an upper bound for the maximum achievable stroke due to mechanical failure. For the C-DP-DP flexure, the yield limit is given by equation (3.59)
6. An initial comb-finger engagement  $U_{y0}$  is needed to overcome fringing effects that are important for small  $Y$  displacements. The minimum initial engagement has been obtained theoretically and for an in-plane comb drive is given by:

$$U_{y0} > 1.98G \quad (5.23)$$

However,  $Y_0$  is much smaller than the maximum  $Y$  displacement and is therefore dropped initially in the design procedure.

We next present a step by step recipe [32] for choosing the dimensions of the CDPDP and comb-drive that employs the analytical knowledge compiled so far. The optimal device would then be fabricated<sup>10</sup> to demonstrate the performance improvements over the existing comb drive actuators:

---

<sup>10</sup> Fabrication was done separately and is not a part of this thesis.

1. Start with assuming a dimension for the flexure beam length  $L$ , which directly impacts the device foot-print. In the first iteration, we start with a value of  $L = 1$  mm.
2. Minimizing the  $T/L$  ratio reduces the bending stress in the flexure beams and therefore increases the material failure limit of the mechanism (equation (3.59)). Equation (1.18) shows that to achieve the best stroke to effort/footprint ratio, we must maximize the ratio  $K_x/K_y^3$ . Inspecting equation (5.23), we see that  $K_x$  is proportional to  $T$  at small displacements and  $T^3$  at large displacements. From equation (5.23),  $K_y$  is proportional to  $T^3$  over the entire range of motion. Thus, the ratio  $K_x/K_y^3$  would be proportional to  $1/T^8$  at small  $Y_{max}$  and  $1/T^6$  at large ones. This implies that to maximize the ratio  $K_x/K_y^3$ ,  $T$  should be kept as small as possible. The lower bound is dictated by practical limits of the micro-fabrication process. In our case, this limit is  $1.7 \mu\text{m}$  and with an adequate safety margin and we choose  $T = 3 \mu\text{m}$ , which corresponds to a  $T/L$  ratio of 0.003.
3. Now, the two key remaining design variables are  $a_0$  and  $G$ . Equation (1.18) can be rewritten for the CDPDP mechanism using equations (5.23) and (5.23):

$$NV_{\max}^2 = \frac{E}{3\mathcal{E}} \left( \frac{T}{L} \right)^3 (U_y|_{\max})^2 \sqrt{\left( k_{11}^{(0)} \right)^3 \left( \frac{1}{k_{33}} - \left( \frac{U_y|_{\max}}{2L} \right)^2 k_{11}^{(2)} \right)} \quad (5.24)$$

The above condition can be plotted on an  $NV_{\max}^2$  versus  $U_y|_{\max}$  graph for multiple fixed values of  $a_0$ . Each solid line, referred to as an *iso- $a_0$*  line represents a fixed value of  $a_0$  and varying values of  $G$ . Similarly, the above equations are solved to eliminate  $a_0$  and the resulting condition is plotted on the same plot for fixed values of  $G$ . For doing this, we first obtain the maximum stroke for a fixed  $G$  but varying  $a_0$  and then substitute this value in equation (5.24) to obtain the corresponding  $NV_{\max}^2$ . Using equation (1.16), the stroke is given as the root of the following equation:

$$U_{y|_{\max}}(a_0, G_c): \frac{K_x(U_{y|_{\max}}, a_0)}{K_y(U_{y|_{\max}}, a_0)} = (1+S) \frac{U_{y|_{\max}}(U_{y|_{\max}} + U_{y0})}{G^2}, G = G_c = \text{constant} \quad (5.25)$$

At large displacements, the elastic term can be dropped from the denominator of the  $x$ -direction stiffness of the ideal CDPDP mechanism ( $\eta = \infty$ ) provided that the thickness is small enough. This limit can be obtained by imposing the constraint that the elastic term is less than or equal to 5% of the elasto-kinematic term at a displacement of about  $0.2L$  i.e. using equation (5.23):

$$\begin{aligned} \frac{1}{k_{33}} &< 0.05 \frac{u_y^2 k_{11}^{(2)}}{4} \\ \Rightarrow \frac{T^2}{12L^2} &< 0.05 \frac{(0.2)^2}{4} \left( \frac{1}{700} \right) \\ \Rightarrow \frac{T}{L} &< 0.003 \end{aligned} \quad (5.26)$$

For this thickness we can approximately write:

$$K_x \approx \left( 2 \frac{EI_{zz}}{L^3} \right) \frac{4L^2}{U_y^2 k_{11}^{(2)}(a_0)} \quad (5.27)$$

Therefore, assuming that  $U_{y0} \ll U_{y|_{\max}}$ , for the CDPDP, we can solve equation (5.25) to obtain:

$$U_{y|_{\max}}(a_0, G_c) \approx \sqrt[4]{\frac{-4G_c^2 L^2}{(1+S)k_{11}^{(0)}(a_0)k_{11}^{(2)}(a_0)}} \quad (5.28)$$

This can be substituted in equation (5.24) to obtain  $NV_{\max}^2(a_0, G_c)$  for every value of  $a_0$  and  $G_c$ . The plots between  $U_{y|_{\max}}$  given by equation (5.28) and  $NV_{\max}^2$  for different values of  $a_0$  but fixed values of the gap size  $G$  are called the *iso-G* lines, shown as dashed lines in figure. Moving along an *iso-a<sub>0</sub>* line, it is clear that for a given beam shape ( $a_0$ ), one can achieve the highest stroke by increasing the comb-gap  $G$ , but this also increases the actuation effort  $NV_{\max}^2$ . Similarly, moving along the *iso-G* line, one can achieve greater stroke by reducing  $a_0$ , which once again leads to a higher actuation effort.

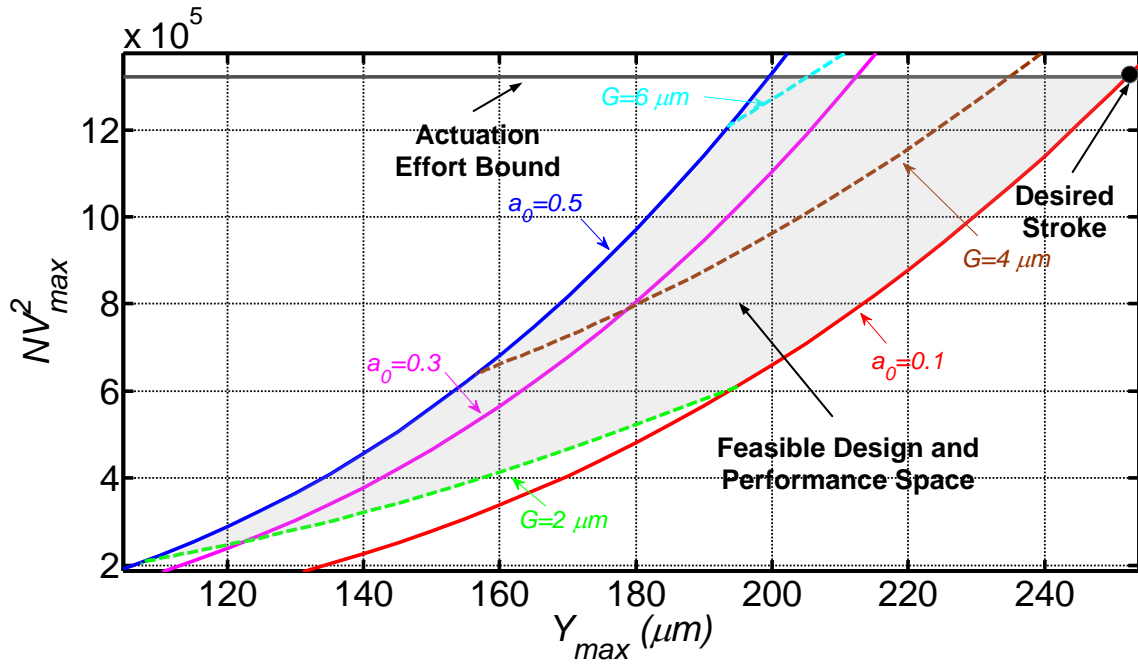


Figure 67: Design and performance space for a C-DP-DP flexure based comb-drive actuators

From the design and performance space presented in figure, one can graphically choose the beam shape  $a_0$  and comb gap  $G$  to maximize stroke while minimizing the actuation effort. There is a lower bound on  $G$  dictated by the micro-fabrication process ( $2 \mu\text{m}$  in this case) and obvious upper and lower bounds on  $a_0$  (0.5 and 0). These bounds produce a feasible design and performance space, indicated by the shaded region in figure.

4. At this point, one can either set a maximum allowable actuation effort and pick the corresponding actuation stroke; or alternatively choose the desired actuation stroke and pick the actuation effort. We choose a desired actuation stroke greater than or equal to  $250 \mu\text{m}$ .
5. For a desired stroke, clearly smaller values of  $a_0$  and  $G$  in the feasible design space result in the lowest actuation effort. However, one has to be cautious while choosing small values of these two design variables. Small  $a_0$  leads to increasingly higher stresses in the flexure beams and the material failure becomes

a concern. For a given  $U_{y\max}$ ,  $a_0$  may be chosen to maintain an adequate margin of safety against material failure using equation (3.59). This condition could be incorporated in figure further shrinking the feasible design space. Separately, the snap-in condition becomes highly sensitive to error motions  $E_x$  for very small  $G$ , and the assumed safety margin  $S$  of 1 can prove to be inadequate. For our final designs, we chose  $a_0 = 0.2$  and  $G$  values in the range of 3–6  $\mu\text{m}$ .

6. Having chosen  $a_0$  and  $G$  in the previous step, we now have a numerical value of the actuation effort from Figure 67. The number of comb-fingers  $N$  can be chosen next, while keeping the maximum actuation voltage  $V_{\max}$  within relevant practical limits. We selected  $V_{\max} = 150\text{V}$  based on our existing instrumentation capabilities.
  
7. One can now start to lay out the flexure mechanism and the comb-drive. The dimensions  $W_1$  and  $W_2$  should be chosen such that rotational stiffness  $K_\theta$  given by equation (5.23) is adequately high. If it is more than an order of magnitude higher than  $K_x L_{\text{off}}^2$  at  $U_{y\max}$ , the contribution of the rotational stiffness can be entirely ignored. Here  $L_{\text{off}}$  is the distance along  $Y$  axis from the center of the flexure mechanism to the tip of the comb fingers (Figure 3). If this condition is not met, then the rotational stiffness should be taken into account in the next iteration using a modified version of the snap-in condition (equation (1.7)). The ratio ( $\gamma$ ) between the reduced actuation stroke due to finite rotational stiffness and the predicted stroke assuming infinite rotational stiffness is graphically illustrated for two values of  $a_0$  in Figure 68.

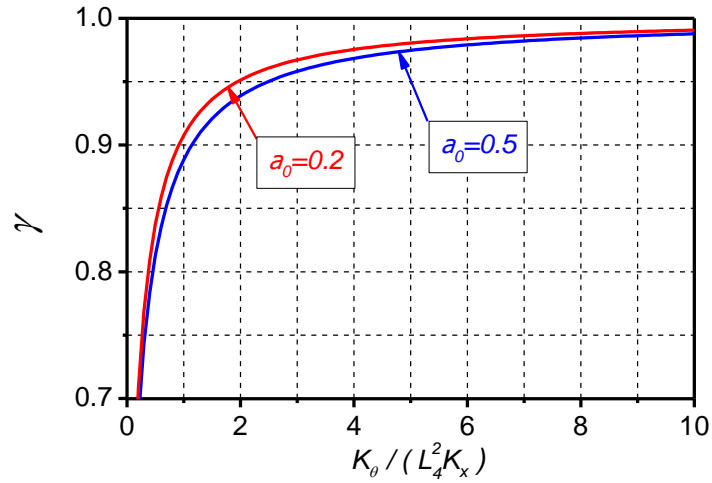


Figure 68: Reduction in predicted actuation stroke in the presence of finite rotational stiffness

8. The external clamp is designed next. Using equation (4.24), choose  $L_3$  to be large enough so that the increase in the motion direction stiffness  $K_y$  due to the clamp over the above-selected  $U_y|_{\max}$  is within a few percent (5%, in our designs). The sensitivity of the footprint to the dimensions  $W_3$  and  $L_3$  dictates the choice of  $T_3$ . For example, if the dimension  $L_3$  affects the footprint more, then we should choose a small value of  $T_3$ . (according to equation (4.24)). For now, we fix  $T_3=T$ . Next, using equation (4.33), we determine  $W_3$ . With an effective clamp thus designed, it can now be included in the overall device layout.
  
9. Next choose the in-plane thickness of the reinforced beam section to be at least 5 times the thickness of the end-segment ( $T$ ), which ensures more than 125 times bending stiffness. Furthermore, choose the in-plane thickness for the motion stage, secondary stage, and the external clamp to be at least 40 times  $T$ . If these dimensions are chosen to be less for whatever reason, then the contribution of these stages to the bearing direction stiffness  $K_x$  should be estimated, and a revised snap-in condition with this reduced effective  $K_x$  should be used in the next design iteration.

10. The initial overlap  $U_{y0}$  can be chosen based on equation (5.23). The comb finger length  $L_f$  should subsequently be chosen to be slightly greater than  $(U_{y0}+U_{y/max})$ . For this comb-finger thickness  $T_f$  should be chosen to avoid local snap-in of individual fingers [65]. This is given by the following condition:

$$T_f \geq \left( 2 \frac{\epsilon L_f^4}{EG^3} V_{\max}^2 \right)^{\frac{1}{3}} \quad (5.28)$$

A margin of safety may be included (1.5, in our case) while using the above relation.

11. The depth of the flexure beams and comb-fingers,  $H_f$  does not play a role in the overall actuator performance and should be selected to be large enough to avoid out-of plane collapse during the fabrication or operation.

This concludes the first iteration of the overall actuator's dimensional layout including the flexure and the comb-drive. If the device foot-print turns out to be too large or too small, one can start the process again from Step 1 with a different value of beam length  $L$ . Once an acceptable foot-print is achieved, a final check on the actuation, snap-in, and material failure conditions should be performed while removing the previously listed assumptions. Specifically, the choice of Stability Margin ( $S$ ) should be dictated by the selected comb-gap value  $G$  and the accuracy of the micro-fabrication process used. Accordingly, a higher value of  $S$  may be used in subsequent iterations. These iterations can lead to further refinement of the flexure and comb-drive dimensions.



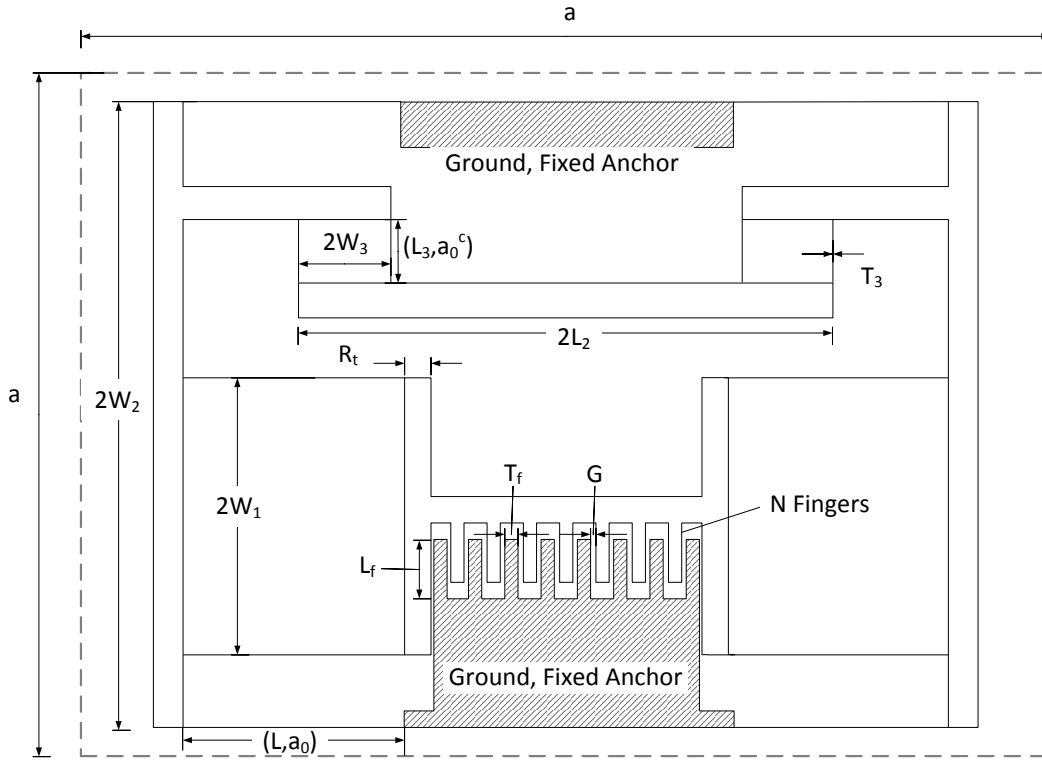


Figure 69: A CDPDP comb drive actuator layout. All rigid sections are assumed to be of the same thickness  $R_t$ .

Alternatively, one might pursue a computational approach to optimize the device dimensions with the objective of maximizing the stroke  $U_{y|_{\max}}$  for a given footprint. Most of the constraints listed here have already been discussed in the previous section. When the device layout is defined, we can analytically obtain the expression for the footprint of the device. For the layout shown in Figure 69, we have:

$$A = 2 \left( L + 2R_t + N(T_f + G) + T_f + 2G \right) \times \left( 2W_2 + 0.5U_{y|_{\max}} \right) \quad (5.29)$$

It is interesting to see that the footprint of the device also includes the area occupied at maximum stroke and therefore, the  $y$  dimension of the device footprint is  $(2W_2 + 0.5U_{y|_{\max}})$ . If the device allowed for bi-directional actuation, this dimension would have become  $(2W_2 + U_{y|_{\max}})$ . If the maximum allowable footprint of the device is  $axa$ , we can impose individual constraints on the dimensions of the device i.e.

$$2(L + 2R_t + N(T_f + G) + T_f + 2G) < a \quad (5.30)$$

$$(2W_2 + 0.5U_y |_{\max}) < a \quad (5.31)$$

Fabrication and testing capabilities would impose the following constraints on the voltage, gap size and the thickness of the beams:

$$V < 150 \quad (5.32)$$

$$G, T > 2\mu m \quad (5.33)$$

The beam separations  $W_1$  and  $W_2$  are related to length of the clamp parallelograms  $L_3$  as follows:

$$2W_2 > 2W_1 + L_3 + 2R_t \quad (5.34)$$

The dimensions of the individual comb fingers are governed by the following relations:

$$L_f > (U_y |_{\max} + U_{y0}) \quad (5.35)$$

$$T_f \geq \left( 2 \frac{\varepsilon L_f^4}{EG^3} V^2 \right)^{\frac{1}{3}} \quad (5.36)$$

The objective function i.e. the stroke of the device can be numerically obtained by solving equation (1.7) with  $L_{off} \approx L_f$  and stiffness expressions given by (Assuming  $H=H_3$  and  $T=T_3$ ):

$$K_y = \frac{EI_{zz}}{L^3} \left( 2k_{11}^{(0)}(a_0) + 1.5\gamma k_{11}^{(1)}(a_0) \left( \frac{U_y}{L} \right)^2 \right), \gamma = k_{11}^{(0)}(a_0^c) k_{11}^{(1)}(a_0) \left( \frac{L^3}{4L_3^3} \right) \quad (5.37)$$

$$K_x = \frac{EI_{zz}}{L^3} \frac{1}{\left( \frac{1}{2k_{33}} + \frac{U_y^2}{8L^2} \left( -k_{11}^{(2)} + \frac{2(k_{11}^{(1)})^2}{(\eta + 2k_{11}^{(0)})} \right) \right)}, \eta = 6 \frac{W_3^2 L^3}{a_0^c L_3 L_2^2 T^2} \quad (5.38)$$

And the rotational stiffness given by equation (5.23). Finally, the  $Y$  direction equilibrium relation given by equation (1.17) imposes a constraint on the motion direction stiffness  $K_y$ . Obviously, the constraints on the thickness of the stages and the rigid sections do not directly affect the above problem and hence, can be separately satisfied. Because of the

coupled nature of the equations presented above, the problem might be computationally very intensive to solve and hence, the application requirements have to be carefully considered to warrant the use of this approach.

In most cases, the simplified iterative procedure provided before would suffice and that is what we employ for designing devices for testing and validation. However, if we have a multi-axis system or additional objectives such as maximizing the resonant frequency as well, then we might have to use the more rigorous computational approach.

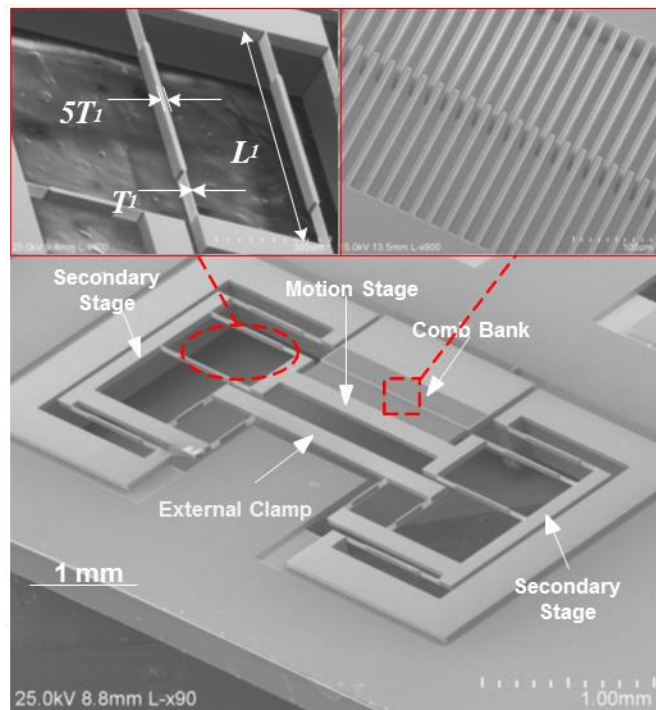


Figure 70: SEM image of a micro-fabricated comb-drive actuator employing the C-DP-DP flexure[32].

The fabrication and testing of the devices designed using the iterative procedure (steps 1 to 11) was carried out separately and is not a contribution of this thesis [32]. A fabricated CDPDP comb drive actuator is shown in Figure 70. Here, we merely present the results in Table 8 which validate the analytical predictions. The measured stroke of conventional DPDP flexure with these dimensions and  $a_0 = 0.5$  was  $50 \mu\text{m}$ . Referring to Table 8, this indicates that  $S = 1$  is a reasonable stability margin to use for the DPDP flexure and the

micro-fabrication process described above. The measured stroke increases to 119  $\mu\text{m}$  for a CDPDP flexure with the same dimensions as the previous DPDP flexure. This stroke was further increased to 141  $\mu\text{m}$  by using reinforced beams with  $a_0=0.2$ , while keeping all other dimensions the same. This stroke is 2.82 times higher than the DPDP flexure, which highlights the superior performance of the reinforced CDPDP flexure compared to the traditional DPDP flexure. In last two cases, Table 8 indicates that  $S = 1$  or 1.5 may not be an adequate stability margin when  $G$  is small (3  $\mu\text{m}$ ) and actuation voltage are relatively higher ( $> 90\text{V}$ ).

As shown previously, the stroke of comb drive actuator can be further improved by increasing the comb gap  $G$ . This is also demonstrated in Table 8, where stroke of 215  $\mu\text{m}$  was obtained using a CDPDP flexure with beam length of 1 mm, comb gap of 4  $\mu\text{m}$ , and  $a_0=0.2$ . The benefit of beam reinforcement is also evident here. With an identical design, the experimentally measured stroke is 170  $\mu\text{m}$  and 157  $\mu\text{m}$  for  $a_0=0.3$  and  $a_0=0.4$ , respectively. Finally, a large stroke of 245  $\mu\text{m}$  at 120V was obtained for a CDPDP flexure with beam length of 1 mm,  $a_0=0.2$ , and comb gap of 6  $\mu\text{m}$ .

In the last four designs, given the larger comb-gap, a stability margin of  $S = 1$  or 1.5 appears to be adequate. In fact, an even smaller stability margin may also be considered because, in these cases, the experimentally measured stroke was limited due to a Y direction pull-in as opposed to the X direction snap-in considered in the design procedure.

Table 8: Comb-drive actuators that were designed, fabricated, and tested. All dimensions are in micrometers.

Flexure Design	G	T <sub>r</sub>	N	L <sub>r</sub>	T	L	L <sub>2</sub>	L <sub>3</sub>	W <sub>1</sub>	W <sub>2</sub>	W <sub>3</sub>	H	a <sub>0</sub>	Predicted/Designed Stroke			Measured Stroke	Voltage at Stroke (V)
														S=0	S=1	S=1.5		
<b>DP-DP</b>	3	6	50	150	4	1000	--	--	400	250	--	50	0.5	59	50	47	50	85
<b>C-DP-DP</b>	3	9	80	210	4	1000	1000	430	790	250	240	50	0.2	228	191	181	141	95
<b>C-DP-DP</b>	3	7	80	180	4	1000	1000	430	790	250	240	50	0.5	164	138	130	119	90
<b>C-DP-DP</b>	4	8	70	240	3	1000	1000	430	810	250	240	50	0.2	272	230	218	215	104
<b>C-DP-DP</b>	4	7	70	210	3	1000	1000	430	790	250	240	50	0.3	224	188	178	170	91
<b>C-DP-DP</b>	4	7	70	190	3	1000	1000	430	780	250	240	50	0.4	202	169	160	157	91
<b>C-DP-DP</b>	6	8	100	290	3	1000	1500	430	875	300	360	50	0.2	341	287	271	245	119

The symmetrical  $K_x/K_y$  stiffness profile of the CDPDP mechanism allows bi-directional actuation, and therefore twice the actuation stroke ( $\sim 500 \mu\text{m}$ ) for approximately the same device footprint and actuation voltage. For unidirectional operation, the stroke can further be improved by pre-bending the beams of a CDPDP flexure. Compared to the DPDP case, here the maximum pre-bend limit is much higher, while maintaining  $S=1$  (Refer to Appendix E for the derivation):

$$U_{ypr} \approx \sqrt{\frac{4GL}{\sqrt{-k_{11}^{(0)}k_{11}^{(2)}}}} \quad (5.39)$$

For typical dimensions ( $L=1 \text{ mm}$ ,  $G=3 \mu\text{m}$ ,  $a_0=0.2$ ), this allowable pre-bend is as large as  $400 \mu\text{m}$ , which in theory could lead to a  $Y$  displacement of approximately  $500 \mu\text{m}$  at snap-in. Thus, ultimately the flexure and the comb drive may be designed such that the actuation stroke is limited by the material failure criteria or the available actuation voltage, instead of sideways snap-in instability.

### Stroke Comparison

While a direct comparison of the actuation stroke with previously reported comb-drive actuators is tricky because of the many variables (beam length, comb gap, maximum voltage, device footprint, etc.) and specific application based constraints involved, we present a simple analytical basis that provides some level of comparison.

At large displacements, we can approximate the bearing direction stiffness of the CDPDP mechanism by equation (5.27). With this stiffness, equation (5.24) can be rewritten as:

$$(U_{y|_{\max}})^3 = \left(\frac{\varepsilon}{E}\right) \left(6 \sqrt{\frac{-2}{(k_{11}^{(0)})^3 k_{11}^{(2)} (1+S)}}\right) (NV_{\max}^2) \left(\frac{L}{T}\right)^3 L \quad (5.40)$$

Here  $S$  is no longer assumed to be 1 instead, it is retained as a function of the error motions  $E_x$ , given in (1.16). It can be separately shown that for most flexure mechanisms based on the parallelogram module (e.g. P, DP-DP, C-DP-DP, etc.) that are used in comb-drive actuation, a relation analogous to the above equation can be derived. However, for devices with pre-bend, the above relation has to be revised. We can still neglect the elastic stiffness term ( $1/k_{33}$ ) w.r.t. the elasto-kinematic term to obtain a relation similar to that in equation (5.27) (Appendix EAppendix E):

$$K_x \approx \left(2 \frac{EI_{zz}}{L^3}\right) \frac{-4L^2}{(U_{y|_{\max}} - U_{ypr})^2 k_{11}^{(2)} (a_0)} \quad (5.41)$$

Thus, equation (5.40) can be rewritten as:

$$U_{y|_{\max}} (U_{y|_{\max}} - U_{ypr})^2 = \left(\frac{\varepsilon}{E}\right) \left(6 \sqrt{\frac{-2}{(k_{11}^{(0)})^3 k_{11}^{(2)} (1+S)}}\right) (NV_{\max}^2) \left(\frac{L}{T}\right)^3 L \quad (5.42)$$

The goal is to maximize the left hand side of the equation for a fixed set of device and material parameters  $N$ ,  $V$ ,  $L$ ,  $T$ ,  $\varepsilon$  and  $E$ . This implies comparing the second non-dimensional term on the right hand side of the above expression which entirely captures the flexure stiffness and error motion properties. As all of the devices that we are considering are silicon based and operated in air, the permittivity and young's modulus do not vary significantly and hence are included in the second term. Thus, in figure, we plot  $(U_{y|_{\max}} (U_{y|_{\max}} - U_{ypr})^2)^{1/3}$  vs  $(NV_{\max}^2 L^4 / T^3)^{1/3}$  for in-plane comb-drive actuators reported in previous literature. The performance of a given device can be estimated by

comparing the slope that it makes at the origin of the plot. The Figure 79 shows a significant performance improvement offered by the CDPDP mechanism.

### **DP-TDP Optimization**

For this device, we would consider a layout shown in Figure 71 similar to that used for the CDPDP actuator in the previous section. As before, we can use the rigorous numerical optimization method to come up with the dimensions of the device. As mentioned before, this mechanism exhibits finite error motions and hence, none of the simplified snap-in conditions (equations(1.6), (1.7) and (1.14)) can be used in this case. Therefore, we would have to resort to using the numerical solution procedure summarized in chapter 1 (equations) to obtain the stroke at snap-in. Moreover, we would have to include finite element analysis in the optimization loop as well to calculate the stiffness and error motions of the mechanism for every set of parameters ( $W_1, W_2, \alpha, \beta, T, a_0, L$ ). Needless to say, this increases the complexity of the problem several fold. A closed form parametric solution for the characteristics of the flexure mechanism can simplify the solution procedure significantly.

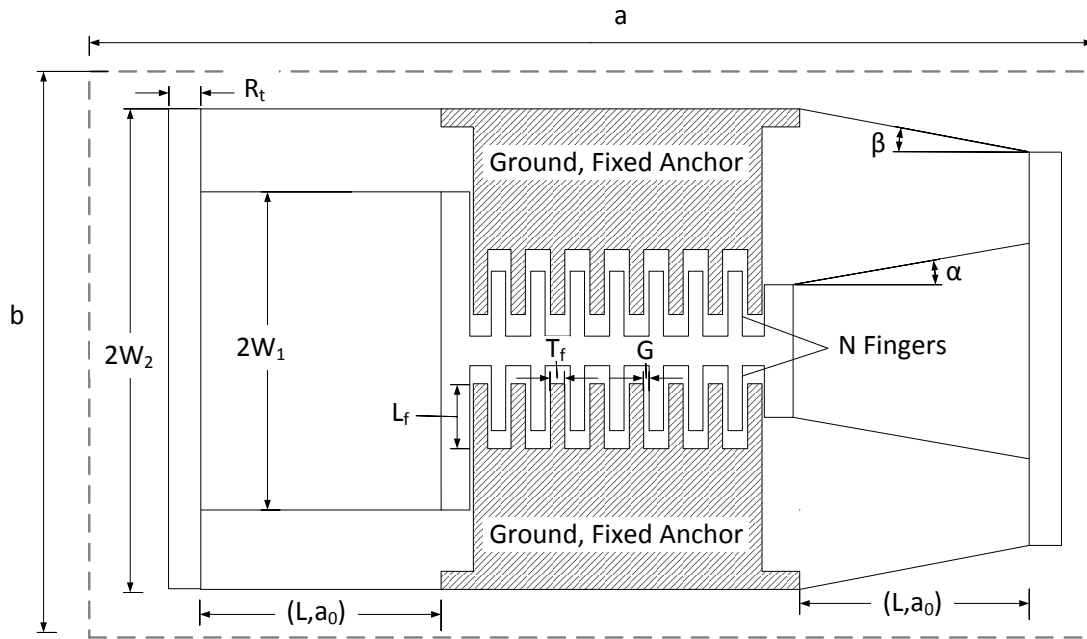


Figure 71: The DP-TDP comb drive actuator layout

We would not pursue the above approach here but use a fairly simplified graphical method to arrive at an approximate solution. Only the tilt angles  $\alpha$  and  $\beta$  are chosen as variables and the rest of the dimensions of the flexure are the same as those considered in chapter 4. Thus, we can directly use the FEA plots of stiffness and error motions from the same discussion in the design of this actuator. From these results, we previously concluded that a value of  $\alpha$  close to  $\beta$  would give the best characteristics of the mechanism. In this section, we take this a step further and with appropriate approximations, converge on values of  $\alpha$  and  $\beta$  that give near-optimal performance i.e. a large stroke for low actuator effort. To begin, we choose a sector around the  $\alpha=\beta$  line such that the  $x$ -error motions are less than the gap size. This sector is the shaded region shown in the contour plot (Figure 72) of Figure 38 for a gap size of  $5 \mu\text{m}$ .



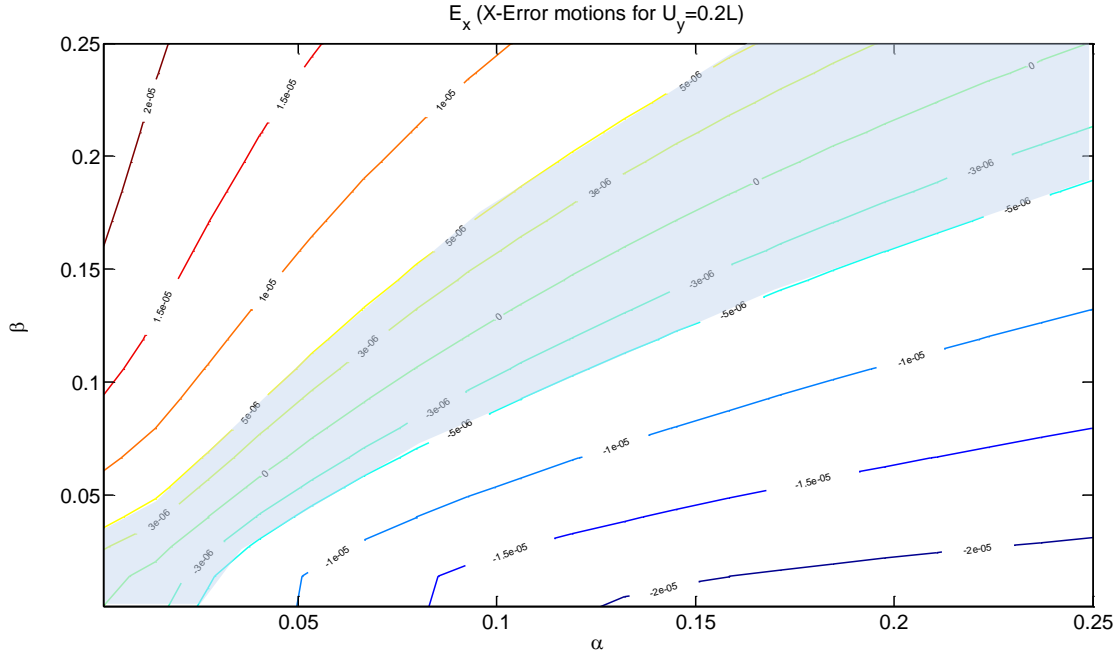


Figure 72: Contour plot of  $E_x(m)$  for the DP-TDP mechanism. The tilt angles are in radians.

Inspecting Figure 72, Figure 73, Figure 74 and Figure 75, we can further narrow down the optimal space to  $\alpha, \beta > 0.1$ . In this region, Figure 73 shows that  $E_{\theta} \leq 0.0005$ . Assuming  $L_f$  and hence  $L_{off}$  for the layout shown in Figure 71 to be around  $200 \mu\text{m}$ , we find that  $L_{off} E_{\theta} \leq 0.1 \mu\text{m}$  which is much smaller ( $< 2\%$ ) in comparison to the gap size. Referring to equations (1.9) and (1.10), this implies that we can neglect the effect of the rotational error motions on the snap-in conditions. Moreover, Figure 76 shows that the ratio between  $K_{\theta}$  and  $K_x L_{off}^2$  is always greater than 5 in the feasible space and hence, for the first iteration we can use a purely one dimensional model for snap-in. We can thus, directly plot (Figure 77) the metric given in equation (1.18) i.e.  $K_x / (I + S) K_y^3$  and choose the configuration corresponding to the maxima in the plot. The maximum occurs at  $\alpha = 0.14$  and  $\beta = 0.17$  radians. For these dimensions, the stroke obtained is around 154 microns.

Beyond this point, we can redraw plots for the error motions and stiffness at  $U_y = 154$  microns and obtain new values of the tilt angles and subsequently the updated stroke. We

can then repeat the process till we converge on a set of tilt angles and the corresponding stroke. Moreover, we can use the one dimensional snap-in model for the subsequent iterations as well as none of the assumptions get violated in this displacement range. For these dimensions, the optimal tilt angles obtained before do not change significantly in the subsequent iterations.

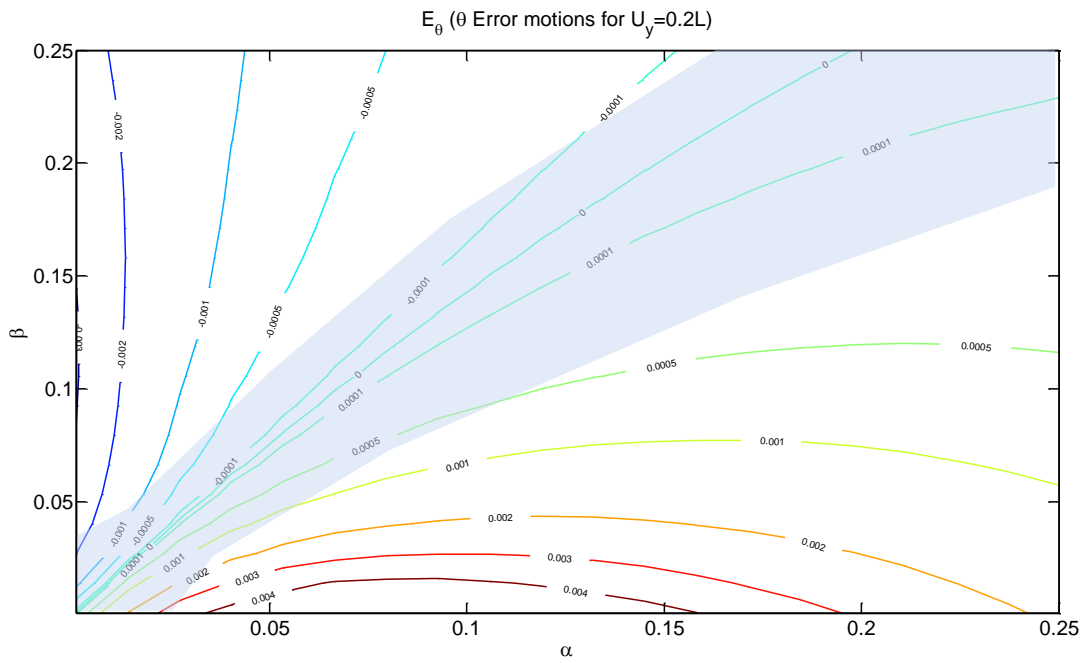


Figure 73: Contour plot of  $E_\theta$ (in radians) for the DP-TDP mechanism.

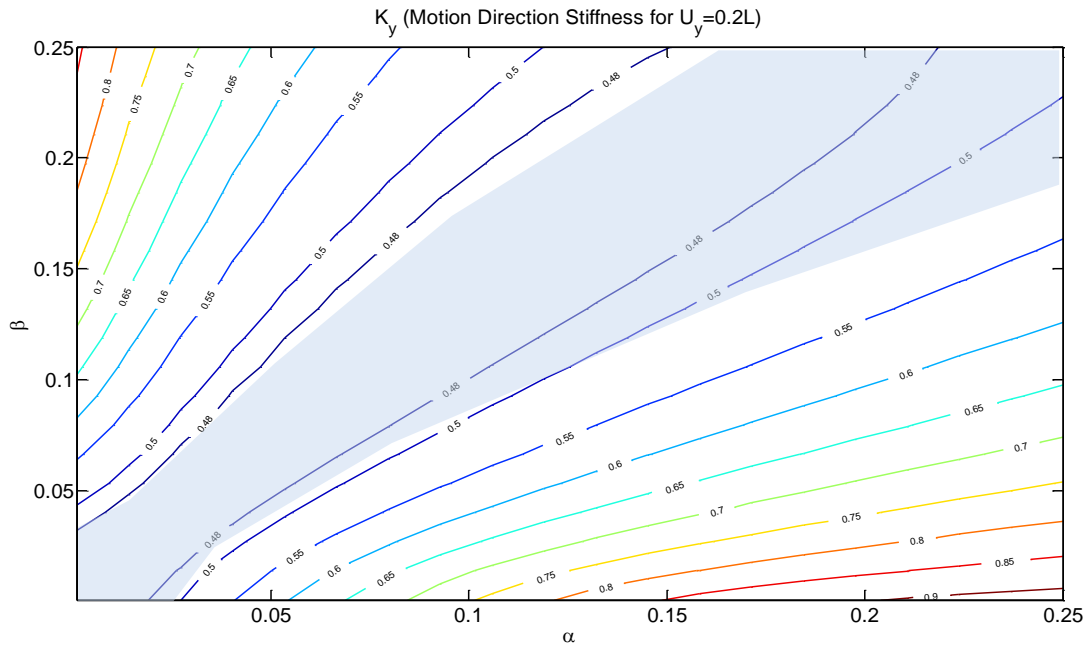


Figure 74: Contour plot of  $K_y$  (in N/m) for the DP-TDP mechanism.

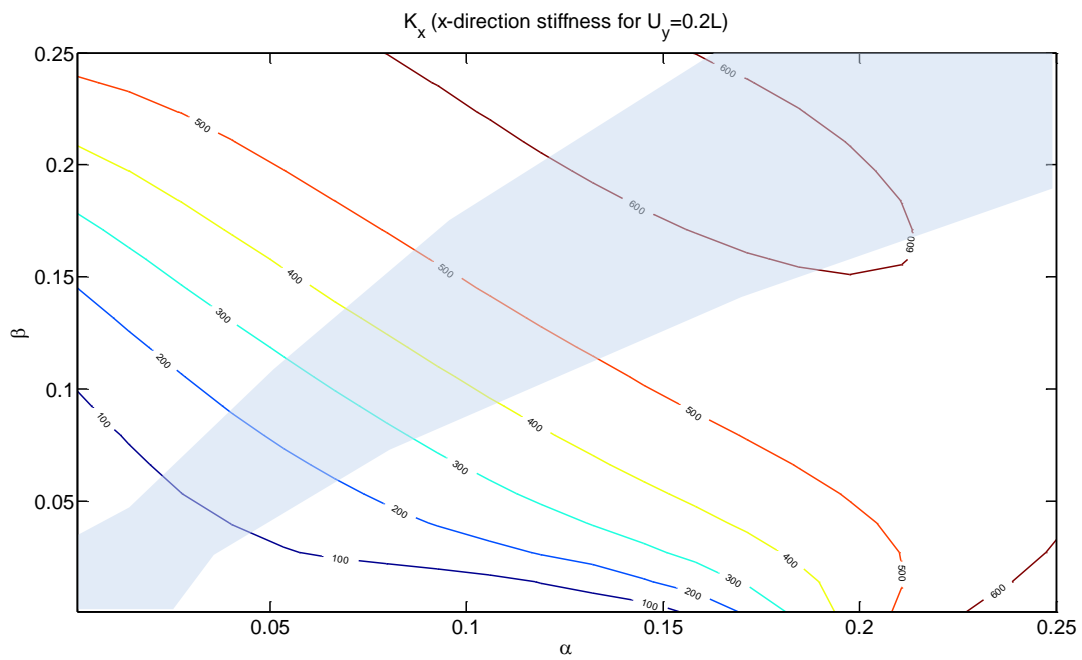


Figure 75: Contour plot of  $K_x$  (in N/m) for the DP-TDP mechanism.

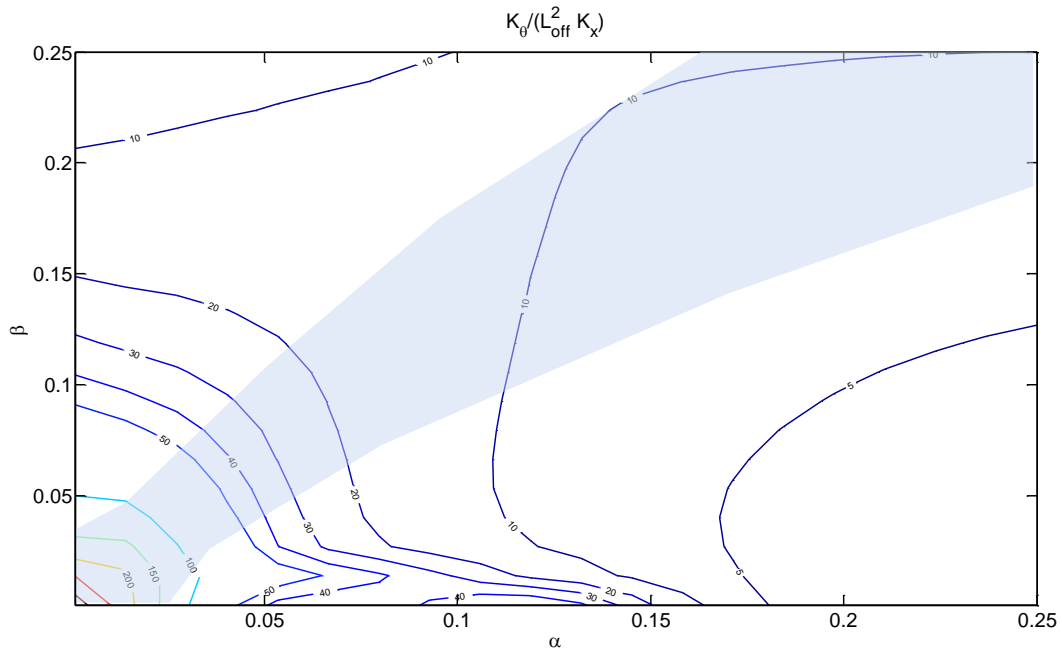


Figure 76: Contour plot of  $K_\theta / (K_x L_{off}^2)$  for the DP-TDP mechanism.

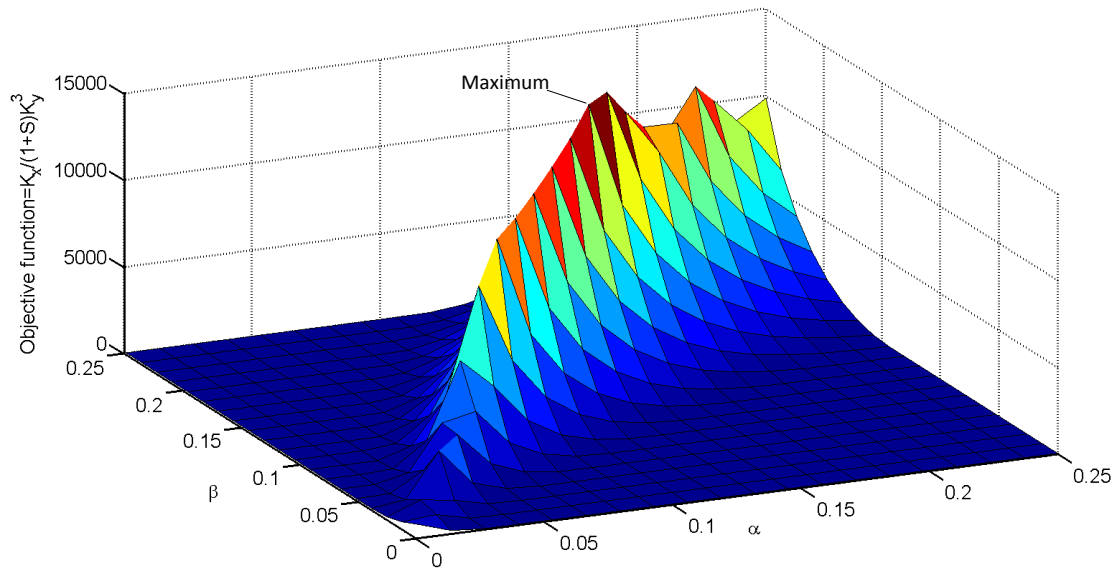


Figure 77: Plot of the objective function for  $U_y = 0.2L$ . The maximum occurs at  $\alpha = 0.14$ ,  $\beta = 0.17$ . The  $(1+S)$  used here is simply the theoretical factor due to axial error motion ( $E_x$ ) and does not include the effect of imperfections

For the actual devices that were fabricated and tested in [36], tilt angles were chosen as  $\alpha=0.11$  and  $\beta=0.14$ <sup>11</sup> while keeping all other dimensions the same as before. The predicted stroke with these dimensions is 141 microns which is not significantly different from that obtained with  $\alpha=0.14$  and  $\beta=0.17$ . The measured actuation stroke at snap-in for the conventional DP-DP flexure with the above dimensions was 75  $\mu\text{m}$  at 45 volts. The actuation stroke for a DP-TDP flexure with the same dimensions was measured to be 125  $\mu\text{m}$  at 70 volts. As expected, an even higher stroke of 149  $\mu\text{m}$  was measured for a DP-TDP flexure with the same overall dimensions but using reinforced beams ( $a_0 = 0.2$ ). On comparison with the predicted actuation stroke (Table 9), these experimental measurements also show that for the DP-DP flexure because of symmetry, a stability margin of  $S = 0$  is acceptable. However, because of asymmetry in the DP-TDP maintaining a stability margin of  $S = 1$  is necessary.

*Table 9: Comb-drive actuators that were micro-fabricated and tested. Comb-drive dimensions are same in all cases:  $G = 5 \mu\text{m}$ , comb-finger length  $L_f = 190 \mu\text{m}$ , in-plane thickness  $T_f = 6 \mu\text{m}$ , out-of-plane thickness  $H_f = 50 \mu\text{m}$ , and  $N = 70$ . Flexure beam length  $L = 1000 \mu\text{m}$  and in-plane thickness  $T = 3 \mu\text{m}$  in all cases. All dimensions are in microns.*

Flexure Design	$W_1$	$W_2$	$a_0$	Designed Stroke		Measured Stroke	Voltage (V)
				$S=0$	$S=1$		
<b>DP-DP</b>	450	250	0.5	76.7	54.2	75	45
<b>DP-TDP</b>	525	325	0.5	141	122	125	70
<b>DP-TDP</b>	525	325	0.2	178	156	149	86

---

<sup>11</sup> These values were obtained with a coarser mesh of  $\alpha$  and  $\beta$

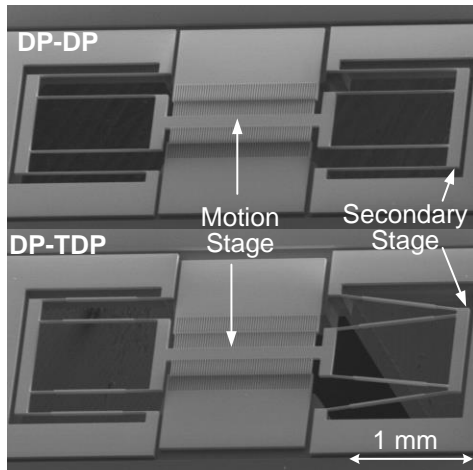


Figure 78: SEM image of micro-fabricated comb-drive actuators based on the DP-DP and DP-TDP flexures.

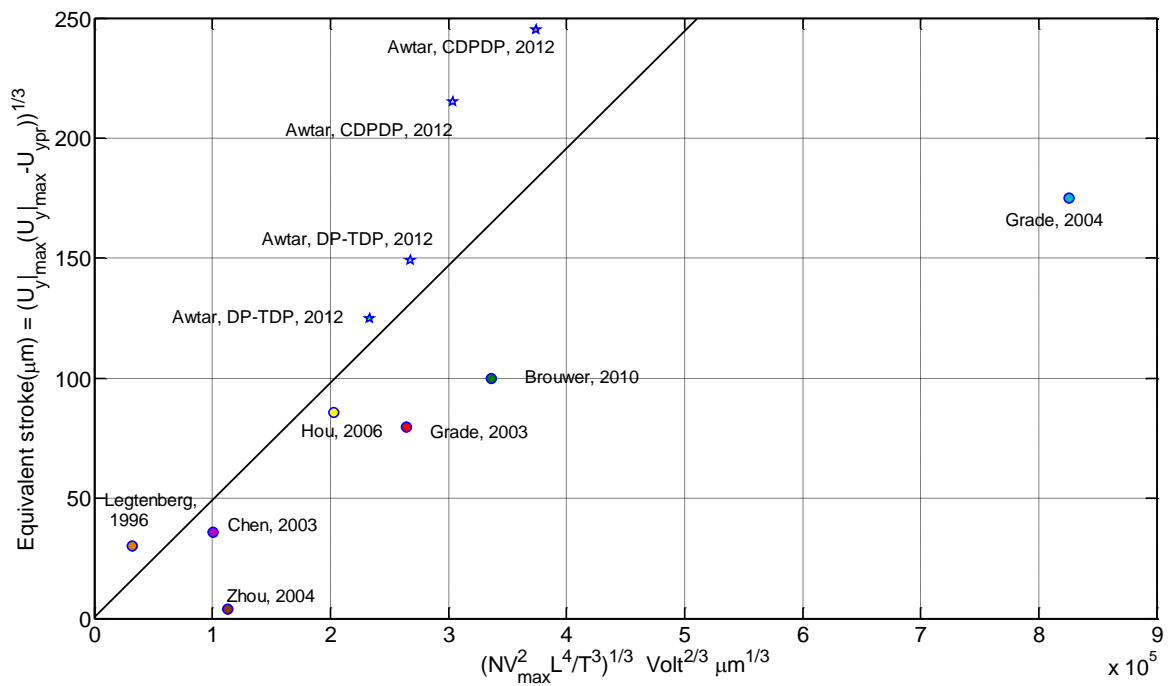


Figure 79: Performance comparison between different comb drive actuators. The references are as follows:  
 Legtenberg, 1996 [33], Chen, 2003 [66], Grade, 2003 [34], Grade, 2004 [67], Zhou, 2004 [37],  
 Hou, 2006 [68], Brouwer, 2010 [54], Awtar, CDPDP 2012 [32], Awtar, DP-TDP [36]

The performance of these devices is also compared with other comb drive designs in Figure 79 which shows the improvement offered by the DP-TDP mechanism. It also shows that the CDPDP mechanism performs marginally better than this mechanism. However, the DP-TDP mechanism offers some other advantages compared to the CDPDP mechanism – a much smaller footprint and bi-directional access to the motion stage. With bi-directional actuation, the net range of motion of this mechanism is twice that for the unidirectional actuation i.e. about 300  $\mu\text{m}$ . With this stroke, the DP-TDP mechanism can perform almost as well as the CDPDP comb drive actuator where it might be difficult to do bi-directional actuation. As before, we can improve the stroke in a particular direction by pre-bending the beams.

In this section, we looked at how using very simple graphical techniques, we were able to optimize the DP-TDP mechanism for obtaining a large stroke. Obviously, this isn't a global optimum but with this approach we could show the relative improvement offered by this mechanism over existing designs. It should be noted that this process was also assisted by some favorable characteristics of the mechanism like small theta error motions and large rotational stiffness in the region of interest. This might not be true for other designs in the future and therefore there is a need to devise parametric and compact criteria for a generalized snap-in as opposed to the numerical approach described in chapter 1.

## Chapter 7: Conclusions and Future Work

### Contributions

The specific contributions of this thesis are summarized below:

1. Development of metrics for comparison of the bearing behavior of single axis planar flexure mechanisms. These were the range of motion, error motions, the motion direction stiffness and the bearing direction stiffness. These offer estimates of only the static or quasi-static performance of the flexure mechanism with scope for incorporating additional metrics for the dynamic performance without reformulating the existing ones. A bearing is said to *perform* well if it offers a large range of motion, small or negligible error motions, small motion direction stiffness and large bearing direction stiffness. Moreover, some applications such as comb drive and voice coil actuators were discussed where these quantities directly affect the behavior of the devices.
2. These metrics were then quantified for some existing flexure mechanism i.e. the parallelogram (P), double parallelogram (DP) and lever double parallelogram (L-DP) for which some additional results were derived based on the existing beam constraint model. These include expressions for the yield criterion of a flexure which limits the range of motion and derivation of the error motion and stiffness characteristics from the force displacement relations derived previously. Where force-displacement relations were not available like in the case of the L-DP mechanism, a qualitative analysis of the performance metrics was done using extensive FEA analysis for various configurations and dimensions of the mechanism.



3. Some variations of these flexure mechanisms were also discussed which do not alter the overall topology of the mechanism like the reinforced beam flexure and the multi-beam parallelogram. Wherever necessary, additional results were derived for the metrics of the mechanisms which incorporate these variations. Moreover, the influence of these modifications on the metrics is also examined to come up with criteria that can further boost the performance of the mechanism.
4. The non-linear strain energy formulation for flexure mechanism that is consistent with the beam constraint model was also revisited for the existing mechanisms. An algorithm was developed to simplify the total strain energy expression for these mechanisms based on order of magnitude estimates, which were obtained using the BCM model and/or finite element analysis for the displacement and dimensional variables involved. This was done in a manner that preserves the force displacement relations that one obtains by applying the principle of virtual work on the actual strain energy expression. This algorithm was then applied to the two-beam and the multi-beam parallelograms to obtain the exact same expressions that were derived using the BCM model.
5. Force-displacement relations for the CDPDP mechanism were derived using the direct BCM model. Appropriate assumptions were made wherever required with justifications to simplify the solution procedure. The obtained relations agreed with finite element predictions for a wide range of dimensions. The sources for any discrepancies were also identified and some measures were suggested which could be used to eliminate them. The relations were extended to incorporate beam reinforcement and multi-beam parallelograms. Finally, some guidelines were laid out for choosing the dimensions of the mechanism in order to obtain optimum performance.

6. The characteristics of the DP-TDP mechanism were discussed qualitatively using finite element analysis in a manner analogous to that for the L-DP mechanism. The difficulties that might be encountered while trying to obtain a closed form parametric solution were also discussed. Some critical dimensions of the mechanism were identified and were used in the parametric FEA. Based on the results, some estimates were made for the optimum choice of these dimensions to obtain the best possible performance.
7. Detailed design, fabrication, assembly and testing of a low cost, reconfigurable and high precision setup to directly measure the properties of the CDPDP mechanism in order to validate the force displacement relations derived before was discussed. One of the possible configurations is the DPDP mechanism and therefore, using the same setup, one could show the performance improvement offered by the CDPDP mechanism. A complete error analysis was done to examine the effect of fabrication imperfections and measurement uncertainties on the stiffness and error motions of the mechanism.
8. As a case study, systematic methods to design a flexure mechanism as a motion guide for a comb drive actuator were laid out with the objective of maximizing the stroke for given footprint and voltage specifications. With the analytical framework for the CDPDP mechanism already presented, the design approach for the CDPDP mechanism was more detailed and deterministic. However, for the DP-TDP mechanism, due to the lack of parametric results for the stiffness and error motions, only a first-pass analysis was done with only a few dimensions chosen as the variables while others chosen almost arbitrarily at the onset of the procedure. MEMS comb drive actuators based on the device designs obtained from these procedures were then fabricated and tested as a part of a separate

project by Dr. Mohammad Olfatnia<sup>12</sup>. It was found that the CDPDP flexure offered a very large stroke of 245 microns and the DP-TDP gave a stroke of 145 microns which are about 5 and 3 times respectively larger than that given by the DPDP mechanism for the same dimensions.

9. A need for a reliable metric for the comparison of the performance of different flexure mechanisms in a comb drive actuator was soon identified. Thereafter, a metric was defined which offers a good measure of comparison between the flexure mechanisms that have been considered in this thesis. Based on this metric, it was found that the CDPDP and the DP-TDP mechanisms offer significantly improved performance over the previously reported comb drive devices. Moreover, the CDPDP mechanism performs marginally better than the DP-TDP mechanism. However, the DP-TDP mechanism makes up for this shortcoming by offering a lower footprint and bi-directional access to the motion stage, which might not be possible in the CDPDP mechanism.

### **Future Work**

In this thesis, it was shown how some valuable insights into the nature of a mechanism can enable us to make some approximations which can significantly simplify the equations describing the characteristics of the mechanism thereby making closed form solutions possible in many cases. A theoretical framework has been created which allows for a lot of scope for future work in this area. Some of the foreseeable work that can be done to improve upon or extend the ideas that have been presented in this thesis is listed below:

1. A metric for the dynamic behavior of flexure mechanisms has to be created which could incorporate resonant frequencies, modes and structural damping. For comb-

---

<sup>12</sup> Department of Mechanical Engineering, University of Michigan, Ann Arbor

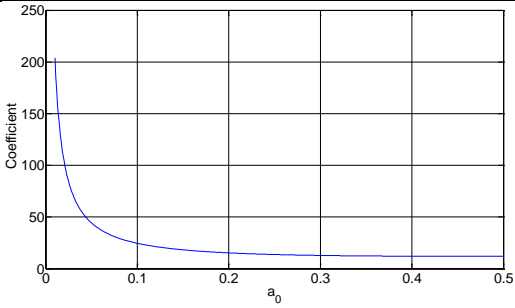
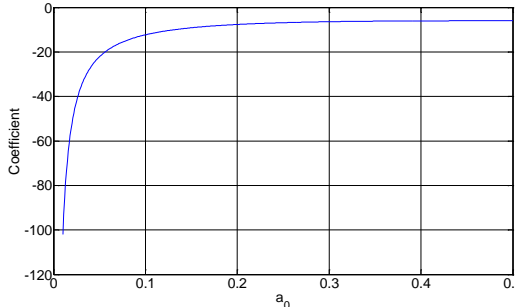
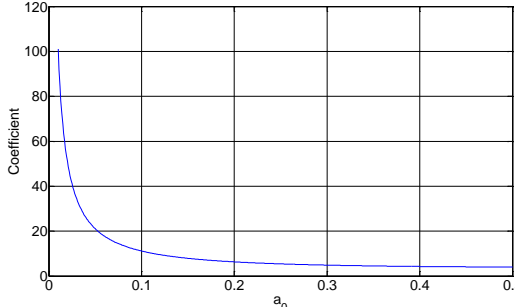
drive actuators this would give a measure of the bandwidth of the device. Obviously, there is a direct tradeoff between bandwidth and stroke, and with this metric in place, we could do a multi-objective optimization to maximize the stroke *and* the bandwidth instead of just the stroke like we did in chapter 6.

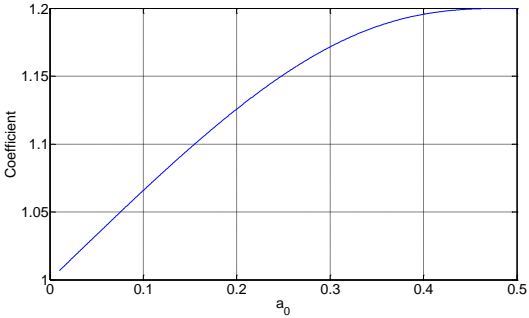
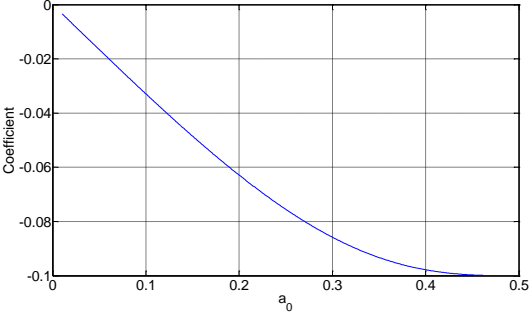
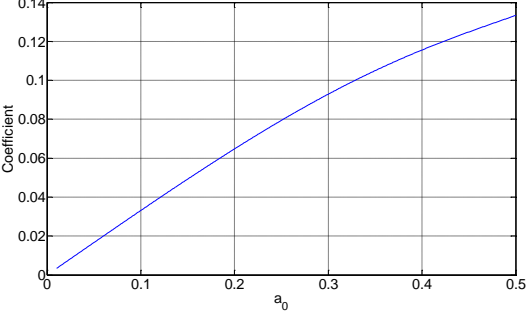
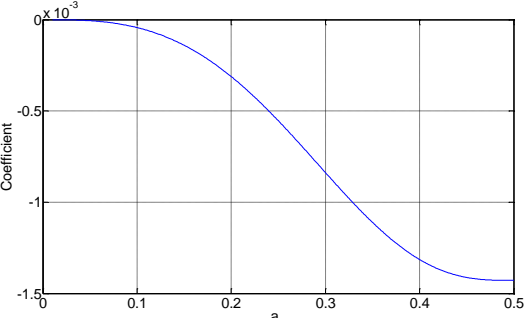
2. Closed form solutions for the system of equations obtained for the DPDP and the CDPDP mechanisms by applying the principle of virtual work could be obtained by applying further approximations on the strain energy expressions for each of these mechanisms. Also, instead of using the parallelogram as the building block, one could use the double parallelogram mechanism as a higher level block for more complex mechanisms. Unlike the parallelogram, the double parallelogram would be a two input-one output block where the two inputs would be forces at the primary and the secondary stages and the output would be the displacement at the primary stage. This would mean that the strain energy would be a function of the forces at the secondary stage and the displacements at the primary stage. Alternatively, one could use the principle of complementary virtual work which would simplify the solution for serial configurations significantly. However, for parallel systems, as before, the problem would again culminate to solving a system of simultaneous multivariate polynomial equations in terms of the *force* variables which might again prove to be difficult to do in closed form. Hence, for systems which contain both serial and parallel elements, we have to come up with a hybrid solution procedure which combines elements from both the approaches.
3. An approximate closed form solution for the DP-TDP mechanism can be obtained for a narrow domain of tilt angles for which the error motions are small. In that case, the kinematic conflict between the two halves of the mechanism would be minimal and so would the internal forces and moments. This in turn would mean that the BCM relations would be valid and can be used to solve for the characteristics of the mechanism.

4. A setup similar to that used for the CDPDP mechanism can be used to validate the stiffness and error motions of the DP-TDP flexure. In fact, one could use the same measurement techniques and replace the plate containing the CDPDP mechanism with a plate carrying a different design.

## Appendix A

### BCM COEFFICIENTS AS FUNCTIONS OF BEAM REINFORCEMENT $A_0$

Coefficient t	Function	Plot
$k_{11}^{(0)}$	$\frac{6}{a_0(3-6a_0+4a_0^2)}$	
$k_{12}^{(0)}$	$-\frac{3}{a_0(3-6a_0+4a_0^2)}$	
$k_{22}^{(0)}$	$\frac{(3-3a_0+2a_0^2)}{a_0(3-6a_0+4a_0^2)}$	

$k_{11}^{(1)}$	$\frac{3(15 - 50a_0 + 60a_0^2 - 24a_0^3)}{5(3 - 6a_0 + 4a_0^2)^2}$	
$k_{12}^{(1)}$	$\frac{-a_0(15 - 60a_0 + 84a_0^2 - 40a_0^3)}{5(3 - 6a_0 + 4a_0^2)^2}$	
$k_{22}^{(1)}$	$\frac{a_0(15 - 60a_0 + 92a_0^2 - 60a_0^3 + \frac{40}{3}a_0^4)}{5(3 - 6a_0 + 4a_0^2)^2}$	
$k_{11}^{(2)}$	$\frac{2a_0^3(105 - 630a_0 + 1440a_0^2 - 1480a_0^3 + 576a_0^4)}{175(3 - 6a_0 + 4a_0^2)^3}$	

$k_{12}^{(2)}$	$\frac{a_0^3 (105 - 630a_0 + 1440a_0^2 - 1480a_0^3 + 576a_0^4)}{175(3 - 6a_0 + 4a_0^2)^3}$	
$k_{22}^{(2)}$	$\frac{a_0^3 \left( 105 - 630a_0 + 1560a_0^2 - 2000a_0^3 + 1408a_0^4 - 560a_0^5 + \frac{1120}{9}a_0^6 \right)}{175(3 - 6a_0 + 4a_0^2)^3}$	
$k_{33}$	$\frac{6}{a_0 t^2}$	



## Appendix B

### JUSTIFICATION AND GUIDELINES FOR APPROXIMATIONS USED IN THE DERIVATION OF THE STIFFNESS EXPRESSIONS FOR THE CDPDP MECHANISM

#### Rotational stiffness of the clamp parallelograms (Equation (4.5))

Using equation (3.35), the non-dimensional rotational stiffness for the parallelograms in the clamp would be given as:

$$K_{\theta} = \frac{EH_3 T_3^3}{12L_3} \frac{2}{\left( \frac{T_3^2}{12L_3^2} - \left( \frac{U_{xl}^2}{L_3^2} \right) k_{11}^{(2)} \right)} \quad (\text{B.1})$$

Using equation (4.9) for  $U_{xl}$  and obtaining the ratio between the elastic and the elasto-kinematic terms in the denominator:

$$\frac{\text{Elastic}}{\text{Elasto-kinematic}} = \frac{T_3^2}{12U_{xl}^2 k_{11}^{(2)}} = \frac{T_3^2}{12 \left( \frac{1}{2} k_{11}^{(1)} \left( \frac{U_y^2}{4L} \right) \right)^2 k_{11}^{(2)}} = \frac{16t_3^2}{3 \left( k_{11}^{(1)} \right)^2 k_{11}^{(2)} u_y^4} \quad (\text{B.2})$$

Using the estimates given in Table 3, this ratio comes out to be of the  $O(10^2)$  and hence, we can neglect the elasto-kinematic component.

#### Motion direction stiffness of the clamp parallelograms (equation (4.6))

Using equation (3.32), the motion direction stiffness of the clamp parallelograms can be written as:

$$K_y = \frac{EH_3 T_3^3}{12L_3^3} \left( 2k_{11}^{(0)} + k_{11}^{(1)} \left( \frac{12F_{y1} L_3^2}{EH_3 T_3^3} \right) \right) \quad (\text{B.3})$$

The force  $F_{y1}$  can be obtained using equations (4.11) and (4.20):

$$F_{y1} = \left( \frac{EHT^3}{12L^2} \right) \left( \frac{\eta f_x k_{11}^{(1)} u_y}{2(\eta + 2k_{11}^{(0)})} \right) \quad (\text{B.4})$$

Obviously, this force is largest when  $\eta = \infty$  when its value is given by:

$$F_{y1} |_{\max} = \left( \frac{EHT^3}{24L^2} \right) f_x k_{11}^{(1)} u_y \quad (\text{B.5})$$

Substituting this value in equation (B.3) and comparing the two terms, we get:

$$\frac{\text{Nominal}}{\text{Stiffening}} = \frac{2k_{11}^{(0)}}{0.5(k_{11}^{(1)})^2 f_x u_y} \left( \frac{L}{L_3} \right)^2 \left( \frac{H_3 T_3^3}{HT_3^3} \right) \quad (\text{B.6})$$

Using some typical values given in Table 3 and a value of  $L_3=0.6L$  (which does not cause appreciable stiffening in the motion direction of the entire mechanism), this ratio comes out to be of  $O(10^2)$  which implies that the stiffening term can be neglected from the motion direction stiffness.

## Appendix C

### UPPER BOUND ON THE CLAMP EFFECTIVENESS IMPOSED BY FINITE ROTATIONAL STIFFNESS OF THE DP UNITS IN THE CDPDP MECHANISM

In the derivation for the bearing stiffness of the CDPDP mechanism, we imposed no constraints on the maximum value that the effectiveness can take, assuming that we can make it arbitrarily large with  $\eta \rightarrow \infty$ . However, this is not true and we would see shortly that the maximum effectiveness of the clamp is directly related to the rotational stiffness of the DPDP unit that it is meant to constrain. This effect explains the small discrepancies between the stiffness predicted by the model and FEA (Figure 33).

The primary assumption that we made in the closed-form derivation of the bearing stiffness was that the rotational stiffness of the DP units is very large, so large that the rotation of the secondary stage is negligible compared to that of clamp ( $\theta_{z1}, \theta_{z2} \ll \theta_{z3}$ ). This is true for small values of effectiveness but fails for larger values when the rotational stiffness of the clamp becomes comparable to that of the DP units. This scenario is depicted in Figure 34.

To simplify the analysis, we assume symmetry between the two halves of the mechanism i.e.  $\theta_{z1} \approx \theta_{z2}$ . Moreover, we can say that equation (4.4) still holds approximately. Thus, rewriting equation (4.5):

$$\begin{aligned} (\theta_{z3} - \theta_{z2}) &= \frac{L_3^2}{2W_3^2} \left( \frac{a_0^c T_3^2}{6L_3^2} \right) \left( \frac{12M_{z2}L_3}{EH_3T_3^3} \right) = (\theta_{z3} - \theta_{z1}) = \frac{L_3^2}{2W_3^2} \left( \frac{a_0^c T_3^2}{6L_3^2} \right) \left( \frac{12M_{z1}L_3}{EH_3T_3^3} \right) \quad (\text{C.1}) \\ \Rightarrow M_{z1} = M_{z2} &= \frac{EH_3T_3W_3^2}{a_0^c L_3} (\theta_{z3} - \theta_{z1}) \end{aligned}$$

Now, the moment  $M_{z1}$  applied on the secondary stage results in a rotation  $\theta_{z1}$ . The rotational stiffness of the secondary stage with the primary stage constrained is simply

given as the sum of the rotational stiffness of the outer and the inner parallelograms of the DP unit i.e.

$$\left( \left( \frac{L^2}{2W_1^2} \left( \frac{T^2 a_0}{6L^2} - k_{11}^{(2)}(a_0) \left( \frac{U_{y1}}{L} \right)^2 \right) \right)^{-1} + \left( \frac{L^2}{2W_2^2} \left( \frac{T^2 a_0}{6L^2} - k_{11}^{(2)}(a_0) \left( \frac{U_{y1}}{L} \right)^2 \right) \right)^{-1} \right) \theta_{z1} \approx \left( \frac{12M_{z1}L}{EHT^3} \right) \quad (C.2)$$

Assuming that the clamp constrains the  $Y$ -displacement of the secondary stages to close to half that of the primary stage i.e.  $U_{y1} \approx 0.5U_y$ , we can rewrite the above equation:

$$\theta_{z1} \approx \left( \frac{3M_{z1}L}{EHT^3} \right) \left( \left( \frac{1}{W_1^2 + W_2^2} \right) \left( \frac{T^2 a_0}{3} - k_{11}^{(2)}(a_0) \frac{U_y^2}{2} \right) \right) = \kappa M_{z1} \quad (C.3)$$

Substituting this relation in equation (C.1), we get:

$$M_{z1} = \frac{\left( \frac{EH_3 T_3 W_3^2}{a_0^c L_3} \right)}{\left( 1 + \kappa \frac{EH_3 T_3 W_3^2}{a_0^c L_3} \right)} \theta_{z3} \quad (C.4)$$

Finally, using equations (4.3) and (4.4) while neglecting the contribution of  $F_{x1}$ , we get:

$$F_{y1} = \frac{\left( \frac{EH_3 T_3 W_3^2}{a_0^c L_3} \right)}{\left( 1 + \kappa \frac{EH_3 T_3 W_3^2}{a_0^c L_3} \right)} \frac{(U_{y2} - U_{y1})}{2L_2} \quad (C.5)$$

$$\Rightarrow f_{y1} = \eta_{eff} (u_{y1} - u_{y2}), \eta_{eff} = \frac{\left( \frac{EH_3 T_3 W_3^2}{a_0^c L_3} \right)}{\left( 1 + \kappa \frac{EH_3 T_3 W_3^2}{a_0^c L_3} \right)} \left( \frac{6L^3}{EHT^3 L_2^2} \right)$$

This shows that as we make the rotational stiffness of the clamp very large, the actual effectiveness becomes proportional to the ratio  $1/\kappa$  which is the rotational stiffness of the DP units at the secondary stage. Figure 80 shows the comparison between the FEA and the theoretical values with the revised expression for effectiveness (equation (C.5)) for

the same dimensions used for the case shown in Figure 33. The error between the two is less than 5% at a normalized  $y$  displacement of 0.15 for different values of effectiveness.

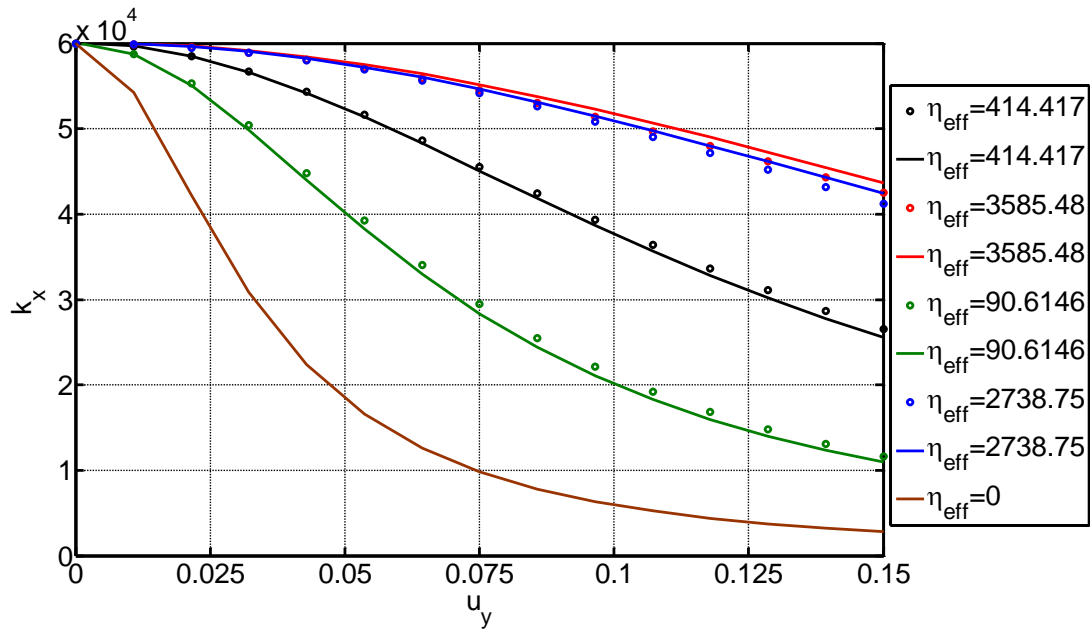


Figure 80: Bearing stiffness of the CDPDP mechanism with a revised value of effectiveness.  $w_1=0.3$ ,  $w_2=0.2$ ,  $l_2=0.9$ ,  $t=1/50$ ,  $h=h_3$

## Appendix D

### NOTES ON THE CENTER OF STIFFNESS OF THE CLAMPED PAIRED DOUBLE PARALLELOGRAM MECHANISM

#### Location of the COS

The CDPDP mechanism with a possible offset between the centers of the primary and secondary stages, shown in figure is used for this analysis. In order to simplify the analysis, we would only consider the case of a near-ideal clamp such that  $U_{y1}=U_{y2}\approx 0.5U_y$ . With this assumption, we can remove the clamp from figure and replace it with appropriate forces (given by equation (3.69) for a DPDP mechanism) and moments given by:

$$\begin{aligned} f_{y1} &= u_y k_{11}^{(1)} f_{x11} \\ m_{z1} &= f_{y1} \end{aligned} \quad (D.1)$$

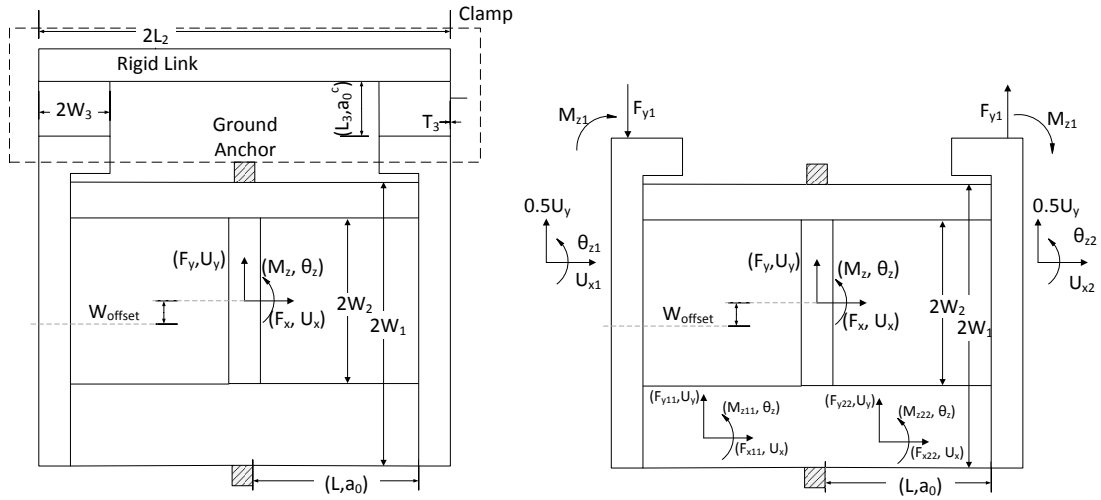


*Figure 81: The simplified model of a near-ideal CDPDP mechanism*

Rewriting equation (3.52) for this configuration:

$$\begin{aligned}
\theta_z |_{DP1} &= \frac{1}{2w_1^2} \left( \frac{1}{k_{33}} - (0.5u_y)^2 k_{11}^{(2)} \right) \left( m_{z11} - m_{z1} + f_{y11} - f_{x11} (w_{offset} + 0.5u_y) + 0.5u_y (2k_{12}^{(0)} - f_{x11} k_{12}^{(1)}) \right) \\
&+ \frac{1}{2w_2^2} \left( \frac{1}{k_{33}} - (0.5u_y)^2 k_{11}^{(2)} \right) \left( m_{z11} - 0.5u_y (2k_{12}^{(0)} + f_{x11} k_{12}^{(1)}) \right) \\
\theta_z |_{DP1} &= -\frac{1}{2w_1^2} \left( \frac{1}{k_{33}} - (0.5u_y)^2 k_{11}^{(2)} \right) \left( -m_{z22} + m_{z1} + f_{y22} + f_{x22} (w_{offset} + 0.5u_y) + 0.5u_y (2k_{12}^{(0)} + f_{x22} k_{12}^{(1)}) \right) \\
&+ \frac{1}{2w_2^2} \left( \frac{1}{k_{33}} - (0.5u_y)^2 k_{11}^{(2)} \right) \left( -m_{z22} - 0.5u_y (2k_{12}^{(0)} - f_{x22} k_{12}^{(1)}) \right)
\end{aligned} \tag{D.2}$$

Moreover,

$$\theta_z |_{DP1} = \theta_z |_{DP2} \tag{D.3}$$

In order to calculate the center of stiffness, we would apply a force  $f_x$  at different locations on the primary stage and determine the location at which  $\theta_z$  goes to zero. We can resolve this force to a force  $f_x$  and a moment  $-f_x d$  applied at the center of the stage where  $d$  is the distance of the force from the center of the primary stage. Thus, using results derived in Chapter 4, we have:

$$\begin{aligned}
m_{z11} + m_{z22} &= -f_x d \\
f_{x11} &= f_{x22} = 0.5 f_x \\
f_{y11} &= k_{11}^{(0)} \left( 1 + \frac{k_{11}^{(1)} f_x}{4k_{11}^{(0)}} \right) u_y \\
f_{y22} &= k_{11}^{(0)} \left( 1 - \frac{k_{11}^{(1)} f_x}{4k_{11}^{(0)}} \right) u_y
\end{aligned} \tag{D.4}$$

Equations (D.1) to (D.4) can be solved to obtain:

$$\theta_z = f_x \left( p(w_1, w_2, w_{offset}, t, u_y) + q(w_1, w_2, w_{offset}, t, u_y) d \right) + O(f_x^2) \tag{D.5}$$

Using the definition of the COS:

$$\begin{aligned}\theta_z = 0 &= f_x \left( p(w_1, w_2, w_{offset}, t, u_y) + q(w_1, w_2, w_{offset}, t, u_y) d_{\cos} \right) + O(f_x^2) \\ \Rightarrow d_{\cos} &\approx \frac{-p(w_1, w_2, w_{offset}, t, u_y)}{q(w_1, w_2, w_{offset}, t, u_y)}\end{aligned}\quad (D.6)$$

Where the functions  $p$  and  $q$  are given below:

$$\begin{aligned}p(w_1, w_2, w_{offset}, t, u_y) &= -(1 - 0.25k_{11}^{(2)}k_{33}u_y^2)(w_1^2 + w_2^2)((w_{offset}(0.25 - 0.0625k_{11}^{(2)}k_{33}u_y^2) \\ &\quad + u_y(0.125 + 0.125k_{11}^{(1)} - (0.03125 + 0.03125k_{11}^{(1)})k_{11}^{(2)}k_{33}u_y^2))w_2^2 \\ &\quad + k_{12}^{(1)}u_y(0.125 - 0.03125k_{11}^{(2)}k_{33}u_y^2)(w_1^2 + w_2^2))\end{aligned}\quad (D.7)$$

$$\begin{aligned}q(w_1, w_2, w_{offset}, t, u_y) &= (-0.25 - k_{11}^{(2)}k_{33}u_y^2(-0.125 + 0.015625k_{11}^{(2)}k_{33}u_y^2))w_1^4 + \\ &\quad (-0.5 - k_{11}^{(2)}k_{33}u_y^2(-0.25 + 0.03125k_{11}^{(2)}k_{33}u_y^2))w_1^2w_2^2 + \\ &\quad (-0.25 - k_{11}^{(2)}k_{33}u_y^2(-0.125 - 0.015625k_{11}^{(2)}k_{33}u_y^2))w_2^4\end{aligned}\quad (D.8)$$

This closed form result matches very well with corresponding FEA results as shown in Figure 82.

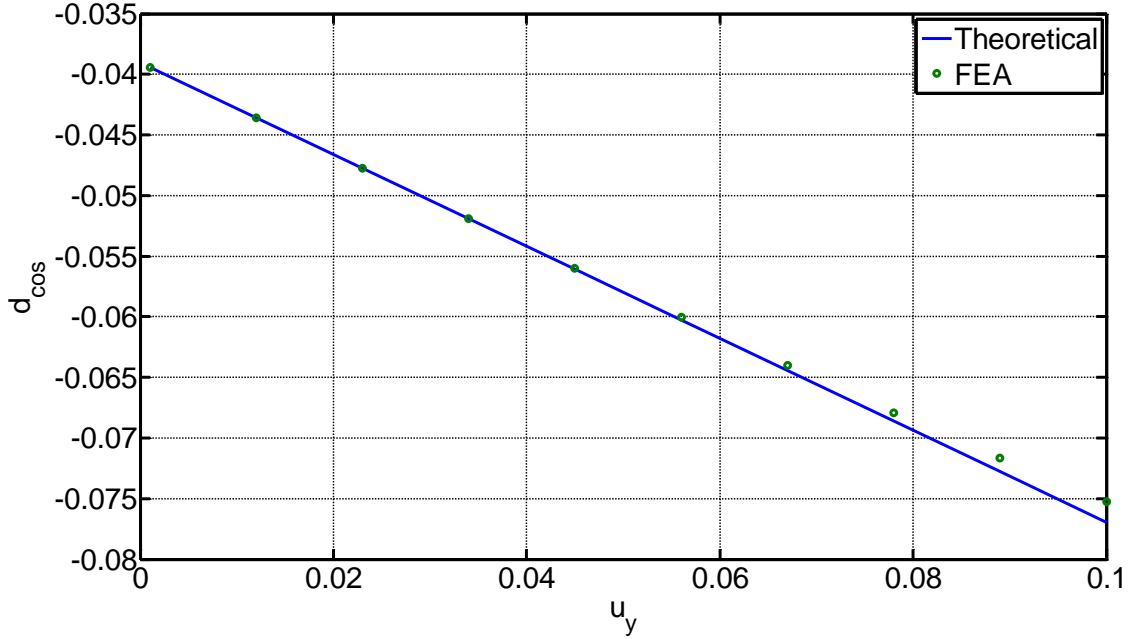


Figure 82: Comparison between theoretical (linear model) and FEA COS for  $w_1=1.0$ ,  $w_2=0.8$ ,  $t=0.0123$ ,  $w_{off}=0.1$ ,  $w_3=0.5$ ,  $l_3=0.3$ . Almost no sensitivity was observed w.r.t.  $f_x$ .



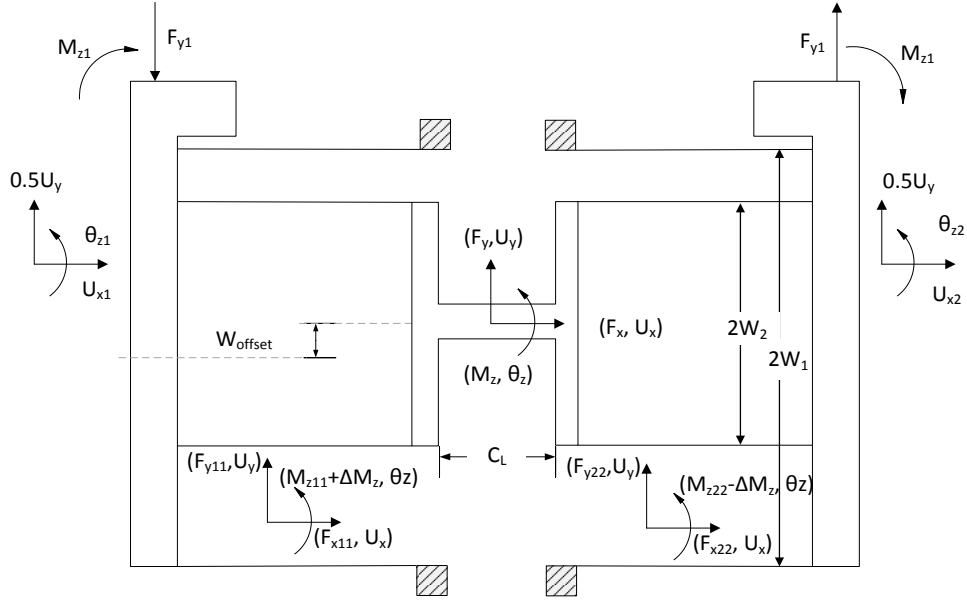


Figure 83: Special case of the CDPDP design.

For the case shown in Figure 83, an extra moment would be applied on each double parallelogram by the motion direction force  $F_y$  and this moment would be given by:

$$\Delta M_z = 0.5F_{y11}C_L \quad (D.9)$$

Using the same procedure as before, the new center of stiffness would be given by:

$$d_{\cos}(w_1, w_2, w_{\text{offset}}, c_l, t, u_y) = -\frac{w_{\text{offset}}w_2^2}{(w_1^2 + w_2^2)} + \left( \frac{(k_{11}^{(1)} + 1)w_1^2}{2(w_1^2 + w_2^2)} - (0.5 - 0.25c_l)k_{11}^{(1)} - 0.5(k_{12}^{(1)} + 1) \right) u_y + O(u_y^2) \quad (D.10)$$

The higher order  $u_y$  terms were observed to be small enough to be ignorable.

### X-direction displacement at COS

In our derivation of the axial stiffness of the CDPDP mechanism, we neglected the contribution of the rotation of the parallelograms in the  $x$ -direction relations i.e. approximate decoupling between the  $x, y$  and  $\theta$  direction relations. However, for the case shown in Figure 83, this might not be true due to the presence of an offset between the

COS of outer parallelogram and the location of the COS of the CDPDP mechanism on the primary stage. This scenario is shown in Figure 84.

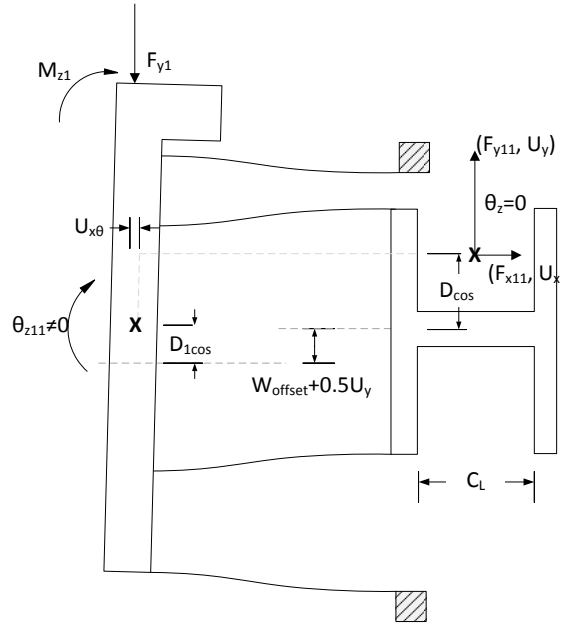


Figure 84: Right half of the CDPDP mechanism when a force is applied exactly at the COS

Using the previous analysis for determining the location of the COS, the rotation  $\theta_{z1}$  of the secondary stage can be easily calculated<sup>13</sup>. The additional displacement  $U_{x\theta}$  would then be:

$$\begin{aligned} u_{x\theta} &= \theta_{z1} \left( -d_{1\cos} + w_{offset} + 0.5u_y + d_{\cos} \right) \\ \Rightarrow u_x &= u_{x-decoupled} + u_{x\theta} \end{aligned} \quad (D.11)$$

Where  $d_{1\cos}$  is the location of the COS of the outer parallelogram. In order to calculate this, we can rewrite equation (3.3) for the rotation of the parallelogram and equate it to zero:

---

<sup>13</sup> The equation is too long to be listed here. It can be found in ‘‘

$$\begin{aligned}
0 &= \frac{1}{2w_1^2} \left( \frac{1}{k_{33}} - \frac{u_y^2}{4} k_{11}^{(2)} \right) [f_{x11} d_{1\cos} - 0.5u_y (2k_{12}^{(0)} - f_{x11} k_{12}^{(1)})] \\
\Rightarrow d_{1\cos} &= \frac{0.5u_y (2k_{12}^{(0)} - f_{x11} k_{12}^{(1)})}{f_{x11}} = \frac{0.5u_y (2k_{12}^{(0)} - 0.5k_{12}^{(1)})}{0.5f_x}
\end{aligned} \tag{D.12}$$

Moreover,  $d_{\cos}$  is COS of the CDPDP mechanism. Using equation (D.11), the new theoretical value of the stiffness for an applied force  $f_x$  is:

$$k_x|_{corrected} = \frac{f_x}{\left( \frac{f_x}{k_x|_{uncoupled}} - u_{x0} \right)} \tag{D.13}$$

Where  $k_x|_{uncoupled}$  is given by equation (4.30). For the design shown in Figure 51 the  $x$ -direction stiffness is plotted in Figure 85. The FEA stiffness and the closed-form stiffness (given by equation (D.13)) match to within 5%.

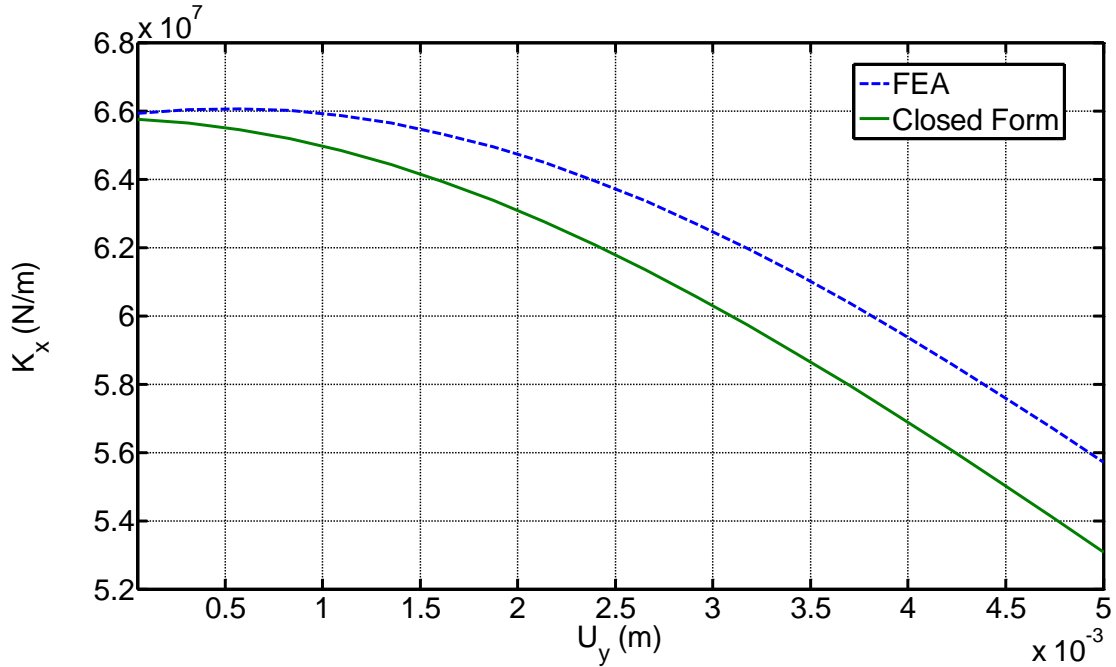


Figure 85: Closed form and FEA  $x$ -direction stiffness for the CDPDP design used in the experiment (Figure 51)

## Appendix E

### DERIVATION OF THE LIMIT ON PRE-BENDING FOR COMB DRIVE ACTUATORS

For the  $x$ -direction stiffness of the pre-bent CDPDP configuration (with a pre-bend of  $U_{ypr}$ ), we can use an approximation similar to that given by equation (5.27). However, the limit on the thickness would now be lower than that given by equation (5.26). Assuming that the thickness is larger than this limit so that the ratio between the elastic and elasto-kinematic terms is larger than 5% but still lower than 10%, or in other words, the elastic term is  $\varepsilon$  times (where  $0.05 < \varepsilon < 0.1$ ) the elasto-kinematic term at the snap in point  $U_y|_{\max}$  i.e.

$$\begin{aligned}
 K_x &\approx 2 \frac{EI_{zz}}{L^3} \frac{1}{\left( \frac{1}{k_{33}(a_0)} - \frac{(u_y|_{\max} - u_{ypr})^2}{4} k_{11}^{(2)}(a_0) \right)} : \frac{1}{k_{33}(a_0)} = -\varepsilon \frac{(u_y|_{\max} - u_{ypr})^2}{4} k_{11}^{(2)}(a_0) \\
 \Rightarrow K_x &= 2 \frac{EI_{zz}}{L^3} \frac{-1}{\frac{(u_y|_{\max} - u_{ypr})^2}{4} k_{11}^{(2)}(a_0) (\varepsilon + 1)} \approx 2 \frac{EI_{zz}}{L^3} (1 - \varepsilon) \frac{-4L^2}{(U_y|_{\max} - U_{ypr})^2 k_{11}^{(2)}(a_0)}
 \end{aligned} \tag{E.1}$$

Using the above relation along with the motion direction stiffness given by equation (5.23) and the axial snap-in criterion given by equation (1.16) with no initial overlap, we get:

$$\begin{aligned}
 2(1+S) \frac{(U_y|_{\max})^2}{G^2} &= (1-\varepsilon) \left( \frac{-4L^2}{(U_y|_{\max} - U_{ypr})^2 k_{11}^{(2)} k_{11}^{(0)}} \right) \\
 \Rightarrow (U_y|_{\max})^2 (U_y|_{\max} - U_{ypr})^2 &= -\frac{2(1-\varepsilon)G^2L^2}{(1+S)k_{11}^{(2)}k_{11}^{(0)}} \\
 \Rightarrow U_y|_{\max} (U_y|_{\max} - U_{ypr}) &= \pm \sqrt{-\frac{2(1-\varepsilon)G^2L^2}{(1+S)k_{11}^{(2)}k_{11}^{(0)}}} \\
 \Rightarrow (U_y|_{\max})^2 - U_{ypr} U_y|_{\max} \pm \sqrt{-\frac{2(1-\varepsilon)G^2L^2}{(1+S)k_{11}^{(2)}k_{11}^{(0)}}} &= 0
 \end{aligned} \tag{E.2}$$

The determinant of this quadratic equation is given by:

$$D = \sqrt{U_{ypr}^2 \mp 4 \sqrt{-\frac{2(1-\varepsilon)G^2L^2}{(1+S)k_{11}^{(2)}k_{11}^{(0)}}}} \quad (E.3)$$

The equation will only have two roots i.e. two intersections only (Figure 66) if one of the determinants is imaginary. This implies that:

$$\begin{aligned} U_{ypr}^2 &< 4 \sqrt{-\frac{2(1-\varepsilon)G^2L^2}{(1+S)k_{11}^{(2)}k_{11}^{(0)}}} \\ \Rightarrow U_{ypr} &< 2 \sqrt{GL \sqrt{-\frac{2(1-\varepsilon)}{(1+S)k_{11}^{(2)}k_{11}^{(0)}}}}} \end{aligned} \quad (E.4)$$

Therefore, the critical pre-bend is given by:

$$U_{ypr} |_{crit} = 2 \sqrt{GL \sqrt{-\frac{2(1-\varepsilon)}{(1+S)k_{11}^{(2)}k_{11}^{(0)}}}} \approx (1-0.25\varepsilon) \sqrt{GL \sqrt{-\frac{32}{(1+S)k_{11}^{(2)}k_{11}^{(0)}}}}} \quad (E.5)$$

This shows that for an  $\varepsilon=0.1$ , the error in the critical pre-bend is less than 2.5%.

For the DPDP mechanism, the critical pre-bend would be exactly similar with the elasto-kinematic term  $k_{11}^{(2)}$  getting replaced by the equivalent term for the DPDP mechanism (equation (3.63)) i.e.:

$$U_{ypr} |_{crit} \approx \sqrt{GL \sqrt{\frac{32}{(1+S) \left( -k_{11}^{(2)} + \frac{(k_{11}^{(1)})^2}{k_{11}^{(0)}} \right) k_{11}^{(0)}}}} \quad (E.6)$$

## References

- [1] R. V. Jones, "Some uses of elasticity in instrument design," *Journal of Scientific Instruments*, vol. 39, pp. 193-&, 1962.
- [2] S. T. Smith, *Flexures: Elements of Elastic Mechanisms*: Gordon and Breach Science, New York, 2000.
- [3] S. T. Smith, *Foundations of Ultra-Precision Mechanism Design*: Taylor & Francis, 2003.
- [4] L. C. Hale, "Principles and Techniques for Designing Precision Machines," Ph.D. Thesis, Mechanical Engineering, Massachusetts Institute of Technology, 1999.
- [5] A. H. Slocum, *Precision Machine Design*. Dearborn, MI: Society of Manufacturing Engineers, 1992.
- [6] G. J. Siddall, "Flexure stage alignment apparatus," U.S. Patent 46944777, 1988.
- [7] Y. Ando, "Development of three-dimensional electrostatic stages for scanning probe microscope," *Sensors and Actuators A: Physical*, vol. 114, pp. 285-291, Sep 2004.
- [8] G. L. Dai, F. Pohlenz, H. U. Danzebrink, M. Xu, K. Hasche, and G. Wilkening, "Metrological large range scanning probe microscope," *Review of Scientific Instruments*, vol. 75, pp. 962-969, Apr 2004.
- [9] A. Sinno, P. Ruaux, L. Chassagne, S. Topcu, Y. Alayli, G. Lerondel, S. Blaize, A. Bruyant, and P. Royer, "Enlarged atomic force microscopy scanning scope: Novel sample-holder device with millimeter range," *Review of Scientific Instruments*, vol. 78, Sep 2007.
- [10] A. Weckenmann and J. Hoffmann, "Long range 3 D scanning tunnelling microscopy," *Cirp Annals-Manufacturing Technology*, vol. 56, pp. 525-528, 2007.
- [11] L. Hongzhong, L. Bingheng, D. Yucheng, T. Yiping, and L. Dichen, "A motor-piezo actuator for nano-scale positioning based on dual servo loop and nonlinearity compensation," *Journal of Micromechanics and Microengineering*, vol. 13, p. 295, 2003.
- [12] C. A. Mirkin, "Dip-pen nanolithography: Automated fabrication of custom multicomponent, sub-100-nanometer surface architectures," *MRS Bulletin*, vol. 26, pp. 535-538, Jul 2001.
- [13] J. A. Kramar, "Nanometre resolution metrology with the molecular measuring machine," *Measurement Science & Technology*, vol. 16, pp. 2121-2128, Nov 2005.

- [14] A. Sebastian, A. Pantazi, H. Pozidis, and E. Eleftheriou, "Nanopositioning for probe-based data storage," *IEEE Control Systems Magazine*, vol. 28, pp. 26-35, Aug 2008.
- [15] R. Duarte, M. R. Howells, Z. Hussain, T. Lauritzen, R. McGill, E. Moler, and J. Spring, "A linear motion machine for soft x-ray interferometry," presented at the Optomechanical Design and Precision Instruments, Bellingham, 1997.
- [16] S. Henein, P. Spanoudakis, S. Droz, L. I. Myklebust, and E. Onillon, "Flexure pivot for aerospace mechanisms," in *10th European Space Mechanisms and Tribology Symposium, Proceedings*. vol. 524, R. A. Harris, Ed., ed 2200 Ag Noordwijk: Esa Publications Division C/O Estec, 2003, pp. 285-288.
- [17] S. Henein, P. Spanoudakis, P. Schwab, L. Giriens, L. Lisowski, E. Onillon, and L. I. Myklebust, "Mechanical slit mask mechanism for the James Webb Space Telescope spectrometer," in *Optical, Infrared, and Millimeter Space Telescopes*, 2004, pp. 765-776.
- [18] K. H. L. Chau, S. R. Lewis, Y. Zhao, R. T. Howe, S. F. Bart, and R. G. Marcheselli, "An integrated force-balanced capacitive accelerometer for low-g applications," *Sensors and Actuators A: Physical*, vol. 54, pp. 472-476, Jun 1996.
- [19] K. D. N., G. Li, and A. C. McNeil, "Single proof mass, 3 axis MEMS transducer," U.S. Patent 6845670, 2005.
- [20] S. E. Alper, K. M. Silay, and T. Akin, "A low-cost rate-grade nickel microgyroscope," *Sensors and Actuators A: Physical*, vol. 132, pp. 171-181, Nov 2006.
- [21] C. Tsou and et al., "A novel self-aligned vertical electrostatic combdrives actuator for scanning micromirrors," *Journal of Micromechanics and Microengineering*, vol. 15, p. 855, 2005.
- [22] G. A. Roman, G. J. Wiens, and Asme, "MEMS optical force sensor enhancement via compliant mechanism," in *Proceedings of the Asme International Design Engineering Technical Conferences and Computers and Information in Engineering Conference 2007, Vol 8, Pts A and B*, New York, 2008, pp. 127-135.
- [23] S. Awtar, "Synthesis and Analysis of Parallel Kinematic XY Flexure Mechanisms," Sc. D. Thesis, Mechanical Engineering, Massachusetts Institute of Technology, 2003.
- [24] S. Awtar, A. H. Slocum, and E. Sevincer, "Characteristics of Beam-Based Flexure Modules," *Journal of Mechanical Design*, vol. 129, pp. 625-639, 2007.
- [25] S. Awtar and A. H. Slocum, "Constraint-based design of parallel kinematic XY flexure mechanisms," *Journal of Mechanical Design*, vol. 129, pp. 816-830, Aug 2007.
- [26] S. Awtar, J. Ustick, and S. Sen, "An XYZ Parallel-Kinematic Flexure Mechanism With Geometrically Decoupled Degrees of Freedom," *Journal of Mechanisms and Robotics-Transactions of the Asme*, vol. 5, Feb 2013.
- [27] J. G. Bednorz, R. L. Hollis, Jr., M. Lanz, W. D. Pohl, and C. E. Yeack-Scranton, "Piezoelectric XY Positioner," U.S. Patent 4,520,570, 1985.

- [28] J. Ustick, "Design, Fabrication and Experimental Characterization of a Large Range XYZ parallel Kinematic Flexure Mechanism," M.S.E. Thesis, Mechanical Engineering, University of Michigan, 2012.
- [29] F. L. Fischer, "Symmetrical three degree of freedom compliance structure," U.S. Patent 4447048, 1984.
- [30] X. Y. Tang, I. M. Chen, and Ieee, "A large-displacement and decoupled XYZ flexure parallel mechanism for micromanipulation," presented at the 2006 IEEE International Conference on Automation Science and Engineering, Vols 1 and 2, New York, 2006.
- [31] L. L. Howell, *Compliant mechanisms*, 2001.
- [32] M. Olfatnia, S. Sood, J. J. Gorman, and S. Awtar, "Large Stroke Electrostatic Comb Drive Actuators Enabled by a Novel Flexure Mechanism," *Journal of Microelectromechanical Systems*, 2012.
- [33] R. Legtenberg, A. W. Groeneveld, and M. Elwenspoek, "Comb-drive actuators for large displacements," *Journal of Micromechanics and Microengineering*, vol. 6, pp. 320-329, Sep 1996.
- [34] J. D. Grade, H. Jerman, and T. W. Kenny, "Design of large deflection electrostatic actuators," *Journal of Microelectromechanical Systems*, vol. 12, pp. 335-343, Jun 2003.
- [35] <http://www.sfu.ca/immr/gallery/actuators.html>.
- [36] M. Olfatnia, S. Sood, and S. Awtar, "Note: An asymmetric flexure mechanism for comb-drive actuators," *Review of Scientific Instruments*, vol. 83, p. 116105, 2012.
- [37] G. Y. Zhou and P. Dowd, "Tilted folded-beam suspension for extending the stable travel range of comb-drive actuators," *Journal of Micromechanics and Microengineering*, vol. 13, pp. 178-183, Mar 2003.
- [38] T. T. Trutna and S. Awtar, "An Enhanced Stability Model for Electrostatic Comb-Drive Actuator Design," *ASME Conference Proceedings*, vol. 2010, pp. 597-605, 2010.
- [39] W. Huang and G. Y. Lu, "Analysis of lateral instability of in-plane comb drive MEMS actuators based on a two-dimensional model," *Sensors and Actuators A: Physical*, vol. 113, pp. 78-85, Jun 2004.
- [40] T. J. Teo, I. M. Chen, G. L. Yang, and W. Lin, "A flexure-based electromagnetic linear actuator," *Nanotechnology*, vol. 19, Aug 2008.
- [41] P. J. Patt, "Frictionless motor material testing," USA Patent 6405599, 2002.
- [42] R. V. Jones, "Parallel and rectilinear spring movements," *Journal of Scientific Instruments*, vol. 28, pp. 38-41, 1951.
- [43] S. Awtar, S. Sood, and M. Olfatnia, "Linear Flexure Bearing Designs with high Off-axis Stiffness," US Patent 7935-3048-1, 2012.
- [44] D. H. Hodges, "Proper definition of curvature in nonlinear beam kinematics," *Aiaa Journal*, vol. 22, pp. 1825-1827, 1984/12/01 1984.
- [45] S. Awtar and S. Sen, "A Generalized Constraint Model for Two-Dimensional Beam Flexures: Nonlinear Load-Displacement Formulation," *Journal of Mechanical Design*, vol. 132, Aug 2010.



- [46] T. R. Tauchert, *Energy Principles in Structural Mechanics*: McGraw-Hill, New York, 1974.
- [47] S. Awtar and S. Sen, "A Generalized Constraint Model for Two-Dimensional Beam Flexures: Nonlinear Strain Energy Formulation," *Journal of Mechanical Design*, vol. 132, Aug 2010.
- [48] R. V. Jones, *Instruments and experiences: papers on measurement and instrument design*: Wiley, 1988.
- [49] S. Awtar and E. Sevincer, "Elastic Averaging in Flexure Mechanisms: A Multi-Beam Parallelogram Flexure Case-Study," *ASME Conference Proceedings*, vol. 2006, pp. 251-257, 2006.
- [50] D. M. Brouwer, "Design principles for six degrees-of-freedom MEMS-based precision manipulators," Enschede, 2007.
- [51] J. E. Plainevaux, "Mouvement parasite vertical d'une suspension élastique symétrique à compensation et asservissement," *Nuovo Cimento*, vol. 11, pp. 626-638, 1954.
- [52] R. V. Jones and I. R. Young, "Some parasitic deflexions in parallel spring movements," *Journal of Scientific Instruments*, vol. 33, p. 11, 1956.
- [53] J. H. Jerman and J. D. Grade, "Minature device with translatable member," U.S. Patent 6664707, 2003.
- [54] D. M. Brouwer, A. Otten, J. B. C. Engelen, B. Krijnen, and H. M. J. R. Soemers, "Long-range elastic guidance mechanisms for electrostatic comb-drive actuators," presented at the Tenth International Conference of the European Society for Precision Engineering & Nanotechnology, Delft, the Netherlands, 2010.
- [55] <http://www.physikinstrumente.com/>.
- [56] [www.metrolog.com](http://www.metrolog.com).
- [57] <http://www.lionprecision.com/>.
- [58] J. W. Wittwer and L. L. Howell, "Mitigating the Effects of Local Flexibility at the Built-In Ends of Cantilever Beams," *Journal of Applied Mechanics*, vol. 71, pp. 748-751, 2004.
- [59] <http://www.matweb.com/>.
- [60] D. M. Brouwer, B. R. Jong de, and H. M. J. R. Soemers, "Design and modeling of a six DOFs MEMS-based precision manipulator," *Precision Engineering*, vol. 34, pp. 307-319, 2010.
- [61] J. Dong and P. M. Ferreira, "Electrostatically Actuated Cantilever With SOI-MEMS Parallel Kinematic XY Stage," *Journal of Microelectromechanical Systems*, vol. 18, pp. 641-651, Jun 2009.
- [62] C. J. Kim, A. P. Pisano, and R. S. Muller, "Overhung Electrostatic Microgripper," *J. Microelectromechanical. Syst.*, 1992.
- [63] D. M. Brouwer, B. R. Jong de, H. M. J. R. Soemers, and J. Dijk van, "Sub-nanometer stable precision MEMS clamping mechanism maintaining clamp force unpowered for TEM application," *Journal of Micromechanics and Microengineering*, vol. 16, pp. S7-S12, 2006.

- [64] H. Jerman, J. D. Grade, and J. D. Drak, "Electrostatic microactuator and method for use thereof," US Patent 5 998 906, 1999.
- [65] D. Elata and V. Leus, "How slender can comb-drive fingers be?," *Journal of Micromechanics and Microengineering*, vol. 15, pp. 1055-1059, May 2005.
- [66] C. C. Chen, C. Lee, Y. J. Lai, and W. C. Chen, "Development and application of lateral comb-drive actuator," *Japanese Journal of Applied Physics Part 1-Regular Papers Short Notes & Review Papers*, vol. 42, pp. 4059-4062, Jun 2003.
- [67] J. D. Grade, K. Y. Yasumura, and H. Jerman, "Advanced, vibration-resistant, comb-drive actuators for use in a tunable laser source," *Sensors and Actuators A: Physical*, vol. 114, pp. 413-422, 2004.
- [68] H. Max Ti-Kuang, H. Gordon Kou-Wei, H. Jing-Yi, L. Ke-Min, C. Rongshun, and Y. Jer-Liang Andrew, "Extending displacements of comb drive actuators by adding secondary comb electrodes," *Journal of Micromechanics and Microengineering*, vol. 16, p. 684, 2006.